ROYAUME DU MAROC
Université Mohammed V - RABAT -
جامعة محمد الخامس – الرباط –
Faculté des sciences
كلية العلوم
CENTRE D'ETUDES DOCTORALES - SCIENCES ET TECHNOLOGIES

N° d'ordre: 3503

THESE

En vue de l'obtention du : **DOCTORAT**

Centre de Recherche : *Sciences des Matériaux*
Structure de Recherche : *Matériaux, Nanotechnologies et Environnement / Optique, Photonique et Nanotechnologie*
Discipline : *Chimie*
Spécialité : *Sciences des matériaux, Optique et Photonique.*

Présentée et Soutenue le : 15/07/2021 par

Ikram ANEFNAF

Advanced and innovative strategies for high efficiency: organic and inorganic solar cells

JURY

Hamid EZ-ZAHRAOUY	PES	Faculté des Sciences, Université Mohammed V de Rabat - Maroc	Président
Noureddine MASAIF	PES	Faculté des Sciences, Université Ibn Tofail de Kenitra – Maroc	Rapporteur / Examinateur
Mohamed BENAISSA	PES	Faculté des Sciences, Université Mohammed V de Rabat – Maroc	Rapporteur / Examinateur
Nacer KHACHANI	PES	Faculté des Sciences, Université Mohammed V de Rabat - Maroc	Rapporteur / Examinateur
M'Hamed TAIBI	PES	École Normale Supérieure, Université Mohammed V de Rabat	Examinateur
Edgardo SAUCEDO	PH	Polytechnic University of Catalonia / IREC Barcelone	Invité
Safae AAZOU	PA	Faculté des Sciences, Université Mohammed V de Rabat – Maroc	Co-Encadrante
Zouheir SEKKAT	PES	Faculté des Sciences, Université Mohammed V de Rabat - Maroc	Directeur de Thèse

Année Universitaire: 2020/2021

✉ Faculté des Sciences, avenue Ibn Battouta, BP. 1014 RP, Rabat –Maroc
☎ 00212(05) 37 77 18 76 🖷 00212(05) 37 77 42 6; http://www. fsr. um5.ac.ma

Dedication

I cannot forget probably the biggest support in my life, my mother, my father and my brothers, as well as my big family. Thanks for your unconditional support, love, and help, for working hard to give me everything I needed. I feel so fortunate to have you, and I am eternally grateful to you, thank to you that I am standing defending the fruit of your support and encouragement.

I humbly address my thanks to all concerned people, and any omission in this acknowledgment does not mean a lack of gratitude.

"Never give up and always let chances come through your door",

Thanks mom for being always by my side in good times and bad.

Never give up!

<u>I dedicate this thesis to</u>

My mother

My father

My brothers

My grand mother

My family

Acknowledgments

The work performed in this dissertation is the fruit of the international collaboration between the laboratory of Materials, Nanotechnology and Environment/ Optics and Photonics and Nanotechnology at Mohammed V University in Rabat (UM5R), Optics and Photonics at the Moroccan Foundation for Advanced Science, Innovation, and Research (MAScIR), the laboratory of Solar Energy Materials and systems at the Catalonia Institute for Energy Research in Barcelona (IREC), and Strasbourg Institute of Material Physics and Chemistry (IPCMs)/CNRS and Laboratory of Engineering, Computer Science and Imagery, Strasbourg University (ICube)/ CNRS. I am grateful to the financial support provided by INFINITE CELL project (H2020-MSCA-RISE-2017 777968) from the European Commission and the project PPR/2015/59 funded by the Moroccan Ministry of Higher Education and Research, and Erasmus+ MEDSOL program. This thesis is supervised by Professor Zouheir SEKKAT and Professor Safae Aazou.

I am writing this note of gratitude as a finishing touch of my thesis. It has been a period of intense learning for me, not only in the scientific research, but also in personal life. I would like to express my gratitude to the people who have supported and helped me throughout Ph.D.

My deepest gratitude and acknowledgments are firstly expressed to my thesis director, ***Zouheir SEKKAT***, PES at Faculty of Sciences/Mohammed V University Rabat, who recommended me an interesting research topic and continually supported my work, and offer scholarship through project and exchanges. Without his patience, guidance, uncountable advices, and help, this thesis would not have been possible. I take this opportunity to thank him sincerely for his guidance, critics, gentities, availability, and human qualities.

I would like to express my profound gratitude to my co-supervisor, ***Safae AAZOU***, PA at Faculty of Sciences/Mohammed V University Rabat, who throughout these years was always available for discussions, valuable remarks, guidance, and encouragement. I am very grateful for her permanent support, scientific guidance, constant optimism and encouragement throughout this long walk with all its “ups and downs”. I deeply appreciate her careful revisions of all my work. I also would like to thank her friendship. Thank you for being so caring and supportive!

I wish to express my gratitude to the jury members that have accepted delightedly to judge this work. First, special thanks to ***Hamid EZ-ZAHRAOUY,*** PES at Faculty of Sciences/Mohammed V University Rabat, for honoring me and accepting to preside my thesis defense committee.

I extend my sincere thanks to ***Noureddine MASAIF***, PES at Faculty of Sciences/Ibn Tofail University Kenitra, for generously offering their time, guidance and good will to review and examine this manuscript and giving valuable feedback and remarks.

I extend my sincere thanks to ***Mohamed BENAISSA***, PES at Faculty of Sciences/ Mohammed V University Rabat, for generously offering their time, guidance and good will to review and examine this manuscript and giving valuable feedback and remarks.

I would like to thank ***Nacer KHACHANI,*** PES at Faculty of Sciences/Mohammed V University Rabat, for generously offering their time, guidance and good will to review and examine this manuscript and giving valuable feedback and remarks.

My appreciation goes to ***M'Hamed TAIBI, PES*** at École Normale Supérieure, Mohammed V University Rabat, for accepting to examine this work and give valuable remarks and insightful comments.

As well, I would like to address my heartfelt gratitude to ***Edgardo SAUCEDO,*** PH at Polytechnic University of Catalonia/IREC Barcelone, for his availability each time I needed his guidance and for all the fruitful meetings. Thanks for accepting the invitation and coming. Thank you for treating me as one of your team.

I am deeply indebted to ***Guy SCHMERBER***, his friendly manner he helped me dramatically improve scientific skills always making me remembers that "There are plenty of other things in life apart from you work and Dream of Philosophy". I am very grateful to ***Thomas HIESER*** for his very solid, clear and well-structured explanations for various types of questions that I have ever asked him. I also need to say thank you to all people from Strasbourg University, IPCMs and ICube Teams, who kindly welcomed me and made me feel home the first day, and who taught me a lot during my stay, especially professor Aziz DINIA, professor Abdelilah SLAOUI, Thomas FIX and Zimmermann Nicolas.

During my Ph.D. thesis, I had the chance to live an incredible experience that has enormously impacted me in many ways, extend my scientific network and discover new culture and fulfill my experimental work plan. My internship at IREC has allowed me to meet amazing souls.

To my Spanish speaking friends from the SEMS group (Solar Energy Materials and Systems), Yudania, Pedro, Rober, Alex, Alex', Diouldé, Sergio, Kunal, Zacharie, Maxim, Nacho and Enas. I sincerely acknowledge their hospitality, unconditional help, and all our discussions about nothing and everything. Thank you … for your assistance and scientific discussion and availability.

I would like to thank MAScIR foundation for providing a good working environment and the access to the platform with cutting edge equipment and leadership to make it a success. A very warm thanks to MAScIR platform staff for their help and guidance during my stay at MAScIR. My deep appreciation goes out to the MAScIR administration who have offer at me infinite support (from different projects) to my Ph.D. project

I will not miss the opportunity to acknowledge Cedoc administration staff, especially professor ***Mohammed LFERD***. Without providing such good administrative facilities, this work would have never seen light.

My appreciation also extends to my laboratory colleagues from Optics and Photonics center: Dr. Siham Refki, Dr. Imad Maouli, Dr. Zakaria Laghfour, Yahya Bougid, Sara Moujdi, Sanae Elhani, Naoufal Ennouhi, Brahim Boudene, Youssef El-Idrissi, Nada Benhaddou and Abdeljalil Errafyg, for sharing great and friendly moments together.

Abstract

The main work of this thesis is divided into two parts: The first has an objective to shed light on the feasibility of developing a novel wide band-gap kesterite based solar cells using pure Ge ($Cu_2ZnGeSe_4$), as an alternative solution to overcome the drawbacks related to free Ge-kesterite solar cells (Tin-kesterite). To fulfill this general objective, the following sub-objectives are proposed and experimented: (i) optimization of sequential processes for $Cu_2ZnGeSe_4$ absorbers synthesis, (ii) study and identification of defect types and concentrations of off-stoichiometric concentrations of CZGeSe and (iii) understanding the main losses mechanisms limiting the performance of kesterite CZGeSe. In the second part, the elaboration and characterization of efficient inverted bulk heterojunction organic devices are presented and discussed. The second part of this thesis is dedicated to optimize and analyze organic solar cells using different organic materials, small molecules (fullerene derivatives) as acceptors and conjugated polymers as donors.

Keywords: Kesterite, CZGeSe, PVD, synthesis, defects, off-stoichiometric, organic solar cells, cathode buffer layer, ZnO, SnO_2, PEIE.

Résumé

Les travaux menés lors de cette thèse sont divisés en deux parties. La première partie a pour objectif de faire la lumière sur la faisabilité du développement d'une nouvelle cellule solaire à base de kesterite à large bande interdite utilisant du Ge pur ($Cu_2ZnGeSe_4$), comme solution alternative pour surmonter les inconvénients liés pour libérer les cellules solaires Ge-kesterite (on remplace donc Sn par Ge). Pour remplir cet objectif, les sous-objectifs suivants sont proposés et expérimentés: (i) Optimisation de procédés séquentiels pour la synthèse d'absorbeurs Cu2ZnGeSe4, consistant à déposer par pulvérisation cathodique des empilements métalliques Cu/Zn/Ge sur des substrats en verre sodo-calcique revêtus de Mo, suivi d’un recuit thermique sous atmosphère Se+Ge, (ii) Etude des concentrations hors stoechiométrie de CZGeSe et identification des types de défauts et (iii) Compréhension des principaux mécanismes de pertes limitant la performances des cellules solaires à base de kesterite CZGeSe. La deuxième partie de cette thèse est dédiée à l'optimisation et à l'analyse des cellules solaires organiques en utilisant différents matériaux organiques : donneur et accepteur.

Mots clés : Kesterite, CZGeSe, PVD, synthèse, défauts, hors stoechiométrie, cellules solaires organiques, couche tampon cathodique, ZnO, SnO_2.

Résumé Détaillé

Les travaux menés lors de cette thèse sont divisés en deux parties. La première partie a pour objectif de faire la lumière sur la faisabilité du développement d'une nouvelle cellule solaire à base de kesterite à large bande interdite utilisant du Ge pur ($Cu_2ZnGeSe_4$), comme solution alternative pour surmonter les inconvénients liés pour libérer les cellules solaires Ge-kesterite (on remplace donc Sn par Ge). Pour remplir cet objectif, les sous-objectifs suivants sont proposés et expérimentés : (i) Optimisation de procédés séquentiels pour la synthèse d'absorbeurs $Cu_2ZnGeSe_4$, consistant à déposer par pulvérisation cathodique des empilements métalliques Cu/Zn/Ge précurseurs sur des substrats en verre sodo-calcique revêtus de Mo, suivi d'un recuit thermique sous atmosphère Se+Ge, à l'aide d'une boîte semi-fermée en graphite dans un four tubulaire conventionnel, (ii) Etude des concentrations hors stoechiométrie de CZGeSe et identification des types de défauts et (iii) Compréhension des principaux mécanismes de pertes limitant la performances des cellules solaires à base de kesterite CZGeSe, y compris l'ingénierie de surface pour compenser et atténuer ces pertes.

La deuxième partie de cette thèse est dédiée à l'optimisation et à l'analyse des cellules solaires organiques en utilisant différents matériaux organiques. Dans ce contexte, une configuration de dispositif inversée est utilisée en utilisant des oxydes métalliques comme couche sélective d'électrons (ESL) et un métal avec un travail d'extraction (WF) élevé (Or) comme anode. Dans cette partie, l'élaboration et la caractérisation de dispositifs organiques à hétérojonction massive inversée efficaces est présentée et discutée. La structure repose sur l'utilisation d'oxydes métalliques tels que ZnO et SnO_2 comme couche de transport d'électrons, pour pallier aux inconvénients associés à la configuration conventionnelle PEDOT : PSS. Pour atteindre cet objectif, les sous-objectifs suivants sont proposés et étudiés: (i) Une nouvelle bicouche tampon cathodique constituée de dioxyde d'étain (SnO_2) combiné à du polyéthylèneimine éthoxylé (PEIE) est utilisée pour surmonter les limitations de la couche tampon cathodique unique pour

les produits organiques par rapport aux cellules solaires basées sur l'hétérojonction massive utilisant une couche active d'ester méthylique d'acide poly (3-hexylthiophène-2,5-diyl):[6,6]-phényl-C71-butyrique (P3HT:PCBM). (ii) Étude du ZnO combiné au PEIE, en utilisant un traitement en solution à basse température, qui peut constituer une excellente couche tampon cathodique pour des cellules solaires organiques inversées efficaces.

Mots clés : Kesterite, CZGeSe, PVD, synthèse, défauts, hors stoechiométrie, cellules solaires organiques, couche tampon cathodique, ZnO, SnO_2, PEIE.

Table of contents

List of Tables

List of Figures

List of acronyms and abbreviations

1.5AM:	Air Mass 1.5 Global
BHJ:	Bulk Heterojunction
CB:	Conduction Band
DSSCs:	Dye Sensitized Solar Cells
Ea:	Activation Energy
E_A:	Electron Affinity
Eg:	Band gap energy
EQE:	External Quantum Efficiency
ETL:	Electron Transporting Layer
eV:	Electron volt
FF:	Fill Factor
HOMO:	Highest Occupied Molecular Orbital
HTL:	Hole Transporting Layer
IPCE:	Incident Photon Conversion Efficiency
J_{SC}:	Short-circuit Current
LUMO:	Lowest Unoccupied Molecular Orbital
o-DCB:	ortho-Dichlorobenzene
OPVs:	Organic Photovoltaic
OSCs:	Organic Solar Cells
PCE:	Power Conversion Efficiency
PL:	Photoluminescence
PV:	Photovoltaic
SEM:	Scanning Electron Microscopy
UV-vis:	Ultraviolet-visible

VB:	Valence Band
V_{OC}:	Open-circuit Voltage
p-Si:	polycrystalline silicon
GaAs:	Gallium Arsenide
Si:	Silicon
a-Si:	amorphous silicon
CIS:	Copper Indium Selenide
CIGS:	Copper Indium Gallium Selenide
CdTe:	Cadmium Telluride
CZTS:	Cu_2ZnSnS_4
CZTSe:	$Cu_2ZnSnSe_4$

Preface and publications

The work presented in the first part of this thesis was carried out at the Catalonia Institute for Energy Research (IREC) in Sant Adrià de Besòs (Barcelona), Spain, in the frame work of INFINITE-Cell project funding from the European Union's Horizon 2020 research and innovation programme under grant agreements N° 777968.

The work presented in the second part of this thesis was carried out at the laboratory of Optics and Photonics at the Moroccan Foundation for Advanced Science, Innovation, and Research (MAScIR), the Institute of Material Physics and Chemistry (IPCMs) and Laboratory of Engineering, Computer Science and Imagery, Strasbourg University (ICube), Strasbourg University, CNRS, France; in the framework of the priority research area project "Development of Organic Solar Cells" MEFCRS PPR/2015/59 funded by the Moroccan Ministry of Higher Education and Research, and the Erasmus+ MEDSOL program.

- The main subject of the first part of my thesis is the development of high-efficiency thin-film photovoltaic technologies based on kesterite $Cu_2ZnGeSe_4$ absorbers, using a sequential process (sputtering of metallic stack precursors followed by reactive thermal annealing), while acquiring a deep understanding on the defects exist in CZGeSe-based materials and comprehend the key factors limiting CZGeSe-based thin-film solar cell performance, in order to push up the CZGeSe solar cells efficiency to a more competitive level.
- The second part focus on elaboration and characterization of efficient inverted organic solar cells (iOSCs) based on bulk heterojunction using a novel cathode buffer bilayer consisting of (i) tin dioxide (SnO_2) and (ii) Zinc oxide (ZnO) cathodes buffer layers combined with polyethylenimine-ethoxylated (PEIE) with

active layer of poly(3-hexylthiophene-2,5-diyl):[6,6]-phenyl-C71-butyric acid methyl ester (P3HT: PCBM) .

This thesis is structured around four articles published in high impact peer-review journals. This manuscript is organized into three axes: the first axe casts light on the general fundamentals aspects of solar cells; the second axe is devoted to the wide bandgap kesterite based on $Cu_2ZnGeSe_4$ solar cells and the last part is dedicated to the bulk heterojunction solar cell based on low-bandgap polymer and soluble fullerene derivative.

This manuscript is organized in several chapters as follows:

Chapter@1: provides an overview over the fundamentals aspect of solar cells and the p-n junction properties, moreover an outlook on the different photovoltaic device generations.

Part I: Wide band gap kesterite based on $Cu_2ZnGeSe_4$ solar cells

Chapter@2:puts the spotlight on the history of kesterite absorber material, the crystallographic structure, and the restricted compositional range leading to high efficiencies. Moreover, insights into the commonly found defects in each kesterite type are given along with secondary phases among other challenges facing this material. Finally, a state-of-art of the solutions suggested by other researchers and the contribution of this work are provided.

Chapter@3:covers the experimental methodology employed throughout this work. First, a brief overview of such methodology is presented. Then, the main characterization, deposition and synthesis techniques used throughout the thesis as well as the pieces of equipment employed to carry them out are described and explained. Finally, the fabrication process followed for the fabrication of kesterite solar cells is thoroughly detailed.

Chapter@4:provides the feasibility of synthesizing PV quality $Cu_2ZnGeSe_4$ absorbers using a deposition of Cu/Zn/Ge metallic stack precursors by DC-magnetron sputtering technique, and then selenized through a reactive annealing. The comprehensive understanding of the factors limiting the performance of $Cu_2ZnGeSe_4$ based solar cells is the purpose of this work, by combining a complete characterization of the morphological, structural, compositional and optoelectronic properties of $Cu_2ZnGeSe_4$ absorbers and devices. Besides, an in-depth investigation of the main limitations is carried out, specifically focusing on studying the origin of the large V_{OC} deficit, the main recombination mechanisms, electric transport properties, band tails and possible $Cu_2ZnGeSe_4$/CdS band offset effects.

Chapter@5: presents a correlation between the structural properties and opto-electrical variations in CZGeSe kesterite semiconductors along with changes in composition. This section has as a purpose to determine the narrow efficient zone and to finely tune the formation of secondary phases and defects thus preventing their shortcomings.

Part 2: Bulk heterojunction solar cell based on low band gap polymer and soluble fullerene derivative

Chapter@6:presents the fundamentals of organic semiconductors and organic solar cells. Current understanding of charge carrier generation, transport and recombination mechanisms along with the state-of-the-art knowledge on latest outstanding results in polymer photovoltaic are described.

Chapter@7: main methods and detailed experimental procedures are featured. Starting from cleaning substrate, preparing the solution and the deposition up to completing solar cells going through different indispensable steps. This part of the thesis broaches the diverse techniques used in the synthesis and in the characterization of the material from a structural, morphological, optical and electrical properties.

Chapter@8:provides a novel cathode buffer bilayer lying of tin dioxide (SnO_2) combined with polyethylenimine-ethoxylated (PEIE) to overcome the limitations of the single cathode buffer layer for inverted organic solar cells.

Chapter@9: is intended to shed light on the origin and the mechanisms underlying the beneficial effect of incorporation of ZnO and PEIE as electron transporting layer in inverted organic solar cells, and further explore the role of this cathode bilayer in high performing inverted organic solar cells.

Scientific production

Research paper

1. **I. Anefnaf**, S. Aazou, Y. Sánchez, P.Vidal-Fuentes, R. Fonoll-Rubio, Kunal. J. Tiwari, S. Giraldo, Z. Jehl Li-Kao, J. Andrade-Arvizu, M. Guc, E. Saucedo and Z. Sekkat," Insights on the limiting factors of $Cu_2ZnGeSe_4$ based solar cells", Solar energy materials and solar cells, 2021, 227, 111106, doi: 10.1016/j.solmat.2021.111106, (Impact factor: 6.984).
2. Enric Grau-Luque , **Ikram Anefnaf**, Nada Benhaddou, Robert Fonoll Rubio, Ignacio Becerril-Romero, Safae Aazou, Edgardo Saucedo, Zouheir Sekkat, Alejandro Perez-Rodriguez, Victor Izquierdo-Roca and Maxim Guc, "Combinatorial and machine learning approaches for the analysis of $Cu_2ZnGeSe_4$: influence of the off-stoichiometry on defect formation and solar cell performance", J. Mater. Chem. A, 2021, 9, 10466-10476, doi: 10.1039/D1TA01299A, (Impact factor: 11.301).
3. **I. Anefnaf**, S. Aazou, G. Schmerber, S. Refki, N. Zimmermann, T. Heiser, G. Ferblantier, A. Slaoui, A. Dinia, M. Abd-Lefdil and Z. Sekkat, "Polyethylenimine-Ethoxylated Interfacial Layer for Efficient Electron Collection

in SnO_2-Based Inverted Organic Solar Cells", Crystals (2020), 10(9), 731, doi:10.3390/cryst10090731, (Impact factor: 2.404).

4. **I. Anefnaf**, S. Aazou, G. Schmerber, A. Dinia and Z. Sekkat, "Tailoring PEIE capped ZnO binary cathode for solution-processed inverted organic solar cells", Optical Materials journal (2021), 116, 111070, (Impact factor: 2.779).
5. Sergio Giraldo, **Ikram Anefnaf**, Kunal J. Tiwari, Robert Fonoll, Yudania Sánchez, Zacharie Jehl Li-Kao, Victor Izquierdo-Roca, "Effect of Alkali Doping Strategies on the Performance of Wide Band Gap $Cu_2ZnGeSe_4$ Thin Film Solar Cells", 2020 47th IEEE Photovoltaic Specialists Conference (PVSC), 2020, pp. 0732-0735, doi: 10.1109/PVSC45281.2020.9300888.
6. **I. Anefnaf**, S. Aazou, G. Schmerber, A. Dinia and Z. Sekkat, "Study the effect of fullerene derivatives ratio on P3HT-based inverted organic solar cells", Proc. SPIE 11474, Organic, Hybrid, and Perovskite Photovoltaic XXI, 2020, 54, doi: 10.1117/12.2568790.
7. **I. Anefnaf**, N. Benhaddou. S. Aazou, M. Abd-Lefdil, Z. Sekkat. "Optical, structural and Photoconductivity properties of organic photovoltaic thin films based on polymer/fullerene". IEEE International Renewable and Sustainable Energy, Conference-IRSEC, Marrakech, Morocco (2016).
8. N. Benhaddou, **I. Anefnaf**, S. Aazou, Zouheir Sekkat."Nanoscale probing of optical and structural properties of polymeric photovoltaic thin films". IEEE International Renewable and Sustainable Energy Conference-IRSEC, Marrakech, Morocco (2016).
9. **I. Anefnaf**, S. Aazou, Y. Sánchez, R. Fonoll-Rubio, Kunal. J. Tiwari, S. Giraldo, Z. Jehl Li-Kao, M. Guc, E. Saucedo and Z. Sekkat, "Evaluation of different buffer layers for solar cells with wide-gap $Cu_2ZnGeSe_4$ absorbers" (In progress).

Oral presentations

1. **I. Anefnaf**, R. Fonoll, Y. Sánchez, K. J. Tiwari , S. Giraldo, Z. Jehl, S. Aazou, Z. Sekkat, and E. Saucedo, Ge-Kesterite Solar Cells: Synthesis and Optimization, nextGen' 19, 2019, Palma, Mallorca, Spain.
2. **I. Anefnaf**, S. Aazou, G. Schmerber, A. Dinia, A. Slaoui, T. Hieser and Z. Sekkat, "Inverted organic solar cells: effect of changing buffer layer on the performance of device". IPCMs workshop'18, IPCMs, CNRS, Strasbourg, France.
3. **I. Anefnaf** , G. Schmerber, S. Aazou , G. Ferblantier, K. Yasaroglua, S. Colis, J. Rehspringer, N. Zimmermann, T. Heiser, A. Slaoui , A. Dinia and Z. Sekkat, "Study the effect of incorporation of tin dioxide on the performance of organic photovoltaic solar cells", 2018, Congrès JNES, Lyon, France.
4. **I. Anefnaf**, S. Aazou, G. Schmerber, A. Dinia, A. Slaoui, T. Hieser and Z. Sekkat, " Investigation of Donor-Acceptor Concentration on Organic Bulk Heterojunction Solar Cells Performance", 2018, Erasmus$^+$ Medsol Project meeting, UM5, Rabat, Morocco.
5. **I. Anefnaf**, N. Benhaddou, S. Aazou, M. Abd-Lefdil, Z. Sekkat, "Investigation on Structural and Optical Properties of Organic Photovoltaic Thin Films Based MEH-PPV/ PCBM fullerene blend, 2017, AMPSECA, Agadir, Morocco.
6. **I. Anefnaf**, N. Benhaddou, S. Aazou, M. Abd-Lefdil, Z. Sekkat, "Structural , Optical and morphological Properties of Organic Photovoltaic Thin Films Based P3HT/ PCBM fullerene blend", 2016, IRSEC16, Marrakesh, Morocco.
7. **I. Anefnaf**, S. Aazou, M. Abd-Lefdil, Z. Sekkat, Comparative study of optical, morphological and structural properties of organic thin films based on MEH-PPV and P3HT, OSA student chapter event, 2016, MAScIR, Rabat, Morocco.

8. **I. Anefnaf**, S. Aazou, M. Abd-Lefdil, Z. Sekkat, Comparative study of optical, morphological and structural properties of organic thin films based on MEH-PPV and P3HT, Doctoriale, 2016, FSR, Rabat, Morocco.

Poster communication

1. **I. Anefnaf**, S. Aazou, G. Schmerber, A. Dinia and Z. Sekkat, "Study the effect of fullerene derivatives ratio on P3HT-based inverted organic solar cells", SPIE optics and photonics, 2020, San Diego, Californie, USA.
2. **I. Anefnaf** , G. Schmerber, S. Aazou, G. Ferblantier, K. Yasaroglua,, S. Colis, J. Rehspringer, N. Zimmermann, T. Heiser, A. Slaoui , A. Dinia and Z. Sekkat, "Study the effect of incorporation of tin dioxide on the performance of organic photovoltaic solar cells" , Congrès JNES, 2018, Lyon, France.
3. **I. Anefnaf**, N. Benhaddou , S. Aazou, M. Abd-Lefdil, Z. Sekkat, 'Performance enhancement of organic solar cell by incorporating ZnO nanoparticles", EMR-S spring meeting, 2017, Strasbourg, France.
4. **I. Anefnaf**, N. Benhaddou, S. Aazou, M. Abd-Lefdil, Z. Sekkat, "Organic Photovoltaic Thin Films Based heterojunction based fullerene /conjugated polymer", AMPSECA, 2017, Agadir, Morocco.

1 General introduction

1.1. Why renewable energy?

Nowadays, the greenhouse gas (GHG) emissions have become a serious concern due to their dramatic effect on the global warming and the climate change. About two thirds of these emissions stem from energy production and use, thus placing the energy sector at the center of attention as one of the keys for their necessary reduction and to fight against climate change [1]. The transition from traditional energy sources based on fossil fuels combustion to a cleaner and efficient energy system is a crucial policy goal, not only for developed countries but also for developing nations. The first concerted effort of the international community to confront the problem of climate change was the birth of the United Nations Framework Convention on Climate Change (UNFCCC) in 1992 (entered into force in 1994) [2], [3]. The UNFCCC established a framework for action to control and stabilize concentrations of GHG in earth's atmosphere. Later on, in 1997, the participants established the Kyoto Protocol, which entered into force in 2005, including legally binding obligations to reduce GHG emissions for developed countries, on the basis that they are historically responsible for the current levels of GHG in the atmosphere [4]. More recently, the Paris Agreement adopted in 2015 was created with the central aim of strengthening the global response to the threat of climate change by holding a global average temperature increase this century well below 2°C above preindustrial levels, and to pursue efforts to limit the temperature rise to 1.5°C [5]. In order to provide a clear and tangible understanding of what will be required for different countries to reduce GHG emissions and achieve the goal of limiting global warming to less than 2°C, the organization DDPP (Deep

Decarbonization Pathways Project) emerged in 2013. According to DDPP, the deep decarbonization is technically feasible while accommodating economic and population growth, and analyzing the different modeled scenarios, the energy-related CO_2 emissions would be reduced by 46% - 56% (or 9.9 - 12.1 Gt CO_2) below 2010 levels, as shown in Figure 1.1 for some of the highest emitting countries[6], [7].

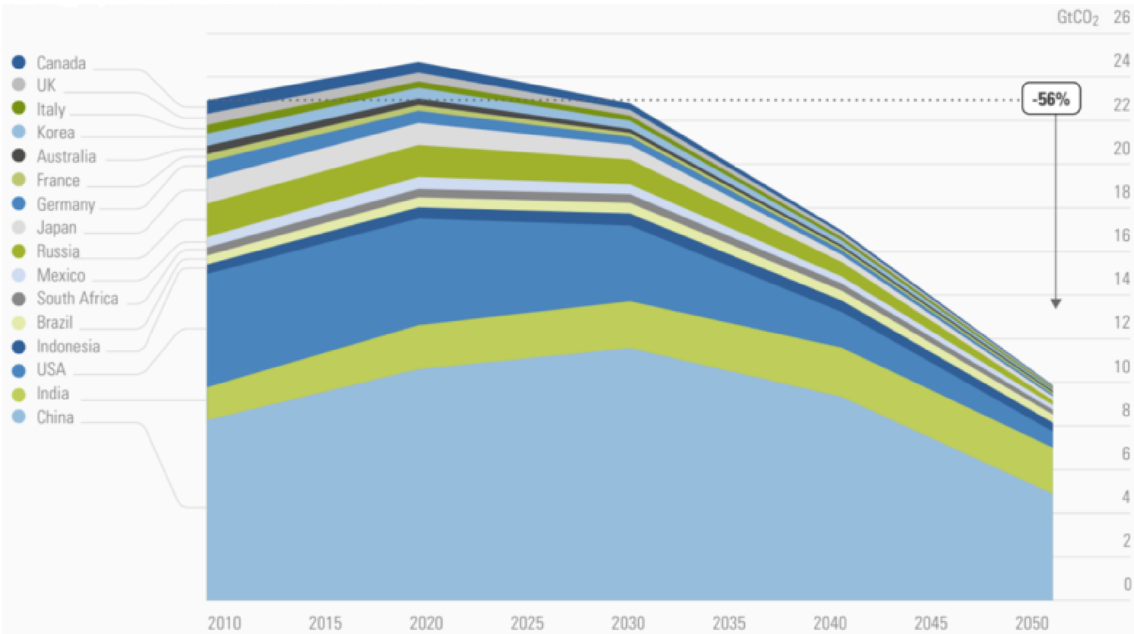

Figure 1.1: *Emissions evolution for energy CO_2, 2010-2050 forecast, showing most ambitious reduction scenarios for several high emitting countries [6].*

In this context, renewable energy can play an important role in the transition to a less carbon-intensive and more sustainable energy system, allowing a significant reduction of GHG emissions. Renewables have grown significantly in the last years, especially solar photovoltaic (PV) with a remarkable cost reduction. PV module prices have fallen by around 80% since 2010, and the global weighted average cost of electricity from solar PV plants commissioned between the years 2010-2020 have also fallen 69%, even reaching the range of estimated fossil fuel-fired power generation costs (see Figure 1.2)[7]. According to the International Energy Agency (IEA), renewables accounted for almost two-thirds of net power capacity around the world in 2016, with almost 165 gigawatts (GW) coming online. Last year, new solar PV capacity grew by 50% (over 74 GW), and for the first time, it increased faster than any other fuel.

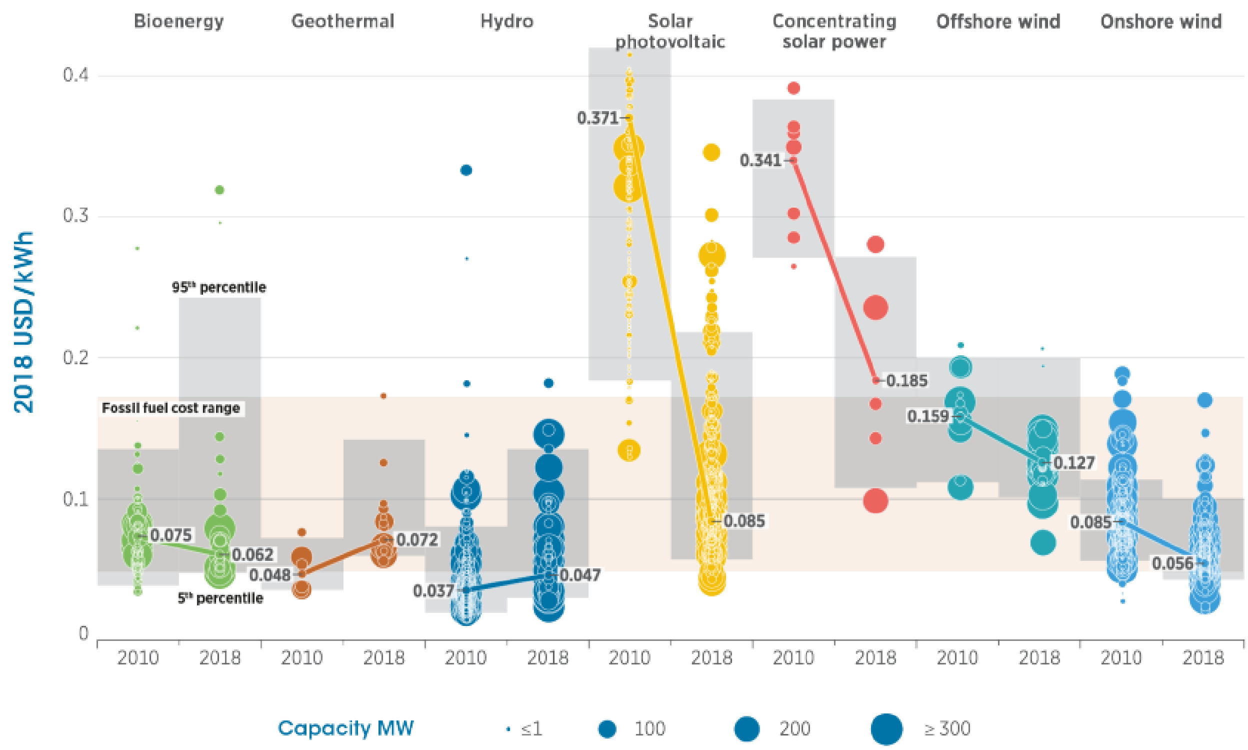

Figure 1.2: *Levelized cost of electricity from utility-scale renewable technologies (ranges and average)[7].*

In view of the foregoing, there is no doubt that solar energy is getting a lot of attention as one of the key renewable energy sources around the world for keeping a gradual decarbonization of the power sector and ensure a sustainable future. In the following section, the main photovoltaic technologies and their current status will be described.

1.2. Photovoltaic technologies

Over the years, the development of PV technology has undergone numerous changes leading to the cells being classified into different generations, originally defined for inorganic materials as high cost/high efficiency (1st generation- 1GEN), low cost/low efficiency (2nd generation- 2GEN) and low cost/high efficiency (3rd generation- 3GEN). Solar cell technology is generally categorized into three main generations as illustrated in Figure 1.3.

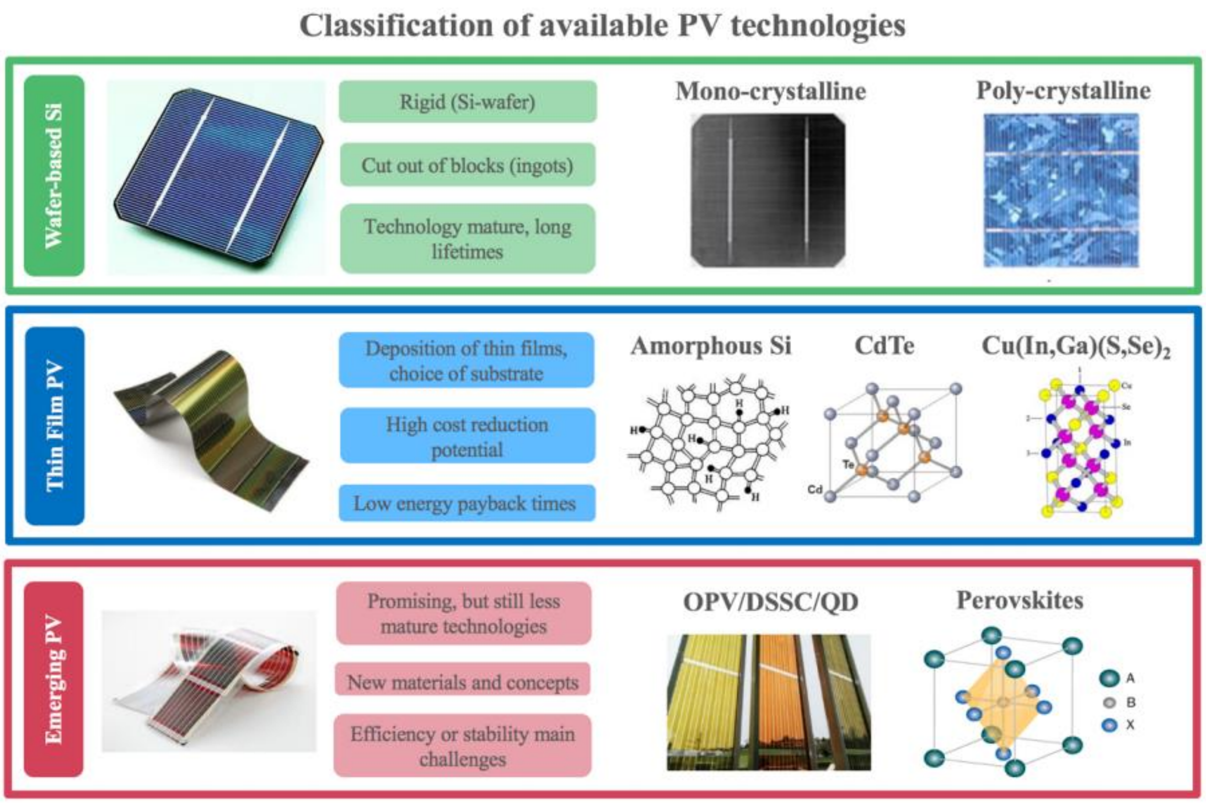

Figure 1.3: *Classification and main characteristics of the available PV technologies.*

➯ ***<u>1st generation PV: crystalline Si solar cells</u>***

Currently, crystalline Si-based solar cells are the dominant PV technology with around a 95% of market share [8]. These are based in p-n homojunction in which boron (p-type impurity) is diffused into a phosphorus-doped (n-type) Si wafer or vice versa (see Figure 1.4) although heterojunction concepts have also been very successfully developed [9].

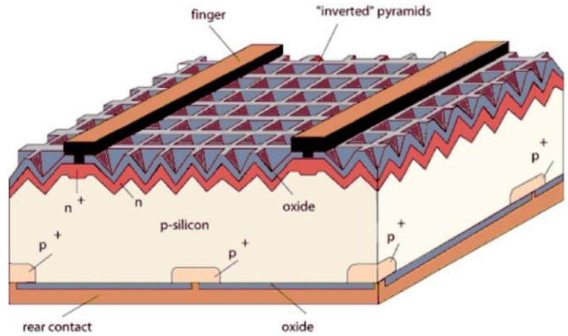

Figure 1.4: *Structure of a monocrystalline Si PERL solar cell.*
Reproduced with permission from [10].

There are two main types of crystalline Si-based solar cells in the market: monocrystalline (c-Si) and polycrystalline (p-Si) (Figure 1.5). The former rely on very high purity monocrystalline Si wafers. The lack of defects and grain boundaries in the semiconductor material allows obtaining very high efficiencies. This combined with an intensive electrical and optical engineering at the front and back sides of the devices has set the current record efficiency at 26.7% for a heterojunction c-Si solar cell [11]. Commercial c-Si solar panels show average efficiencies around 15-19% with the best ones exceeding 20% [12]. Their market share is around 45% [8]. However, their high efficiencies carry a counterpart: their production is very energy intensive, complicated and expensive since it requires a very precise control to obtain flawless monocrystalline ingots through the so-called Czochralski crystal pulling process [13].

In order to reduce production costs by avoiding pulling processes, p-Si technology was developed. Multicrystalline ingots are casted from molten Si controlling the cooling temperature so that the grains grow in a columnar structure [13]. Although the individual grains possess high crystalline quality, there is a higher density of crystallographic defects due to dangling bonds at the grain boundaries but also to dislocations and point defects [14]. However, extensive research on crystal growth and on the passivation of such defects, together with front and back side optical engineering has allowed the technology to get very close to c-Si with a record efficiency of 22.3%

[15]. Commercial modules currently range 13-17% efficiency and represent a market share of around 50% [10].

Figure 1.5: *Pictures of p-Si (left) and c-Si (right) solar cells.*
http://www.tindosolar.com.au/learnmore/poly-vs-mono-crystalline/

Si is a very mature and well-performing technology. However, the fabrication costs, even of p-Si, are very high. This is due to several reasons [14], [16]:

- Although Si is very abundant in nature, it mainly occurs in the form of SiO_2. In order to reduce it to metallurgic-grade (98% pure) Si, very high temperatures (~1800°C) are necessary. This process requires around 50 MJ to produce 1 kg of Si.
- The covalent nature of silicon-silicon bonds, in combination with an indirect 1.14 eV bandgap, results in poor defect tolerance, which necessitates high-purity material so additional purifying and high temperature (~1300°C) chemical vapor deposition (CVD) processes are necessary.
- The manufacturing of Si ingots requires melting the purified material again (~1400°C) as well as complex pulling/casting process. This is especially critical for c-Si.
- Wafers need to be cut from ingots with thicknesses usually >100 µm due to the low light absorption and fragility or Si. During the sawing process, there is a considerable loss of material so that 3-9 g of raw (before sawing) Si are necessary per peak watt (W_p) at the module level.

↬ ***2nd generation PV: thin film solar cells***

The so-called 2nd generation PV started to be developed as a response to the high production costs of Si solar cells. This generation of PV is based on the usage of direct band-gap and highly light-absorbent materials that allow reducing the thickness of solar cells down to a few microns, in contrast to Si wafers. The fabrication of such devices consists on the deposition of thin layers with different functionalities (back contact, absorber, emitter, etc.) onto low cost substrates. This is why they are widely known as thin film PV.

The wide ranges of substrates, materials and deposition techniques that can be employed for its fabrication provide 2nd generation PV with an enormous versatility, a large potential for cost reduction and opens the door to many innovative applications. Currently, there are 3 main technologies competing with crystalline Si with a non-negligible market share: amorphous silicon (a-Si), CdTe and Cu (In,Ga)Se_2 (CIGS). Thin-film solar cells (TFSCs) include amorphous silicon (a-Si), micro-crystalline silicon (μ-Si), copper indium selenide/ sulfide (CI(S)Se), copper indium gallium selenide/sulfide (CIG(S)Se), cadmium telluride (CdTe) and kesterite (CZTS(S)Se).

↬ ***Third-generation PV: Emerging Thin Films***

The evolution of third-generation solar cells was a great development in this field as they came up with a drastically high efficiency when compared with the second generation solar PVC's. This generation solar PVC's provide an alternative to its countervail made up of p–n junctions and thin cells respectively as these cells surpass the Shockley Queisser limit of 33.7% PCE [17] for single band-gap solar PVCs. This solar generation uses organic materials such as small molecules and polymers as photoactive material and also includes highly efficient and expensive multi-junction solar PVCs.

Their high production cost limits its commercial application. Polymer solar cells or plastic solar cells, has emerged as a simple, quick and inexpensive large-scale organic option; as the use of polymer photoactive materials makes it readily available and potentially inexpensive. In comparison to first and second generation the third generation solar PVCs usage is limited; but researchers believe in its great potential and more devices are still in progress. An a-Si or GaAs contribute as the layers of the multilayered structure of common third-generation systems; many researchers have proposed frequency conversion in solar cell. The wavelength conversion enables usage of light that the solar cell cannot absorb to light spectra that it can utilize, these results in more output power. The use of hot carrier effects and other multiple-carrier ejection techniques are also used to enhance PCE.

In the end of this section, one can notice that each generation has its own advantages and inevitable drawbacks. Many efforts have to be done to mature the different semiconductors, and to push forward the various technologies to the best efficiency-stability-low cost compromise with the aim to be commercialized on a large-scale area.

Through this thesis, we have chosen to focus on axes the first one is organic materials and the second one is kesterite material. In this context, the first paramount step towards any optimization is very important to know the material from different angles with the aid of the colossal background gathered in this sense, then; pinpointing the weaknesses and strengths of this semiconductor is of extreme importance, which will be the purpose of the following chapters.

1.3. Fundamentals of solar cells

The photovoltaic solar cells can convert light into electricity. This is possible thanks to the so-called photovoltaic effect that consists in the creation of a voltage and an electric current in a material upon exposure to light. It was first observed by Edmond Becquerel in 1839. Although the first solid state solar cell based on selenium was developed in 1877 by Adams and Day [18], it was not until 1954 that the first device with significant power conversion efficiency was developed by Bell laboratories [19]. Bell's solar cell was based on silicon under the influence of the rapid development of the electronics industry and set the basis for the future development of PV. At first, intensive research on PV solar cells was triggered by their successful application in satellite-powering at the beginning of the space era [19]. However, once that the technology was well-established for space applications and after 1973 OPEC's oil embargo the focus changed towards terrestrial power generation [20]. Since then, there has been a huge development of PV owing to continuous research efforts that have made PV a competitive means of power generation. Si-based solar cells are the dominant technology today. However, the intensive research carried out in the last decades has allowed the development of many other successful and emerging technologies that will be analyzed later on. Regardless the technology, the same concept lies behind the operation of every photovoltaic device:

1. A material capable of generating electric carriers under illumination.
2. An internal structure capable of selectively separating and transporting those carriers out of the material and into an external circuit to generate a useful electric current.

A p-n junction diode possesses those two properties. As for the first point, diodes are formed by semiconductor materials which, due to their band structure with a full valence band and an empty conduction band (at T = 0 K, at higher temperatures some electrons have enough thermal energy to jump to the conduction band), are capable of transforming radiative energy into electric carriers. More specifically, if a photon with an energy equal or higher than the energy gap (E_g) between the bands (bandgap) hits an electron in the valence band (VB), the latter can be promoted to the conduction band (CB) leaving a hole (equivalent to a positively charged particle) behind thus creating and electron-hole pair (EHP) (Figure 1.6). However, if the charges are not separated and extracted, the EHP will eventually recombine giving off the energy absorbed. This is why not just a semiconductor but a p-n junction is necessary for a solar cell.

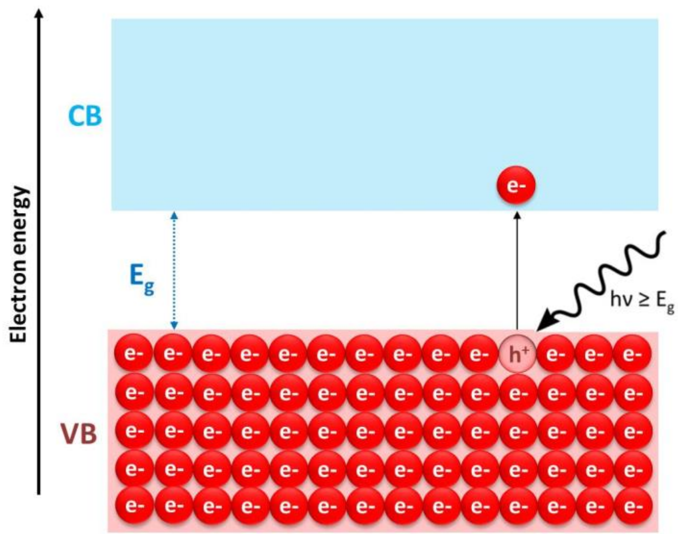

Figure 1.6: *Band diagram of a semiconductor. VB and CB stand for valence and conduction band, respectively; E_g stands for the energy of the bandgap and hv is the energy of an incident photon.*

A p-n junction is the junction between an n-type semiconductor and a p-type semiconductor. In an intrinsic semiconductor, the concentration of electrons (n) and holes (p) is always equal:

$$\mathbf{p = n = n_i} \qquad (1.1)$$

Where n_i is called intrinsic concentration. In contrast to intrinsic semiconductors, n-type semiconductors possess donor impurities or defects with a concentration N_D that give away electrons to the conduction band where they become mobile charges.

The number of free electrons donated by the donor atoms exceeds n_i and unbalances Equation (1.1) so that:

$$\mathbf{n >> p = n_i} \qquad (1.2)$$

This makes the conductivity of n-type semiconductors much greater than that of intrinsic semiconductors. The semiconductor is called n-type because the majority carriers have a negative charge. Similarly, in p-type semiconductors there are acceptor impurities or defects within the semiconductor with a concentration N_A that are filled with electrons from the valence band leaving holes behind so that:

$$\mathbf{p \gg n = n_i} \qquad (1.3)$$

The conductivity is also greatly improved compared to an intrinsic semiconductor. In this case, the semiconductor is called p-type because the majority carriers have a positive charge.

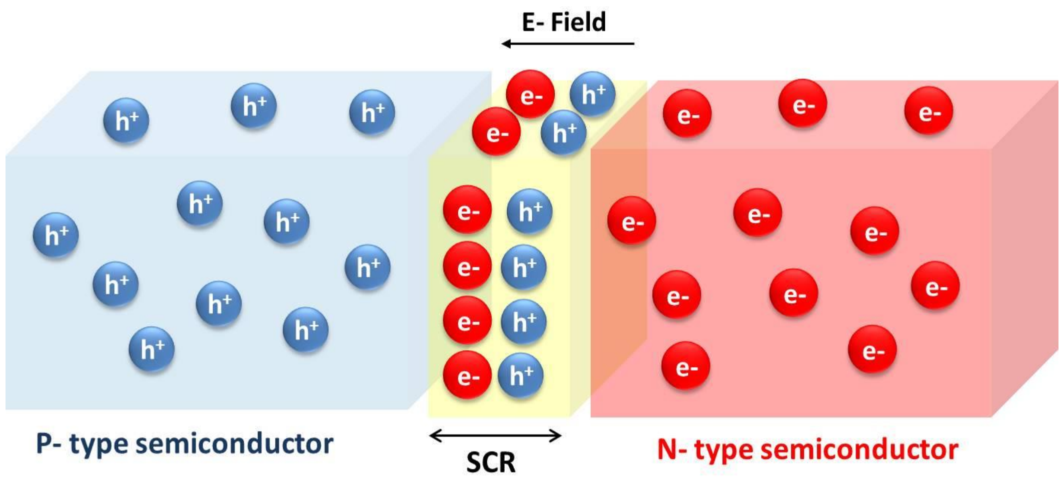

Figure 1.7: *Schematic of P-N junction with the space charge region and the built-in electric field created across the junction.*

A p-n junction can be fabricated by introducing donor impurities and acceptor impurities in opposite sides of a semiconductor (homo-junction) or by putting in close contact an n-type semiconductor with a p-type semiconductor (heterojunction). When this is done, due to the different charge concentrations (i.e. charge chemical potential) at both sides of the junction, holes diffuse out from the p side towards the n side and free electrons diffuse out from the n side towards the p side leaving uncompensated ions behind (Figure 1.7). This causes the p-type side to become negatively charged and the n-type side to become positively charged generating an electric field (E-Field) across the junction directed from the n to the p side that, in turn, opposes the diffusion process. When the force exerted on the carriers by the electric field equals the diffusion force, equilibrium is reached. This process leaves a carrier-free zone around the junction called the depletion region or the space-charge region (SCR). If the electron-hole pair (EHP) is generated by photon absorption and reaches the SCR, the hole and the electron will be drifted away from each other (the electron towards the n region and the hole towards the p region) by the built-in electric field generating an electric current.

However, a build-in electric field is not really mandatory to fabricate a solar cell but rather a material capable of generating carriers (absorber) and selective membranes for each kind of carrier [21]. With a proper band alignment, an n-type semiconductor can allow electrons to pass and block most of the holes and, vice versa, a p-type semiconductor can be very permeable to holes and almost impermeable to electrons. In addition, the conductivity of a semiconductor can be expressed as:

$$\sigma_T = \sigma_e + \sigma_h = n\mu_e q + p\mu_h q \qquad (1.4)$$

Where σ_e and σ_h are the conductivities and μ_e and μ_h are the mobilities for electron and holes, respectively. Taking into account Eq (1.2) and (1.3), it is easy to see that $\sigma_e \gg \sigma_h$ for n-type semiconductors and $\sigma_h \gg \sigma_e$ for p-type semiconductors. Blocking one type of carrier while efficiently conducting the other provides n and p-type semiconductors with the properties required for a selective membrane. Forgetting about the built-in electric field, when EHPs are being generated continuously in the absorber of such a device they diffuse in every direction.

Since they cannot pass efficiently through the membranes, holes and electrons will tend to accumulate near the n and the p semiconductors, respectively (Figure 1.7). This, in turn, will cause a gradient in the chemical potential of the carriers along the device that will eventually drive holes towards the p part and electrons towards the n part selectively separating the charges. Thus, such a device can transform light into an electric current without the effect of a build-in electric field.

It should be noted that the electrons promoted to the conduction band are in an excited state so recombination is always present in solar cells during the processes described above. When a solar cell is at a steady state it means that generation and recombination processes keep continuously taking place but they have reached equilibrium. Now that the fundamentals behind EHP generation and separation have been analyzed, the question that follows is how to extract power from the devices. For this matter, it is useful to look at what happens in solar cells under illumination in two limiting operating conditions: open circuit and short-circuit. In open circuit conditions (i.e. charges cannot escape the solar cell), at some point the concentration of charges inside and outside the membranes will be the same and no more diffusion can take place. In addition, as the number of charges increases so does recombination.

In equilibrium, all the new charges generated will recombine. Since both membranes are "filled" with the highest possible number of charges, the electrochemical potential between them (which translates into a voltage) is at its maximum. This voltage is called the open circuit voltage (V_{OC}). Logically, since charges cannot leave the device, there is no current and no power can be extracted from the cell. In short-circuit conditions (i.e. charges can freely escape the solar cell through an external ideal non-resistive wire), once equilibrium is reached all the charges generated that do not recombine inside the device, will reach the membranes and flow outside towards the opposite membrane generating a current. Since all the charges reaching the membranes are escaping the device, the current generated by the cell is at its maximum. This current is called the short circuit current (J_{sc}). However, since the charges can flow freely towards the opposite membrane through the wire and recombine, the membranes are "empty" so there is no electrochemical potential between them, no voltage can build up and no power can be extracted from the cell.

Logically, in order to extract power from a cell, an intermediate situation is needed. If an external load is connected to the device, the charges generated can accumulate inside the membranes to a certain extent until the electrochemical potential (voltage) between them is high enough to leave the cell generating a current and producing work at the load. Finally, it is necessary to take a quick look at the internal structure of a solar cell to understand how the light reaches the devices and how the charges are extracted from the cells. As depicted in Figure 1.8, the basic structure of a p-n solar cell consists of:

- **An absorber** → most of the light is absorbed and the carriers are generated in this part. Its bandgap should be around 1-1.5 eV in order to efficiently absorb sunlight [22]. Depending on the technology, it can be either an n-type or a p-type or even an intrinsic semiconductor.
- **An emitter** → it must be as transparent as possible to sunlight so this can reach the absorber.
- **A back and a front contact** → the contacts collect the carriers and allow them to travel into an external circuit. Metals are usually employed due to their high conductivity. However, other materials like transparent conductive oxides are also commonly employed.

Each part is usually composed of a combination of different layers to optimize its properties for charge generation, separation and/or collection and to avoid any incompatibilities between them that can cause losses. This way, each technology has its own optimized layer structure.

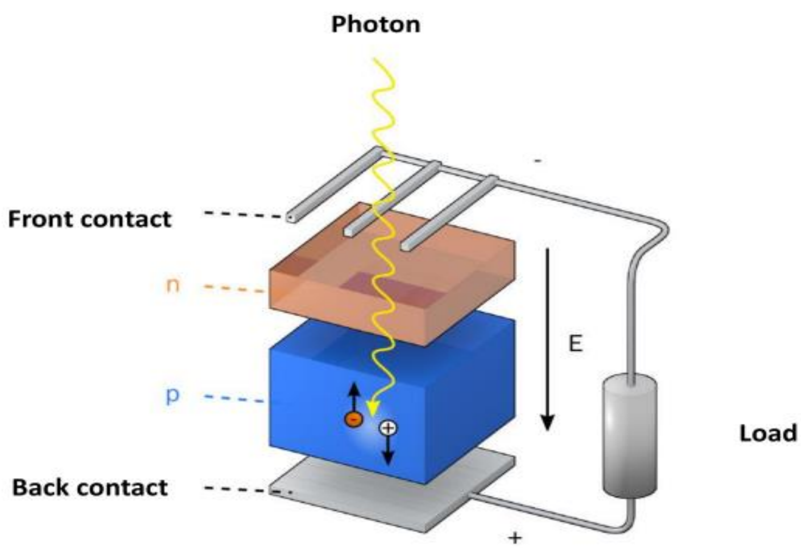

Figure 1.8: *Schematic of the basic structure of a p-n junction solar cell.*

1.4. Main parameters of solar cells

The behavior of a solar cell is commonly described by a simple electric circuit adopting one diode model. In dark conditions, the current density as function of voltage is obtained through the ideal Shockley diode equation as follows:

$$J\ (V) = J_0\ \left(exp\left(\frac{qV}{K_B T}\right) - 1\right) \qquad (1.5)$$

Where J_0 is the reverse saturation current of the diode (i.e. the current due to the diffusion of minority carriers from the n and p regions towards the SCR), q is the elemental charge, K_B is Boltzmann's constant and T is the temperature.

Once illuminated with sunlight, additional charge carriers are created to participate in the total current generated, it is represented by J_{ph}, the following equation constitutes the equivalent circuit of the current source and the diode connected in parallel:

$$J\ (V) = J_0\ \left(exp\left(\frac{qV}{K_B T}\right) - 1\right) - J_{ph} \qquad (1.6)$$

This equation is equivalent to a circuit with a current source and a diode connected in parallel. Figure 1.9 represents the previous equations graphically. From it, it is possible to extract the main parameters that describe the operation of solar cells.

The maximum possible voltage of a solar cell, Voc is obtained at J = 0 and the maximum current density, J_{sc}, at V = 0. Their product defines the maximum theoretical power (P_{theo}) of the cell (it should be noted that this power is not achievable even in perfect devices). However, in real operating conditions, the maximum power that can be extracted from a solar cell (P_{max}) is given by the point of the J-V curve that maximizes the product of J by V and is called the maximum power point (MPP). The MPP defines the current density and voltage at maximum power denoted by J_{mp} and V_{mp}, respectively.

The ratio between P_{max} and P_{theo} is called the fill factor (FF):

$$FF = \frac{P_{max}}{P_{theo}} = \frac{J_{mp} * V_{mp}}{J_{sc} * V_{oc}} \qquad (1.7)$$

This parameter measures the squareness of a J-V curve with respect to an ideal diode. Finally, the power conversion efficiency (η) of a solar cell, i.e. the ratio between the maximum power generated by the device (P_{max}) and the power reaching the cell (P_{in}), is usually expressed as:

$$\eta = \frac{P_{max}}{P_{in}} = \frac{J_{SC} * V_{OC} * FF}{P_{in}} \qquad (1.8)$$

In standard measuring conditions, P_{in} corresponds to the power extracted from the integration of the solar spectrum AM1.5G (~1000 W/m^2).

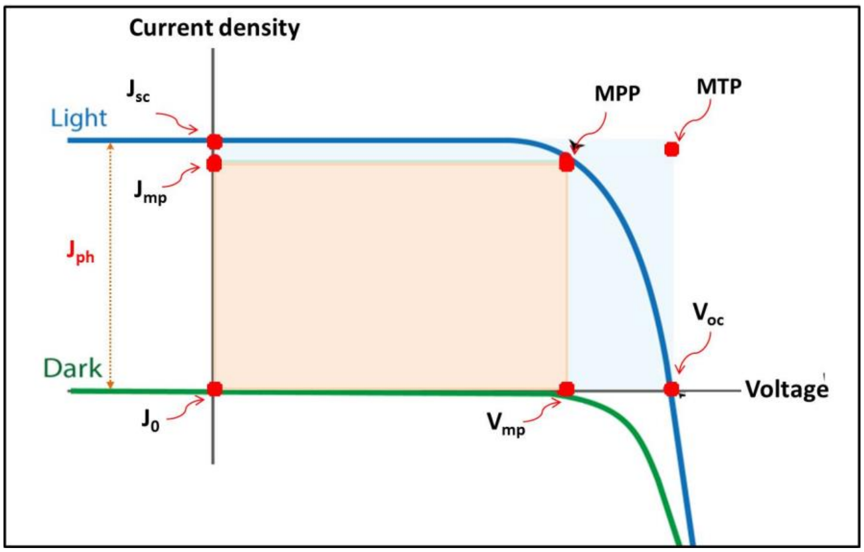

Figure 1.9: *Characteristic J-V curves of a solar cell represented by equations (1.5) and (1.6) (with the sign of the Y axis inverted) and the main parameters used for its description. MTP stands for maximum theoretical power point.*

Up to this point, it has been assumed that solar cells behave as ideal diodes. However, a real solar cell exhibits manifold losses. These can be encompassed in two terms: the series resistance (R_s) and the shunt resistance (R_{sh}). The former includes all the resistive losses along the device (i.e. due the electrical resistance of the different layers and the contact resistance between them at the interfaces) while the latter accounts for losses caused by alternative current paths (shunts). These terms can be included in Eq (1.6) as follows:

$$J(V) = J_0 \left[exp\ \left(\frac{qV-qJR_s}{K_BT}\right) - 1\right] + \frac{V-JRs}{R_{sh}} - J_{ph} \qquad (1.9)$$

This equation describes the circuit depicted in Figure 1.10. Eq (1.9) works well for ideal p-n homojunction solar cells in which the main recombination process is radiative (i.e. an electron falls directly from the conduction to the valence band emitting a photon) and takes place in the neutral region. However, in the case of far from ideal p-n junctions, like heterojunction, there are important losses due to recombination in the SCR. This recombination can have both radiative and non-radiative components. Inside non-radiative, the main recombination mechanisms are Shockley-Read-Hall (SRH) in which an electron falls from the conduction band to a mid-bandgap state and, then, to the valence band; and Auger in which an electron falls from the conduction to the valence band and the energy difference is given to another electron. These losses can be included in Eq (1.9) by means of an extra term called the diode quality factor, A:

$$J(V) = J_0 \left[exp\left(\frac{qV-qJR_S}{AK_BT}\right) - 1\right] + \frac{V-JR_s}{R_{sh}} - J_{ph} \qquad (1.10)$$

The factor A typically varies from 1 (ideal solar cell with mainly radiative recombination at the neutral regions) to 2 (main recombination at the SCR) [23], [24].

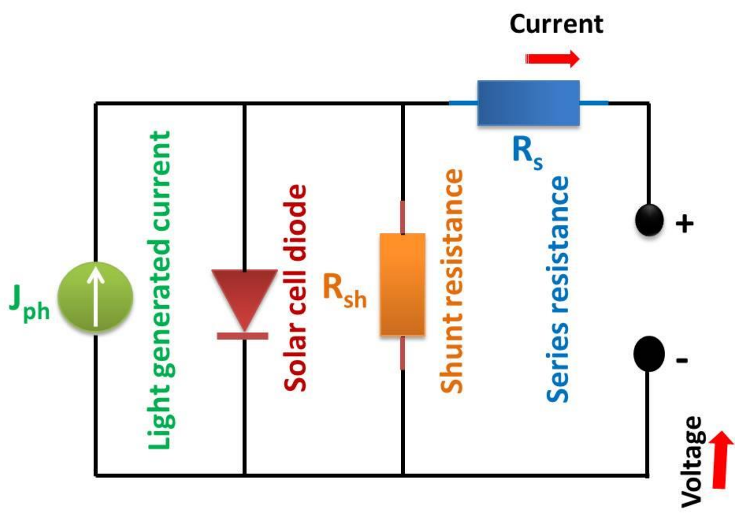

__Figure 1.10:__ Equivalent electrical circuit of a solar cell with resistive and shunt losses.

Through this thesis, we have chosen to focus on kesterite and organic solar cells. The first paramount step towards any optimization is to know this material from different angles with the aid of the colossal background gathered in this sense, then, pinpointing the weaknesses and strengths of this semiconductor is of extreme importance.

Part

1

Wide band gap kesterite based on $Cu_2ZnGeSe_4$ Kesterite solar cells

The main objective of this part is to shed light on the feasibility of developing a novel kesterite solar cells wide band gap based on pure Ge ($Cu_2ZnGeSe_4$), as an alternative solution to overcome the shortcomings related to Sn in the classical form of kesterite (free germanium).

We focused on important three axes, namely:

- ✓ The optimization of the vital conditions for a best efficiency based $Cu_2ZnGeSe_4$ solar cells.
- ✓ The analysis of defect types and concentrations of CZGeSe. off stoichiometric.
- ✓ Identify and address the main issues limiting the CZGSe performance.

2

Kesterite solar cells : background

2.1. Kesterite solar cells: history

Photovoltaic thin films technologies suggests more versatility compared with silicon (Si) owing to their compelling features of light-weight and compatibility to both flexible and rigid substrates, tunability of light spectrum response for single-junction and tandem devices, and compatibility to both opaque and semitransparent architectures [25]–[28]. They are an important branch of photovoltaic in realizing cost-effective, durable and compatible products for future multiple PV markets, such as build-integrated PV, vehicle integrated PV, semitransparent PV, flexible PV as well as weak light PV [29], [30], etc. In this area, chalcogenide CdTe and $Cu(In,Ga)(S,Se)_2$ (CIGS) materials-based solar cells have demonstrated beyond 20% efficiency with long-term stability and have been commercialized for more than a decade [31]. However, their market share has stagnated due to, not only the rapid fall in the cost of Si-based PV, but also the use of rare (In, Ga) and toxic (Cd) constituents [31], [32]. These either limited the cost reduction or raise environmental concerns, thus undermining the competitiveness of chalcogenide PV compared to Si PV. Hence, sustainable terawatt level deployment of photovoltaic will eventually require the design and development of compounds based on critical raw materials (CRM)-free and environmentally benign materials and fabrication processes.

Cu_2ZnSnS_4 thin films were first synthesized, studied and identified as a potential material for PV for the first time in 1988 under the influence of the success of $CuInSe_2$ solar cells [33]. The great similarity between both materials, led the PV community to try and apply the available knowledge on CIGS to the development of kesterite based-solar cells. This way, the first CZTS based solar cell with a significant power conversion efficiency (0.66%) was fabricated by Katagiri et al. in 1997 by sulfurization of electron beam evaporated Cu/Sn/Zn precursors and using a similar cell configuration as CIGS: SLG/Mo/CZTS/CdS/ZnO/Al [34]. The possibility of successfully applying CIGS's already developed PVD-based techniques and knowledge allowed the group of Katagiri to rapidly optimize their process and increase 10-fold the efficiency of their devices in a decade reaching a 6.8% in 2008 by sulfurization of RF-sputtered Cu/SnS/ZnS precursors [35]. At that time, IBM was researching on solution deposition processes as a possible route to reduce the cost of high vacuum-based CIGS manufacturing. Mitzi et al. succeeded and obtained efficiencies >10% employing a hydrazine-based chemical route [36]. With the feasibility of producing efficient kesterite solar cells proven, they joined the quest for improving the technology and, in 2010, by applying their novel CIGS solution-based process to CZTSSe they achieved a remarkable 9.6% efficiency device [37]. Further optimization of their hydrazine process led IBM in 2013 to the current certified record: 12.6% efficiency [38], however, the record efficiency of CZTSSe solar cells (12.6%) is still significantly lower than those of its predecessors $Cu(In,Ga)Se_2$ (CIGS) and CdTe thin-film solar cells. This record has remained for several years. The main obstacle for this stagnation is unanimously attributed to the large open-circuit voltage (V_{OC}) deficit.

Nowadays, CZTSe, CZTS and CZTSSe have been widely studied and successfully synthesized by a wide variety of vacuum and non-vacuum routes. The history of kesterite remains short in comparison with the more mature CIGS and CdTe solar cells that are under continual development for almost 40 years, and there is still much more unknown details to investigate and unveil about this compound in order to develop it further.

This chapter presents an overview of the crystalline structure of kesterite CZTS thin films besides the challenges preventing its performance evolution. Afterwards, a summary of the different attempts proposed in the literature to overcome the cited issues is given, along with what we suggest as solution in the present thesis.

2.2. CZTSSe crystal structure

The most common semiconductor used for photovoltaic applications is from the IV column of the periodic table. This element has 4 valence electrons and crystallizes in the diamond crystalline structure. The formation of I_2-II-IV-VI_4 compounds like CZTSSe can be achieved from II–VI semiconductor by sequential replacement of cations in which the octet rule is respected and the total charge remains neutral (Figure 2.1).

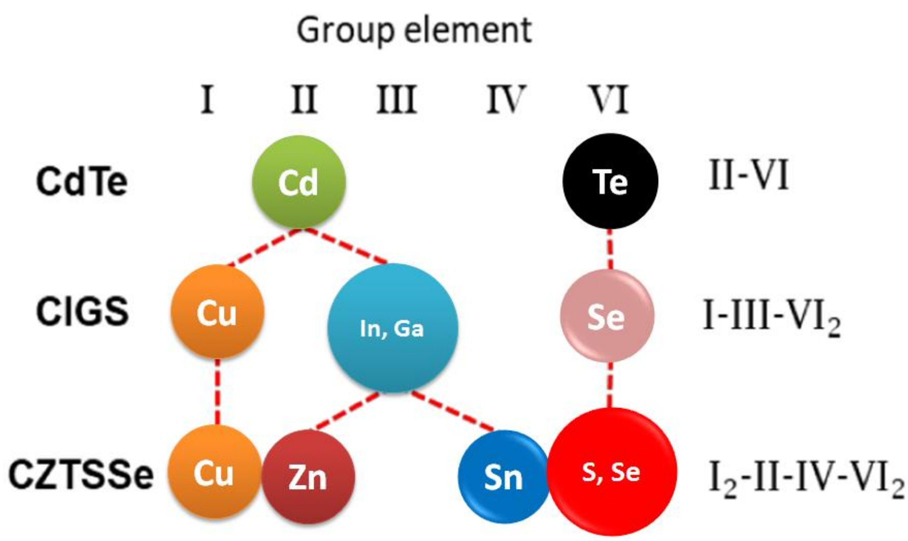

Figure 2.1: *Formation of CZTSSe (I_2-II-IV-VI_4) compounds by sequential replacement of cations.*

The CZTSSe crystal structure follows the same crystal structure as CdTe (zincblende). Schematic of CZTSSe crystal structure and cation substitution phenomena is shown in Figure 2.2. Additionally, CZTSSe can be crystallized as kesterite (space group $I\bar{4}$) or stannite (space group $I\bar{4}2m$). Kesterite and stannite structures differ by the cations stacking sequences on the axis c [39], [40]. Figure 2.2 shows a stack of the type (···-[CuSn]-[CuZn]-[CuSn]-[CuZn]-···) for the kesterite structure, while the stack for the stannite structure is of the type (···-[ZnSn]- [Cu_2]-[ZnSn]-[Cu_2]-···). Both structures are very likely to be found in a material because their formation energy differs very little (about 3 meV per atom). But, the kesterite structure has the lowest formation energy and would be the most stable one [41].

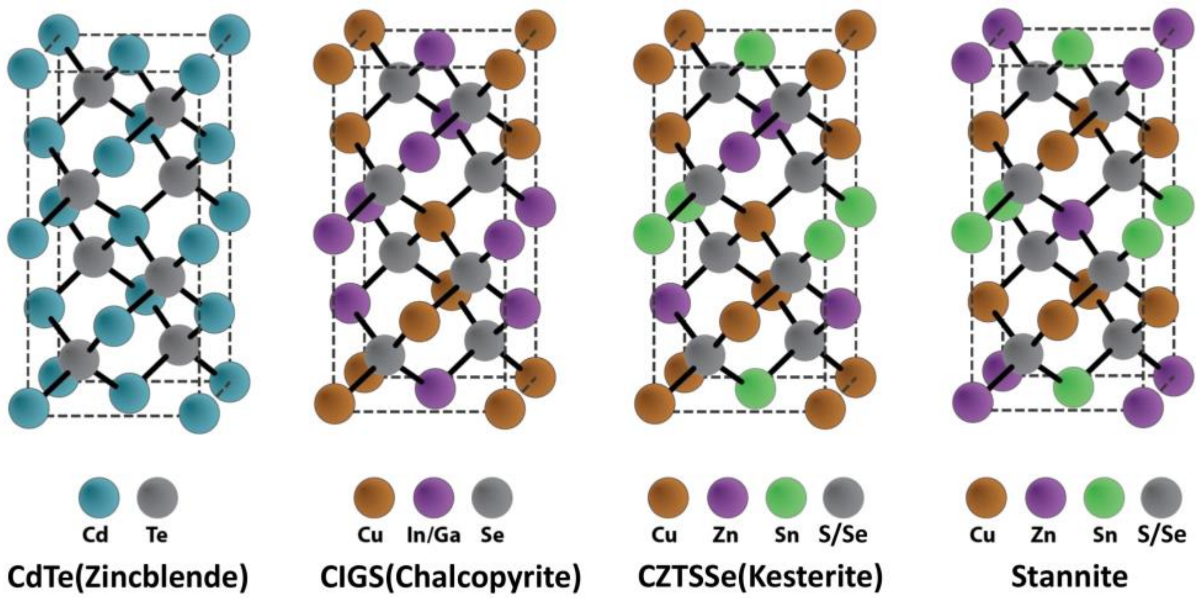

Figure 2.2: *Elemental cells of CdTe (zincblende), CIGS (chalcopyrite) and CZTSSe (kesterite and stannite) structure, showing the development of each structure by the cationic substitution of the previous structure. Taken with permission from [42].*

Finally, it is also possible to encounter disordered kesterite crystal structure. CZTSSe is composed of the alternation of two cationic planes along the c axis of the mesh (see figure 2.3):

- The Cu and Sn planes located at z=0 and z=1/2.
- The planes of Cu and Zn located at z=1/4 and z=3/4.

Anion planes separate each of these planes. The Cu_{Zn} and Zn_{Cu} anti-sites have low enthalpies of formation due to the similar size of the cations. It follows that a kesterite structure exists in which Cu and Zn sites are occupied in a random way by atoms of Cu/Zn [43]. This disordered structure is highlighted by Schorr et al. [30] using neutron diffraction measurements. The degree of disordered state in the absorber depends on the metal ratio (especially [Cu]/[Zn+Sn]) and the heating or cooling profile used during the synthesis [44].

A transition from partially ordered to disordered kesterite occurs at 260°C for CZTS (pure sulfur-based kesterite) [45] and 200°C for CZTSe (Pure selenium-based kesterite) [46] compounds. Completely disordered kesterite shows lower bandgap compared to more ordered kesterite. Nevertheless, it is still under debate if this is the main reason behind the lower efficiency of CZTSSe solar cell.

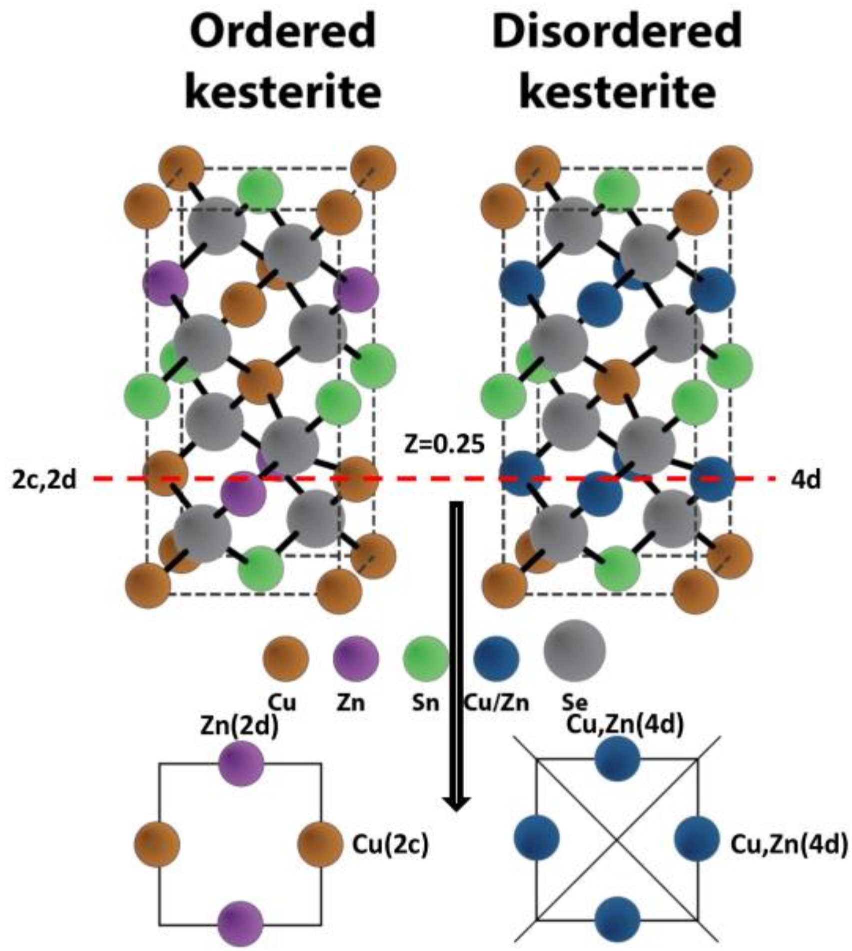

Figure 2.3: *Crystalline structure of disordered kesterite phase. Taken with permission from [42]*

2.3. The limitations factors for kesterite based solar cells

In spite of the similarity between CIGS and CZTSSe absorbers, there is a very large performance gap between the record devices of each technology as shown in Table 2.1. The main parameter limiting the efficiency of kesterite solar cells is their high Voc deficit. This parameter is defined as the difference between the maximum V_{OC} theoretical value according to the Shockley–Queisser (SQ) limit and the measured Voc of the device [47]:

$$\textit{SQ, } V_{OC} \textit{ deficit} = V_{OC} \textit{ (SQ limit)} - V_{OC} \textit{ (exp)}$$

Figure 2.4: *Comparison of the record CIGS and CZTSSe solar cells*

	Eg (eV)	V_{OC} (mV)	J_{SC} (mA/cm²)	FF (%)	η (%)	V_{OC} (mV)
CZTSSe [38]	1.13	466	38.9	69.8	12.6	664
CIGS [48]	1.13	746	38.5	79.7	22.9	384

There have been intense researches efforts trying to understand the origin this problem a kesterites have been found to possess a manifold of intrinsic problems that can lie at the origin of the V_{OC} deficit. The main issues limiting the V_{OC} of kesterite solar cells are reviewed below.

➭ *Formation of secondary phases*

Kesterites are complex quaternary compounds and their single phase formation thermodynamic region is very narrow compared to that of CIGS (Figure 2.4) [49]–[51]. This implies that the formation of unwanted secondary phases is very likely to occur together with the kesterite phase. In addition, high efficiency devices have been shown to require Cu-poor Zn-rich compositions [52], [53].Taking a look at the bottom-right part of Figure 2.4, it is easy to see how the size of the stable region decreases for Cu-poor conditions aggravating the situation. Working in this regime, the formation of Zn(S,Se) phases is, thus, extremely likely to happen [54]. What is more, the loss of Sn and Se during high temperature absorber synthesis has been identified as a critical issue for kesterites due to the high volatility of Sn(S,Se) compounds [55], [56].

A common approach to minimize the loss of these materials is to increase their vapor pressure by working in an excess Se and Sn atmosphere. However, besides preventing material loss, these annealing conditions also promote the formation of $Sn(S,Se)_x$ secondary phases.

Other secondary phases like Cu_x (S,Se), Cu_2Sn $(S,Se)_3$ or SnO_2, although less likely to be formed in Cu-poor Zn-rich conditions, have also been reported, especially at the front and back sides of the absorber [57], [58].

Secondary phases could be avoided by a very precise control of the kesterite formation mechanism, and, especially, of the partial pressures of the different compounds during annealing processes. However, this is very challenging technologically. A more practical approach proposed by several authors is to accept defeat and allow some secondary phase formation only to later eliminate them from the surface of as-annealed CZTSSe absorbers using selective chemical etchings [59]–[61]. Either way, the formation of these phases within the bulk of the absorber is very difficult to eliminate completely and can lead to compositional fluctuations at the kesterite/secondary phase interfaces that can induce the formation of defects that act as recombination centers and ultimately cause V_{OC} losses [62]–[64].

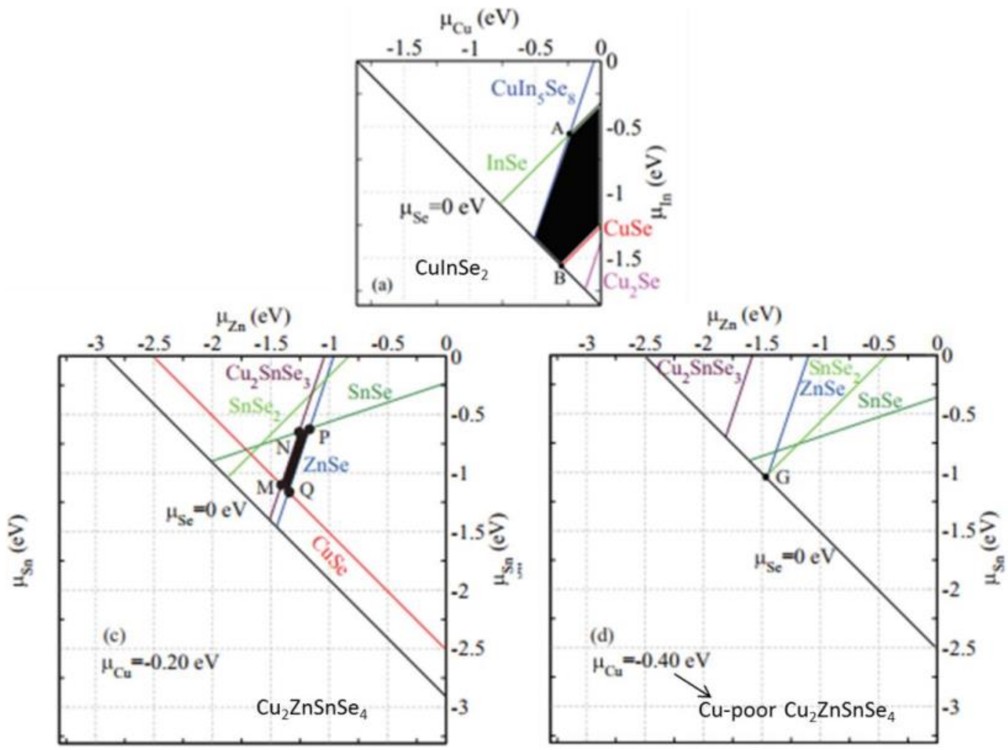

Figure 2.5: *Chemical potential equilibrium diagrams for $CuInSe_2$ (top) and $Cu_2ZnSnSe_4$ (bottom). The black area represents the stable one phase region. Reproduced with permission from [49].*

➷ ***High density of defects***

Although theoretical calculations have proven that the kesterite crystal structure is the most energetically favorable for CZTSSe compounds, the energy difference with the stannite crystal structure (see Figure 2.5, (a)) is very small [41]. This small difference, together with the isoelectronicity and similar ionic radii of Cu and Zn, induces a strong tendency to the formation of Cu_{Zn} and Zn_{Cu} anti-site defects [39]. In particular, the donor–acceptor defect complex [Cu_{Zn} + Zn_{Cu}] has an extremely low formation energy which results in a high concentration of these defects, widely known as the Cu/Sn disorder [39], [65].

On the other hand, in Cu-poor Zn-rich compositions, V_{Cu} is the defect with lowest formation energy and is expected to be the main responsible for p-type conductivity of CZTSSe absorbers (Figure 2.5, (b))[49]. This way, a high concentration of V_{Cu}, Cu_{Zn} and

Zn_{Cu} is expected in CZTSSe absorbers. In addition, it has been proposed that deep defects like Sn_{Zn} and defect clusters such as [$2Cu_{Zn}$ + Sn_{Zn}] can also occur during kesterite formation even in Zn-rich conditions [66], [67].

All these charged defects and defect clusters, depending on their spatial distribution, induce point defects (isolated defects), bandgap fluctuations (spatial correlation of the defects in the VB and the CB) and/or potential fluctuations (uneven spatial distribution of charged defects) that translate into a series of permitted states within the bandgap (see Figure 2.5, (c)) [68], [69]. This phenomenon is known as band tailing since it is characterized by sub-bandgap absorption that can be described as:

$$\propto \sim exp\left(-\frac{E_g - E}{E_U}\right) \tag{2.1}$$

where α represents absorption and E_U stands for the so called Urbach energy. The states within the bandgap can act as recombination centers and, thus, strongly reduce the V_{OC} in kesterite devices. In fact, a near-linear correlation between E_U and the Voc deficit of different technologies was found a De Wolf et al. [70].

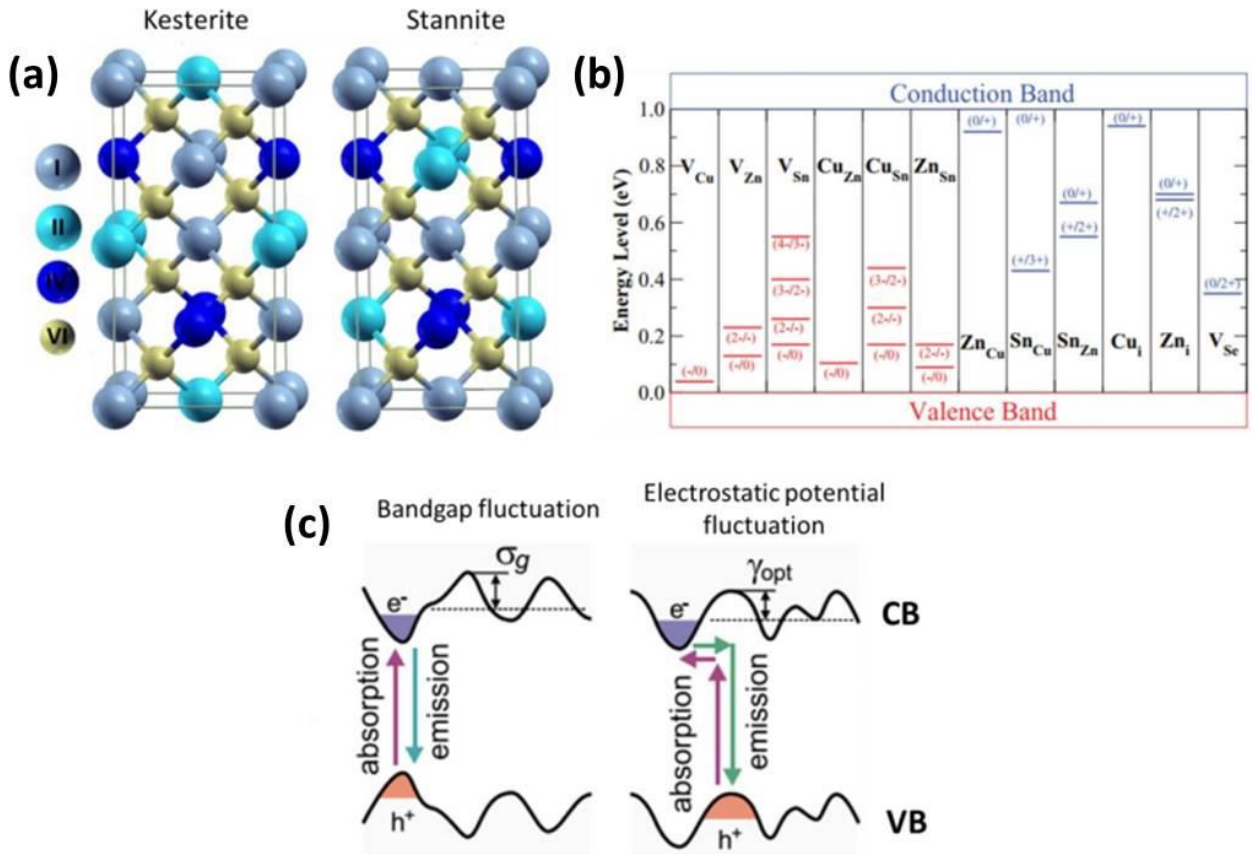

Figure 2.6: *Comparison between the kesterite and stannite crystal structures (a). Adapted with permission from [71]. Ionization levels of intrinsic defects in the band gaps of* $Cu_2ZnSnSe_4$. *The red bars show the acceptor levels and the blue bars show the donor levels, with the initial and final charge states labelled in parentheses (b). Reproduced with permission from [49]. bandgap and electrostatic potential fluctuations due to the uneven spatial distribution of defects (c). Reproduced with permission from [72].*

➥ ***Other limiting factors***

Some other factors that have been considered to limit the V_{OC} of kesterite solar cells to a lesser extent are: (i) Front interface (CdS/CZTSSe) recombination due to non-optimum band alignment, especially for wide bandgap [73]–[75], back interface recombination due to a defective CZTSSe/Mo coupling and chemical instability [73]–[76], short minority carrier lifetime [77] and grain-to-grain non-uniformities [78].

As a final remark, it should be born in mind that all the different factors affecting the V_{OC} deficit of kesterites discussed above are not isolated one from each other and that there are deep relationships between them [78], [79].

2.4. The way to improve kesterite Solar Cell performance

Inspired by the successful approaches executed to the chalcopyrite CIGS technology. The kesterite based solar cells has been following the path of its predecessor to get rid of its limitations and go forward with higher efficiencies. In this regard, there is a particular research axis targeting the reduction of defect density to boost device performance by optimizing processes of surface and grain boundary passivation [80], [81]. Additionally, the issues of optical losses [82]. Nevertheless, the intrinsic point defects are still a critical issue in the bulk of the absorber [83]. The alternative solution to decrease cation disorder in the CZTSSe compound is the cationic substitution: Zn with Cd [84], Zn with Ba [85], Cu with Ag [86] and Sn with Ge [87].

2.4.1. Doping and alloying kesterite

Getting motivated by the successful approaches executed to the chalcopyrite CIGS technology. The kesterite has been following the way of its predecessor to get free of its limitations and go forward with higher efficiencies. In this regard, we present hereafter solutions among others proposed in the literature. However, before given more details about what has been done in the literature, one should keeping in mind that the initial goal of doping is (i) to modify the electronic of thin-film kesterite properties (ii) to maximize the collection of photo-generated carriers without changing the crystal structure or altering the optical properties of the host material. However, alloying is referred to an isoelectronic cation substitution to introduce ionic size mismatch, which can be particularly interesting for the absorber band engineering [88].

2.4.1.1.Doping kesterite

➯ ***Alkali doping:***

The alkaline elements doping of the absorbers has been observed to be a critical issue for the development of CIGS and CZTSSe solar cells and an effective way of reducing the large Voc deficit of the technologies. Alkalis, especially Na, have the ability of modifying the synthesis process and improving the morphological and electrical properties of the absorbers, which results in enhanced device performance. The following sections review the evolution and main effects of alkaline doping in kesterite solar cells.

Sodium (Na): The discovery of the beneficial effects of Na doping in CIGS absorbers was one of the major breakthroughs in the development of the technology [66], [89], [90]. They were first described by Hedström et al. in 1993 [91]. They fabricated CIGS devices in different substrates (soda lime glass, borosilicate, sapphire and alumina) and observed that the absorbers grown on soda-lime glass exhibited a superior crystal structure and performance and associated it to the presence of Na coming from SLG [92]. Since then, Na doping became a hot research topic and its presence was ultimately found to be a requirement to achieve high efficiencies [89], [90]. Following the success of Na doping in CIGS, the beneficial effects of alkali doping in kesterites solar cells have also been a major topic of research in the last years. Na has been found to produce similar effects in kesterite devices than in CIGS and to be crucial to achieve high efficiencies [93]. Principally, Na acts three-fold:

- As a fluxing agent and increasing crystal size;
- As a grain boundary passivator;
- As a carrier concentration booster.

These effects translate into devices with a highly improved performance due to enhanced Voc and FF, mainly. It is widely accepted that Na ions have a large mobility in kesterites during high temperature annealing easily migrating through Cu vacancies due to the low energy formation of Na_{Cu} [94]–[96] and that Na tends to accumulate at the grain boundaries where, due to their synergy with oxygen [96], [97] or help create a positive potential that facilitates charge separation [97].

2.4.1.2. Alloying kesterite

The alloying strategies based mainly on cationic substitution using isoelectronic elements from the same column. For instance, the partial substitutions of Cu by (Ag, Li, K, Na), the Zn substitution is possible by (Cd, Ba, Mn, Fe, Co, Ni) due to their analogous structure and finally, Sn substitution is feasible by Ge and Si.

In this thesis, we focus on the Sn substitution by Ge.

➢ ***Germanium (Ge)***

Germanium (Ge) is probably one of the most suitable and interesting group IV elements for adding into the kesterite structure, in particular at the Sn-sites. Considering the most stable oxidation states of these two elements, +4 is more likely to occur with Ge than with Sn [98], thus avoiding presence of potentially harmful +2 oxidation states [99]. Additionally, a bandgap range from 1.0 to 2.25 eV is possible with the $Cu_2Zn(Sn_{1-x}Ge_x)(S_{1-y},Se_y)_4$ alloy [100], [101].

Several works can be found on the Ge addition in the kesterite host, from doping levels to alloying, including partial and total substitution of Sn. Regarding doping strategies, Giraldo et al. reported the beneficial effect of Ge as dopant in CZTSe [102], [103], observing a large efficiency improvement for very small quantities of Ge (less than 0.5% relative to Sn), followed by addition studies further exploring the origin/mechanism involved in this approach [103], [104]. Firstly, a strong impact on the morphology and grain size has been observed, frequently obtained large grains [105], [106]. This was related to the formation of Ge-Se liquid phase (at 380 °C) during the reactive annealing, acting as crystallization flus. Other beneficial efforts of Ge have been reported, including interaction with Na with effect carriers concentration [105], modification of the reaction pathways minimizing Sn-Se phase formation (avoiding to a large ectent the Sn loss and secondary phase formation) [107], passivation of detrimental grain boundaries related to high recombination [106], annihilation or minimization of Sn-related deep defects [108]. Through the optimization of doping strategies, by adding Ge nanolayers at the bottom and on top metallic precursors, Ge doping has contributed to considerably reduce the Voc deficit to less than 0.57V thus achieving a record efficiency of 11.8% [107].

On the other hand, alloying approaches have been also investigated recently. As in the case of doping, Ge alloying of kesterite has immediately demonstrated a great potential, with device efficiencies ranging from 6.8 to 12.3% [109]–[111]. Among them, it is interesting to note that the best efficiency was achieved with a relative Ge content of 39% (i.e.(Ge/(Ge+Sn)=0.39), through the optimization of a thermal annealing containing $GeSe_2$ [111], [112] leading to an improvement of the V_{OC} deficit by reducing band tailing, and a reduced carrier recombination at the absorber/buffer interface and/or in the space-charge region. Collord et al. studied almost the full range of possible Ge/(Ge + Sn) compositional ratios (from 0 to 90%) by preparing a continuously graded sample with combinatorial mixing of Ge and Sn containing inks [113], and achieved an 11% efficiency solar cell with an optimized 25% Ge substitution (x= 0.25) with E_g= 1.2 eV), leading to a remarkable reduction of the V_{OC} deficit.

After the fast progress Ge has demonstrated, a particular attention has been paid in the few past years to the total substitution of Sn by Ge especially with the aim to widen further its band gap for a potential application as a top cell in multi-junction solar cells. In the very beginning, studies on pure Ge based kesterite have been mainly focused on the structural and optical properties of this new compound [114]–[116].

Among the most relevant pure Ge kesterite results, Schnabel et al. reported efficiencies exceeding 5% for a sulfo-selenide CZGSSe (Eg= 1.5 eV) solar cell [117], while for the selenide CZGSe (Eg= 1.4 eV) compound, Sahayaraj et al. published a 5.5% efficiency device with a remarkable V_{OC} of 744 mV [118]. Intriguingly, the Ge based kesterite showed less electrical losses from band tailing/electrostatic potential fluctuations compared to Ge free devices [118], [119]. However, the main limiting factors were linked to a high series resistance, leading to imperfect current collection and a high interface recombination [120]. Trying to address these issues, a detailed optimization of the CdS chemical bath deposition has allowed achieving a record efficiency of 7.6% for a CZGSe (Eg= 1.36 eV) absorbers [121].

By an impression of the relevance and the boost in efficiency that CZGeSe has demonstrated in short time compared to other technologies. The work presented this thesis has the same optic and aims to develop and optimize for pure germanium kesterite absorbers for any future integration as a top cell in tandem solar cells. In the contrary of what has been used in other experiments, the series of studies given in this thesis promise a much more secure and less toxic synthesis environment with efficiencies at the level of the best reported ones for this new compound.

More details about the synthesized CZGeSe along with the characterization techniques used in this dissertation are presented in the next chapter (chapter 3).

3

Methodology I

3.1. Techniques and pieces of equipment

The general aspects of the methodology employed throughout this thesis part are presented. However, the specific experimental features of the different investigations presented in this thesis, will be detailed in their corresponding chapters. In order to carry through the goals exposed above and study the feasibility of developing high efficiency kesterite solar cells based on Cu_2ZGeSe_4 compound, the methodology employed is based on the following basics:

- Identification of the main issues for solar cell fabrication.
- Solar cells fabrication on the Mo coated SLG by using a two-step process involving the chalcogenization of sputtered metallic precursors.
- Absorbers and completed devices characterization.

The main processing and characterization techniques performed throughout the thesis (kesterite part), as well as the pieces of equipment used to carry them out will be briefly presented. After that, the standard procedure employed for the kesterite solar cells fabrication will be explained in detail.

3.1.1. Structural, compositional and morphological characterization

➾ ***X-ray fluorescence***

X-ray fluorescence (XRF) is a phenomenon in which atoms emit radiation upon X-ray illumination. Energetic X-rays can be absorbed by electrons located at the inner shells of an atom, which are subsequently promoted to an excited state leaving a vacancy behind. An electron from a higher energy shell can then fall into the low-energy vacancy emitting the energy difference between both energy levels as a photon. The possible energies of the emitted photons depend on the electronic structure of the atom and, thus, are characteristic of each element. By analyzing the spectrum emitted by a sample under X-ray illumination, it is possible to obtain information about its elemental composition. However, different elements possess distinct mass absorption coefficients so the intensity of their fluorescence is different. In addition, this factor is also influenced by the density of the material, which largely depends on the technique employed for its synthesis/deposition. Finally, for complex multilayers stacks like the ones employed in this work, the radiation emitted by the layers at the bottom is attenuated by the upper layers before escaping the sample. This attenuation will depend on the thickness and density of the different layers above. Therefore, it is not possible to extract quantitative information from XRF measurements in a direct way. The spectra obtained need to be fitted employing a model that takes all these issues into consideration.

A Fischerscope XVD XRF analyzer (Figure 3.1) was employed to measure and control the thickness and composition of Mo back contact layers, precursor metallic stacks and kesterite absorbers, mainly. The software of this XRF system allows creating complex layer models (recipes) and fits the obtained spectra to them through an iterative process in order to provide information about the composition and thickness of the different layers. Three types of layer model have been mainly employed throughout this work:

- **SLG/Mo**: for measuring the thickness of Mo back contacts.
- **SLG/Mo/CuZnGe**: for measuring the thickness and composition of precursor metallic stacks
- **SLG/Mo/$Cu_2ZnGeSe_4$**: for measuring the thickness and composition of kesterite absorbers.

The same measuring parameters were employed in the three recipes: an accelerating voltage of the primary X-ray source of 50 kV, a Ni10 filter to reduce background signal, a spot size of 1 mm and an integration time per measuring point of 45 s. Usually, a 9 to 16-point measuring grid was distributed throughout the surface of the sample and the mean compositional and thickness values were calculated. Due to the fairly complex layer systems measured and to the fact that the density of the materials deposited and synthesized in this thesis differs from standard bulk values, in order to obtain accurate values from the fittings of the measuring recipes, these had to be calibrated employing reference samples with known thicknesses and compositions.

The thickness and composition of the reference samples was measured by high-precision techniques prior to the calibration of the XRF system.

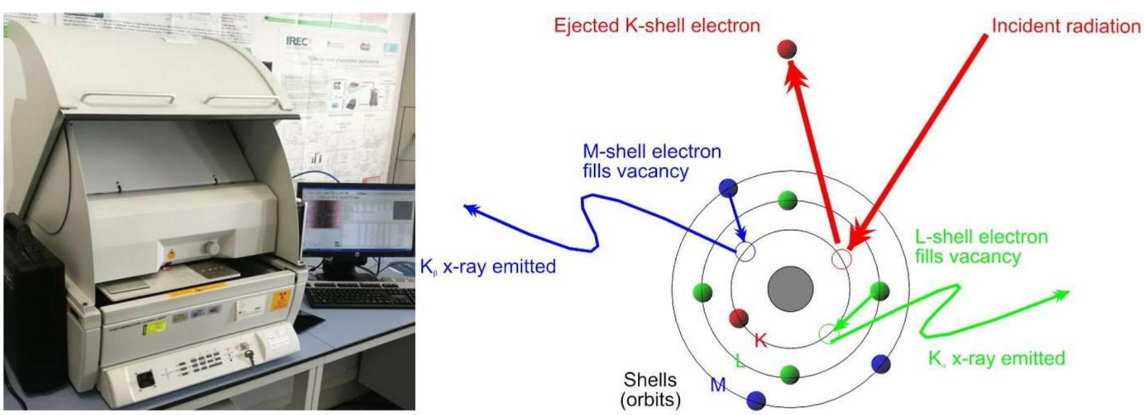

Figure 3.1: *image of Fischerscope XVD X-ray fluorescence analyzer (left) and representation of characteristic X-ray fluorescence principle.*

Field emission scanning electron microscopy and energy dispersive X-ray spectroscopy

An electron microscope is a type of microscope that uses electrons as the source of illumination. Owing to the shorter wavelength of electrons compared to visible photons, the resolving power of an electron microscope is far higher than that achievable with standard optical microscopes. In a field emission scanning electron microscope (FESEM), a small diameter and highly coherent beam of electrons is generated by a field emission gun, focused on the surface of the sample and raster scanned in a rectangular area. The beam interacts with the atoms in the specimen producing several signals that can be detected individually using different types of detectors. The FESEM microscope employed in this work, a ZEISS Series Auriga (Figure 3.2), is capable of detecting, mainly, three types of signal:

- **Back scattered electrons:** This signal corresponds to the electrons from the scanning beam, which are elastically back-scattered by the atoms of the sample. Since the probability of back scattering increases with the atomic number of the element, this signal produces micrographs in which areas with different composition appear with a different contrast and thus provides spatial-compositional information.
- **Secondary electrons:** This signal is generated by low energy electrons ejected from the surface of the sample as a result of an inelastic scattering process. The number of emitted secondary electrons depends on the interaction volume of the beam with the sample which, in turn, depends on the angle between them. This way, edges and steep surfaces (in which the interaction volume is higher) appear brighter than flat surfaces providing micrographs with a well-defined contrast that enable structural and topographical analyses.
- **Characteristic X-rays:** This signal arises from the interaction of the incident electron beam with the low-energy electrons located at the inner shells of the

atoms of the sample. The incident beam can promote these electrons to an excited state. A high-energy electron from an outer shell can then occupy the low energy vacancy emitting the energy difference between both states as an X-ray photon. Since the energy difference between the different electronic shells is dependent on the atom itself, each element generates photons with characteristic energies. Thus, by analyzing the radiation emitted by the sample, it is possible to get precise information about its elemental composition. This process is called energy dispersive X-ray spectroscopy (EDX).

The results presented in this thesis are based, mainly, on secondary electron imaging employing a standard Everhart-Thornley detector. This detector consists of a collector which is at around +350 V in order to attract the electrons emitted by the sample, a scintillator system and a photomultiplier to overcome the low emission rate and energy of secondary electrons and obtain a sufficiently strong signal useful for imaging [122]. This way, FESEM was employed to analyze the surface of kesterite absorbers (top view) and/or the layer structure of complete devices (cross section) through detailed micrographs acquired from secondary electrons. The micrographs were normally obtained using a 5 kV accelerating voltage and a 30 μm aperture for the electron beam as well as a working distance ranging from 4 to 7 mm. Additionally, the FESEM microscope was employed to analyze the surface composition of some selected kesterite absorbers employing an EDX Oxford Instruments XMax detector integrated in the system. A 15 kV accelerating voltage was employed for this purpose.

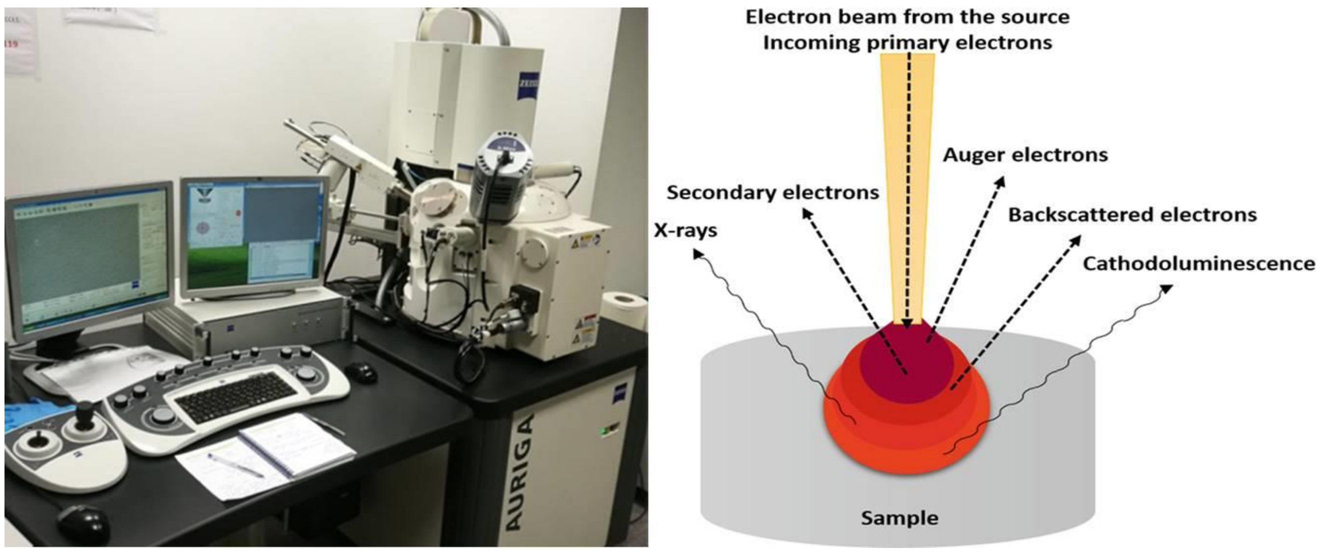

Figure 3.2: image of ZEISS Series Auriga field emission scanning electron microscope (left) and scheme illustrating the working principle of Scanning Electron Microscope (right).

➷ ***Raman spectroscopy***

Raman spectroscopy is an advanced characterization technique based on the analysis of inelastic scattering processes of light with the vibrations (phonons) of the atoms or molecules in a material. A Raman spectrum is obtained by illuminating the material and measuring the in-elastically scattered radiation arising from it as a function of its frequency (usually called Raman shift). For crystalline materials, a Raman spectrum consists of individual Lorentzianshaped peaks, each of them related to an individual phonon. The parameters of the individual peaks can be directly related to the vibrational properties of a material which, in turn, depend on its composition and internal structure. This way, the symmetries of its crystalline structure determine the type of vibrations, the number of atoms in the unit cell influences the number of possible phonons and the frequency of the phonons is defined by the type of atoms (i.e. chemical composition). Thus, Raman spectroscopy can be used to determine the presence of different phases in a material, their composition, crystalline structure and crystalline quality. Raman measurements were carried out to investigate different properties of selected kesterite absorbers synthesized throughout this work. In particular, their crystalline quality, S-Se composition and/or the presence of secondary phases were evaluated. A Raman setup developed at IREC (Figure 3.3) was employed for this purpose. It consists of a Raman probe coupled by optical fibers to two spectrometers: a Horiba Jobin Yvon FHR640 (optimized for the ultraviolet-visible spectral region) and a Horiba Jobin Yvon iHR320 (optimized for the near infrared-infrared region) which are coupled, in turn, to cooled CCD detectors. Several lasers with wavelengths ranging from 325 to 1024 nm are available as excitation sources depending on the properties and materials studied. The selection of the laser is particularly important for investigating the presence of secondary phases. By coupling the excitation wavelength with the bandgap of a specific secondary phase (usually called resonant Raman conditions), a highly increased sensitivity is achieved enabling the detection of very small concentrations almost undetectable otherwise.

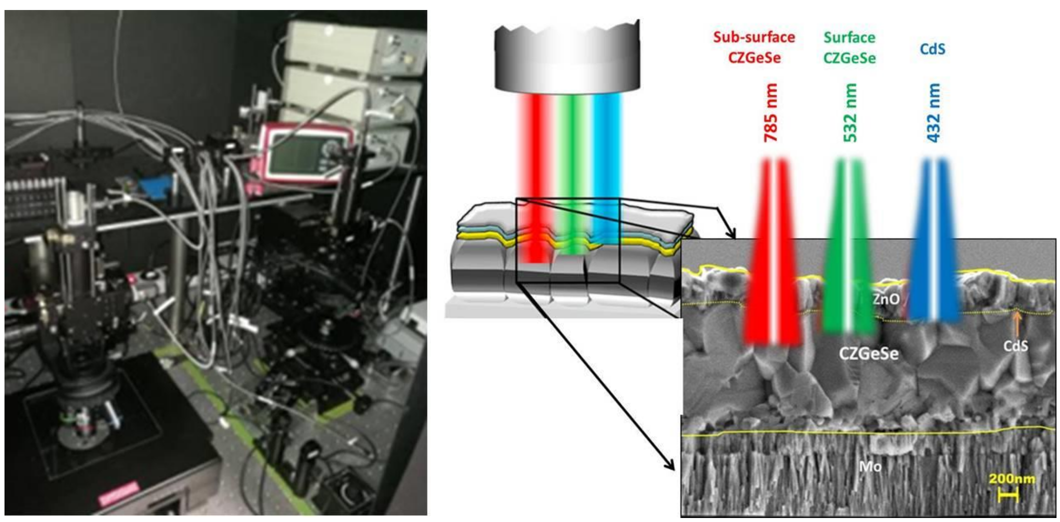

Figure 3.3: *image of Raman spectroscopy setup developed at IREC (left) and Scheme of the Raman analysis depths for the excitation wavelengths of 442, 532 and 785 nm.*

3.1.2. Electrical characterizations

➱ ***Four- point probe***

Four-point probe (**4pp**) is an electrical measurement setup consisting of four terminals: a pair of outer current-carrying electrodes and a pair of inner voltage-sensing electrodes.

By applying a current through the outer electrodes and due to the high impedance of the voltmeter, almost no current will flow through the sensing wires avoiding contact and wire resistances and enabling the measurement of very small resistances. This technique was employed to measure the sheet resistance (R_{sheet}) of conductive layers such as Mo and TCOs. An Ever being setup with 4 equidistant measuring tips connected to a Keithley 2420 power source (Figure 3.4) was employed for this purpose.

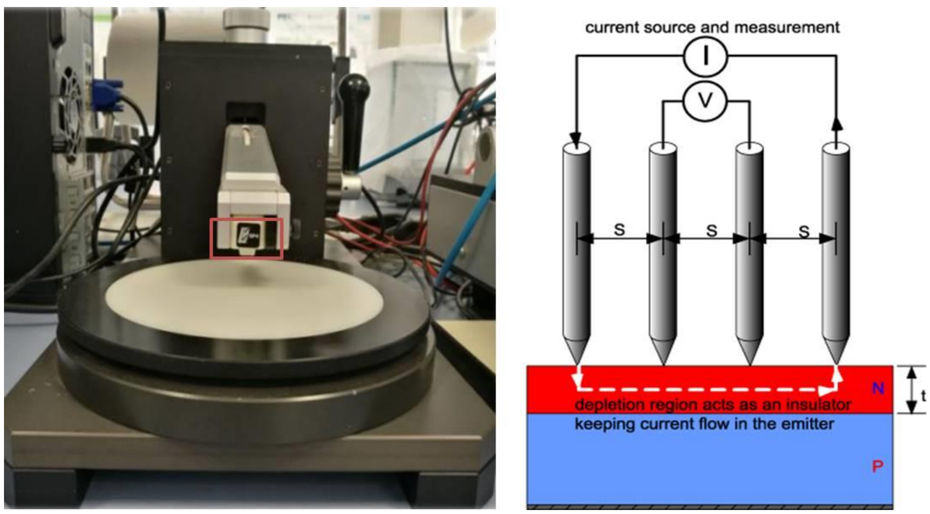

Figure 3.4: *image of Everbeing four-point probe (left) and scheme representation of 4pp.*

➯ ***Capacitance-voltage***

Capacitance-voltage (C-V) measurements provide information about the carrier concentration and the width of the surface charge region (SCR) of a solar cell based on the assumption that a p-n junction can be modeled as a parallel plate capacitor. In kesterite solar cells, the doping level of the n side of the junction (CdS) is orders of magnitude higher than that of CZTSSe and, in addition, its thickness is orders of magnitude lower. This way, the SCR can be assumed to be located entirely at the p side. In this approximation, the charge (Q) “stored” in the capacitor is equivalent to the number of doping impurities within the width of the SCR (W) times the elemental charge (q). By applying a bias voltage to the p-n junction, the width of the SCR varies and so does the charge:

$$\mathrm{dQ} = qN(W)\,dW \rightarrow \mathrm{N(W)} = \frac{1}{\mathrm{q}}\frac{dQ}{\mathrm{dW}} \qquad (3.1)$$

where N(x) is the linear density of doping impurities. On the other hand, the capacitance of a capacitor can be expressed as:

$$C = \frac{\epsilon A}{x} \rightarrow x = \frac{\epsilon A}{C} \qquad (3.2)$$

where ε is the dielectric constant, A the overlapping area of the parallel plates and x the width of the capacitor (W for a p-n junction). In the case of a p-n junction, if the space charge region is varied by applying a voltage, its capacitance will also vary:

$$dW = -\frac{\epsilon A}{C^2}\,dC \qquad (3.3)$$

Finally, the change of the charge stored in a capacitor when the voltage is between its terminals is varied can be obtained from the fundamental definition of capacitance:

$$C = \frac{dQ}{dV} \rightarrow dQ = CdV \qquad (3.4)$$

Combining Equations (3.1), (3.3) and (3.4), it is possible to calculate n (W) (the carrier concentration as a function of the SCR width) from C-V measurements:

$$n(W) = -\frac{\mathrm{C}^3}{q\epsilon \mathrm{A}^2}\frac{dV}{dC} \rightarrow n(W) = \frac{2}{q\epsilon \mathrm{A}^2}\left(\frac{\mathrm{dC}^{-2}}{dV}\right)^{-1} \qquad (3.5)$$

C-V measurements were performed on complete devices by applying a 50 mV oscillating AC voltage at various frequencies and measuring the quadrature current response at different bias voltages. The measurements were carried out employing a Keysight E4990A impedance analyzer and a homemade Faraday cage sensor box (Figure 3.5). The measurements were used to calculate the carrier concentration and the width of the space charge region of selected devices.

Figure 3.5: *image of Keysight E4990A based capacitance-voltage measurement setup.*

➷ *Current-voltage analysis*

The fundamentals of current-voltage (J-V) analysis were explained in section 1.2. A setup consisting of a Keithley 2400 source and a pre-calibrated Sun 3000 Class AAA solar simulator by Abet Technologies (Figure 3.6) was employed to carry out the J-V measurements of the different devices fabricated in this work. The measurements were carried out at 25 ^{o}C and both in the dark (for selected devices) and under simulated AM1.5 illumination (1000 W/m^2). The main parameters of the solar cells were extracted from the J-V curves: V_{OC}, J_{SC}, FF and η. In some cases the shunt and series resistances (R_{sh} and R_s) were also calculated from the J-V curves.

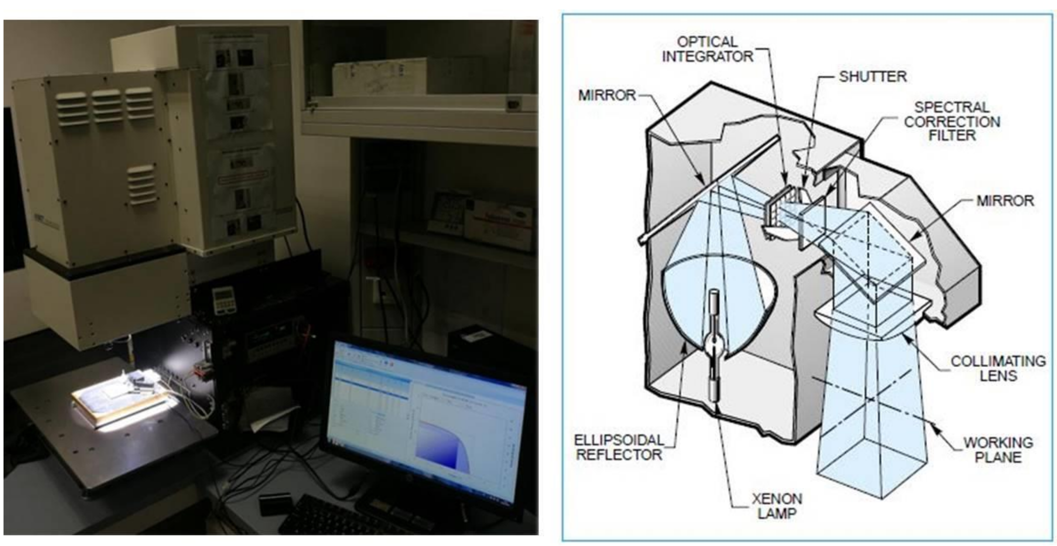

Figure 3.6: *image of J-V analysis setup based on a calibrated Sun 3000 Class AAA solar simulator by Abet Technologies.*

➫ ***External quantum efficiency***

External quantum efficiency (EQE) is an optoelectronic characterization technique that complements J-V analyses by providing information about charge collection as a function of the illumination wavelength. This way, in EQE measurement, the sample is illuminated with monochromatic light and the ratio between the numbers of incident photons to the number of collected EHPs is measured at different wavelengths to provide a collection spectrum.

By integrating the EQE spectrum times the AM1.5 illumination spectrum, it is possible to obtain the J_{SC} of the device. EQE measurements were performed on selected devices to study their collection. A Bentham PVE300 spectral response system consisting on X_e and halogen light sources, a mono-chromator and a lock-in amplifier was employed for this purpose (Figure 3.7).

Figure 3.7: *image of spectral response system used for EQE measurements Solar cell fabrication.*

3.1.3. Solar cell fabrication

➯ ***Direct current magnetron sputtering***

Direct current (DC) magnetron sputtering is a PVD coating technique that allows the deposition of thin films of a wide variety of materials. An inert gas plasma (usually Ar) is generated inside a chamber by applying a high voltage between a cathode (usually the target material) and an anode (usually the deposition substrate) (Figure 3.8). The plasma is confined around the target through a strong magnetic field generated by a magnetron.

The moving ions in the plasma hit the target material and sputter atoms out from its surface. Most of the sputtered atoms are neutral so are not affected by the electromagnetic field and fly away in straight lines from the target. This way they can reach a substrate and stick onto it. By varying the inert gas pressure and/or plasma power, it is possible to control the sputtering rate (which determines the growth rate of the layer) and the kinetic energy of the sputtered atoms (which influences the density, morphology and adhesion of the deposited layer). The substrate can be heated up during deposition to improve or tune the crystallization of the deposited material. In addition, by introducing a reactive gas in the plasma, like O_2, it is possible to make the sputtered atoms react with it before being deposited. This is called reactive sputtering.

DC magnetron sputtering is an ideal technique for metal deposition due to their high conductivity that facilitates the creation of the plasma. When depositing low conductivity materials, charge can build up on the surface of the target and, in addition, the target can heat up substantially complicating the deposition process. In order to minimize these issues, a pulsed DC source can be employed to generate the plasma.

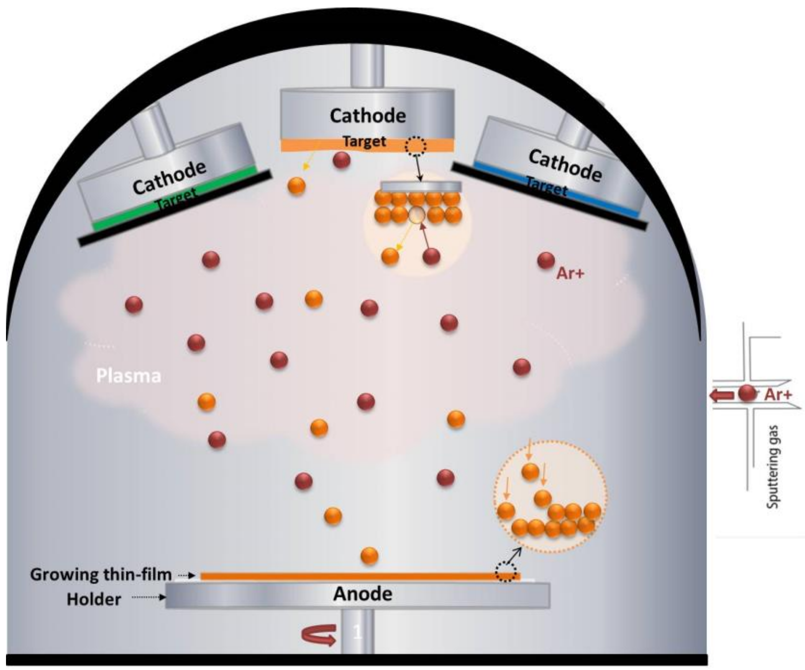

__Figure 3.8:__ Schematic illustration of DC magnetron sputtering operation.

Two different sputtering systems were employed throughout the CZGeSe experiments in order to deposit the different layers required for the fabrication of kesterite solar cells:

- Alliance Ac450 (Figure 3.9, left): This system is comprised by a load lock and a deposition chamber connected to a mechanical pump and a turbo-molecular pump. Inside the deposition chamber there are three cathodes located at the top where 101 mm diameter targets can be placed. The substrate is placed at the bottom. It is equipped with a DC generator (TRUMPF Truplasma DC 3002) for sputtering and a RF generator (TRUMPF PFG 300 RF) for plasma etching surface treatments. This system was used for the deposition of metallic layers (Mo, Cu, Zn and Sn). The depositions were performed using Ar plasma.
- Alliance CT100 (Figure 3.9, right): This system is comprised by a load lock and two deposition chambers each of them connected to independent mechanical and turbo-molecular pumps. There are two cathodes at the left chamber and three at the right chamber where 101 mm diameter targets can be placed. It is equipped with a pulsed DC generator (Advanced Energy DC pinnacle plus). The left

chamber was employed for Mo and Mo: Na deposition and the right chamber for the deposition of TCOs (ZnO and In_2O_3 : SnO_2).

- The deposition of Mo and Ge was performed in continuous DC mode using Ar plasma and the deposition of TCOs was carried out in pulsed DC mode employing Ar + O_2 plasma.

Figure 3.9: *image of DC- magnetron sputtering systems*.

➯ ***<u>Chemical bath deposition</u>***

Chemical bath deposition (CBD) is a thin film deposition technique in which the substrate is introduced into a solution containing dissolved precursor materials.

Then, a synthesis and/or a nucleation reaction are triggered so that the targeted compound is synthesized within the solution and grown onto the substrate. By controlling the chemical route and solution parameters such as concentration, pH and temperature it is possible to control the deposition characteristics and tune the properties of the deposited layers. CBD was employed to deposit the CdS buffer layer of the devices fabricated in this thesis employing a homemade setup consisting in a thermocouple-controlled hot plate and a double beaker bain-marie system for a more precise and homogeneous temperature control and heat distribution (Figure 3.10).

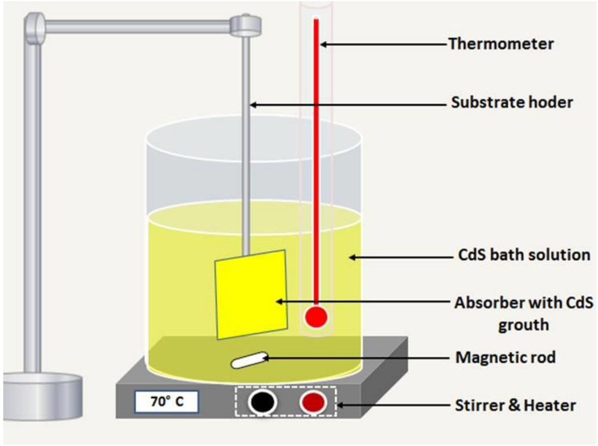

Figure 3.10: *image (left) and scheme (right) of setup for CdS chemical bath deposition.*

➢ ***Reactive annealing***

A reactive annealing is a synthesis technique based on a thermal treatment carried out in a reactive atmosphere. This technique was employed to synthesis kesterite absorbers out of metallic precursor stacks. The precursors were placed into graphite boxes with crucibles containing Se and and $GeSe_2$ (Figure 3.11). The graphite boxes were placed, in turn, inside a Hobersal three-zone tubular furnace (Figure 3.12) consisting of a quartz tube and resistance-based heating elements. The tube is connected to a mechanical pump at the rear end and to an Ar inlet at the front.

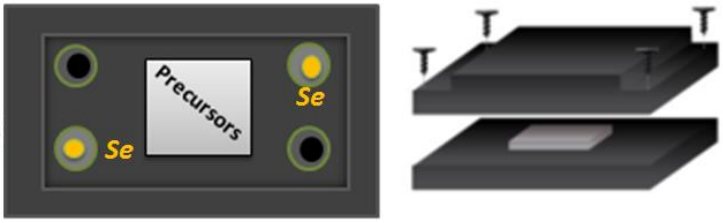

Figure 3.11: *image (left) and Scheme representative (right) of Graphite box for reactive annealing.*

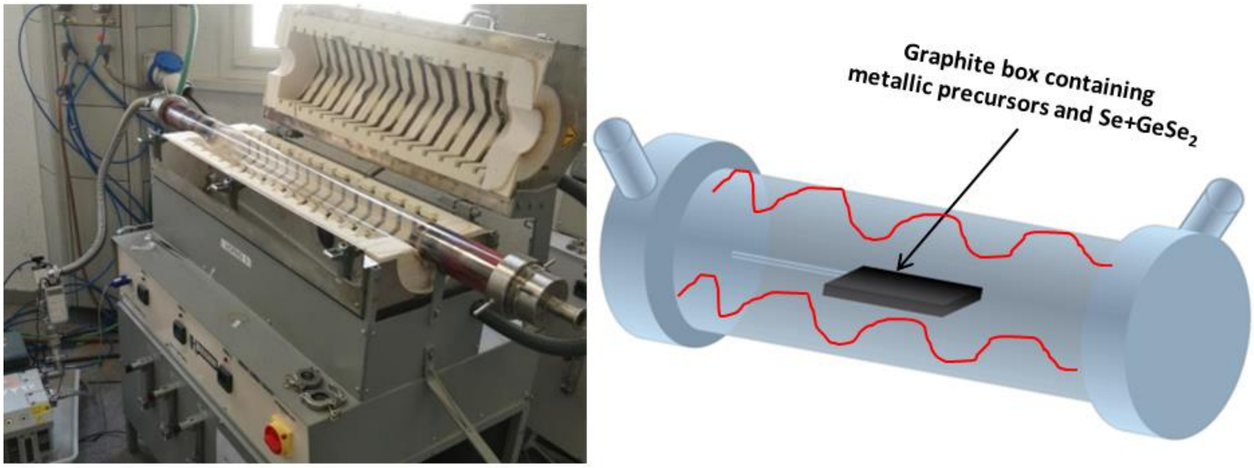

***Figure 3.12**: image of Hobersal three-zone tubular furnaces (left) and scheme representation of Tubular furnace.*

3.2. Solar cell fabrication procedure

3.2.1. Substrate cleaning

The employed substrates for device fabrication were cleaned prior to the deposition processes. The cleaning routine started with a water rinse to wash away inorganic salts, followed by acetone to dissolve organic traces that water cannot eliminate. The substrates were then dipped in isopropanol and deionized water to finally dry with a Nitrogen gun. Each step is performed within 15 minutes at 55 °C.

3.2.2. Back contact deposition

The back contacts adopted in the experiments of CZGeSe solar cells Molybdenum (Mo).
Molybdenum back contact was deposited (670-800 nm) on SLG substrates by DC magnetron sputtering. A trilayer configuration, developed at IREC and similar to the one described in the reference [123], was employed. This configuration consists of a Mo_A (250-500 nm)/Mo_B (120-500 nm)/Mo_A (30-50 nm) stack where Mo_A refers to a dense and conductive layer deposited at high power and low pressure, and Mo_B refers to a porous layer deposited at lower power and higher pressure. All these layers were deposited from a mono-block Mo target (Neyco, 99.99% purity, 101 mm diameter). The growth rate (GR) of the different layers was controlled by XRF thickness measurements. The

final resistivity of the back contact was measured by four points probe technique. Typical resistivity values ranged 0.25-0.5 Ω/sq.

The typical purpose behind this back contact configuration is:

- ✓ The first Mo_A layer provides the back contact with a good adhesion and conductivity.
- ✓ The Mo_B layer, rich in oxygen, acts as a barrier for Se.
- ✓ The last Mo_A layer is a sacrificial layer completely selenized during the reactive annealing.

3.2.3. Precursor deposition

The metallic stack precursor was deposited by DC magnetron sputtering (Alliance Ac450) on top of the Mo-back contact with the stack order: Copper/Zinc/Germanium. This configuration was based on previous works carried out in IREC [76], [124]. The thin layers were deposited from pure metal mono-block targets (Neyco, 99.99% purity, 101 mm diameter). The thickness of the different layers was selected to obtain Cu-poor (Cu/(Zn+Ge)~0.67) and Zn-rich (Zn/Ge~1.1) compositions. The compositional ratios of the precursors and of CZGeSe absorber films was carried out using X-ray fluorescence (XRF, Fischerscope XVD), which has been previously calibrated with inductively coupled plasma optical emission spectroscopy (ICP-OES). The total precursors' thickness was about 540 nn and was controlled by XRF thickness and compositional measurements.

3.2.4. Absorber synthesis

In order to synthesis the CZGeSe absorbers the as-deposited precursors were submitted to a thermal reactive annealing. They were first were placed inside a graphite box together with crucibles containing Se (Alfa-Aesar, powder, 200 mesh, 99.999%) and $GeSe_2$ (Alfa-Aesar, powder, 100 mesh, 99.995%). Then, the graphite boxes were introduced into a 3-zone tubular furnace where a 2-step thermal annealing was performed consisting of: the first step was carried out at 330 °C during 30 min with a heating rate of 20 °C/min under 1.5 mbar Ar pressure, and for the second step was maintained at 480 °C during a dwell time of 15 min in 1 bar Ar pressure (see Figure 3.13). The cooling down process to room temperature occurred naturally taking around 2 hour. The final thickness of the absorbers given by XRF was in the range of 1.45 µm.

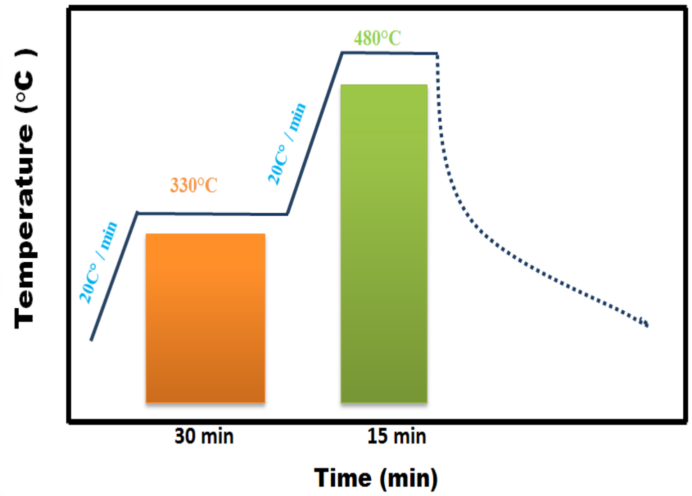

Figure 3.13: *Thermal treatment profile of CZGeSe.*

3.2.5. Chemical etchings for secondary phase removal

The solar cells are completed after etching the synthesized absorbers with KCN solution (2% w/v, 2 min) to clean and remove the possible superficial secondary phases.

3.2.6. CdS buffer layer deposition

CdS buffer layer (~40-60 nm) was deposited onto the absorbers by chemical bath deposition (CBD). $Cd(NO_3)_2$ (0.12 M) was employed as the cadmium precursor salt together with thiourea (0.3 M) as the sulphur source. The deposition was carried out with a solution pH = 9.5 and at 70°C for 40 min.

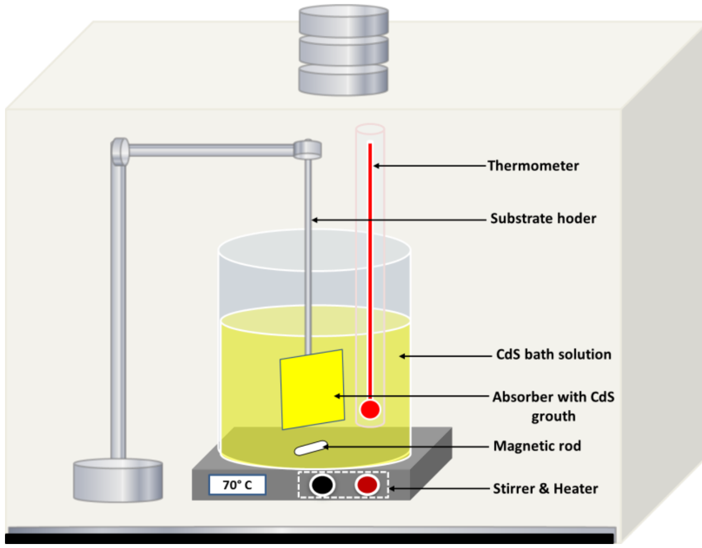

Figure 3.14: *Schematic of Chemical bath deposition (CBD).*

3.2.7. Window layer/front contact deposition

Immediately after CdS deposition, an i-ZnO (50 nm)/ITO (200-300 nm) bilayer was deposited by pulsed DC magnetron sputtering employing Cu-back plated targets (Neyco, ZnO, 99.99% purity; and Neyco, In_2O_3:SnO_2 90:10 wt.%, purity 99.99%) and an Ar/O_2 plasma. An additional piece of SLG was included during the deposition in order to measure the resistivity of the bilayer by four-point probe. Typical resistivity values range 35-80 Ω/sq. The thickness was controlled by XRF.

3.2.8. Solar cell scribing and contact

Once the layer structure was complete, individual 3x3 mm^2 solar cells (8.7 mm^2 active area) were electrically isolated employing a manual microdiamond scriber (OEG MR200) (Figure 3.15). The scribing lines were performed down to the back contact. A small area at one of the edges of the sample was scratched to expose the back contact and some indium was welled onto it. Owing to the small size of the cells, no additional contacts were used and the electrical measurements were carried out by contacting directly the ITO of each cell and the indium pad.

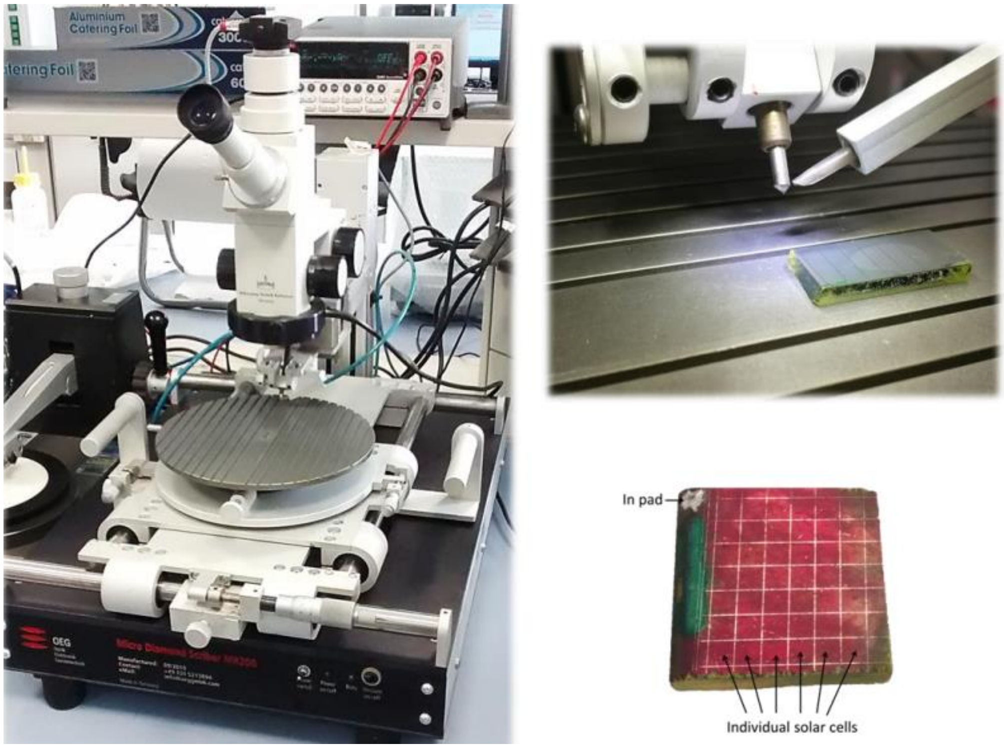

Figure 3.15*: image of Microdiamond scriber used in this experiment.*

4

Insights on the limiting factors of $Cu_2ZnGeSe_4$ based solar cells

4.1. Introduction

$Cu_2ZnSn(S_xSe_{1-x})_4$ (CZTSSe) is a promising candidate for thin-film photovoltaic applications [125], thanks to their advantageous properties including its ideal direct bandgap that can be tuned between 1.0 and 1.5 eV, high absorption coefficient (~10^4 cm^{-1}) and non-toxicity make it suitable for solar cell application (single and tandem solar cells) [126]–[130]. However, the best reported efficiency, so far, for CZTSSe is 12.6% with bandgap energy of E_g=1.13 eV [131], which is about half of the efficiency of the close-cousin CIGS-based solar cell and much lower than the theoretical Shockley-Quiesser limit for CZTSSe, (32.8%)[132]. One of the focal challenges so far for CZTSSe based solar cells is the poor open circuit voltage (V_{OC}) [133], [134]. The maximum V_{OC} depends mostly on the absorber bandgap but can be strongly affected in case of high recombination or defects pinning the Fermi level. Thus, to compare absorbers with different bandgap, the so called V_{OC}-deficit is introduced, defined as $E_g/q-V_{OC}$ (where E_g is the absorber bandgap energy, V_{OC} is the open circuit voltage and q is the electron charge) and offering a figure of comparison between materials of different bandgap values, and it is around 0.6 eV for the record CZTSSe based solar cell [131]. Some studies identify that the main culprits for the large V_{OC} deficit are the intrinsic defects and the band tail [135]–[137]. Furthermore, several causes for the large V_{OC} deficit are suggested: (i) the disordering and lattice defects are acting as an effective recombination centers, and are resulting from the CZTSSe nature, including anti-sites (e.g., Sn_{Cu}, Sn_{Zn}), vacancies (e.g., V_{Zn}, V_{Sn}) and interstitial (e.g., Zn_i) defects in the system [33],[34].

Particularly, the anti-site defects related to the Cu/Zn disordering (Cu_{Zn} and Zn_{Cu}) are almost unavoidable in CZTSSe compound due to the similar ionic radius of Cu and Zn as well as their chemical properties [138], [139]. (ii) the tail state formation which is ascribed to high defect concentrations producing electrostatic potential fluctuations [68], [140], [141] or spatial variations in the crystalline system and/or composition, driving to a nanoscale bandgap fluctuations [73], [142], [143]. (iii) the non-ideal band alignment between the absorber and the CdS, possibly causing high recombination at the absorber/CdS interface and hampering minority carrier transport [144], [145]. There is a particular research axis targeting the reduction of defect density to boost device performance by optimizing processes of surface and grain boundary passivation [80], [81], [146]. Additionally, the issues of optical losses [82], anti-reflection coating and bulk CZTSSe quality [147] are also regularly addressed by the community. Nevertheless, the intrinsic point defects are still a critical issue in the bulk of the absorber [83]. The alternative solution to decrease cation disorder in CZTSSe compound is the cationic substitution: Zn with Cd [84], Zn with Ba [85], Cu with Ag [86], [87] and Sn with Ge. [148].

Several groups showed that partial substitution of Sn with Ge led to a performance enhancement of these thin film solar cells compared to their previous baseline cells. This is in particularly was achieved by improved crystalline quality and grain size, thus boosting the V_{OC} [55],[56]. Table 4.1 shows a summary of some successful studies introducing Ge in the CZTSSe solar cells. A significant improvement in the cell's voltage is obtained from very small quantities <0.005% (doping) up to around 40% (solid solution) substitution of Sn with Ge.

Figure 4.1: *Summary of the beneficial effects of Ge on thin films kesterite solar cells (the bottom section of the table contains data with Sn-free devices).*

Synthesis technique	Ge/(Ge+Sn)	Eff. (%)	FF (%)	J_{SC} (mA/cm²)	V_{OC} (V)	E_g (eV)	V_{OC}-deficit* (V)	Ref
Molecular precursor solutions	0.25	11.0	33.6	33.6	583	1.15	0.31	[113]
Nano-crystal inks printing	0.30	9.4	63.8	31.9	460	1.19	0.48	[110]
DC Sputtering	< 0.005	11.8	66.3	38.3	463	1.04	0.31	[107]
DC Sputtering	< 0.005	10.6	66.7	33.6	473	1.05	0.30	[105]
DC Sputtering	< 0.005	10.1	66.8	33.6	453	1.04	0.31	[102]
Co-evaporation	0.22	12.32	72.7	32.2	527	1.11	0.35	[149]
Co-evaporation	0.22	10.03	62.7	29.5	543	1.19	0.39	[111]
Synthesis technique	**Cu/(Zn+Ge)**	**Eff. (%)**	**FF (%)**	**J_{SC} (mA/cm²)**	**V_{OC} (V)**	**E_g (eV)**	**V_{OC}-deficit* (V)**	**Ref**
Evaporation	1.0	5.5	46	16	744	1.4	0.39	[118]
Evaporation	0.9	7.6	58	22.8	558	1.36	0.54	[121]
DC Sputtering	1.0	6.5	60	19.6	556	1.45	0.63	[112]
Evaporation	0.9	8.5	55.7	24.4	625	1.39	0.50	[150]
DC Sputtering	**0.67**	**6.5**	**60**	**17.8**	**606**	**1.47**	**0.60**	**This work**

* Respected to Shockley–Queisser limit (SQ) and calculated by the authors with the available data in the different references.

The best efficiency reported so far for pure Ge-kesterite (CZGeSe) thin film solar cell is 8.5%, using metallic stack precursors annealed under H_2Se atmosphere [150]. On the other hand, the highest open circuit voltage V_{OC} reported so far for pure Ge-kesterite (CZGeSe) is 744 mV with an efficiency of 5.5% [118] (see the bottom part of Table 4.1).

Research studies on pure Ge-kesterite devices could be benefit to broaden the spectrum of kesterite compounds application, and specifically for efficient photovoltaic tandem solar cells in combination with Si or narrow bandgap chalcogenide compounds. There are still several limitations to overcome due to the scarcity of studies of Ge-based compounds, when considering their Sn counterpart, besides the first studies recently published about physical and fundamental properties of Ge-compounds [67],[68]. In this context, it is of a prime importance to acquire deeper understanding of the defects existing in CZGeSe-based materials and comprehend the key factors limiting CZGeSe-based thin film solar cell performance to push up the CZGeSe solar cells efficiency to a more competitive level. To the best of our knowledge, no previous studies investigating and identifying the defects and limitations for CZGeSe-based thin film solar cell are available. For that purpose, our work intent is to assess and unveil limitations on complete CZGeSe solar cells. In the present study, a complete analysis of morphological, structural and compositional characterization of the prepared CZGeSe thin film based solar cell is presented. The highest performance achieved in this study is 6.5%, with V_{OC} of 606 mV, J_{SC} of 17.8 mA/cm^2 and FF of 60%. Furthermore, a broad range of material characterizations provides valuable insights on the factor limiting state-of-the-art devices, and specifically on the defects and recombination mechanisms.

4.2. Experimental detail

4.2.1. Metallic stack deposition

At room temperature, the $Cu_2ZnGeSe_4$ thin-films are prepared by sequential deposition of Cu, Zn and Ge metallic stack precursors by DC-magnetron sputtering (Alliance AC450), with the elemental layer stack order Cu/Zn/Ge onto Mo-coated soda-lime glass substrates, 750 nm Mo is deposited by DC-magnetron sputtering. The ratios of metallic stack precursors: Cu/(Zn + Ge) and Zn/Ge are kept near 0.67 and 1.07, respectively, as measured by X-ray fluorescence (XRF). The total metallic stack thickness is around 550 nm.

4.2.2. Reactive annealing

The optimized thermal annealing process to growth $Cu_2ZnGeSe_4$ absorbers is carried out in a dedicated tubular furnace using graphite box with 100 mg of elemental Se and 5 mg of $GeSe_2$. The thermal treatment used consists of a two-step annealing process, first step at 330°C for 30 min, with 20 °C/min ramping, in Ar dynamic pressure (1.5 mbar), followed by a second step at 480°C for 15 min, 20 °C/min ramping, in Ar static pressure (1 bar). The absorber composition is selected to obtain Cu-poor and Zn-rich condition (Cu/(Zn+Ge)=0.66 and Zn/Ge=1.1). The atomic compositions of the obtained $Cu_2ZnGeSe_4$ absorbers are 17.6, 14.2, 12.6 and 55.6 % for Cu, Zn, Ge and Se, respectively.

4.2.3. *Device fabrication*

The solar cells are completed after etching the synthesized absorbers with KCN solution (2% w/v, 2 min) to clean and remove the possible superficial secondary phases and oxides. Immediately after the chemical etching, a 50 nm CdS layer is deposited by chemical bath deposition (CBD) from nitrate salts [153]. Then the transparent front electrode i-ZnO (50 nm) and In_2O_3:SnO_2 (ITO, 200 nm, 60 Ω/sq) is deposited by DC-pulsed sputtering (Alliance Concept CT100). Finally, the solar cells are mechanically scribed (3×3 mm^2) with a microdiamond scriber (OEG MR200). Neither antireflective coating nor metallic grids are used for the optoelectronic characterization of the fabricated devices.

4.2.4. *Films and devices characterization*

The composition and precursor thicknesses is characterized by using XRF system (Fischercope XDV) previously calibrated by inductively coupled plasma mass spectrometry (ICP). The scanning electron microscope (SEM) micrographs are acquired with a ZEISS Series Auriga microscope using an acceleration voltage of 5 kV. Raman scattering spectra are measured by FHR 640 and iHR 320 monochromators from Horiba Jobin Yvon both coupled with CCD detectors. The first system is optimized for UV-visible spectral range and used with 442 and 532 nm excitation wavelengths. The second system is optimized for NIR range and used with 785 nm excitation wavelength. The lasers power densities are in the range 100-150 Wcm^{-2}. The characterizations are performed in a backscattering configuration though probe designed at IREC. Moreover, the in-depth chemical composition profiles of Ge-kesterite absorber layer is investigated by Glow Discharge Optical Emission Spectroscopy (GDOES) using Horiba Jobin Yvon GD Profiler 2 spectrometer with 4 mm anode diameter. J-V measurements are performed on the completed devices using a calibrated Sun 3000 class AAA solar simulator (Abet Technologies, 25°C, AM1.5G illumination). The EQE spectra of the elaborated solar cells are measured by Bentham PVE300 system calibrated with Si and

Ge photodiodes. The capacitance-voltage (C-V) measurements are done in the dark, at room temperature with a modulation voltage of 50 mV with a Novocontrol Technologies impedance analyzer. J–V–T measurements are performed using a cryostat (Cold-Head model RDK-101D Sumitomo Heavy Industries Ltd.) cooled by helium closed cycle compressor (Zephyr HC-4A from Sumitomo cryogenics).

4.3. Results and discussions

➯ <u>SEM analysis</u>

The SEM micrographs of $Cu_2ZnGeSe_4$-based solar cells with the following configuration SLG/Mo/$Cu_2ZnGeSe_4$/CdS/i-ZnO/ITO are investigated. The cross section of the entire $Cu_2ZnGeSe_4$ solar cell, as well as the top view of the absorber surface are presented in Figure 4.1. The top view image of the absorber reveals large and closely packed grains well connected with each other's. The cross sectional image of the full device (after chemical etchings and CdS/TCO deposition) indicates large grains in the bulk extending throughout the whole thickness. Unlike to CZTSe layers, CZGeSe seems not to (or just slightly) form the typical bilayer structure, with very few small crystals segregating at the back. In this sense, the cross sectional morphology of CZGeSe appears much better than of CZTSe layers. The average absorber thickness is around 1.45 μm. However, it is very difficult to define the exact thickness of $MoSe_2$ layer, which appears to be quite thin most probably due to the lower temperatures used for the synthesis of CZGeSe when comparing with CZTSe (480 ºC vs. 550 ºC, respectively).

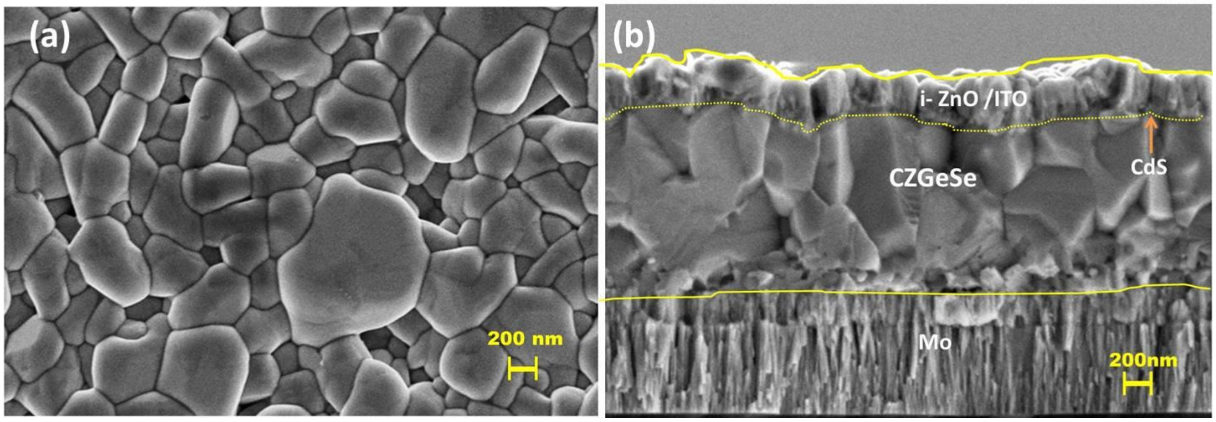

Figure 4.2: *SEM micrographs of the $Cu_2ZnGeSe_4$ (a) top view of the absorber and (b) Cross-section of the SLG/Mo/$Cu_2ZnGeSe_4$/CdS/i-ZnO/ITO.*

↳ <u>Raman analysis</u>

Multi-wavelength Raman scattering analysis was performed in order to verify possible presence of different secondary phases, which can be formed in a row with CZGeSe quaternary phase, and are easily detected due to resonance effect. This specific approach for the detection of small amount of secondary phases in quaternary compounds by Raman scattering spectroscopy already showed an impressive potential, and its sensitivity for detection of some of the secondary phases exceeds the possibilities of a more commonly used for this purpose X-ray diffraction techniques [154]. Particularly, used 442 nm excitation wavelength is resonant for the ZnSe [155] and $GeSe_2$ [156] phases, while 785 nm excitation wavelength is close to resonance for a crystalline orthorhombic polymorph of a GeSe phase [157]. Other possible secondary phases (elemental Ge, Cu_2GeSe_3 or Cu_2GeSe_4) have low band gaps [158]–[160], which suggests that their Raman peaks should be well detected under any used excitation wavelength. A scrupulous analysis of the measured Raman spectra (Figure 4.2) showed absence of any additional peaks except of Raman peaks of CZGeSe phase [155], [161]. The full width at the half maximum of the most intense Raman peak was ~7 cm^{-1} (under 532 nm excitation), denoting a good crystalline quality of the absorber layer, which is consistent with the aforementioned SEM images (Figure 4.1).

On the other hand, a significant change of the Raman spectra measured under 785 nm excitation is related to the correlation of the excitation energy with the main optical transitions in the CZGeSe compound. This resonance effect results to a significant increase of the LO assigned Raman peaks and was described in details for the kesterite type compounds elsewhere [162], [163]. To conclude, the Raman scattering analysis suggests that comparatively low efficiency of $Cu_2ZnGeSe_4$ based solar cells cannot be ascribed to morphological or phase-composition issues, as both appear fully compatible with high efficiency devices.

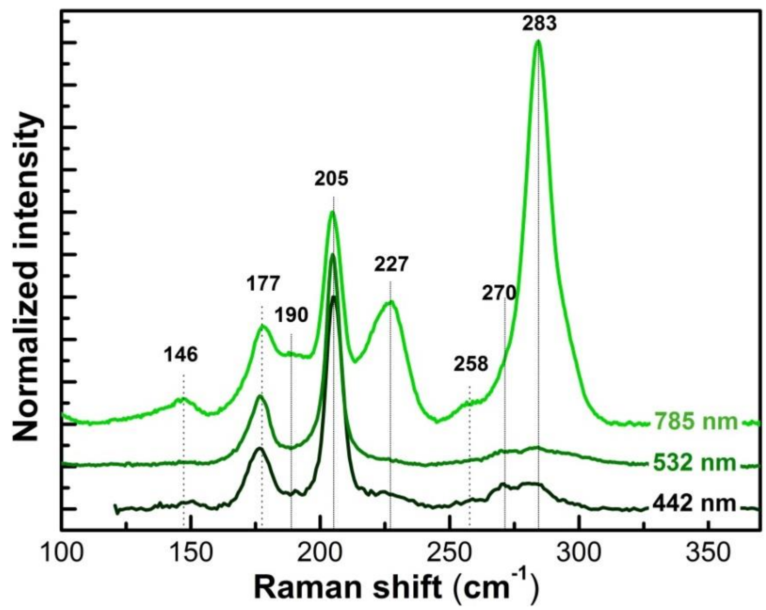

Figure 4.3: *Raman scattering spectra of $Cu_2ZnGeSe_4$ absorber layers measured under different excitation conditions. Numbers indicate the peaks position.*

➯ ***<u>Glow discharge optical emission spectroscopy (GDOES) profiles</u>***

One can notice that from the glow discharge optical emission spectroscopy (GDOES) profiles of Cu, Zn, Ge, Se and Mo (Figure 4.3), the cation distribution is relatively uniform at the top half of the absorber, whereas Cu tends to decrease and Ge to slightly increase (as compared to the other elements) towards the back region of the absorber. This can suggest that Ge-rich phases are accumulated towards the back region, as it is proven in this system where Ge tends to naturally be present with higher concentration at the back area [164]. In such case, some secondary phases can be expected at the back and affect the device performance (mainly the J_{SC} and the FF). On the other hand, a decrease in Cu content toward the back interface may result in an increased carrier concentration through increased amount of V_{Cu} point defects, which in return may reduce the photo-carriers' mobility in that region of the film. As such, this Cu-poor region may contribute to reduced quantum efficiency in the low energy spectral range, as will be discussed below.

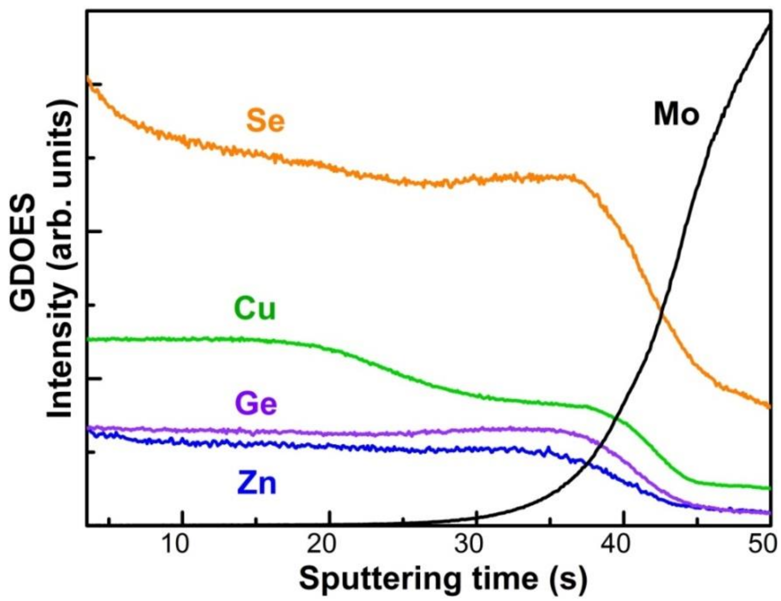

Figure 4.4: *Depth composition profiles of $Cu_2ZnGeSe_4$ absorber layer performed by a glow discharge optical emission spectrometry analysis (GDOES).*

↳ ***J-V and EQE measurements***

To further analyze the best device, the current density-voltage (J-V) characteristics and EQE measurements are performed. The performance characteristics obtained from 13 solar cells were statistically summarized and are shown as box charts in Figure A.01 (Appendix). The best device reveals a 6.5 % efficiency with a V_{OC} of 606 mV (Figure 4.4 (a)), it is very important to highlight that neither anti-reflection coating nor metallic grid are used in this work. The optoelectronic parameters of the device are summarized in Table 4.2.

J-V curves exhibit a distinct cross-over between dark and light characteristics (Figure 4.4 (a)), which is often related to the defect states at the CZGeSe/CdS interface or in the bulk of CdS layer, and leads to acceptor-like buffer traps states [153].

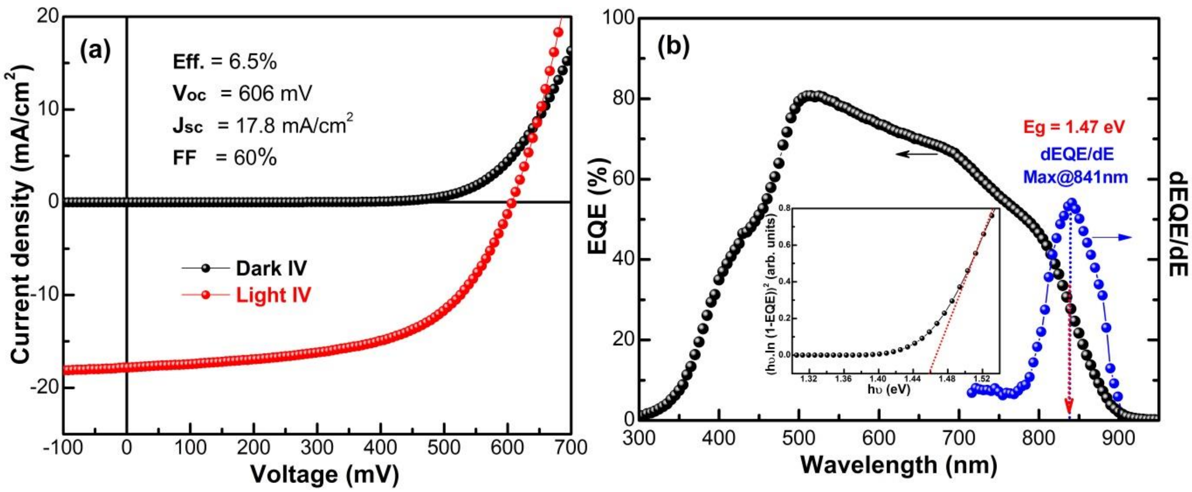

Figure 4.5: (a) J-V characteristics and (b) EQE spectrum with the inset graph shows the band gap calculation of $Cu_2ZnGeSe_4$ by plotting $(h\nu \times \ln(1-EQE))^2$ vs. energy.

<u>*C-V measurements*</u>

To further understand the main limitations in the $Cu_2ZnGeSe_4$ absorber layer, the device is characterized by C-V measurements under 5.6 KHz. The carrier concentration and the depletion region width are calculated from capacitance–voltage (C-V) profile measured at room temperature (RT) on $Cu_2ZnGeSe_4$ device. Figure 4.5 displays the charge carrier versus the distance to the front interface (N_{CV} (x)). This later is calculated from C-V measurement of the solar cell and can include contributions of superficial and deep defects. The profile demonstrated in Figure 4.5 reveals a distinct U-shape, this profile was previously attributed to presence of deep defect levels in the band gap, interface defects and/or back contact barriers effects [165]–[167]. Moreover, the lowest value of U-shape can be taken as an approximation of the charge density. The carrier concentration reflects the properties of $Cu_2ZnGeSe_4$ near depletion region is of 1.7×10^{15} cm^{-3} and a space charge region width (SCR) of 310 nm. This carrier concentration is at least one order of magnitude lower than the one reported typically in high efficiency CZTSe devices, indicating that $Cu_2ZnGeSe_4$ doping is not as easy. In fact, this lower carrier concentration can explain at least in part the reduction of the V_{OC}.

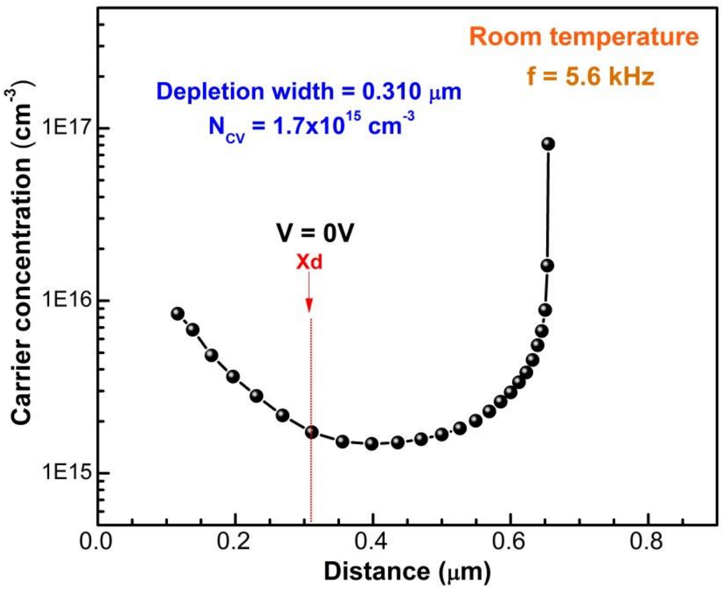

Figure 4.6: *Charge carrier density versus the distance to the junction interface extracted from Capacitance-Voltage measurements of a $Cu_2ZnGeSe_4$ device.*

Figure 4.7: *Summary of the optoelectronic parameters obtained for the best device presented in this work.*

Parameters	*Value*	*Units*
Eff.	6.5	%
V_{OC}	606	mV
J_{SC}	17.8	mA/cm^2
FF	60	%
SQ, V_{oc} deficit	0.60	V
V_{oc} deficit	0.86	V
R_S	0.14	Ω. cm^2
R_{sh}	8700	Ω. cm^2
J_0	1.6×10^{-4}	mA/cm^2
A	1.7	--
Carrier concentration	1.7×10^{15}	cm^{-3}
SCR	310	nm
E_g	1.47	eV
E_U	22	eV
Ext. V_{oc} (0 K)	0.94	eV

Table 4.2 shows a summary of the determined optoelectronic parameters from the J–V characteristics, EQE, temperature-dependent V_{OC} and C–V measurements. The following information on the figures of merit (Figures 4.4–4.7) of the fabricated solar cell could be obtained from:

Open-circuit voltage (V_{OC}): The estimated built-in potential between the CdS and the absorber is 800 mV, as shown on the simulated band diagram (Figure A. 1). The results reveal a V_{OC} of 606 mV and is very close to that of the record cell [150] (Table 4.1). The calculated V_{OC} deficit remains however high and can be considered as the main factor limiting the device efficiency. This high value might be attributed either to Fermi level pinning, and/or to intrinsic point defects. According to reference [168], the CdS and the $Cu_2ZnGeSe_4$ have no conduction band offset; while this is theoretically the most favorable case, the presence of interface defects can often lead to reduced performances a small spike-like interface as in the CIGSe/CdS is preferable. Hence, it is possible that interface defects are a limiting factor in our case, specifically through the pinning of the quasi-Fermi level reducing the cell's voltage. The effect of a Fermi level pinning at the p-n interface is illustrated in Figure A.03, with a clear decrease of the voltage above an interface defect density threshold while the current remains unaffected. The V_{OC}-deficit compared to the Schockley Queisser limit (SQ) is estimated at ~0.60 V for the CZGeSe solar cell.

Short-circuit current density (J_{SC}): the device has a J_{SC} of 17.8 mA/cm^2, which is still lower than CZTSe recorded device [103]. This lower value of J_{SC} was discussed when commenting the EQE, and is attributed to a poor collection of photo-carriers generated by low energy photons (deeper in the absorber) due to a limited carrier diffusion length or back contact recombination.

Fill factor (FF): our best device achieved a FF of 60 %, and is to our knowledge the highest value reported for this type of material (Table 4.1) [150]. This high value indicates the formation of a relatively good CdS/CZGeSe interface in terms of carrier collection, which is consistent with our conclusion from the EQE curve.

As for the other parameters extracted from the fitting of the dark J-V characteristics using a single diode model, the reverse saturation current density (J_0) can be considered more or less in the range compared to CZTSSe (7×10^{-5} mA/cm^2) [131] and higher than CIGSe (8.3×10^{-5} mA/cm^2) [169], which indicates a higher recombination rate [170]. Concerning the diode ideality factor (n), it remains below 2 (~1.7) suggesting that the device's current is limited by only one type of non-radiative recombination, which we believe takes place in the bulk as previously discussed.

To further investigate the origin of the losses in the device, reflectance measurements were calculated for the device and Internal Quantum Efficiency (IQE) was therefore performed to investigate the collection mechanisms in the device; the results are presented Figure 4.6 (a) and compared with the previously described EQE curve. As shown Figure 4.6 (a), the non-polarized EQE and IQE yield an integrated J_{SC} of 16.76 mA/cm^2 and 18.83 mA/cm^2 respectively. This integrated J_{SC} difference of 2.07 mA/cm^2 would translate to an efficiency of 6.81% if a perfect antireflective coating was used. We previously mentioned that carriers generated in the 600-950 nm spectral range are outside of the depletion width (W_d) and thus rely on diffusion for collection without the assistance of a drift electric field. It is admitted that a large W_d can facilitate the collection of minority charges carriers inside the bulk of the absorber [171]. To further enlarge the depletion width of the device, a reverse bias voltage of (-1.0V) is applied to the device during the EQE measurements. From the results presented in Figure 4.6 (a), comparing reverse bias voltage IQE measurement with the unbiased IQE, one can notice that the device shows an improvement in the photo-generated charge carrier for long wavelengths specifically (for reverse bias of -1.0V), leading to an enhancement in the IQE signal. The ratio of the -1.0 V reverse bias voltage IQE and the unbiased-IQE response (0V) reveals the influence of the SCR width on the charges collection. As presented Figure 4.6 (b), the ratio increases for longer wavelength, which confirms our hypothesis that carriers generated outside of the space charge region are not collected efficiently. It is therefore possible that the minority carrier diffusion length is insufficient in our $Cu_2ZnGeSe_4$ film, thus limiting the performance of the device. An alternative explanation relates to back contact recombination, as no specific passivation of the back interface is used in those devices. This would also align well with the hypothesized presence of secondary phases segregating at the back side of the film. In future experiments, increasing the absorber thickness will allow to discriminate between both suppositions, as back recombination would become irrelevant above a sufficient absorber thickness. Additionally, conduction band engineering strategies may allow to improve carrier collection outside of the space charge region by assisting the diffusion current with a drift component.

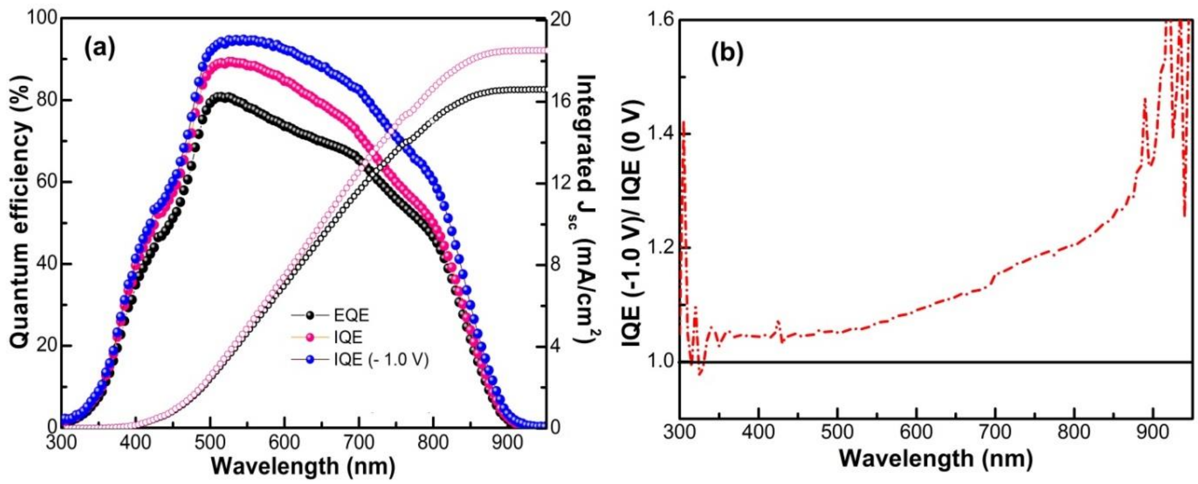

Figure 4.8: *Response of the spectral characterization of the CZGeSe device: (a) external, internal, and biased internal (reverse at -1.0 V) quantum efficiency, the integrated JSC estimated from EQE (black cycles) and IQE (pink cycles) and (b) IQE (-1.0 V)/IQE (0V).*

To further analyze the band tailing of the device, the Urbach energy (E_U) is estimated from the IQE as presented in equations (4.1):

$$\alpha(h\nu) = \begin{cases} A_0\sqrt{\frac{E_U}{2\exp(1)}}\exp\left(\frac{h\nu - E_G}{E_U}\right) \text{ for } h\nu < E_G + \frac{E_U}{2} \\ A_0\sqrt{h\nu - E_G} \quad \text{for } h\nu \geq E_G + \frac{E_U}{2} \end{cases} \tag{4.1}$$

According to equation (4.1), an inverse slope between ln (1-IQE) in the long wavelength edge and hυ gives the E_U. From the linearization of equation (4.1), equivalent to the Y-axis on Figure 4.7, the E_U value extracted as the inverse of the slope of the linear fit on the region E-Eg < 0; Urbach energy (E_U) in semiconductors is defined as the width of the Urbach tail. Urbach tail model and IQE fitting give band tailing Urbach energy parameter E_U of ~22 meV. According to reference [172], an Urbach energy above 20 meV is the threshold for a high voltage deficit while it does not have a direct relation to the current. This observation is consistent with the previously developed hypothesis that interface defects, in our case, are primarily a detriment to the voltage rather than the current, which also aligns well with the model's result shown in the Figure A. 03 of appendix. It is important to highlight that the estimated E_U value in this work is smaller compared with the previously reported one for a similar absorber CZGeSe with a value of ~28 meV [119]. An E_U of about 33 meV is moreover reported for the record CZTGSe device [149]. However, the E_U value for Sn-kesterite is estimated to be ~60 meV for CZTSSe [173], and 70 meV for CZTS [174]. Values in the range of 30 meV are reported for the best CZTSe devices [175]. Hence, this comparison tends to indicate that the substitution of Sn by Ge in kesterite solar cells can possibly benefit in reducing the crystalline disorder resulting in an Urbach tails drop, which is consistent with the previously discussed high crystalline quality.

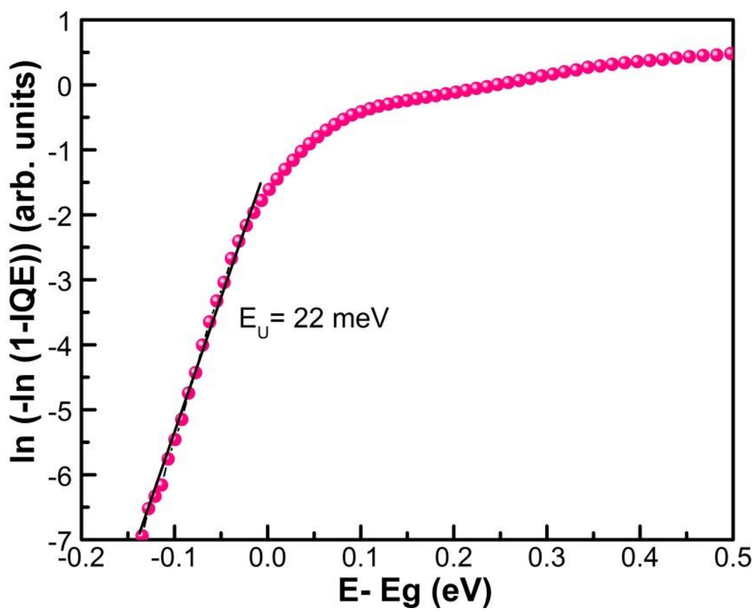

Figure 4.9: *Urbach energy extracted from IQE of the $Cu_2ZnGeSe_4$ device.*

The V_{OC} deficit issues could thus be attributed to a combination of bulk Ge-related defects [176] and Fermi level pinning at the p-n interface at room temperature. Discriminating between both hypotheses would require a more advanced electrical characterization, and specifically a temperature dependent admittance spectroscopy analysis [177]. While of major interest, such study is beyond the current scope of this work and may be tackled in future investigations. A basic numerical modeling of an equivalent solar cell structure (showed Figure A. 03) reveals that above a certain defect density threshold, interface defects will indeed pin the Fermi level and severely hamper the voltage of the solar cell.

To gain additional insights on this limitation, temperature dependent J−V is carried out for the CZGeSe device (Figure 4.8). The V_{OC} is associated to the temperature T as follows [178]:

$$V_{OC} = \frac{E_A}{q} - \frac{AkT}{q} \ln\left(\frac{J_{00}}{J_{SC}}\right) \qquad (4.2)$$

Where E_A is the activation energy of the dominant defect, A is the diode ideality factor, k is the Boltzmann constant, J_{00} is the reverse saturation current pre-factor and J_{SC} is the short circuit current density. Following relation (4.2), the V_{OC} is linearly related to the temperature, and the V_{OC} extrapolation at 0 K gives the E_A. An activation energy of 940 mV is calculated, significantly lower than the band-gap value of the film. Following an interpretation similar to reference [179], such value can be ascribed to a voltage limitation at the buffer/absorber interface; as we previously established that no significant conduction band offset exists in our devices, this limitation is thus consistent with a defect-related pinning of the Fermi level at the p-n interface. A more detailed admittance spectroscopy analysis would be needed for unequivocally conclude on that matter.

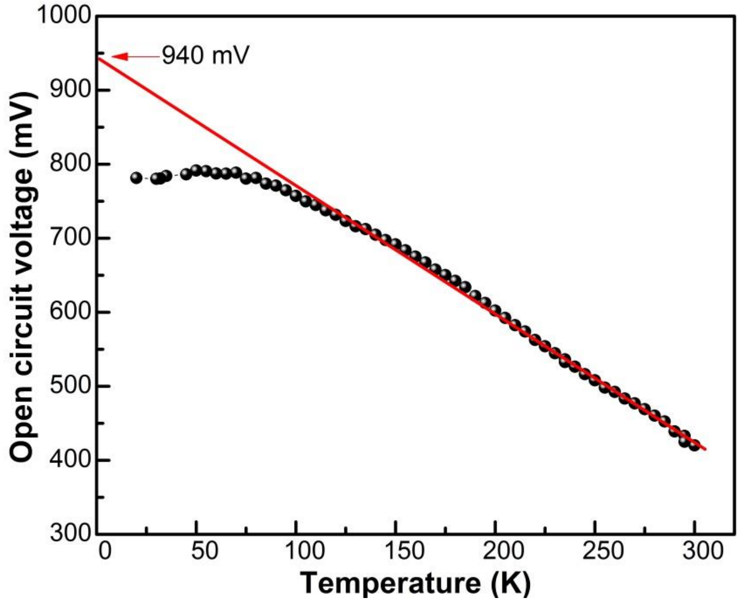

Figure 4.10: *Temperature dependence of V_{OC} of the device with data extrapolated to 0 K to extract the activation energy (E_a) of the recombination mechanism.*

4.4. Conclusions

The present work demonstrates the feasibility of synthesizing PV-quality $Cu_2ZnGeSe_4$ absorbers using a deposition of Cu/Zn/Ge metallic stack precursors by DC-magnetron sputtering technique, and then selenized through a reactive annealing. The champion solar cell device presented in this work shows a PCE of 6.5%, FF of 60 %, V_{OC} of 606 mV, and J_{sc} of 17.8 mA/cm^2.

This work paves the way towards a better identification and understanding of the factors limiting $Cu_2ZnGeSe_4$ solar cells performance.

The following conclusions are drawn from our study:

- The large V_{OC} deficit can likely be ascribed to a Fermi level pinning at the interface, though the influence of bulk defects shouldn't be yet discarded. A spike-like absorber/buffer junction could alleviate this issue.
- The EQE analysis and the ratio between IQE (0V) and IQE (-1V) demonstrate that carriers generated outside of the depletion region are not efficiently collected, which we believe is related to a limited minority carrier diffusion length in the

CZGeSe film or back contact recombination. While we believe that a defect state is pinning the Fermi level at the p-n interface, it is unlikely that this defect participates to the current limitation as the EQE exceeds 80% in the low wavelength / high-energy range.

- A high crystalline quality is obtained, confirmed by SEM observation, Raman analysis, and the comparatively low Urbach energy (E_U = 22 meV).

To further improve the devices presented in this work, several strategies could be followed. The Cu content of the films presented in this study is comparatively low in regard to the literature of the field. While this value yielded the highest performance in our process, it is likely that optimizing absorbers with higher Cu content may be a pathway for the efficiency increases. The use of alkali post-deposition treatments has demonstrated a spectacular improvement in the carrier lifetime in CIGSe solar cells, especially when using heavier elements such as Rb or Cs. A similar approach could be followed in $Cu_2ZnGeSe_4$ solar cells with a higher Cu content. Additionally, the buffer layer composition may also be positively altered by substituting a limited amount of Cd by Zn and obtain a spike-like p-n interface, which could help alleviating the interface voltage limitation.

5

Combinatorial and machine learning approaches for the analysis of $Cu_2ZnGeSe_4$: influence of the off-stoichiometry on defect formation and solar cell performance

5.1. Introduction

$Cu_2ZnSn(S,Se)_4$ (CZTSSe) based compounds, more widely known as kesterites, are considered as the natural earth-abundant and low toxicity successors of the more mature inorganic thin film photovoltaic (PV) technologies $Cu(In,Ga)Se_2$ (CIGS) and CdTe which are based on scarce and/or toxic materials [98]. Although a considerable amount of progress in the technological development and fundamental understanding of kesterites has been achieved in the last years, the record power conversion efficiency at laboratory scale has barely evolved since 2014 and is stagnated at around 13% [38].

Sn is often regarded as the main culprit of this stagnation due, mainly, to the volatility of $Sn(S,Se)_x$ species [56] that leads to morphological and compositional problems [181], and the instability of the Sn oxidation state that may lead to the formation of deep defects [102], [110] ultimately causing kesterite PV devices to exhibit a high Voc deficit. In this regard, the substitution of Sn by Ge is currently regarded as a promising strategy to improve the kesterite technology. Ge doping (CZTSSe:Ge) and alloying (CZTGSSe) has been demonstrated to enhance the performance of kesterite devices significantly by improving the Voc of the devices which is commonly attributed to the formation of liquid phases and better intermixing during high temperature synthesis, to improvements in carrier lifetime and to a reduction of band tailing [107], [111], [182]. In addition, the partial substitution of Sn by Ge increases the bandgap of the kesterite semiconductor material enabling the creation of a graded bandgap through the development of in-depth compositional engineering strategies[164], [183]. On the other hand, the total substitution of Sn by Ge (CZGSSe) appears as an even more promising approach since, in addition to completely avoiding Sn-related issues, the wider bandgap of the material (~1.5 eV for CZGSe and ~2.2 eV for CZGS)[184], [185] opens the door to semi-transparent, tandem and photocatalytic water splitting applications. Significant advances have been made in the last years in pure Ge kesterite solar cells leading to CZGSe devices with efficiencies of up to 8.5% [150]. Although promising, this value is very far from those of the best CZTSe devices. The highest efficiency levels reported for CZGSe are commonly achieved imitating the standard CZTSe and employing off-stoichiometry Cu-poor Zn-rich absorber compositions[112], [121], [150]. However, this compositional ratio might not be the optimal one for CZGSe and might be one of the reasons holding back the development of this technology towards higher efficiencies as compared with the standard CZTSe. As such, fundamental studies that investigate the formation of CZGSe, secondary phases and point defects off-stoichiometry represent a very valuable asset for understanding this material and for paving the way to the development of strategies that may lead to a further development of the technology. In this context, Gunder et al. carried out a detailed investigation of defect formation in off-stoichiometric CZGSe powder [118]. However, mainly Zn-rich and Cu-rich powder samples were synthesized, with few Cu-poor samples.

Finally, solar cells based on quaternary kesterite compounds and multilayer stacks like CZGSe are complex systems where the variation of one parameter can result in changes in the whole system, and, as consequence, in the global performance of the devices. In this way, analyses that take into account this complexity are necessary in order to overcome the existing limitations of this promising Earth-abundant photovoltaic technology.

In chapter, we present a systematic study of a combinatorial CZGSe sample comprised by almost 200 individual solar cells with different [Zn]/[Ge] compositions in the Cu-poor regime. Structural, compositional and optoelectronic characterization are applied in a combinatorial way. Firstly, a complex analytical approach allows defining the off-stoichiometric limits of formation of the CZGSe kesterite phase and the optimum compositional range to obtain the highest efficiencies (up to 6.3%) in terms of the [Zn]/[Ge] ratio. This includes the study of solar cell performance dependence on the concentration of point defects. Secondly, we demonstrate the potential of applying machine learning (ML) for the analysis of the combinatorial sample. The ML methodology proves to enable effective prediction of cell efficiency based only on Raman spectra and compositional data, while the resulting discriminants show a linear correlation with point defect concentration and device efficiency pointing at a strong fundamental interconnection between point defects, Raman spectra, composition and cell performance. This works serves both as a fundamental study that provides valuable results for the development of the CZGSe technology and as a powerful example of how combinatorial analysis and machine learning can be used to unravel the critical parameters that govern the performance of complex optoelectronic devices.

5.2. Experimental detail

5.2.1. Metallic stack deposition

A CZGSe combinatorial sample was prepared through the selenization of a compositionally graded Cu/Zn/Ge metallic stack precursor deposited by DC magnetron sputtering (Alliance AC450) on a 5 × 5 cm^2 soda-lime glass/Mo substrate. In order to generate a compositional gradient, the Cu and Zn precursor layers were homogeneously deposited over the substrate while the Ge layer was deposited without substrate rotation generating a thickness gradient and, in turn, a [Zn]/[Ge] compositional gradient.

5.2.2. Reactive annealing

A 3-zone tubular furnace (Hobersal) was employed to synthesize the CZGSe absorber. The 3 zones were kept at the same temperature during the whole process to ensure spatial homogeneity throughout the entire length of the furnace. Samples were placed inside a graphite box (69 cm^3) together with crucibles containing 100 mg of Se (Alfa-Aesar powder, 200 mesh, 99.999%) and 5 mg of $GeSe_2$ (American Elements, power, 99.999%) to perform a 2-step reactive thermal annealing in a Se + Ge atmosphere. It consisted in a first stage in which the furnace was kept at 330 °C and 1.5 mbar Ar pressure for 30 minutes and a second step at 480 °C and 1 bar Ar pressure for 15 minutes. The heating rate was set to 20 °C min^{-1} in both steps. The samples were let to cool down naturally.

5.2.3. Etching treatments

The as-synthesized absorber was submitted to a chemical etching in diluted KCN (2% w/v, room temperature, 2 min).

5.2.4. Device fabrication

Immediately after, a CdS layer was deposited by chemical bath deposition (the process is detailed in ref. [186]). The solar cell structure was then completed with i-ZnO (50 nm) and ITO (200 nm, 60 Ω sq^{-1} sheet resistance) layers deposited by DC-magnetron sputtering (Alliance Concept CT100). The sample was then scribed into 196 individual 3 × 3 mm^2 solar cells (see Figure B. 1) using a manual microdiamond scriber (MR200 OEG). Neither anti-reflective coating nor metallic grids were used in the devices presented in this work.

5.2.5. Characterization

The elemental composition of the different cells of the combinatorial sample was determined by X-ray fluorescence (XRF) using a Fischerscope XDV system with a 1 mm spot diameter, a 50 kV acceleration voltage, a Ni10 filter and a 45 s acquisition time. Raman analysis with blue (442 nm) and green (532 nm) excitation wavelengths were performed on the bare absorber, while measurements with NIR (785 nm) were performed in complete devices using Horiba Jobin Yvon FHR640 and iHR320 monochromators coupled with CCD detectors. The first monochromator is optimized for the UV and visible spectral ranges and was used with 442 nm (He–Cd gas laser) and 532 nm (solid state laser) excitation wavelengths. The second monochromator is optimized for the NIR range and was used with a 785 nm (solid state laser) excitation wavelength. The power density of the lasers was kept below 150 W cm^{-2} and the spot size was ~70 μm. The measurements were performed in a backscattering configuration through a specific probe designed at IREC.

The J–V characteristics of the devices were obtained under simulated AM1.5 illumination (1000 W/m^2 intensity at room temperature) using a pre-calibrated Class AAA solar simulator (Abet Technologies Sun 3000).

5.2.5.1.Machine learning methodology

A machine learning (ML) driven methodology based on a linear discriminant analysis (LDA) algorithm was employed to deepen into the complex dependence of solar cell optoelectronic parameters and composition on the different parameters found in the analysis of the Raman spectra. LDA is a dimension-reduction algorithm, capable of reducing high-dimensionality problems into a bi-dimensional one, discerning and employing the most relevant dimensions of the dataset. In order to test and implement the machine learning based LDA algorithm, the Python programing environment with the Scikit-Learn library [187] was used. All the Raman spectra measured under different excitation conditions for each cell were used as input features (588 spectra, in total), and the data were randomly divided in 70% for training and 30% for testing. The algorithm was trained for 3 different classification targets, namely [Zn]/[Ge] ratio, Voc and efficiency. For each trained algorithm, the data was divided in 4 classification groups of approximately an equal amount of data. The amount of experimental data employed for the analysis (196 cells) is far from being considered "big data" and the results presented below are susceptible to further improvement for a more precise classification through the use of a higher number of training inputs. Nevertheless, this approach illustrates the applicability and potential of this methodology for material analysis by spectroscopic techniques.

5.3. Results and discussions

5.3.1. Off-stoichiometry limits and secondary phases

The chemical composition of every individual solar cell of the combinatorial samples was obtained by XRF. The mappings of the cationic ratios are presented in the Figure B. 01 (Appendix) and, in Figure 5.1, the obtained values are combined with the different off-stoichiometry kesterite types (see ref. [71] and [108] for more details about the off-stoichiometry lines of kesterite type compounds). It can be observed that the compositions of the different cells of the combinatorial samples cross the A- (almost perpendicularly), J- and L-type lines. On the one hand, the [Zn]/[Ge] ratio covers a wide range from almost 0.7 to 1.4, allowing to explore not only the typical Zn-rich compositions commonly used for kesterite type compounds, but also the Zn-poor region. This allows investigating the origin of the positive effect of Zn-rich compositions in kesterite PV devices. On the other hand, the [Cu]/([Zn]+[Ge]) ratio was maintained well below 1, ensuring the Cu-poor condition for all cells. It is worth mentioning that the non-stoichiometric compositions were quite different from previous studies of the same compound [151], where mainly Zn-rich and Cu-rich powder samples were synthesized and the few Cu-poor samples contained secondary phases.

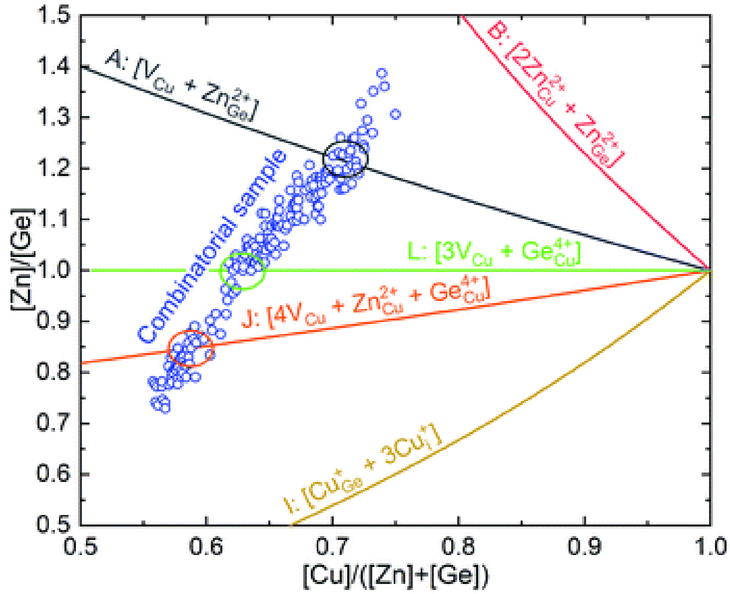

Figure 5.1: *Cationic ratios of the CZGSe combinatorial sample (blue open circles) represented together with off-stoichiometric types of kesterite compounds (solid lines)[155].*

Raman spectroscopy was used as the main tool to analyze phase formation in the CZGSe absorber layer with varying [Zn]/[Ge] ratio. A multi-wavelength analysis allowed to detect possible secondary phases and variations in the main kesterite phase (see Figure 5.2). The blue excitation wavelength is well-known to be highly sensitive for detecting the ZnSe secondary phase [155], [189]. As shown in the figure, this secondary phase was found in cells with Zn-rich composition (see the spectrum of the [Zn]/[Ge] = 1.25 cell in Figure 5.2, left). What is more, the cells on which a strong ZnSe peak was detected, also presented a shift to lower wavenumbers and an increase of the full width at half maximum (FWHM) of the main and the second most intense peaks of the kesterite phase under different excitation wavelengths not sensitive to ZnSe (see the spectrum of a cell with [Zn]/[Ge] = 1.25 under green excitation wavelength in Figure 5.2, middle). This, according to the previous interpretations of the kesterite type compounds, can be related with an increased Cu/Zn disorder [190] or with a phonon confinement effect due to a low grain size in the absorber [191]. Since all the cells of the combinatorial sample were processed at the exact same temperature, the appearance of strong variations in the Cu/Zn disordering is unlikely (e.g. see ref. [192] and [193]). In addition, it is hard to envision how the formation of the ZnSe phase could influence Cu/Zn disordering in the CZGSe compound. On the other hand, even taking into account the optimal temperature treatment for the formation of good crystalline quality CZGSe phase [65],[114], the presence of ZnSe grains can greatly influence the formation and size of the kesterite grains [195], leading to a worsening of its crystalline quality and grain size, and causing the appearance of phonon confinement in agreement to the observed red shift and broadening of the kesterite Raman peaks.

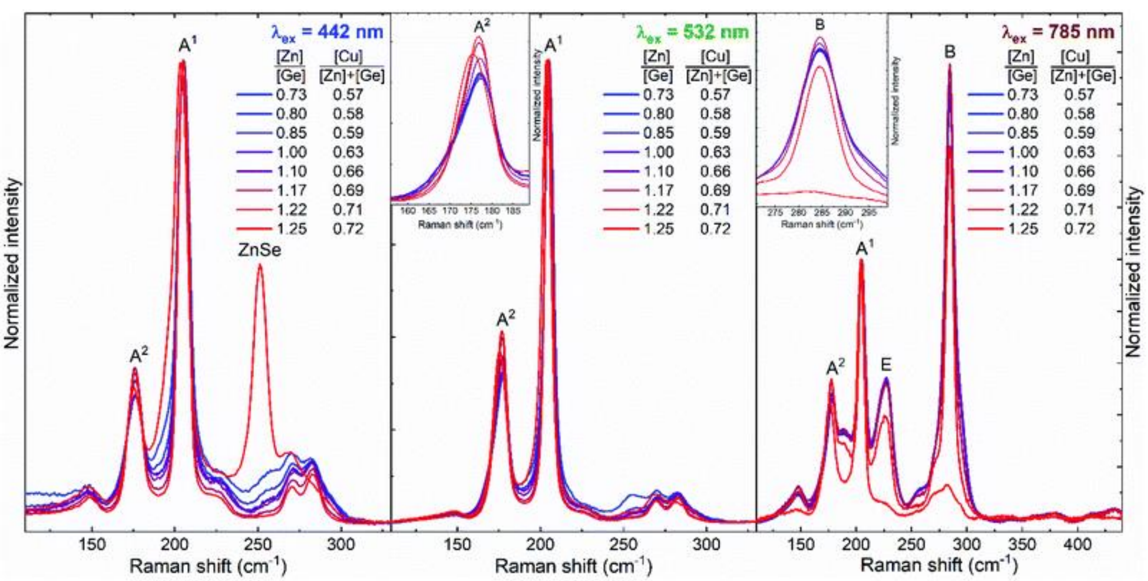

Figure 5.2: Examples of Raman scattering spectra measured in cells with different compositions under different excitation wavelength.

In addition to the ZnSe phase, the blue excitation wavelength is also sensitive to the $GeSe_2$ phase. This is a 2D compound that has a direct band gap of ~2.7 eV (close to the energy of the blue laser line −2.8 eV) and has its main Raman peak at around 210 cm^{-1}. The latter is strongly overlapped with the main peak of CZGSe (A1 symmetry peak at 205 cm^{-1}), which compromises the detection of this secondary phase. However, a strong resonance with the blue excitation wavelength should result in the appearance of, at least, a shoulder at the high wavenumber side of the main kesterite peak. However, the spectra in Figure 5.2 (left) show no evidence of the presence of $GeSe_2$, even for the lowest [Zn]/[Ge] ratios (highest Ge-content). Another Ge-based binary compound is GeSe. The orthorhombic crystalline polymorph of this binary compound has a direct band gap of about 1.53 eV and an intense A_1 symmetry mode at 188 cm^{-1} [157]. This band gap value is very close to the resonant condition of this secondary phase under a 785 nm excitation wavelength. Nevertheless, no clear Raman peak of GeSe phase can be observed in the spectra acquired (Figure 5.2, right). On the other hand, although the properties of the amorphous $GexSe_{1-x}$ phase strongly depend on the x value, an intense Raman band close to 200 cm^{-1} and assigned to the stretching mode of the $GeSe_{4/2}$ corner-sharing tetrahedra can be defined as representative for most of the compositional polymorphs of these amorphous phases [196]. Moreover, a GeSe [113] liquid phase, recently found as one of the intermediate phases during the formation of CZGSe [112], might remain at the surface of the absorber layer. In the spectra measured under the green excitation wavelength, a slight broadening of the main peak of CZGSe with the decreasing [Zn]/[Ge] ratio can be observed. However, it cannot be unequivocally ascribed to the presence of amorphous Ge_xSe_{1-x} or liquid GeSe [113] secondary phases since it could also be explained by intrinsic changes in the kesterite phase, that will be further discussed. Finally, elemental Ge and Ge-containing ternary phases (like Cu_2GeSe_3 or Cu_2GeSe_4) can be formed in very Zn-poor conditions. Although a good sensitivity of Raman spectroscopy to these phases is expected, their narrow band gap (below 1 eV, see ref. [158], [159], [197] for band gap and fingerprint Raman spectra) does not allow working in resonant conditions making the detection of small amounts of elemental Ge and Ge-containing ternary phases very challenging. In this way, it can be concluded that no Ge-related secondary phases are forming even for very Zn-poor compositions, or that the amount of these secondary phases is negligibly small, as no strong/sharp changes of the spectra of the cells of the CZGSe combinatorial sample with different compositions can be observed (in the [Zn]/[Ge] = 0.7–1.2 range). This differentiates the pure Ge-based from the pure Sn-based kesterites, where the formation of Sn-containing secondary phases has been observed even at Zn-rich compositions

[198], [199]. Finally, it should be noted that no Cu-containing binary secondary phases are expected due to Cu-poor composition of all the cells of the combinatorial sample (see Figure 5.1).

According to the phase formation analysis performed by means of Raman spectroscopy presented above, only a ZnSe secondary phase was clearly detected in the combinatorial sample under Zn-rich compositions. ZnSe becomes the dominant phase for [Zn]/[Ge] > 1.2 in some of the cells. This squeezes the upper limit in which the pure CZGSe kesterite phase can be formed to [Zn]/[Ge] ratios close to 1.2. On the contrary, the lower limit for the formation of the pure CZGSe kesterite phase can be considered close to 0.7, comparable with CZTSSe compounds [198]. However, the presence of small amount of Ge-based secondary phases is hard to exclude from the data presented. Nevertheless, taking into account previous studies [155] and the results presented here, it can be concluded that replacing of Sn with Ge does not lead to a significant shortening of the off-stoichiometry range for the formation of the CZGSe kesterite type structure. Likewise, the stoichiometry flexibility of CZGSe compounds might be one of the culprits for the existing limitations of the PV devices in the same way as for other kesterite-based compounds [181].

5.3.2. *Point defect formation*

As mentioned above (see Figure 5.1), the chemical composition of most of the cells is in the range from J-to A-type kesterite off-stoichiometric lines. According to this, the main point defect expected in the combinatorial sample are copper vacancies (V_{Cu}) and zinc or germanium in copper position (Zn_{Cu} and Ge_{Cu})[71], [118],[120]. In order to define the influence of these point defects on the Raman spectra, specific cells with chemical compositions close to the three off-stoichiometric lines crossed by the combinatorial sample (A-, J- and L-type lines) were analyzed. Measurements under different excitation wavelengths resulted in the detection of the characteristic features that differentiate the Raman spectra of the different off-stoichiometry types of the CZGSe kesterite compound (see Figure 5.3). Here, the spectra of the cells around the J- and L-type lines present a great similarity with just very subtle changes in the intensity of the band at 176 cm^{-1} and E/B symmetry peaks in the high wavenumber range (220–300 cm^{-1}), which are mainly observed under 785 nm excitation (Figure 5.3, right). In contrast, strong differences are observed for the spectra of the cells close to the A-type line with a decrease of the relative intensity and width of the peaks, except for the band at 176 cm^{-1}. In previous works, the change in the intensity of the second most intense Raman band in the CZTSe compound was correlated, mainly, with a change of the concentration of V_{Cu} point defects, and was shown to have a crucial impact on the properties of the CZTSe absorber and on device performance [115], [121],[122]. Taking this into account, it can be inferred that in the combinatorial sample analyzed in this work, there is a higher concentration of V_{Cu} for the cells close to the J- and L-type lines, and it is reduced for the cells around the A-type line. This is in line with the observations made above, where an increase of the intensity of the Raman band at 176 cm^{-1} is observed with the increasing [Zn]/[Ge] ratio (see Figure 5.2). However, the concomitant increase of the [Cu]/([Zn] + [Ge]) ratio (see Figure 5.1), even if much smaller than the increase of the [Zn]/[Ge] ratio, is also expected to have a critical influence on the concentration of V_{Cu}.

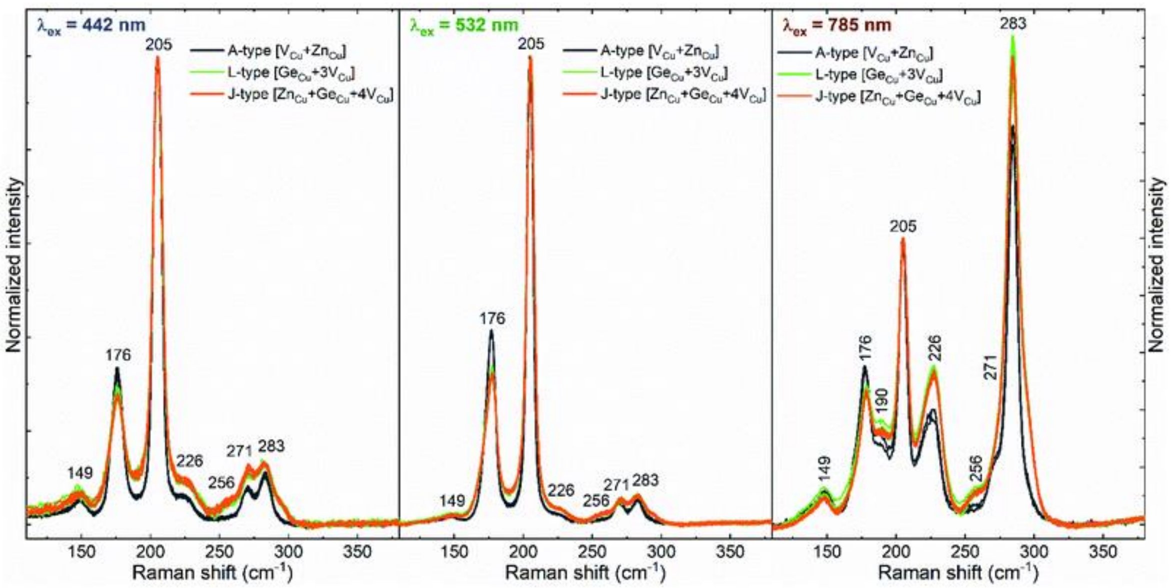

Figure 5.3: *Examples of Raman spectra in the vicinity of different off-stoichiometric type lines measured under different excitation wavelength.*

Taking a look at Figure 5.3, a great similarity between the spectra corresponding to cells around the J- and L-type lines can be seen regardless the presence of the Zn_{Cu} point defect in some cells and its absence in others. This allows concluding that the Zn_{Cu} defect has a low influence on the Raman scattering spectra of the CZGSe compound. On the other hand, the Ge_{Cu} substitutional defect presents a more significant influence on the Raman spectra, but mainly in the high wavenumber range (220–300 cm^{-1}), where the relative intensity of the peaks increases with the higher Ge content (or lower [Zn]/[Ge] ratio). Nevertheless, it is hard to strictly distinguish the influence of the two substitutional point defects on the intensity of the peaks at the high frequency range and both of them will be considered in the analysis of the influence of the point defects on device performance presented in the next section.

Finally, it should be borne in mind that, for the analysis carried out above, only cells without ZnSe were used since the presence of this phase results in significant changes in the spectra measured under any excitation condition (e.g. see Figure B.02 where spectra of the cells with similar compositions close to A-type off-stoichiometric line, but with and without ZnSe phase are presented). This indicates that Raman spectroscopy is a critical investigation tool to control the quality and phase purity of the kesterite type compounds [155].

5.3.3. *Influence of point defects on device performance*

This section studies the influence of the point defects detected by Raman spectroscopy on solar cell performance. First, the analysis is focused on the dependence of the optoelectronic properties of the devices on the relative integrated intensity of the band at 176 cm^{-1} (calculated as $A_{176}/(A_{176} + A_{205})$ with A_{176} calculated in the 168–183 cm^{-1} range and A_{205} calculated in the 198–211 cm^{-1} range from the spectra measured under 532 nm excitation wavelength), which is inversely related to V_{Cu} concentration as previously reported [40], [195], [201]. Figure 5.4 (a), shows a clear dependence of the efficiency of the solar cells with the concentration of V_{Cu}, with the highest efficiency achieved for a certain optimum concentration range of this defect, which corresponds to a relative integrated intensity of the Raman band at 176 cm^{-1} lying in the 0.325–0.350 range. Outside this optimum range, a deficit (higher band intensity) or excess (lower band intensity) of V_{Cu} defect concentration is expected, both having a negative influence on device performance. As such, three different regions (deficit, excess and optimum V_{Cu}) can be distinguished. A more detailed analysis of the evolution of the optoelectronic properties with defect concentration (Figure 5.4 b–d) reveals that the main driving force behind the evolution of solar cell efficiency are the changes in the fill factor (FF) and short circuit current density (J_{sc}). Both parameters exhibit a similar tendency with defect concentration. Copper vacancies are a well-known beneficial point defect in kesterite and chalcopyrite based solar cells, which leads to the formation of a shallow acceptor level and has a strong influence on the electrical conductivity of the absorber layer [33], [123]. In this way, a deficit of this beneficial defect leads to a decrease of the charge carrier concentration. However, an excess results in the formation of a high amount of scattering centres which significantly decreases the mobility of the charge carriers. Both effects have a direct influence on the electrical conductivity of the absorber layer and, in turn, on the FF and J_{sc} of the final devices as observed in Figure 5.4.

On the other hand, the open circuit voltage (V_{OC}) shows only a slight dependence on V_{Cu} concentration, with only a sharp increase in the optimum defect range. These results differ from a previously published analysis of CZTSe samples, where the V_{oc} was found to depend on the change of the relative intensity of the second most intense kesterite band (I_2 around 170 cm^{-1})[201]. However, it should be noted that only cells around the A-type off-stoichiometric line were selected in the mentioned reference, which strongly reduces the number of possible parameters that can influence solar cell performance, at least from the point of view of point defects.

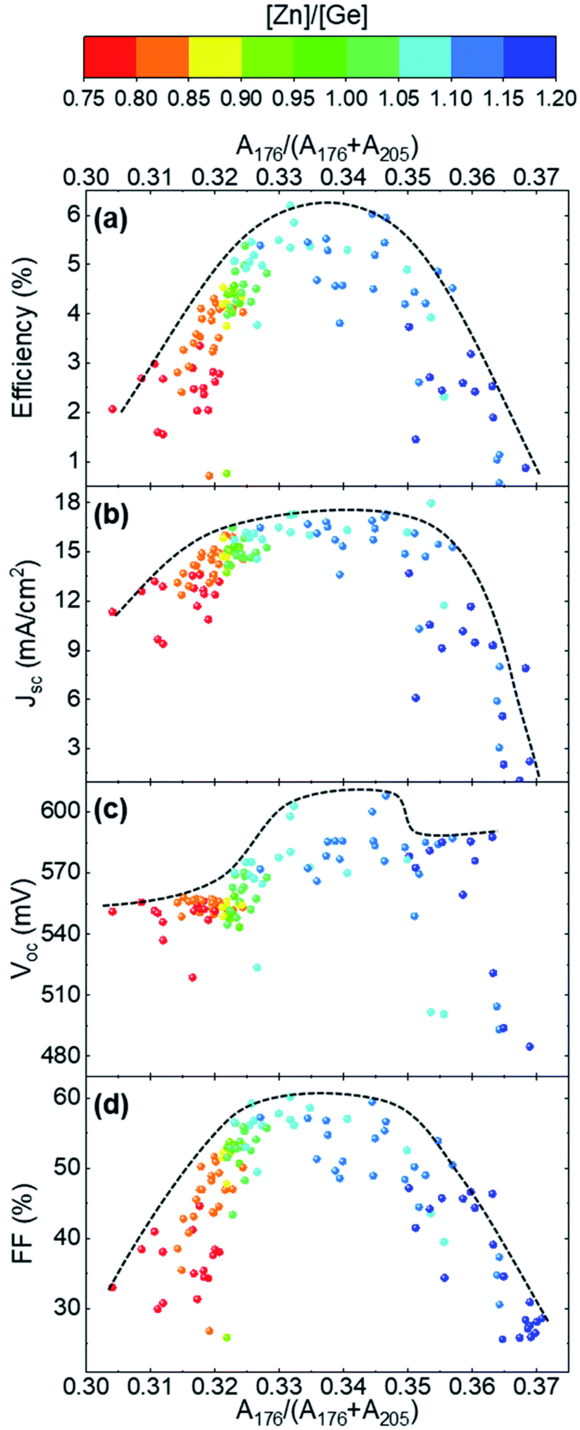

Figure 5.4: *Dependence of optoelectronic properties (efficiency (a), short circuit current (b), open circuit voltage (c), fill factor (d)) of the cells from the relative integrated intensity of the Raman band at 176 cm^{-1}. The color scale corresponds to the [Zn]/[Ge] ratio.*

Then, on a second stage, the influence of Zn_{Cu} and Ge_{Cu} substitutional point defects on the optoelectronic properties of the devices was analyzed. According to previous results, an increase of the relative intensity of the peaks in the high wavenumber range correlates with a higher concentration of substitutional defects[115],[121]. Figure 5.5 (a) shows a parabolic dependence of solar cell efficiency with the variation of the relative integrated intensity of the Raman peaks in the range 235–300 cm^{-1}. As in the case of V_{Cu} (see Figure 5.4 (a)), this shape is mainly governed by the changes in FF and J_{sc} (Figure B.03) although in a less pronounced manner. This can be related to a slightly lower influence of the substitutional defects on these optoelectronic parameters. On the other hand, the analysis of the dependence of the Voc on the relative integrated intensity of the peaks in the 235–300 cm^{-1} range (Figure 5.5 (b)) shows a clearer influence of the substitutional defects on this parameter. Similarly to the analysis above, three regions can be distinguished: (1) low amount of defects ($A235–300 < 0.190$); (2) optimum amount of defects ($0.190 < A235\text{-}300 < 0.215$); (3) high amount of defect ($A235\text{-}300 > 0.215$). A relatively constant Voc value can be observed in region 1, followed by a sharp decrease in the second one, and a gentle decrease in region 3. Taking into account the [Zn]/[Ge] ratio, it can be seen that region 3 corresponds to Zn-poor conditions, for which Ge_{Cu} substitutional defects are expected to prevail over the Zn_{Cu} defects. The former defect can form a deep donor defect (based on first principle calculations of the familiar Sn-containing kesterite compounds [49]) that increases the amount of non-radiative recombination, which finally decreases the V_{OC} [203], [204].

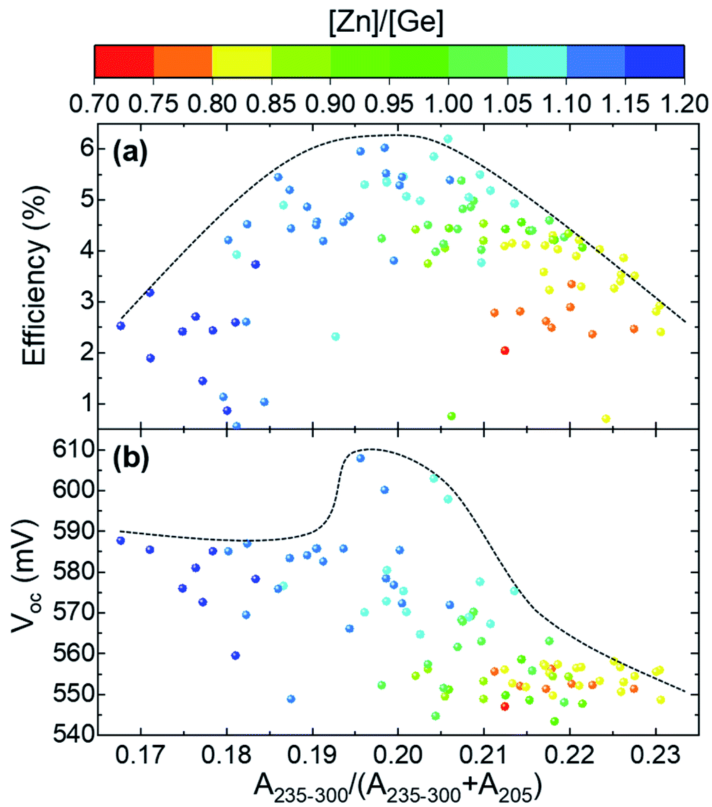

Figure 5.5: *Dependence of (a) efficiency and (b) open circuit voltage of the cells on the relative integrated intensity of the Raman peaks in the range 235–300 cm^{-1}. The color scale corresponds to the [Zn]/[Ge] ratio.*

A further analysis of the Raman spectra measured under different excitation wavelengths allows to establish additional failure mechanisms that lead to the decrease of the performance of the solar cells outside the optimum compositional range. A deep analysis of the spectra measured under blue and NIR excitations reveals that the lower efficiency in these ranges can be explained by two factors: the appearance of the ZnSe secondary phase and the change of the band gap of the absorber. The former effect can be seen in Figure 5.6 (a) where the relative intensity of the ZnSe peak is presented. The figure shows a clear decrease of solar cell performance with the increasing content of the ZnSe phase, proving the strong detrimental effect of this secondary phase. On the other hand, the band gap of CZGSe (around 1.5 eV) exhibits a resonant behavior under NIR excitation conditions that leads to an increase of the intensity of the LO components of the E and B symmetry modes in kesterite type compounds [163], [205]. In the present study, this is observed by a strong enhancement of B symmetry peak at 283 cm^{-1} (see Figure 5.2 and 5.3). However, the latter is not similar in all the cells, with some of them showing a rather low intensity of this peak (Figure 5.6 (b)). This can be related to the distancing of the CZGSe band gap from the excitation laser line. Previously, several works mentioned the effect of defects in the cations sublattice on the band gap of kesterite materials, but mainly the disorder of the Cu/Zn cations was discussed [41],[127],[128], while changes in the concentration of point defects was just briefly tackled [207], [208]. As mentioned above, in the combinatorial sample analyzed in this work, it is not expected to have a significant difference in Cu/Zn disorder, while a clear change in the concentration of V_{Cu}, Zn_{Cu} and Ge_{Cu} is observed. This implies that the concentration of point defects can lead to significant enough changes in the band gap of the CZGSe material that result in the observed decrease of the resonant effect in the Raman spectra.

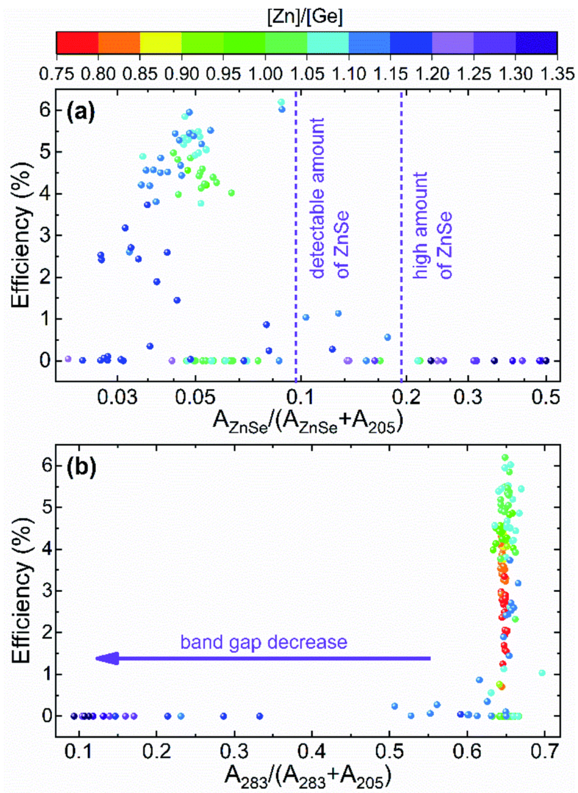

Figure 5.6: Dependence of solar cell efficiency with (a) relative integrated intensity of the ZnSe peak (spectra measured under 442 nm excitation), (b) relative integrated intensity of the peak at 283 cm^{-1} (spectra measured under 785 nm excitation).

The color scale corresponds to the relative integrated intensity of the band at 176 cm^{-1} calculated from the spectra measured under 532 nm excitation.

Finally, the complex analysis presented above reveals that the optimum compositional cationic range that allows achieving high efficiency devices is [Zn]/[Ge] = 1.05–1.15. This is in agreement with previously published values for high efficiency solar cells based on CZGSe [63],[65],[114]. Furthermore, the efficiency of the devices seems to be less dependent on the [Cu]/([Zn]+[Sn]) ratio, as long as the Cu-poor condition is respected (e.g. similar efficiencies were obtained for [Cu]/([Zn]+[Sn]) = 0.67 in ref. [112] and 0.78 in ref. [118]). Deviations from this optimum cationic ratio range towards stoichiometric and Zn-poor compositions result in an increase of the amount of both V_{Cu} and substitutional defects. This can be assumed to be the reason for the slight increase of the FWHM of the Raman peaks in the spectra measured in the cells with [Zn]/[Ge] ≤ 1.0, as discussed above (see Figure 5.2). On the contrary, an increase of the Zn concentration in the system with [Zn]/[Ge] > 1.15, results in the decrease of both V_{Cu} and substitutional defects, in bandgap narrowing, and in an increase of the probability of the detrimental ZnSe secondary phase being formed. Note that the ZnSe phase was found to form also in cells within the optimum cationic range strongly influencing device performance and, as such, the formation of this phase should be controlled during the production process.

5.3.4. Machine learning approach for device performance analysis

The results presented in the previous section clearly indicate that there is a complex dependence between solar cell performance and the different parameters obtained from Raman spectroscopy, such as V_{Cu}/Zn_{Cu}/Ge_{Cu} defect concentration or the presence of secondary phases. In this regard, the application of machine learning to the analysis of the Raman spectroscopic data can not only significantly reduce the analysis time, but also yield methodologies for solar cell efficiency prediction. For the present study, a LDA dimension-reduction algorithm was applied. This type of algorithm is widely used for spectral data analysis in different methods and fields of application [209]–[212], [212], [213]. This is because of the high dimensionality nature of the spectroscopic data analyzed in this work and the ability of LDA to reduce these dimensions to just a few while preserving most of the information, which allows for feature extraction rather than feature selection. Using the Raman spectra of each cell obtained with different wavelengths as input, the LDA algorithm was used to classify the different cells of the combinatorial sample according to the following classification targets: efficiency, V_{oc} and [Zn/Ge] ratio. The 2-dimensional outputs for each classification targets are presented in Figure 5.7 as a function of two discriminants (D1 and D2, with labels a, b, c for the three mentioned targets, respectively), along with the classification groups and training/test scores. As already mentioned above, the amount of data employed for the analysis (196 cells) is far from being considered “big data” and, as such, this methodology and the results presented below should be taken as a first approach and are susceptible to further improvement for a more precise classification through the use of a higher number of training inputs. In the case of the efficiency and V_{oc} targets, a defined data classification clustering is observed with comparable scores. In Figure 5.7(a), it can be observed that low efficiency (<3.4%) cells are relatively well classified and separated from the groups with medium (3.4–4.4%) and high (>4.4%) efficiency. On the contrary, for the Voc target, while the cells with the highest voltages are well differentiated, the rest of groups show high overlapping (Figure 5.7(b)). However, despite the relatively low classification score, it is worth noticing that there is no clear over fitting occurring by comparing the individual and overall scores of the algorithm, indicating that a larger data set could greatly improve the classification.

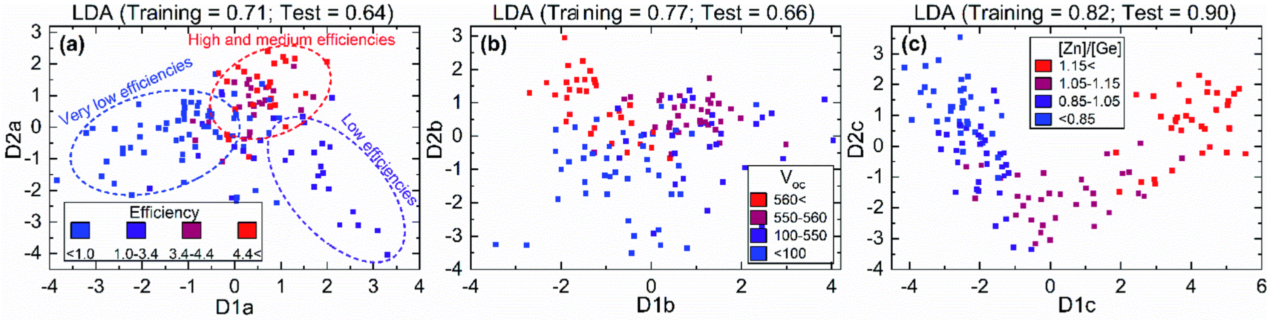

Figure 5.7: *Results of the machine learning analysis of the Raman spectroscopic data for different classification targets: (a) efficiency, (b) Voc and (c) [Zn]/[Ge] ratio. The training and test scores obtained for each run are presented on the top of the panels.*

In the case of the [Zn]/[Ge] ratio target shown in Figure 5.7(c), the classification resulted in a clear sequential correlation between the discriminants, from lower to higher ratios. The first 2 groups, cells with 0–0.85 and 0.85–1.05 [Zn]/[Ge] ratios, show significant overlapping leading to misclassifications in both training and test data which is reflected in the LDA algorithm scores. On the other hand, a good clustering is shown for the 1.05 < [Zn]/[Ge] < 1.15 and [Zn]/[Ge] > 1.15 groups. Even though the discriminants in LDA algorithms are of unclear nature and do not necessarily follow an underlying physical concept (at least in a straightforward way), the resulting curve in Figure 5.7 (c)shows great resemblance with that obtained from the analytical analysis of the influence of point defects on device performance (Figure 5.4 (a)). Bearing this in mind, the relative integrated intensity of the Raman peak at 176 cm^{-1} and efficiency of the solar cells in the combinatorial sample were plotted against the classification discriminants D1c and D2c (Figure 5.8). The latter were mainly selected as they show the clearest differentiation between the different classification groups, and, thus, were expected to have a more pronounced dependence from the physical parameters of the solar cell devices.

Despite the fact that none of the analytical parameters (relative integrated intensity of the Raman peak and solar cell efficiency) was directly used for the LDA algorithm, a pronounced linear-like correlation between parameters and the LDA discriminants can be observed. Moreover, a closer look to the obtained correlation, allows to define that the points that deviate from the correlation forming a cloud in Figure 5.8 (a) (highlighted with a dotted oval) correlate with zero efficiency solar cells. In this way, the behavior of these cells is probably not related to the concentration of V_{Cu} defects, but to other critical parameters of the devices (i.e. presence of ZnSe in absorber, or bad absorber/buffer interface, etc.). Similarly, in case of the correlation of cell efficiency with the D2c parameter (Figure 5.8 (b)), the points that lie far from the proposed dashed line probably present some additional issues, not directly related to the absorber layer itself that is strictly analyzed in the present study. These correlations, however, firstly, allow to get a glimpse of the possible physical meaning behind the D1c and D2c discriminants, and, secondly, prove that there exists a strong correlation of the V_{Cu} defects with the Raman spectra [Zn]/[Ge] ratio and solar cell efficiency. In this way, the variations of the V_{Cu} parameter are directly reflected on the other parameters. These multi-variable correlations are intrinsic to the CZGSe material itself and of importance to derive its properties. Moreover, this finding makes possible to predict solar cell efficiency using only Raman spectra and compositional data. This has an enormous potential both for research and industrial process monitoring applications. In addition, the results presented here illustrate a powerful example of why combinatorial analysis should be established as a standard procedure for the study of complex systems such as thin film solar cells based on chalcogenide compounds in order deepen into the critical parameters that govern their efficiency.

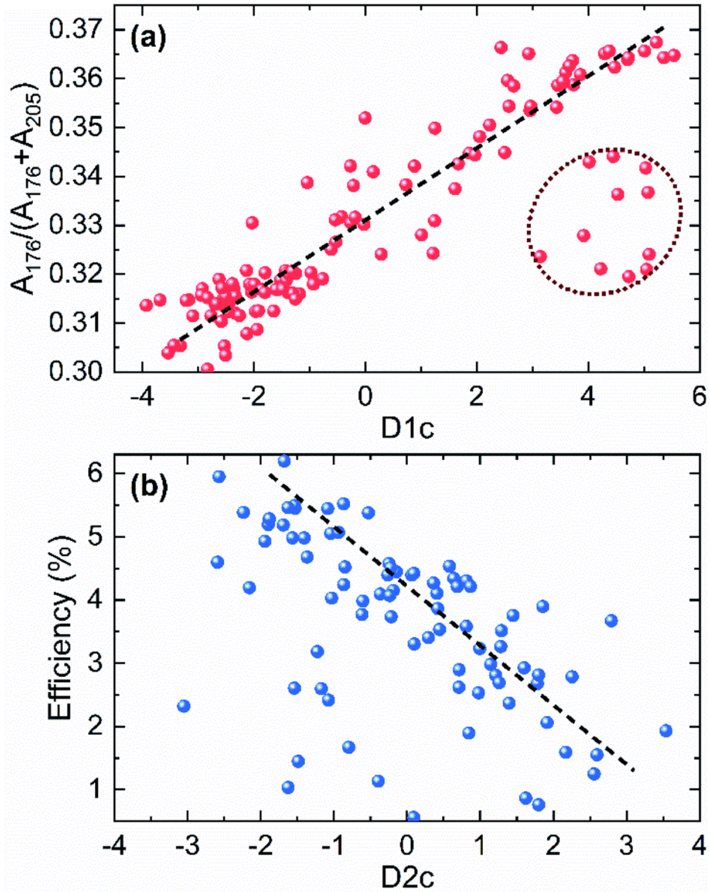

Figure 5.8: *(a) Relative integrated intensity of the Raman peak at 176 cm−1 plotted against discriminant D1c, and (b) efficiency of the solar cells plotted against discriminant D2c of the [Zn]/[Ge] ratio LDA classification target. The explanation of the dotted oval line can be found in the main text.*

5.4. Conclusions

This work has presented a complex analysis of the formation of secondary phases and point defects under off-stoichiometry conditions, as well as of their effect on PV performance, in a combinatorial CZGSe sample comprised by almost 200 individual solar cells covering a wide range of [Zn]/[Ge] compositions in the Cu-poor regime. Firstly, an analytical approach based on Raman spectroscopy and XRF has allowed defining the off-stoichiometric limits of formation of the CZGSe kesterite phase: 0.7 < [Zn]/[Ge] < 1.2. It has been observed that, close to the top limit, the probability of forming ZnSe increases and, above it, it may become the dominant phase, while the formation of other secondary phases is almost negligible in the whole range studied. As for defect formation, the footprint of V_{Cu} and substitutional Zn_{Cu} and Ge_{Cu} defects on the vibrational properties of the CZGSe material has been analyzed. Strong V_{Cu}-induced variations in the Raman spectra have been found, especially close to the J- and L-type off-stoichiometry lines, whereas a softer effect (mainly at high wavenumbers) has been observed for the substitutional defects. Finally, the complex analytical correlation of compositional, spectroscopic and optoelectronic data for each of the 200 solar cells, has allowed revealing that V_{Cu} controls the J_{sc} and FF of the devices while the substitutional defects have their main influence on the V_{oc} leading to an optimum cationic compositional range of [Zn]/[Ge] = 1.05–1.15 for achieving the high efficiency (~6%) solar cell devices. This has been further explored through the application of an LDA machine learning algorithm. Using just Raman spectra as input, the algorithm employed has been shown to be able to classify the different cells in terms of composition and optoelectronic parameters. These results confirm the deep intrinsic intertwining of the V_{Cu} defect concentration with the Raman spectra, [Zn]/[Ge] ratio and solar cell efficiency, and represent a powerful solar cell performance prediction methodology both for research and industrial process monitoring environments. As such, this work not only provides valuable insight for understanding and further developing the CZGSe photovoltaic technology and but also gives a practical example of the potential of combinatorial analysis and machine learning for the study of complex systems in materials research.

Part

2

Bulk heterojunction solar cell based on low-band gap polymer and soluble fullerene derivative.

Organic solar cells become one of the highly active research fields in material science for renewable energy. Organic photovoltaic systems hold the promise for a cost-effective, lightweight solar energy conversion platform, which could benefit from simple processing of the active layer. Using organic materials such as polymers and fullerene derivatives show great potential being electron donors and acceptors.

A combination of narrow band donor polymer and one of the fullerene derivatives provide a possible solution for the production of efficient organic solar cells.

The main goal of this part is shed light on the feasibility of OSCs optimization using a novel inorganic electron-transporting layers (SnO_2 and ZnO), as a way to overcome the shortcomings associated with the PEDOT: PSS conventional configuration.

6

Organic photovoltaic solar cells: Scientific background

6.1. Brief history of organic solar cells

Over the last few decades, bulk-heterojunction organic photovoltaic devices comprising an intimately mixed donor-acceptor blend have gained serious attention due to their potential for being cheap, light weight, flexible and environmentally friendly. The organic photovoltaic (OPV) technology is thought to provide an excellent alternative to Si-based PVs in those applications where the importance of price and mechanical properties dominate over high performances or lifetime. The rise of organic photovoltaic is a consequence of the development of conductive polymers. In 1977, Shirakawa et al. reported that the conductivity of polyacetene can be increased by seven orders of magnitude after exposure to halogens [214]. Allan J. Heeger, Alan MacDiarmid and Hideki Shirakawa received the Nobel Prize of chemistry in 2000 “for the discovery and development of conductive polymers”. Before that, in 1959 Kallmann and Pope observed a photovoltaic effect in organic crystal using anthracene [215]. In the next 20 years, using a metal-organic junction approach, several organic photovoltaic solar cells were reported but with a very limited efficiency (0.1%) [216]. One of the major breakthroughs happened in 1986 when Tang fabricated a two layer organic solar cell using copper phthalocyanine (CuPc) and a perylene tetracarboxylic (PV) derivative [217]. It’s assumed that the two materials contribute to photons absorption and that the generated excitons dissociate at the interface of the two organic layers. Following dissociation, the holes were transported in the CuPc layer and the electrons in the PV layers. This was the first use of a combination of a donor and an acceptor, concept that is still prevalent nowadays. The second major breakthrough was the incorporation of the donor and the acceptor in the same layer called Bulk Heterojunction (BHJ). It was done first by co-evaporation of the molecules [218] and later by solution processed [219]. Another important aspect of the organic solar cells is the use of fullerene derivative as acceptors. The first report of the use of semiconducting polymer: C60 came in 1993 where C60 was evaporated on top of a MEH-PPV layer [220]. Using the fullerene derivative PC61BM/PC71BM as acceptors became the norm in solution processed OPV for the next 20 years and the research had been focused on the synthesis of new donors as well as understanding the fundamentals. A lot of work has been focused on the pair P3HT: PCBM which is still a model system nowadays. The efficiencies of polymer: fullerene have reached more than 10% [221], [222] and the reader can find an extended literature on polymer donors in specialized reviews [223], [224]. Looking at device efficiency swapping polymer donors with small molecule SM was not successful and only a few systems (i.e. exceptions) were reported before 2014 prior to the beginning of this work. In 2012, Sun et al. reported the DTS $(PTTh_2)_2$ molecule that gives 6.7% PCE in BHJ. Before this result, the efficiencies of SM:PC71BM BHJ were less than half of their polymer counterpart [23]. At the end of the same year, the donor DERHD7T was published with 6.10% PCE [225]. In 2013, Liu et al. introduced the molecule SMPV1 with a certified 8.02% PCE [226]. In early 2015, Sun et al. reported the molecule BTR that can achieve a maximum of 9.3% [227]. Later the same year, PCE over 10% was reported for the first time using DRCN5T molecule [228]. In 2017 the maximum PCE reported for SM:PC71BM device is 11.5% [229]. A new era has started with the rise of non-fullerene acceptors (NFAs). During years achieving high efficiencies using acceptors that are not fullerene derivatives was challenging and no suitable candidates were found. Replacing fullerene acceptors by others systems opened a new way to improve device efficiencies as well as stability. The advantages of NFAs are: contribution to light absorption, tuning of the energy levels and potentially better stability [230]–[232]. NFAs are now widely used with polymer donors but also with SM donors and the best efficiency reported so far is more than 13% [233].

6.2. Organic semiconductors

Carbon atom (C-atom) is the main element constituting polymer materials. The type of bonds between two adjacent C-atom formed by their valence electrons determines the overall electronic properties of a given polymer. Those chemical bonds could be either saturated or unsaturated bonds. Saturated polymers are insulators since all the four valence electrons of C-atom are used for the formation of covalent bonds (i.e. *sp3* hybridization orbitals), while most conductive polymers have unsaturated conjugated structure. The electronic configuration of π-conjugated polymers stems from their alternated single and double carbon-carbon bonds. Therefore, the fundamental source of the semiconducting property of conjugated polymers originates from the overlapping between the molecular orbitals formed by the valence electrons of chemically bonded C-atoms. It is arisen from the π-delocalization of single *2pz* valence electrons along the polymer backbone. This phenomenon is occurring when one *2s* orbital in C-atom is mixed with two of the *2p* orbitals of C-atom to forms 3 sp^2 hybrid orbitals, leaving one *p* orbital in C-atom un-hybridized (See Figure 6.1). The sp^2 carbon hybrid orbitals are known to form a different bond length, strength and geometry when compared to other hybridized molecular orbitals. The sp^2 hybridization has one unpaired electron (π-electron) per C-atom. The three sp^2 hybrid orbitals of a C-atom arrange themselves in three-dimensional space to attain stable configuration. Their geometry is trigonal planar geometry, where the bond angle between the sp^2 hybrid orbitals is 120^o. The unmixed pure pz orbital lies perpendicular to the plane of the three sp^2 hybrid orbitals points out small periodic changes in the C-C distance.

The π-electrons are highly delocalized and are at the origin of the opto-electronic properties of organic semiconductors (Figure 6.1). This delocalization allows electrons to move freely along the conjugated backbone up to a distance referred to as conjugation length.

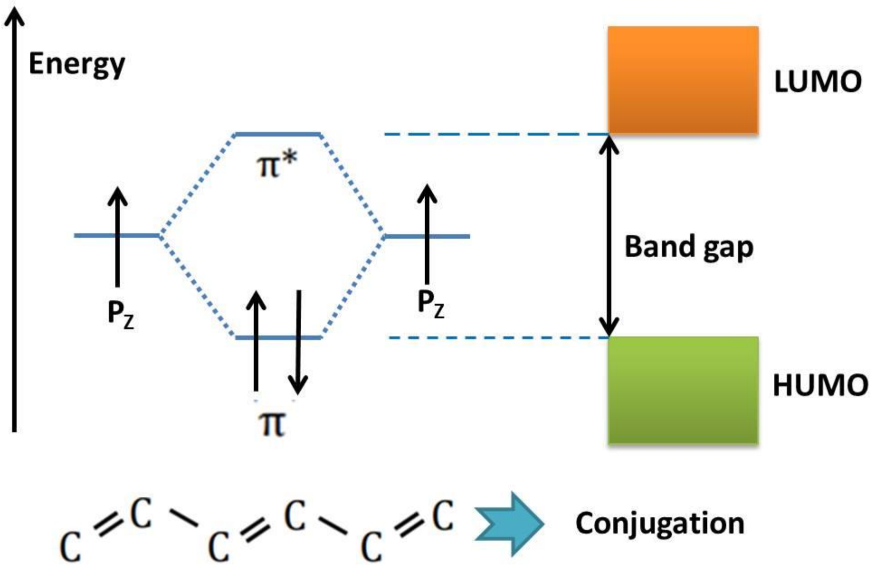

Figure 6.1:*pz orbital overlap to form π (bonding) and π* (anti-bonding) band in C-C system.*

The overlap of pz orbitals of C atoms result in bonding (π) and anti-bonding (π*) orbitals (Figure 6.1). The bonding one which is lower in energy and occupied with electrons is defined as the highest occupied molecular orbital (HOMO). The anti-bonding one, higher in energy and non-occupied is called the lowest unoccupied molecular orbital (LUMO). In thin films, the electron energy levels are broadened but remain strongly correlated to the molecular HOMO and LUMO levels. The corresponding HOMO and LUMO "bands" are analogs of the valence and conduction bands, respectively, in conventional inorganic semiconductors. The energy offset between the HOMO and the LUMO levels is called the energy band gap. If the conjugation length is increased, the energy bands shift slightly (upwards for the HOMO and downwards for the LUMO) and the band gap is reduced.

Before going into a deeper analysis on OPV devices, a comparison between the properties of semiconducting inorganic and organic materials could be useful to understand the main advantages and drawbacks for their application in the photovoltaic technology.

6.3. Comparison between inorganic and organic semiconductors

The key differences between inorganic and organic semiconductors lie in their electronic structures. Traditional inorganic semiconductors are crystalline ordered solids where atoms are covalently bounded and electrons (and their wave's functions) are spatially delocalized over the crystalline lattice. The energy states allowed for these electrons form the semiconductor valence and conduction bands, which are dense (continuous) energy bands separated by an energy gap (the band gap, E_g).

In inorganic PV cells, an electron can be promoted from the valence to the conduction band upon light absorption (or other excitation mechanisms), generating free delocalized charges which can be driven to the electrodes through the application of an external electrical potential. On the opposite, traditional organic semiconductors are conjugated molecular or polymeric compounds with a structure characterized by a sequence of sp^2 hybridized carbon atoms with un-hybridized pz atomic orbitals. These atomic orbitals give rise to molecular σ and π electronic orbitals respectively. The bonding (π) and anti-bonding (π*) orbitals of molecules compose the valence and conduction bands of the organic semiconducting material, identified as the highest occupied and lowest unoccupied molecular orbitals respectively (HOMO and LUMO). Since polymeric semiconductors are usually disordered (amorphous) materials, with weakly interacting Van-der-Waals bonded macromolecules, a narrower band width distribution and a much weaker delocalization of electronic wave-functions among neighboring molecules occur, causing the HOMO and LUMO bands to be discrete and not continuous. Therefore in OPV devices, the usual product of light absorption is a tightly bounded electron-hole pair, also called Frenkel exciton or mobile excited state [234], which is an electrically neutral species which, to first order, is unaffected by electric fields. The intrinsic electronic diversity between inorganic and organic materials causes firstly a significant difference in the relative importance of interfacial processes in inorganic PV and OPV devices, which is closely related to the described charge generation mechanisms. While in inorganic PV cells free charges are directly generated upon light absorption under normal conditions, light absorption in organic materials results in the production of a mobile excited state which can dissociate into free charges only at an hetero-interface where the exciton dissociation driving force overcomes the coulombing interaction which tightly bounds the electron-hole pair [235]. This notably influences the photoactive material structure, at the micro- and nanoscopic level, necessary for the inorganic and organic PV devices to function most efficiently. Another consequence of the intrinsically different electronic structure of organic and inorganic semiconducting materials is their charge transport mechanism. Band transport is the mechanism typically observed in inorganic semiconductors, where delocalized charges are efficiently screened by the surrounding lattice, due to the high dielectric constant of inorganic materials, and are transported through the material bulk in the continuous conduction band of the semiconductor without important energy losses. Differently, in amorphous organic semiconductors the conductive electronic states are more localized. Charges, poorly screened by the neighbor molecules due to the low dielectric constant of organic materials [236], polarize and distort the surrounding lattice forming the polarons, which diffuse between adjacent molecules through a thermally activated and less efficient hopping mechanism, comparing to band transport [237]. This explains the much lower charge mobility of amorphous organic solids (usually lower than 10^{-2} $cm^2/V{\cdot}s$) [238] comparing to that of crystalline inorganic semiconductors. The very different cohesion forces in crystalline inorganic solids and polymeric organic solids easily explain also the different physical and mechanical properties of the two materials. While inorganic crystalline semiconductors are rigid and brittle, have high processing (fusion) temperatures and are reasonably stable to degradation processes with water and oxygen, organic amorphous or semi-crystalline polymeric materials are flexible and lightweight, can be dissolved at low temperatures (this rendering their processing cheaper, easier and transferrable to industrial processes in continuum), but often suffer of easy degradation in ambient conditions. The electronic structures of inorganic and organic semiconductors also determine a difference in their light absorption properties, leading organic materials to have higher absorption coefficients in the visible light range (~10^5 cm^{-1}) compared to inorganic semiconductors (~10^3 - 10^4 cm^{-1}). On the other hand, lower Eg values can be obtained for p- and n-doped inorganic semiconductors, allowing an efficient absorption of solar light in its most extended spectral region (the infrared), while only band gaps limited to values higher than 1.4-1.5 are obtainable for organic semiconductors, confining the solar light absorption to the visible spectral region. Finally, it should be reminded that the number of the synthetically available inorganic semiconducting compounds is extremely lower than their organic counterparts. Therefore an easier tuning of the chemical and physical properties by accurate molecular design and engineering, increasing the control on the performances optimization, is achievable for organic semiconductors comparing to inorganic ones.

Table 6.1*: comparison between organic and inorganic semiconductor devices*

Properties	**Organic semiconductor**	**Inorganic semiconductor**
Chemical bonding	Van der Waals	Covalent/ionic
Charge transport	Polaron hopping	Band transport
Charge mobility	< 1 cm^2/Vs	~1000 cm^2/Vs
Conduction levels	Frontier orbitals	Bands
Exciton species	Frenkel	Wannier-Mott
Exciton Radius	~ 10Ǻ	~100 Ǻ
Exciton binding energy	10-1000 meV	10-100 meV
Dielectric constant (Ɛ)	~ 1.5-4	~10-100

6.4. Working principle of organic solar cells

The working principle of an organic solar cell can be briefly described by the following steps: (1) formation of an exciton upon light absorption, (2) diffusion of the exciton to the interface between two materials, (3) subsequent exciton dissociation into free charges, and (4) transport of free charges (electrons and holes) followed by (5) their extraction at the respective electrodes.

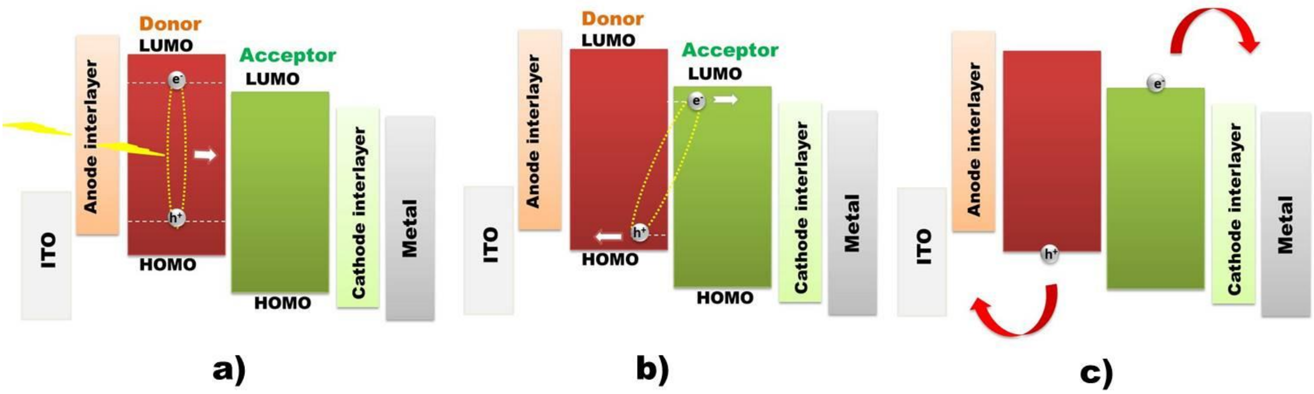

Figure 6.2: *The energy diagram of typical organic solar cell and different stages of the photocurrent generation process (a) exciton generation, (b) charge transfer state dissociation, (c) charge transport and extraction.*

6.4.1. Light absorption and exciton generation

The generation of a photocurrent in an organic solar cell starts with the absorption of light. In general, photoactive organic materials have very high molar absorption coefficients (α) that are typically around 10^5 cm^{-1}. This important feature allows a thin organic layer (d = 150-200 nm) to absorb a sufficient amount of photons within a given spectrum diapason [239]. For comparison, the absorption coefficients of conventional inorganic semiconductors like polycrystalline silicon are in the range of 10^3-10^4 cm^{-1} in the visible wavelength range, which requires much thicker films to absorb the same amount of light for a given wavelength. Upon absorption, electrons in the active layer (mainly in donor material for the systems using fullerene derivatives as acceptors) are excited from the HOMO to the LUMO and neutral species called excitons (bound intra-molecular electron-hole pairs) are formed. Due to the low dielectric constants and localized electronic states in organic semiconductors, a strong Coulombic attraction exists between an electron-hole pair, which does not allow direct generation of free charges. These bound electron-hole pairs have exciton binding energy of 100-1400 meV [240], [241] unlike their inorganic counterparts that have exciton binding energy of around a few meV. For instance, for the well-known and widely used P3HT (poly(3-hexylthiophene-2,5-diyl)), used as donor material, an exciton binding energy of ≈ 700 meV has been reported [242]. Therefore, ambient thermal energy is not enough to separate the electron-hole pairs. As the lifetime of excitons is of the order of nanoseconds [243], [244], a fast and efficient way is needed to avoid geminate recombination. A solution to this issue has been proposed by Tang et al. in 1986, who demonstrated an organic solar cell based on two different materials with properly aligned energy levels [217].

6.4.2. Exciton diffusion and dissociation at the D/A interface

After an exciton is formed, it needs to travel towards the D/A interface in order to be dissociated. This distance needs to be less than the exciton diffusion length. The energy offset between the D and A materials should allow to overcome the exciton binding energy and efficiently dissociate electron-hole pairs. It is generally believed that this value must be larger than 0.3 eV [245], [246]. Currently, in solution-processed BHJs, soluble fullerene derivatives like [6,6]-phenyl-C61/C71 butyric acid methyl ester (PC61BM/PC71BM) remain as the most frequently used acceptor material. Though, today non-fullerene rivals are under extensive investigation and show high efficiencies as well [247]–[249]. Recent literature data suggest that for the systems using fullerene derivatives as acceptor materials a ΔLUMO as low as 0.1 eV can be sufficient [250]–[252]. The charge transfer (CT) process in conjugated polymer-fullerene system is known to occur in a very short timescale (< 100 fs) [253], [254], which is roughly 10 000 times smaller than the exciton lifetime and thus much faster and relatively efficient.

When the CT step is successfully realized, hole and electron reside in neighboring donor and acceptor molecules, respectively. The resulting CT states are intermediate species between coulombically bound exciton and free charges (Figure 6. 2). At this stage, due to the delocalized nature of holes and electrons on their respective molecules, the binding energy between them is notably weaker. Therefore, they can either be thermally dissociated or separated by an electric field. The underlying mechanism of electron-hole pair dissociation is not fully understood yet and remains an important issue in organic photovoltaic (OPVs). For instance, the energy losses in CT states strongly affects the open circuit voltage [255]–[257] and thus the power conversion efficiency of the final solar cell. In-depth reviews on charge generation process in organic solar cells can be found in references [258], [259].

6.4.3. Charge carrier transport

Once the electron-hole pairs are dissociated, the free charge-carriers must be transported towards their respective electrodes to participate to the photocurrent. Here, charge transport within the organic semiconductor plays an essential role. The fundamentals of charge transport in disordered organic materials are totally different from their inorganic counterparts. The crystal structure, which is present in classical crystalline inorganic semiconductors, allows delocalization of the electron wave function. This in turn permits electrons and holes to behave as quasi-free particles (band transport). In organic semiconductors the electronic states are more localized. While the intra-molecular charge transport is considered to be fast, the inter-molecular transport within the localized states is a rate-limiting factor and is thermally activated. Such a charge carrier hopping mechanism is strongly influenced by the presence of energetic and structural disorder.

6.4.4. Charge carrier extraction

The last step to complete the solar energy conversion in a PV system is the extraction of charge carriers at the respective electrodes. The selection of contact materials plays a key role in the charge extraction process. In particular, the work functions of the anode and cathode need to be aligned with the HOMO energy level of the donor and LUMO energy level of the acceptor materials, respectively, in order to avoid any energy barrier. If a barrier exists, the extraction/injection rate of charge carriers will be hindered. This may lead to the accumulation of charges close to the active layer/contact interface and result in low device performances, especially low fill factors (FF). It has been shown by numerical simulations that the formation of space-charges near the surface could result in deformed (S-shaped) current-voltage curves [260]. Additionally, the misalignment of active layer/electrode energy levels may strongly affect the open circuit voltage (Voc) of the final solar cell [261]–[263]. Another factor which hampers the device performances is the collection of charges at the wrong electrodes i.e. electrons at the anode or holes at the cathode. To overcome this issue electron/hole transporting layers (ETL/HTL), also referred to as “buffer layers”, are often implemented between the active layer and the electrode, improving the selectivity of the contacts. Extended and comprehensive reviews on ETL/HTL materials and their roles in organic solar cells are reported in references [264], [265].

6.5. Organic device architectures

The active semiconducting materials used in polymer solar cells is always carbon based organic compounds either in the form of small molecules, dendrimers or polymer which converts solar energy into electric energy. Such type of OSCs can be divided into three structures: single layer or monolayer, bilayer and bulk heterojunction (BHJ) structured cells.

6.5.1. Single layer structure

Single layer organic photovoltaic cells are the simplest form. These cells are made by sandwiching a layer of organic electronic materials between two metallic conductors, typically a layer of indium tin oxide (ITO) with high work function and a layer of low work function metal such as Aluminum, Magnesium or Calcium. The basic structure of such a cell is illustrated in Figure 6.3. The difference of work function between the two conductors sets up an electric field in the organic layer. When the organic layer absorbs light, electrons will be excited to the LUMO and leave holes in the HOMO, thereby forming excitons. The potential created by the different work functions helps to split the exciton pairs, pulling electrons to the positive electrode (an electrical conductor used to make contact with a non-metallic part of a circuit) and holes to the negative electrode.

This configuration is simple but the absorption is usually low using a single type of molecule. Since both positive and negative charges travel through the same material, recombination losses are generally high.

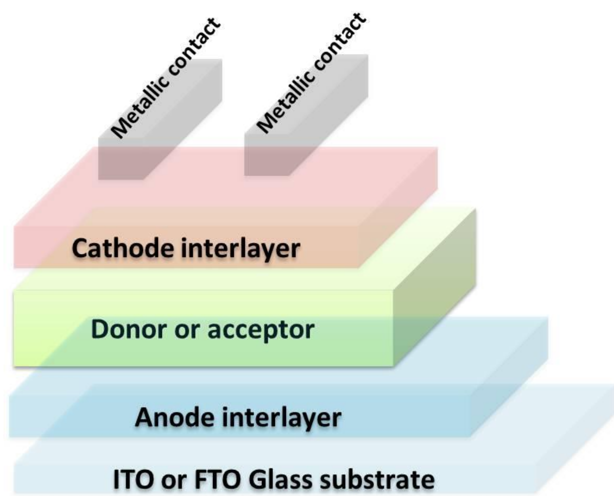

Figure 6.3: *Schematic OPV structure of single layer.*

6.5.2. Planar Bilayer device

In a bilayer OSCs (Figure 6.4), photoactive layers containing donor and acceptor organic materials absorb sunlight and generate photocurrents. The donor material (D) is usually electron rich molecules, which are capable of donating electrons that create holes whereas the acceptor material (A) should have capacity to accept electrons. This photoactive layer harvest photons from sunlight to form excitons. Excitons are the state of electrons in which it gets excited from the valence band into the conduction band. This creation of excitons in donor layer resulted in concentration gradient phenomenon and due to this; excitons start to diffuse towards donor/acceptor interface and then separates into free holes and electrons. As soon as this charge separation process takes place free holes and electrons moves to the corresponding electrodes and resulted in photovoltaic. In a bilayer heterojunction device, p-type and n-type materials are consecutively placed with each other [266]. Different combinations of materials used in bilayer devices using organic semiconductors were reported [215], [258].

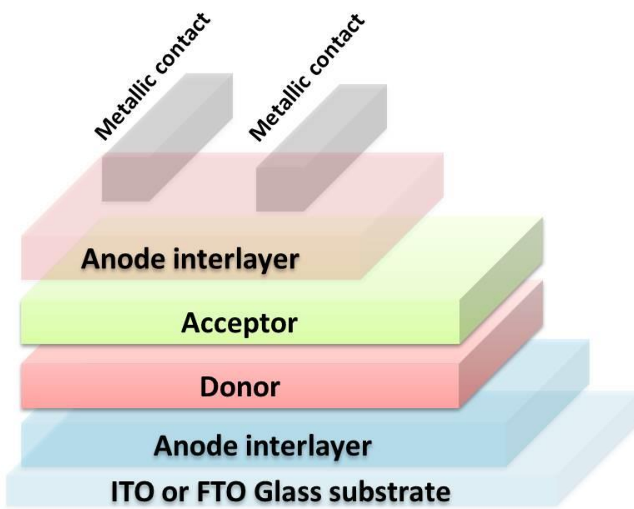

Figure 6.4: *Schematic OPV structure of planar bilayer.*

6.5.3. Bulk heterojunction device

The bulk heterojunction device (Figure 6.5) shows improved interfacial area where charge separation occurs as compared to bilayer device. Bulk heterojunction is prepared by bulk volume mixing of donor and acceptor components which results in very small exciton diffusion length at donor-acceptor interface. In such type of devices, excitons are generated on photon absorption of organic materials. Then dissociation of excitons gives charge collection at corresponding electrodes and this process occurs at the heterojunction interface.

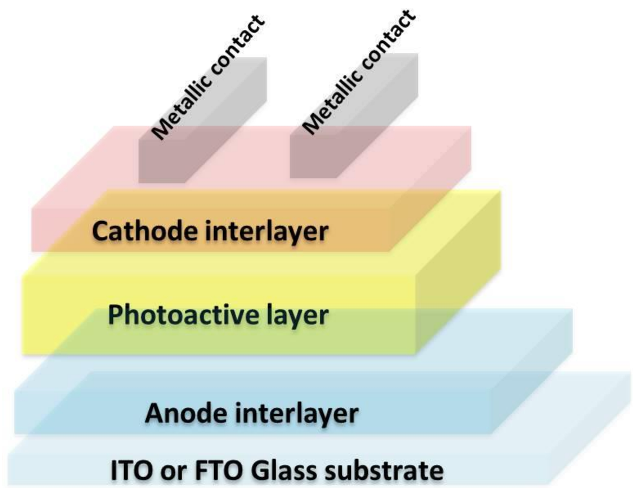

Figure 6.5: *Schematic OPV structure of bulk heterojunction.*

6.6. Limitations factors for organic solar cells

According to the literature, there are a lot of factors that can limit the performance of OSCs [256], [258], [259]. In this part, we discuss the factors that limit the OSCs performance during their whole lives in terms of metastable morphology, diffusion of electrodes and buffer layers, oxygen and water and irradiation.

⇘ <u>Metastable morphology and diffusion of electrodes and buffer layers</u>

An active layer is the key component of OSCs, in which there are generally two or three phases (the donor phase, the acceptor phase and the donor/acceptor mixed phase). Phase separation is always metastable due to the strong mobility of organic materials.

Like the donor and acceptor materials, the electrodes and buffer layers also show mobility. As shown in Figure 6.6, the indium (In) of ITO can diffuse into the PEDOT:PSS layer and the active layer (Figure 6.6, left); the Al can diffuse into the PEDOT:PSS layer and the active layer; and the PEDOT:PSS layer can also diffuse into the active layer (Figure 6.6, right). Such diffusion of metals and buffer layers will reduce the performance of OSCs by changing the energy levels of buffer layers and acting as the traps for charge recombination.

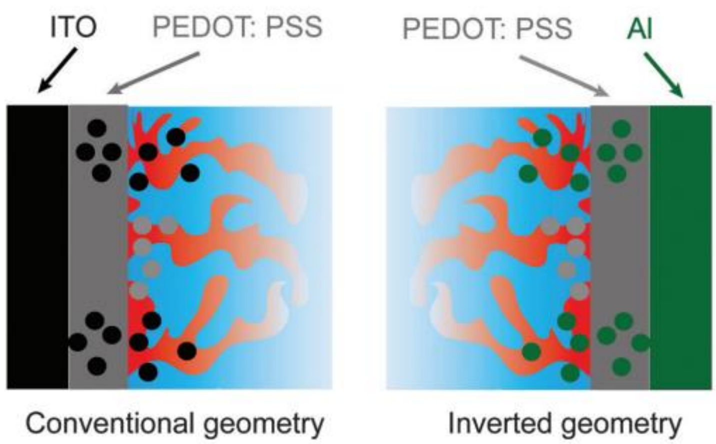

Figure 6.6: *Schematic diagram of the diffusion of electrodes and buffer layers.*

⇘ <u>Oxygen and water</u>

Oxygen can reduce the performance of OSCs (Figure 6.7). Firstly, the metal electrodes (e.g. Al and calcium (Ca)) with a low work function (WF) can be oxidized by oxygen permeation. The electrically insulating metal oxide layer, which is formed between the electrode and the buffer layer or the electrode and the active layer, will create a transport barrier and eventually induce an S-shaped I–V curve and degrade the performance of the device [267]. Secondly, the penetrative oxygen in the active layer takes part in the various photo-oxidation reactions of donor and acceptor materials [268]. The changed structures of donor and acceptor materials will change their photon absorption, energy levels and charge carrier mobilities. Thirdly, the oxygen doping in the active layer can enhance hole concentration, which results in an increase of the density of deeper traps for electrons and a decrease of the fill factor (FF) and the open circuit voltage (V_{OC}) [269].

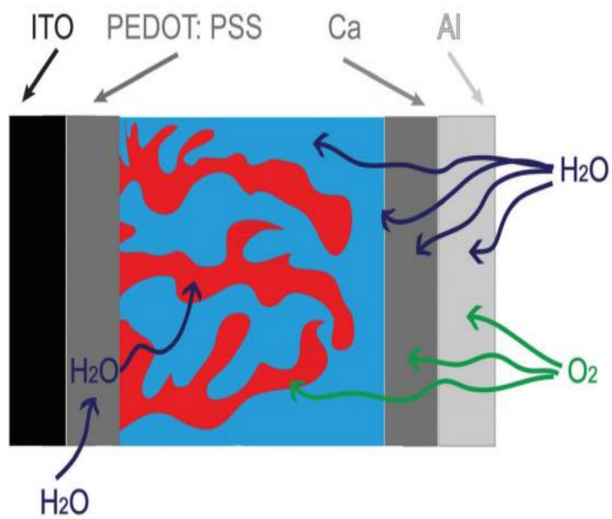

Figure 6.7: *Schematic diagram of the diffusion of oxygen and water.*

The ingress of water in the device is another important factor limiting the performance (Figure 3. 4). Water can diffuse into the device via the hygroscopic PEDOT:PSS buffer layer and metal electrodes Firstly, water can damage the low WF metal electrodes as an oxidation agent [270]. It was observed that large defects were appeared on the Al electrode after the exposure of water [271]. These defects can act as pinholes to allow more ingress of water [271]. Secondly, the ingress of water into the interface of the active layer and the electrode can form a insulating metal oxide interlayer, leading to a decrease of effective active layer/electrode interface area which is harmful to charge extraction [272]. Thirdly, water diffusing into the active layer can move PC61BM and thus induce excessive aggregation of fullerenes. The larger scale of phase separation decreases the D/A interfaces, which is harmful to exciton dissociation and causes a huge reduction in device performance [273].

➯ Irradiation

The original reasons for the instability of the device upon irradiation are photochemical degradation and photo-physical degradation in the active layer, the buffer layer and the active layer/electrode interface. The main photochemical degradation is photo-oxidation reaction in the active layer.

➯ Some strategies to increase the stability of OSCs

Mainly six types of strategies are included: material design of the active layer (molecular skeletons and side chains of donors, and fullerene/non-fullerene acceptors), device engineering of the active layer (ternary blends and processing methods), employing inverted geometry, optimizing buffer layers (hole/electron transport layers), using stable electrodes (new transparent/back electrodes) and encapsulation. In this context, the main goal of this work is elaboration and optimization of inverted organic solar cells based on inorganic compounds used as electron transporting layer (ZnO and SnO_2).

7

Methodology II

7.1. Techniques and pieces of equipment

7.1.1. Optical, Structural, electrical and morphological characterization

➷ ***Ultraviolet-visible spectroscopy***

Ultraviolet-visible (UV/Vis) spectroscopy is a technique used to measure quantitatively the absorption or reflectance of a material either in solution (absorption) or in thin films. The working principle is based on shining a monochromatic light on the sample and analyzing the transmitted or reflected fraction of the light. The equipment used in UV/Vis spectroscopy is a UV/Vis spectrophotometer that usually includes a radiation source, an adjustable sample holder, a mono-chromator for light dispersion, and a photo detector. The light source is a tungsten wire, a xenon arc lamp (160-2000 nm), and a deuterium lamp that is continuous in the 190-400 nm wavelength range. The detector is generally a photodiode or a charge-coupled device. In our case, the UV/Vis spectrophotometer measures the transmitted light intensity (I_n) and compares it to the incident light intensity (I_{n0}) as a function of the wavelength. The corresponding ratio $T=I_n/I_{n0}$ gives the transmittance. If the reflectance and non-specular light diffusion are negligible, the absorbance (AB) can be estimated using:

$$AB = log\left(\frac{1}{T\ \%}\right) \qquad (7.1)$$

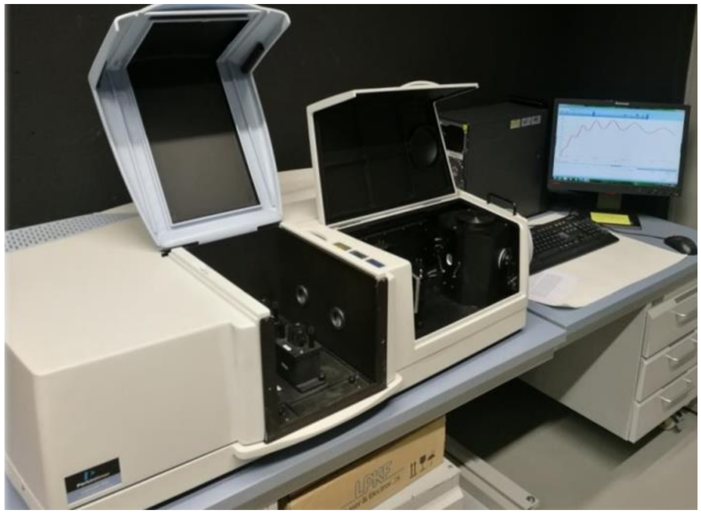

Figure 7.1: *Image of UV-vis-NIR spectrophotometer.*

➥ **X*-ray diffraction***

X-ray diffraction (XRD) is a powerful technique that allows the identification of crystalline phases in a target material and provides information about their orientation, crystallinity and texture. It is based on the interaction of monochromatic X-ray electromagnetic waves with a regular array of atoms. The incident radiation makes the electrons in the sample to re-emit secondary X-ray waves (elastic scattering). These secondary waves interact with each other through interference processes. In a crystalline structure, where atoms are ordered in different planes, these waves interfere constructively if the Bragg's law is fulfilled:

$$2dsin\theta = n\lambda \qquad (7.2)$$

Where d is the spacing between diffracting planes, θ is the incident angle, n is an integer number and λ is the wavelength of the incident radiation (see Figure 7.2). By scanning a sample in the θ coordinate, it is possible to detect the different diffracting planes present in the sample which are parallel to its surface. Then, comparing the position of the peaks in the obtained diffractogram with reference patterns, it is possible to identify the crystalline phases present in the sample as well as their crystallographic orientation. In addition, by analyzing the height and shape of the peaks, it is possible to get an insight on the crystalline quality and texture of the material.

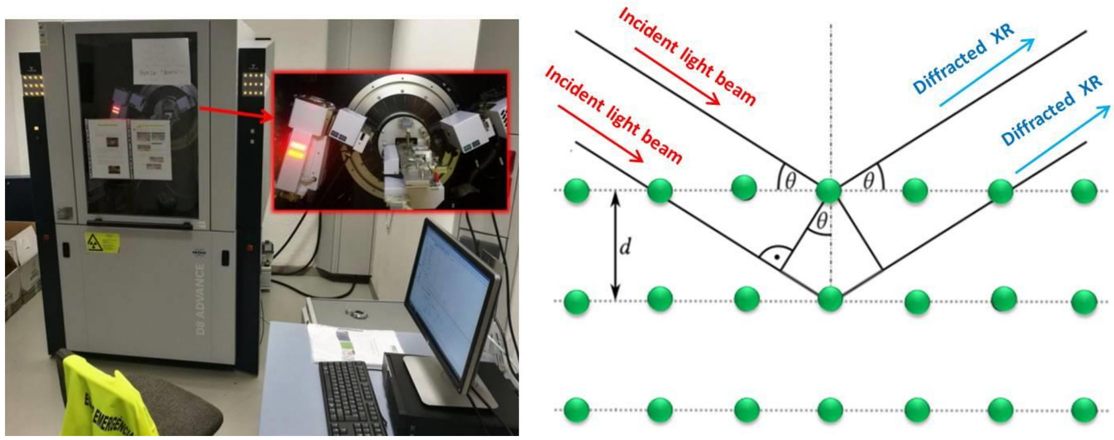

Figure 7.2: *image of Bruker Advance X-ray diffraction system (left) and scheme representation of X-ray diffraction principle (right).*

The measurements were carried out employing a Cu Kα radiation source (λ = 1.5418 Å) at 40 kV and 40 mA, in θ-2θ (Bragg-Brentano) configuration, at 2θ angles from 10^{o} to 90^{o} in 0.017^{o} steps, with an integration time of 2s per step and with sample rotation. The diffractograms were analyzed and compared with reference patterns using X'pert High Score Plus software.

➯ ***Profilometer spectroscopy***

Thicknesses of thin film layers were determined ex-situ by Veeco DEKTAK 150 profilometer (Figure 7.1). The profilometer measures the vertical depth of a material across a specified horizontal length. The profile is displayed on a graphical interface. Uses for this equipment include measuring etch depth, deposited film thickness, and surface roughness. The resolution of a step to determine the film thickness is about tens of nanometers.

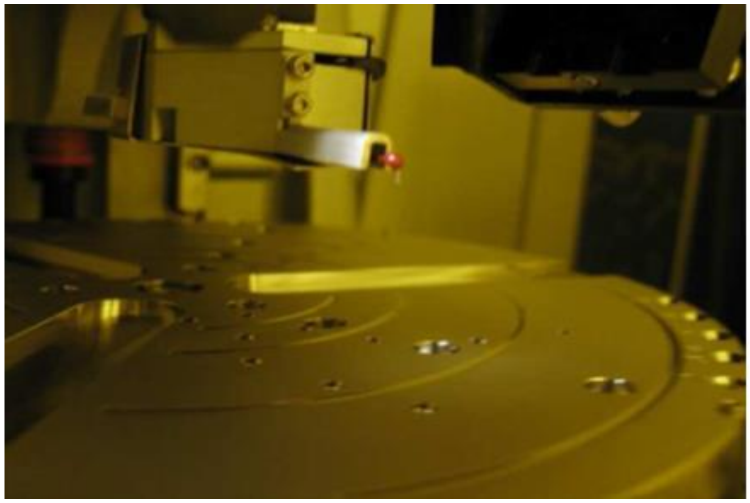

Figure 7.3: *image of DEKTAT Stylus.*

➯ ***Atomic-force microscopy***

The AFM technique is used in the so-called tapping mode to measure the surface morphology. The measurement is based on the small-distance interactions between the scanning probe and the sample surface. Figure 7.4 presents a simplified scheme of the AFM tapping mode principle. A sharp tip (probe) mounted to a free edge of a cantilever is brought close to the sample surface. Vibrations transmitted from the piezo-actuator make the cantilever oscillate close to its resonant frequency (f). The signal detection is realized by four-sectional photodiodes that catch the reflection of the laser beam focused on the edge of the cantilever. In order to tune the spacing between the tip and surface, a feedback mechanism is used that keeps the amplitude of vibrations constant while the tip is scanned over the sample surface. As a consequence the surface topography can be built-up.

In the tapping mode it is also possible to measure the phase shift between the probe oscillations and the electrical signal applied to the piezo-actuator. The latter depends on the inelastic interaction between the tip and the sample and allows one to distinguish between the materials or different phases (e.g. crystalline versus amorphous domains in a semi-crystalline polymer). We used the technique to characterize the surface morphologies of bulk heterojunctions. Besides the thin film roughness, AFM allows to assess the approximate domain sizes of both donor and acceptor materials.

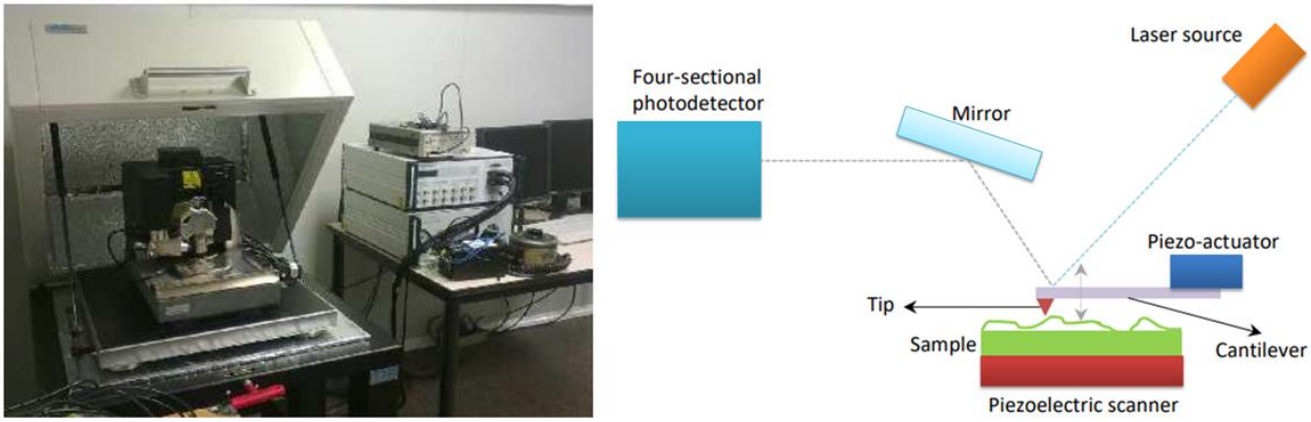

Figure 7.4: *Atomic Force Microscope Dimension 3100 Nanoman from Veeco (left) and the simplified scheme of an AFM assembly (right).*

7.1.2. Electrical characterizations

➷ ***<u>Current-voltage analysis</u>***

Current-voltage (I-V) characteristics of solar cells were measured using a LabViewcontrolled Keithley 2400 SMU. Measurements were performed in the dark and under light using an ABET Technologies Sun 3000 solar simulator with an AM1.5G filter. The standard light-intensity condition (100 mW/cm^2) was controlled by a calibrated Si solar-cell, while for the measurements under different light intensities; neutral optical filters with various transmittances were employed. The details on measured (I-V) curves and main solar cell parameters are given in section 1.

↳ *Quantum efficiency (QE) measurements*

As has been said in previous sections, once the charges are generated within a solar cell they have to be collected at the electrodes in order to contribute to the current.

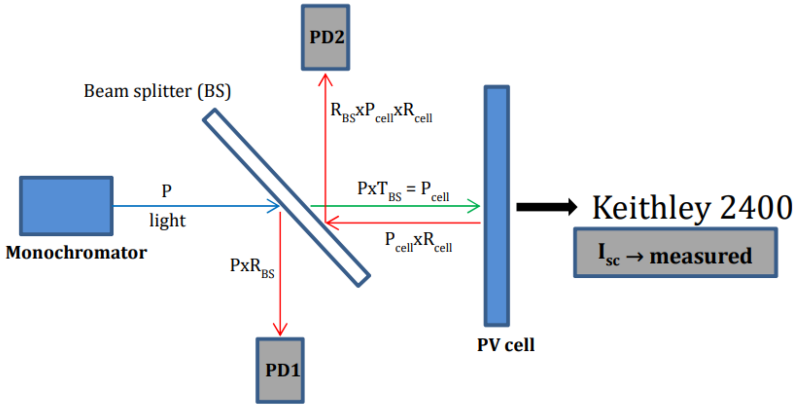

Figure 7.5: *Schematic view of EQE/IQE measurement setup at ICube (Strasbourg university). P– power of incident light; PD1 – photodiode 1; PD2 – photodiode 2; TBS and RBS – transmittance and reflectance of the beam splitter, respectively;* P_{cell} *and* R_{cell} *– light power incident to PV cell and reflectance of PV cell, respectively;* I_{sc} *– measured short circuit current.*

However, the carriers at this stage may also recombine without contributing to the external circuit. Here, quantum efficiency is a powerful tool to assess quantitatively the amount of photons that are finally converted into collected charges. Two types of QE are often determined for solar cells. They are:

- The external quantum efficiency (EQE), which is the ratio of the number of collected charge carriers to the number of incident photons at short-circuit conditions.
- The internal quantum efficiency (IQE), which is the ratio of the number of collected charge carriers to the number of photons absorbed by the PV device at short-circuit conditions.

Figure 7.5 illustrates the EQE/IQE measurement setup scheme used in this work. In general, EQE is expressed as follows:

$$EQE = \frac{\text{Measured current A /elementary charge (C)}}{\text{Power of incident light}(W)/\ energy\ of\ a\ single\ photon\ (Eph)}$$

If we convert equation the above equation to what we measure with the setup depicted in Figure 7.5, we obtain:

$$EQE = \frac{I_{sc}}{q_e}\frac{hc}{P_{cell}\lambda} \qquad (7.3)$$

Keeping in mind the following:

$$IQE = \frac{EQE}{1-R_{cell}} \qquad (7.4)$$

We get an analytical expression for IQE as well:

$$IQE = \frac{I_{sc}}{q_e}\frac{hc}{P_{cell}\ (1-R_{cell})\lambda} \qquad (7.5)$$

where I_{sc} is measured current from the PV cell, q_e is elementary charge, P_{cell} is the light power received by the PV cell, R_{cell} is the reflectance estimated from the specularly reflected light intensity from the PV cell (recorded by PD2), h is Planck's constant, c is the velocity of light in vacuum and λ is wavelength.

7.1.3. Solar cell fabrication

➪ ***Thermal evaporation***

In thermal evaporation a crucible/boat containing a material is heated up by an intense electric current under high vacuum. When the appropriate pressure and temperature are reached, the material evaporates. Due to the high vacuum, the particles in the vapor can travel almost freely around the evaporation chamber. When they reach a colder surface, they condense onto it thus enabling the deposition of thin films. By varying the heating power of the crucible/boat, it is possible to control the deposition rate.

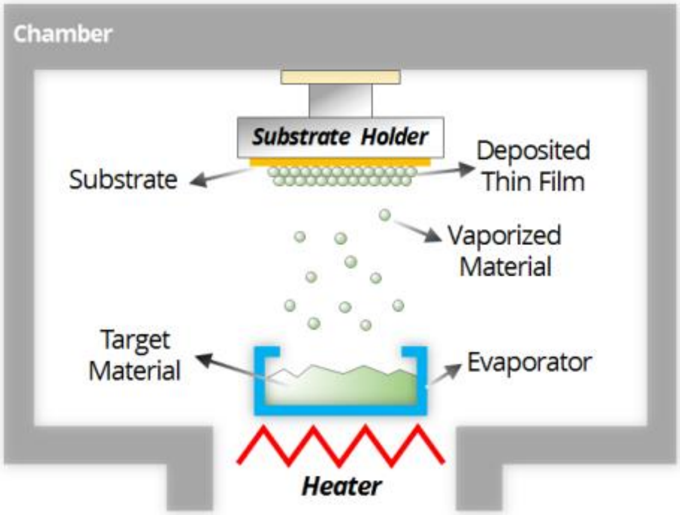

Figure 7.6: *Scheme of thermal evaporation deposition.*

➫ *Spin coater*

Spin coater is a common technique used to produce thin film coatings on flat substrates. For materials solar cell research it has found a particularly widespread use as it provides a quick and easy way to create uniform and thin films (Figure 7.6). As the name might allude to, spin-coating works by placing a solution of the coating material on a substrate and subsequently spinning it until a dry film has formed. The thickness of the resulting films can be adjusted by controlling a variety of parameters, such as the rotation speed.

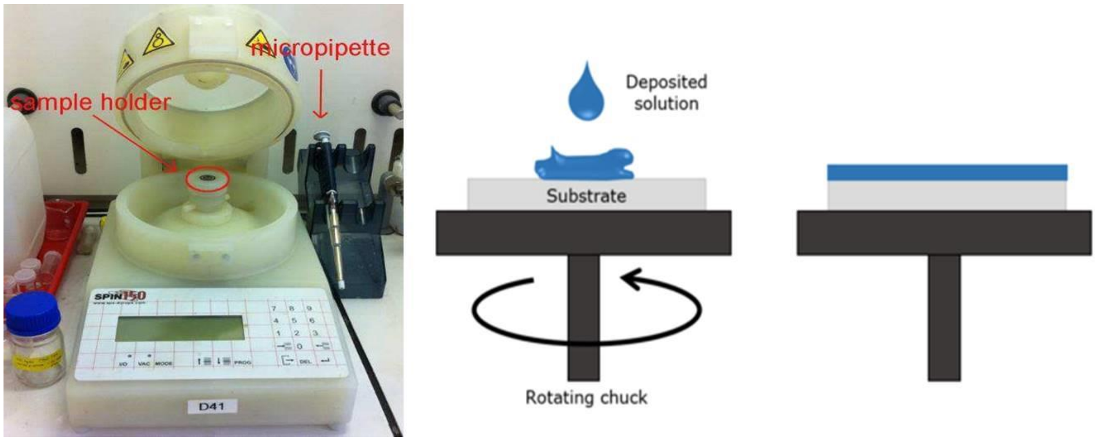

Figure 7.7: *image of spin coater technique (left) and schematic representation of the principle of spin coating process (right).*

➯ ***Glovebox***

In order to prevent the devices degradation, all organic solar cells elaborated in this work were carried out inside glovebox.

Figure 7.8: *Glovebox MB200B from MBraun with thermal evaporator, solar simulator and EQE techniques inside chamber.*

7.2. Solar cell fabrication procedure

7.2.1. Substrate cleaning

ITO coated glass substrates were cleaned at 45°C for 20 minutes for each step in ultrasonic bath in the following order: deionized water, acetone and 2-propanol. After that, UV/Ozone treatment has been performed for 30 min to remove residual organic contaminants.

7.2.2. Electron transporting layer deposition

In the present thesis, the attention will be focused on the effects of the ZnO and SnO_2 as electron transporting layers (ETLs). In this thesis, we used two type of electron transporting layer for inverted organic solar devices: ZnO and SnO_2.

The synthesized ZnO solution: was deposited by chemical way, which is spin coater, in this case the synthesis ZnO solution was coated onto clean ITO substrate with a speed of 2500 rpm for 30 s and annealed at 200° C for 30 min. for the SnO_2 was deposited by physical way using DC- magnetron sputtering with different thicknesses. The deposition time was varied to deposit different thicknesses of the SnO_2 layer: 10, 20, 30, 40 and 60 nm.

For the surface modifier layer polyethylenimine-ethoxylated (PEIE) preparation was spin coated on SnO_2 or ZnO ETLs with the following steps:

1. Preparation of PEIE solution diluted in 2-methoxyethanol (0.6% of PEIE by mass);
2. Spin-coating at 5000 rpm, with acceleration of 1000 rpm/s, during 60 sec;
3. Cleaning the PEIE with ethanol from part of the substrate (Figure 7.9);
4. Annealing of PEIE layer at 100°C for 15 minutes in nitrogen-filled ambient (glove box) to remove the residual solvent.

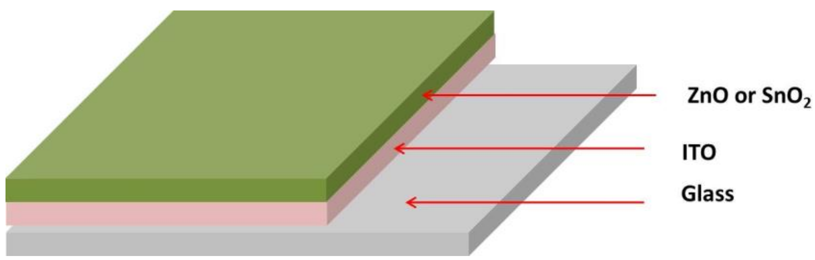

Figure 7.9: *Schematic view of interfacial layers coated on ITO after cleaning from one side.*

7.2.3. Photoactive layer deposition

The inverted organic solar cells developed in this thesis were fabricated using P3HT (98.5% regioregular, Sigma-Aldrich) as an electron donor and PC71BM (99.5%, Solenne B.V.) as an electron acceptor. The photo-active layer was prepared based on P3HT:PC71BM blend solution dispersed in 1 mL o-dichlorobenzene (99%, anhydrous, Sigma-Aldrich).

The photoactive layers were deposited onto the previous prepared films using a spin-coater with 1200 rpm for 60s and then annealed at 150 ◦C for 15 min.

7.2.4. Hole electron transporting and back contact layers deposition

In order to complete the photovoltaic devices, MoO_3 (7nm) and Ag (120 nm) were thermally evaporated in a vacuum of 1.10^{-6} Torr, acting as inverted device electrodes (Figure 7.10).

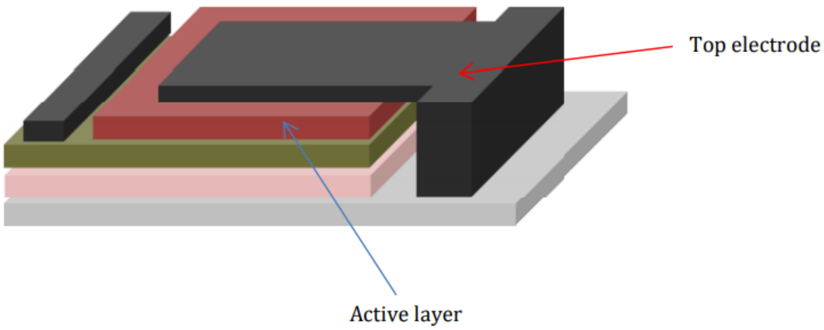

***Figure 7.10**: Schematic view of final photovoltaic device.*

8

Polyethylenimine-Ethoxylated Interfacial Layer for Efficient Electron Collection in SnO_2 Based Inverted Organic Solar Cells

8.1. Introduction

Third-generation photovoltaic technology based on conjugated polymers has drawn much attention over the past decade due to advantages such as simple preparation, light weight, low cost, solution-based fabrication on large-area and low-temperature solution process ability that allows for fabrication on flexible substrates via roll-to-roll manufacturing for solar energy conversion [266], [274]–[276]. Recently, efforts have been made to enhance power conversion efficiency (PCE) of organic solar cells (OSCs), reaching a power conversion efficiency above 15–17% [277], [278]. To do so, the research was focused on the development of device architecture [279]–[281], design semiconductor polymers and development of non-fullerene acceptors (e.g.,2,2′-[[6,6,12,12-Tetrakis(4-hexylphenyl)-6,12 dihydrodithieno[2,3-d:2′,3′-d′]-s-indaceno[1,2-b:5,6-b′]dithiophene-2,8diyl]bis[methylidyne(3-oxo1H-indene-2,1(3H)diylidene)]] bis[propanedinitrile]family (ITIC)) [249], [282], [283], control morphology [284], [285] and interfacial engineering between layer materials and the active layer that provides a powerful strategy to enhance both stability and efficiency of organic photovoltaic devices. Generally, the structure of OSCs could be classified into two categories, namely conventional and inverted structures; the conventional architecture is based on a bulk heterojunction active layer sandwiched between a transparent conducting electrode, such as indium tin oxide (ITO), and a low work function metal electrode (Ca/Al, LiF/Al or Al) [286]. On one hand, one of the major problems for the conventional structure is the long-term stability when exposed to air due to the use of a cathode that is sensitive to air and moisture, which leads to its rapid oxidation. On the other hand, poly(3,4 ethylenedioxythiophene):polystyrene sulfonic acid (PEDOT:PSS) has an acidic and hydrophilic nature [287], [288], which is detrimental to the active layer and can etch the ITO via the increase of the interfacial resistance through indium diffusion into the active layer; this leads to the deterioration of the device performance [289]–[291]. To overcome these issues, the inverted configuration is the appropriate solution to make PEDOT: PSS-free device, where the polarity of charge collection is opposite to that in the conventional one. Inverted organic solar cell (iOSC) configuration allows the use of high work function metal contact that is less air-sensitive, and a low work function metal oxide as electron transporting layer to modify the ITO surface.

Current researchers have used several methods to improve iOSC performance, including using a metal oxide layer as an electron transporting layer (ETL) between the active layer and the ITO cathode, which is indispensable so that ohmic contact for the decrease or elimination of the electron-extraction barrier can be formed. N-type metal oxides such as titanium oxide (TiO_x), zinc oxide (ZnO) and tin oxide (SnO_2) can be introduced as a cathode buffer layer (CBL) to modify ITO as an effective electron-collecting electrode in inverted OSCs [292]–[294].

In particular, tin dioxide (SnO_2) has recently received more attention as an interfacial material for organic photovoltaic (OPV) devices because of its beneficial properties, namely good optical transparency, high resistivity, high electron mobility, high transmittance in visible region and high chemical and thermal stabilities compared to other transparent conductive oxides [295], [296]. Several works have studied the effect of SnO_2 on the inverted organic solar cell performance [297], [298].

An efficiency of 4.05% was achieved by a Korean group using P3HT: PCBM absorber materials and aqueous solution processed SnO_2 combined with ionic liquid (IL) as a buffer layer. Besides this work, Shuai Huang et al. [299] deposited SnO_2 by a sol–gel process in a P3HT:PC71BM-based inverted solar cell, and they obtained an efficiency of 4.25%.

Nowadays, polyethylenimine-ethoxylated (PEIE) is used as an interlayer to reduce the electrode material's work function (WF). PEIE contains simple aliphatic amine groups that can produce surface dipoles; as a consequence, the WF of the ITO electrode decreases [300]–[302]. The created interfacial dipole induces a vacuum level shift, which effectively causes a reduction of the WF of the underlying electrode [303]–[306]. Recently, Courtright et al. [307] studied separately PEIE and PEI as the ETL for PBDTT-FTTE:PC70BM-based iOPVs on top of zinc oxide. They found that the incorporation of PEIE as a cathode buffer layer gave an enhancement of the cell performance with 7.37%. Using PEI, an efficiency of 8.22% was reached.

In the present study, the work is devoted to an inverted organic solar cell based on bulk heterojunction using poly (3-hexylthiophene-2,5-diyl):[6,6]-phenyl-C71-butryric acid methyl ester (P3HT:PCBM) as an absorber. The originality of our study is to overcome the limitations of the use of a single cathode buffer layer, using the cathode buffer bilayer tin dioxide (SnO_2) with PEIE. The SnO_2 layer was deposited by magnetron reactive sputtering with different thicknesses, and then PEIE thin film was deposited via an aqueous solution-process. It has been found that with the combination of SnO_2 and PEIE as a cathode buffer bilayer, the short circuit current density (J_{sc}) was obviously improved, resulting in better device performance with an efficiency reaching 2.84%, compared to reference devices with pure SnO_2 and PEIE as a cathode buffer layer.

8.2. Experimental detail

8.2.1. Thin Film Preparation

➭ ***<u>SnO_2 thin film deposition</u>***

The cleaning process of the pre-patterned ITO (sheet resistance 5–15 Ω, Lumtec) glass substrates was done in an ultrasonic bath successively in detergent, deionized water, acetone, 2-isopropanol and de-ionized water, then dried with nitrogen gas flow followed by UV-ozone treatment for 15 min. SnO_2 layers were deposited onto clean ITO at 200 °C by radio frequency (RF) reactive magnetron sputtering in a commercial sputtering system (Orion 3 device from AJA International Co.) using pure target of Sn (99.99%). The sputtering SnO_2 was done in an argon–oxygen gas mixture, with 8 sccm argon and 4 sccm oxygen. The sputtering parameters used in this work were optimized in a previous work [308], [309], and the deposition time was varied to deposit different thicknesses of the SnO_2 layer: 10, 20, 30, 40 and 60 nm.

➯ ***PEIE deposition***

PEIE (Mw = 70,000 g/mol, Sigma-Aldrich), an 80% ethoxylated-based solution, was prepared by diluting 0.2% by mass in 2-methoxyethanol (99.8%, Sigma-Aldrich), which was deposited onto ITO/SnO_2 substrates by a spin-coater at 1500 rpm for 60s. Afterward, a part of the PEIE was wiped away from the borders with ethanol. Then, the prepared structures were placed inside the nitrogen-filled glove box for further treatment and depositions to complete the device structure; the samples were annealed at 100 °C for 15 min before depositing the active layer.

➯ ***Organic solar cells fabrication***

Inverted organic solar cells (iOSCs) were fabricated using P3HT (98.5% regioregular, Sigma-Aldrich) as an electron donor and PC71BM (99.5%, Solenne B.V.) as an electron acceptor. The photo-active layer was prepared based on P3HT:PC71BM solution with a ratio of 1:0.7 dispersed in 1 mL o-dichlorobenzene (99%, anhydrous, Sigma-Aldrich). The absorber layer was deposited onto the previous prepared films using a spin-coater with 1200 rpm for 60s and then annealed at 150 °C for 15 min. Next, MoO_3 (7 nm) and Ag (120 nm) were thermally evaporated in a vacuum of 1.10^{-6} Torr, acting as inverted device electrodes. We fabricated a series of inverted PSC devices with various SnO_2 thicknesses of PEIE with the following structure: glass/ITO/SnO_2/P3HT: PCBM/MoO_3/Ag; another kind of device was also fabricated by incorporating an ultrathin PEIE layer with structure glass/ITO/ SnO_2/ PEIE/ P3HT: PCBM/MoO_3/Ag. The final architecture of the inverted device (ITO/SnO_2/PEIE/P3HT: PCBM/MoO_3/Ag) is illustrated in Figure 8.1(a); the device working area was about 0.12 cm^2.

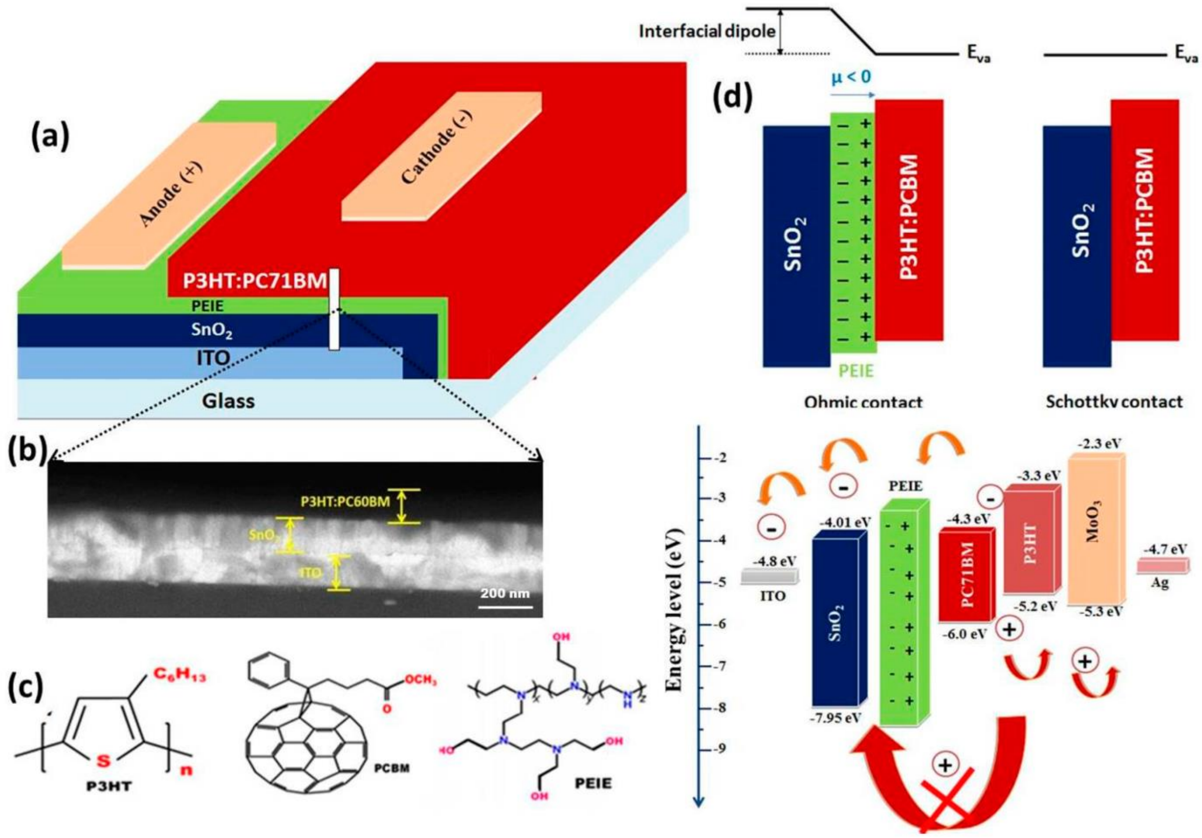

Figure 8.1: *(a) Schematic structure of the inverted hybrid solar cell. (b) Cross-sectional SEM figure of device used in this study. (c) Chemical structure of P3HT, PCBM and PEIE. (d) Energy level diagram of the inverted hybrid solar cells investigated in this work.*

8.2.2. Characterization set up

Structural, morphological and optical properties of the prepared films as well as the inverted devices were analyzed with different techniques. The films were analyzed by X-ray diffraction (XRD) and grazing incident X-ray diffraction (GIXRD) in the 20°–80° 2θ range by means of a Rigaku Smartlab® diffractometer (9 kW) equipped with a $CuK\alpha_1$ incident source (λ = 1.54056 Å) and a Ge (220) × 2-bounce front monochromator. Morphological analysis was carried out by scanning electron microscopy (SEM) on a Zeiss GEMINI 500 scanning electron microscope. A UV–Visible–NIR spectrophotometer (Perkin-Elmer Lambda 950) with an integrating sphere of 150 mm was used to obtain the transmission/absorption spectra of the films in the wavelength range of 200–1000 nm. Atomic force microscopy (AFM) images were obtained in tapping mode with a

Nanoscope Dimension 3100 from Veeco Instruments. Scanning electron microscopy (SEM) images were recorded by JEOL 6700F microscope. The resistivity, carrier concentration and Hall mobility of the SnO_2 films were determined by a Hall effect measurement system at room temperature using ECOPIA equipment (HMS-5500 Van der Pauw). The electrical characterizations of the inverted devices were done inside a glovebox under a nitrogen atmosphere; the current density–voltage (J–V) characteristics were measured with an HP Agilent source measurement unit, in dark and under illumination using a solar simulator with AM1.5G conditions (Oriel Xenon 150 W, model 96000), after calibration using a standard silicon solar cell with 100 mW/cm^2. The external quantum efficiency (EQE) was also measured inside the glovebox for the elaborated devices.

8.3. Results and discussions

8.3.1. Single Layer

➷ ***X-ray Diffraction Study***

The structural properties of SnO_2 and P3HT thin films are depicted in Figure 8.2. The XRD pattern of SnO_2 with 100 nm revealed peaks at 26.66°, 33.89°, 37.94°, 51.77° and 54.75° assigned respectively to planes (110), (101), (200), (211) and (220) of crystalline tin-dioxide tetragonal rutile structure with space group P42/mnm, which matched well with JCPDS card (Joint Committee on Powder Diffraction Standards) no 00-041-1445 and exhibited (101) plane as the preferred orientation. The XRD pattern of P3HT demonstrated a high crystalline structure, with peaks located at low angles 5.3°, 10.7° and 15.90°, which were attributed respectively to planes (100), (200) and (300), with a preferential orientation toward the (100) plane; these peaks were related to lamellar ordering of the phase separated structure by alkyl side chains [310], [311].

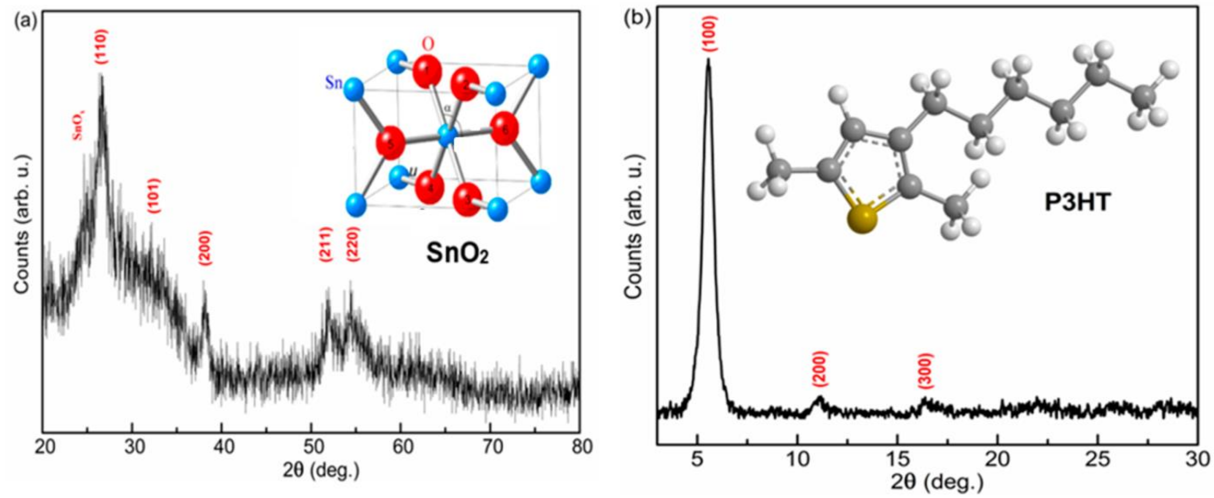

Figure 8.2*: X-ray diffraction patterns of (a) sputtered SnO_2 deposited on quartz substrate and (b) P3HT spin-coated on glass substrate.*

⇘ ***UV-Visible Study***

To investigate the transmittance of SnO_2 layers as well as photoactive layer absorption, a UV-visible study was conducted on our samples. Figure 8.3 (a) presents the absorption spectra of P3HT, PCBM and the P3HT: PCBM mixture. The conjugated polymer P3HT had a wide and strong absorption band in the range of 400–650 nm and revealed a maximum at ~550 nm. Nevertheless, PCBM presented a broad absorption in ultraviolet in the range of 300–575 nm with a maximum absorption at ~375 nm. One can see that the optical absorption spectra of P3HT:PCBM (1:0.7) based thin film exhibited a first absorption shoulder at 300–350 nm attributed to PCBM and a second dominant peak located at higher wavelengths corresponding to P3HT absorption. The peak at 450 nm (2.75 eV) corresponded to band-to-band transitions inferred from π–π* transitions from the highest occupied molecular orbital (HOMO) to the lowest unoccupied molecular orbital (LUMO) [312], and this peak was located at a lower photon energy of 2.25 eV for pure pristine P3HT films. The absorption shoulders located at ~600 nm (2.07 eV), ~550 nm (2.25 eV) and ~515 nm (2.41 eV) revealed the three absorption features (S_0, S_1, S_2) of P3HT excitonic absorption with Frenkel excitons absorption; these bands were the so-called vibronic absorption shoulders [313], [314]. The excitonic absorption S_0 at 600 nm indicated singlet exciton generation; the absorption S1 at 558 nm implied one exciton and one phonon generation. The peak S_2 at 509 nm revealed the beginning of one exciton and two phonons.

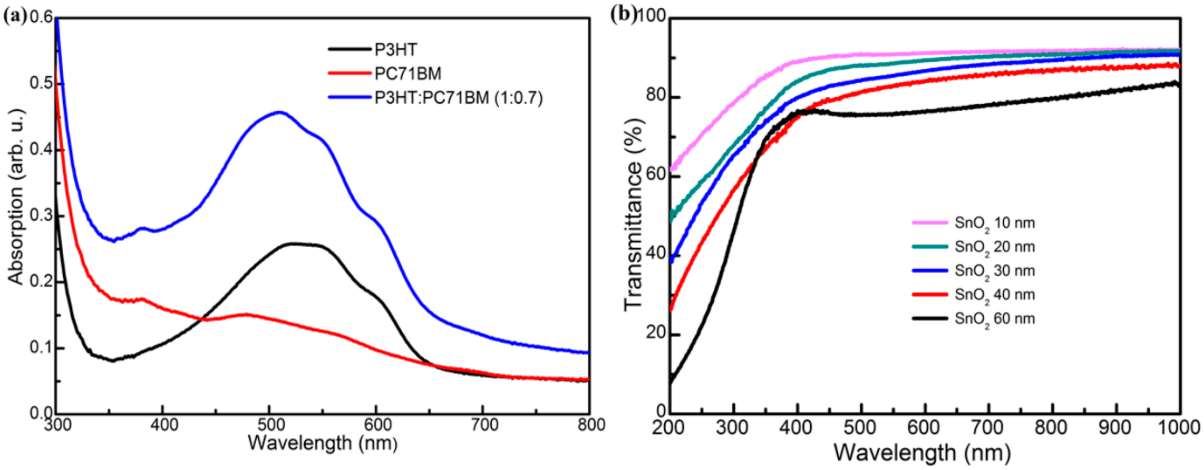

Figure 8.3: *(a) Absorption spectra of P3HT: PCBM deposited on glass substrate and (b) transmittance spectra of SnO_2 with different thicknesses deposited on quartz substrate.*

The optical transmittance spectra of SnO_2 thin films with different thicknesses were measured in the wavelength range of 200–1000 nm and are depicted in Figure 8.3 (b). One can noticed that, in the visible range 380–780 nm, the transmittance of the SnO_2 buffer layer was found to decrease gradually from 87 to 75.1% with increasing SnO_2 thickness from 10 to 60 nm. The average transmittance value of ~82% in the visible range was recorded for the prepared SnO_2 samples.

↳ ***SEM and AFM Micrographs***

In order to study the thickness effect on SnO_2 surface morphology and topography as well as the film's roughness, AFM and SEM images were recorded for different film thicknesses with and without PEIE on the ITO substrate, as illustrated in Figure 8.4.

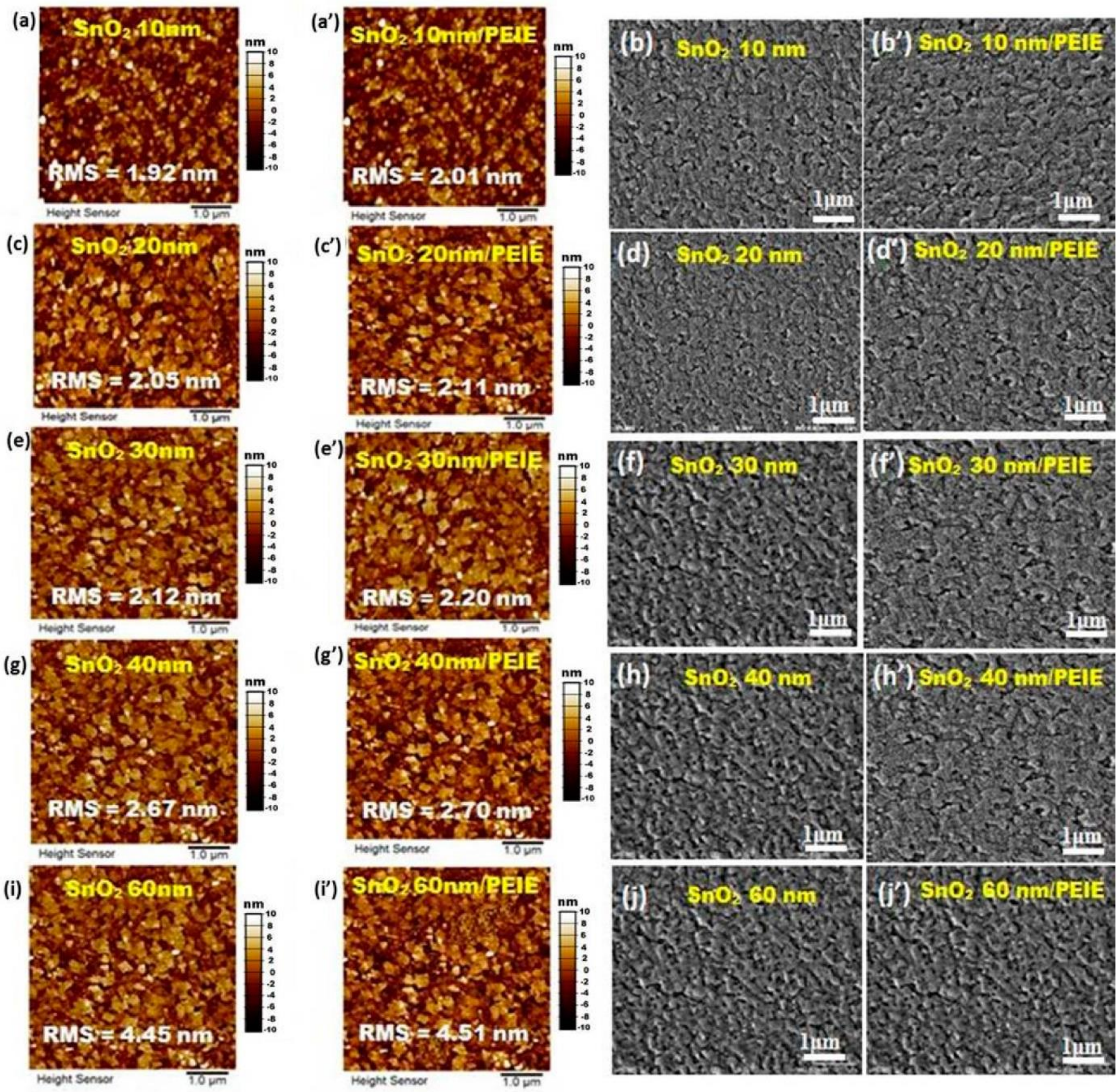

Figure 8.4: The 2D-AFM and SEM micrographs of sputtered SnO_2 without PEIE for 10 nm (a,b), 20 nm (c,d), 30 nm (e,f), 40 nm (g,h), 60 nm (i,j) and with PEIE coated on SnO_2 10 nm (a',b'), 20 nm (c',d'), 30 nm (e',f'), 40 nm (g',h') and 60 nm (i',j').

One can see that the SnO_2 film surface changed with thickness, and the surface morphology was rather homogeneous with surface RMS roughness (root mean square roughness) of 1.92, 2.05, 2.12, 2.67 and 4.45 nm, with an approximate error of 1%, for SnO_2 films with thicknesses of 10, 20, 30, 40 and 60 nm, respectively without an ultrathin layer of PEIE. As can be seen from the AFM and SEM micrographs images, continuous films were formed on ITO substrates, and the nucleation process was completed and nucleus growth had already preceded. After PEIE deposition onto SnO_2, AFM and SEM micrographs showed no agglomeration of PEIE on the surface and no significant changes compared to samples without PEIE.

⇘ *Hall Effect Study*

Hall effect measurement was performed to investigate electrical properties of SnO_2 films with different thicknesses. The obtained parameters of bulk concentration (n), resistivity (ϱ) and mobility (μ) are listed in Table 8.1. The electrical properties confirmed the n-type character of SnO_2; moreover, the resistivity increased with SnO_2 thickness, and the charge carrier concentration varied with the thickness and presented a maximum value at 20 nm.

Table 8.1:*Hall effect measurements of sputtered SnO_2 deposited on quartz.*

Samples	n (10^{20} cm^{-3})	ρ (10^{-3}Ω. cm)	μ (cm^2/V.s)
10 nm	- 1.83 ± 0.03	1.87 ± 0.02	4.72 ± 0.02
20 nm	- 2.62 ± 0.02	1.78 ± 0.03	11.12 ± 0.02
30 nm	- 2.13 ± 0.04	5.54 ± 0.02	4.70 ± 0.03
40 nm	- 2.15 ± 0.03	6.24 ± 0.04	4.30 ± 0.02
60 nm	- 1.78 ± 0.02	8.33 ± 0.02	4.20 ± 0.03

8.3.2. Solar Cell Device Characterizations

⇘ *XRD and GIXRD Study*

The effect of PEIE at the SnO_2/P3HT: PCBM interface was investigated through various structural, optical and electrical analyses in order to understand the buffer bilayer effect on inverted solar cell performance. XRD and GIXRD patterns of the prepared solar cells were based on the following structure: glass/ITO/SnO_2/PEIE/P3HT: PCBM, as depicted in Figure 8.5 (a) and (b). Figure 8.5 (a) reports the XRD patterns of the prepared solar cells with different SnO_2 thicknesses (10, 20, 30, 40, and 60 nm). One can notice that the patterns demonstrated diffraction peaks corresponding to ITO, SnO_2 and P3HT, suggesting a well-defined crystal structure of these materials.

Diffraction peaks identifying polycrystalline structure of ITO were attributed to (211), (400) and (411) planes. Comparing the P3HT:PCBM blend diffractograms with that of pure P3HT (Figure 8.2), it was evidenced that the blend was characterized by (100), (200) and (300), which were attributed to the P3HT crystalline structure; the diffraction peak (100) at $2\theta = 5.3°$ corresponded to the interchain spacing of 16.32 Å associated with inter-digitated alkyl [314]. The SnO_2 diffraction pattern was dominated by the (110) peak positioned at 2θ~26.52° regardless of the SnO_2 thickness. This peak, for all prepared devices with different SnO_2 thicknesses, was an indication of the well-textured growth of SnO_2 by sputtering [315].

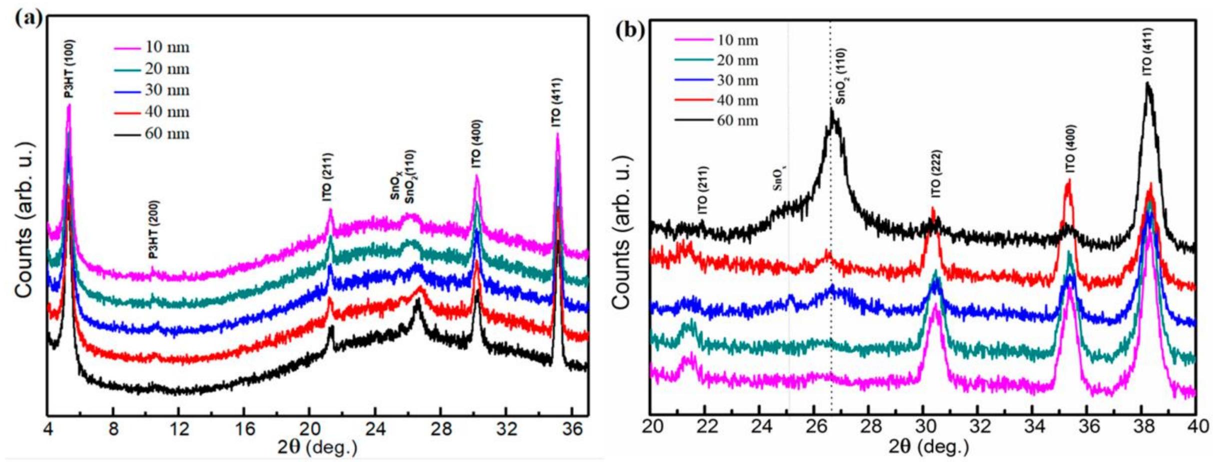

Figure 8.5:*XRD (a) and GIXRD (b) patterns of all device glass/ITO/SnO_2/PEIE/P3HT: PCBM/MoO_3/Ag structures with different thicknesses of SnO_2 (10, 20, 30, 40 and 60 nm).*

The elaborated devices were characterized by XRD and GIRXD using an incident angle of 0.5° (Figure 8.5 (b)) to localize all the peaks attributed to SnO_2; the main peak of the latter was positioned at 2θ~26.52° and was attributed to the (110) plane; these patterns exhibited another weak peak at 2θ~25° that belonged to the SnO_x orthorhombic phase (in accordance with JCPDS card no. 00-013-0111). Moreover, the GIXRD patterns revealed an increase in the peak intensity corresponding to the SnO_2 tetragonal phase by increasing SnO_2 thickness from 10 to 60 nm, which became sharper with a slight shift with respect to the JCPDS card; therefore, the crystallinity improved as well. This indicates that SnO_2 surface morphology depends on SnO_2 thickness, which was also proven by SEM and AFM images.

↳ *J–V Characterization and EQE Measurements*

The metrics parameters of the elaborated inverted organic solar cells with and without PEIE were extracted from the current density–voltage (J–V) characteristics under illumination using AM1.5G with an irradiance of 100 mW/cm^2. The determined parameters are summarized in Table 8.2, displaying short-circuit current density (J_{SC}), open-circuit voltage (V_{OC}), fill factor (FF) and power conversion efficiency (PCE).

Table 8.2: *Characteristics of P3HT: PCBM-based bulk heterojunction devices with different electron transporting layer.*

ETLs	Thickness of SnO_2 (nm)	J_{SC}* (mA/cm^2)	V_{OC}* (V)	FF* (%)	PCE* (%)
SnO_2	20	1.25± 0.10	0.22± 0.05	30.0± 0.9	0.08± 0.10
PEIE	-	6.25± 0.09	0.55± 0.01	55.8± 0.4	1.91± 0.07
	10	7.08± 0.02	0.56± 0.01	63.1± 0.8	2.50± 0.07
	20	7.86± 0.05	0.57± 0.02	63.5± 0.5	2.84± 0.04
SnO_2/PEIE	30	6.55± 0.01	0.56± 0.01	66.6± 0.6	2.44± 0.04
	40	6.54± 0.02	0.56± 0.01	66.3± 0.6	2.42± 0.06
	60	5.60± 0.01	0.55± 0.03	42.8± 0.7	1.31± 0.02

* The averaged values were calculated from 8 solar cells.

The J–V characteristics of glass/ITO/SnO_2/P3HT: PCBM/MoO_3/Ag inverted solar cells based on SnO_2 exhibited lower efficiencies (see Figure 8.6 (a)). These low efficiencies were due to the high work function (WF) of SnO_2 that prevented charge carrier mobility, which interrupted charge transfer from the active layer to SnO_2 and/or charge trapping by interfacial ITO/SnO_2 and SnO_2/P3HT: PCBM. In order to enhance the performance of these devices, the surface modifier PEIE was introduced on top of SnO_2 to elaborate a cathode bilayer device with the configuration ITO/SnO_2/PEIE/P3HT:PCBM/MoO_3/Ag while maintaining a constant thickness of PEIE (≈ 10 nm) and changing SnO_2 thickness (10, 20, 30, 40 and 60 nm).

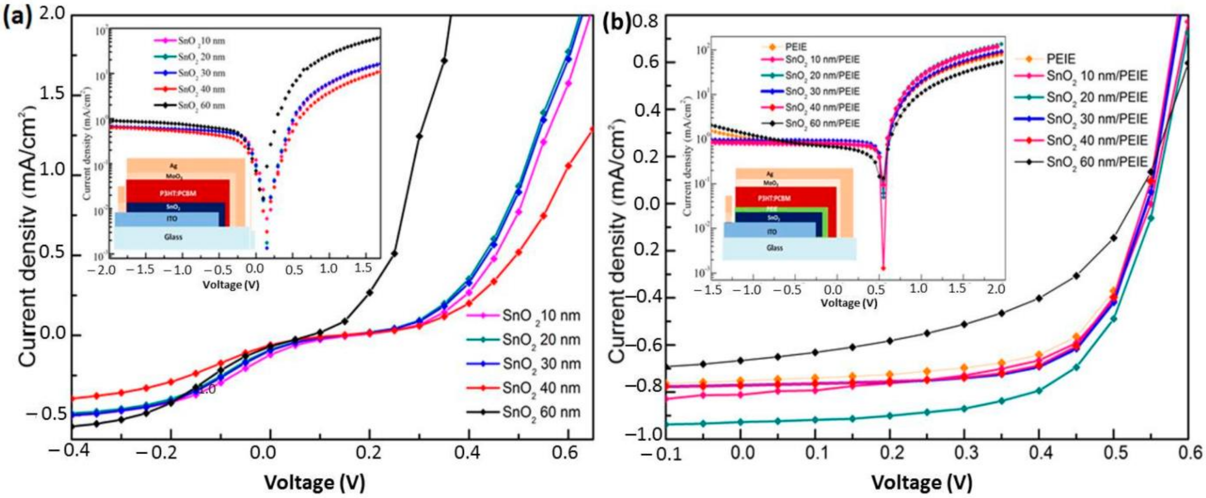

Figure 8.6:*J–V characteristics of glass/ITO/SnO_2/P3HT:PCBM/MoO_3/Ag (a) and glass/ITO/ SnO_2/ PEIE /P3HT: PCBM/MoO_3/Ag; (b) devices with different thicknesses of SnO_2 (10, 20, 30, 40, 60 nm).*

The J–V characteristics for the elaborated devices with and without PEIE are depicted in Figure 8.6. The inverted organic solar cells with an SnO_2/PEIE cathode bilayer demonstrated better performance compared to those without PEIE; the device with 20 nm thickness of SnO_2 showed the highest performance with a short-circuit current density J_{SC} = 7.86 mA/cm^2, an open-circuit voltage Voc = 570 mV, a fill factor FF = 63.5% and a power conversion efficiency PCE = 2.84%. The use of SnO_2/PEIE as a cathode bilayer increased the device parameters compared to those obtained for devices with a single PEIE or SnO_2 cathode layer only; the extracted photovoltaic parameters of the elaborated cells are presented in Table 8.2.

The incorporation of the PEIE layer improved the interface quality as well as enhanced charge collection ability, which revealed an improvement of the photovoltaic performance [29], [316].

The difference in device performance, with different electron transport layers, was mostly due to the increase or decrease in the short circuit current densities, which were consistent with external quantum efficiency (EQE) measurements.

The EQE is defined as number of charges (N_e) extracted at the electrodes divided by the number of photons (N_{ph}) of a certain incident wavelength on the solar cell.

$$EQE = \frac{N_e}{N_{ph}(\lambda)} \tag{8.1}$$

The external quantum efficiency and internal quantum efficiency spectra of the best 20 nm device of SnO_2 with/without the PEIE layer are depicted in Figure 8.7 (a) and (b). These spectra exhibited broad and high spectral responses ranging from 400 to 600 nm. The best device with SnO_2 (20 nm)/PEIE exhibited a maximum of 60% and 64% for EQE and IQE, respectively, around 550 nm. The device with only SnO_2 showed maxima of 55% and 53% for EQE and IQE, respectively, around 550 nm. The best performing device with combined layers of SnO_2 (20 nm) and PEIE was attributed to the well-aligned dipoles of PEIE on top of the SnO_2 layer.

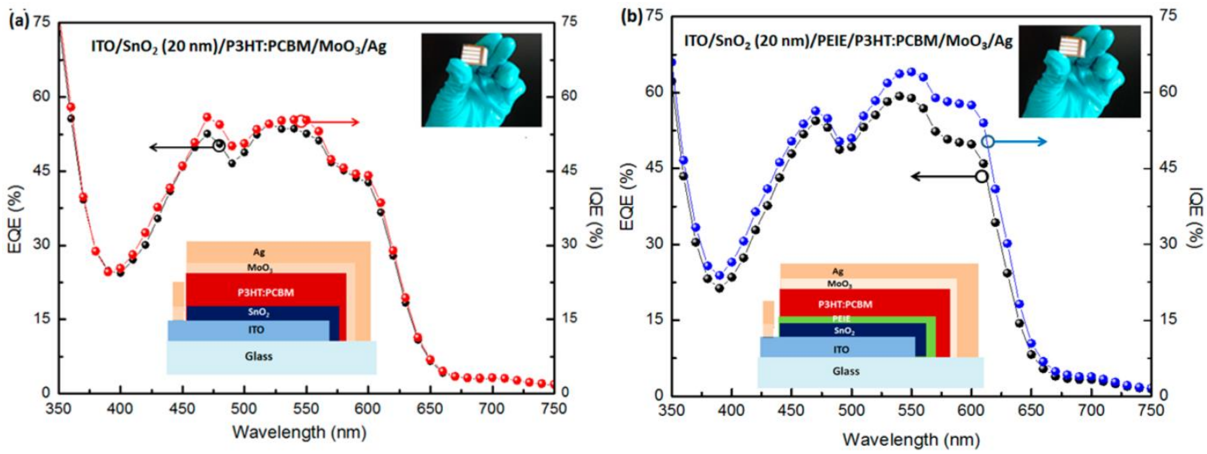

Figure 8.7: *EQE and IQE curve of (a) the device with only-SnO_2 (20 nm) and (b) best cell based on glass/ITO/SnO_2 20 nm)/PEIE ETL.*

8.4. Conclusions

In this chapter, we demonstrated an efficiency enhancement of inverted organic solar cells based on heterojunction by combining aqueous solution processed PEIE and sputtered SnO_2 as a cathode buffer bilayer by overcoming the limitations using a single cathode buffer layer and tuning the work function of ITO. The PEIE surface modifier within the sputtered SnO_2 layer is a promising alternative buffer bilayer to maximize the percolation of electron charge carriers by the formation of a thin interfacial dipole between the electron-transporting layer ITO/SnO_2 and the LUMO of PCBM. This facilitates electron transport to the electrode by lowering the energy barrier between the active layer and the ITO/SnO_2 interface, and by suppressing trap-assisted recombination, as well as improving the wettability between these layers, which leads to increases in the short-circuit current density and the fill factor. The optimization of SnO_2 deposition parameters led to a highly efficient device using the following structure: ITO/SnO_2 (20nm)/PEIE/P3HT: PCBM/MoO_3/Ag. An increase from 0.08% for a single buffer layer up to 2.84% using the SnO_2 (20 nm)/PEIE cathode buffer bilayer was obtained.

9

Tailoring PEIE capped ZnO binary cathode for solution-processed inverted organic solar cells

9.1. Introduction

Over past few years, solution-processed based polymer solar cells have attracted considerable attention because of their broad advantages, including low cost, mechanical flexibility and large-area fabrication compatibility with roll-to-roll process [317]–[320]. Recently, the research in polymer solar cells (PSCs) has led to incredible advances in power conversion efficiency (PCE), with efficiencies for single-junction devices over 15–16% [321]–[326] and over 17% for multi-junction devices [326]. Generally, it is well known that PSCs structure can be classified into two major configurations: conventional and inverted device architectures. The inverted structure has been broadly used due to its long-term stability and light-harvesting capability. The light window of organic solar cells (e.g. indium tin oxide, (ITO) is modified by electron transporting layer (ETL) with low work function (WF). The insertion of proper ETLs plays a vital role to promote the derived organic device performance [327], [328].

The metal oxide semiconductors are broadly deposited onto the ITO electrode like titanium oxide (TiO_x), tin dioxide (SnO_2) and zinc oxide (ZnO) [329]–[332]. Specifically, ZnO gained popularity due to its beneficial properties such as simple solution process, high optical transparency, high electron mobility, low-cost, and environment-friendly nature [333]–[335].

The polymer solar cell was influenced by unfavorable interfacial contact due to its high hydrophilicity feature [333]. In this context, it is very essential to take some alternatives to solve these problems. The surface modifier e.g. polyethylenimine-ethoxylated (PEIE) was used as an effective solution to improve the interface properties in plastic solar cells.

The non-conjugated surface modifier PEIE contains aliphatic amine groups, which are able to create a strong dipoles on the surface, as consequence, the work function of the ITO is decreasing [302], [336]. The incorporation of PEIE can decrease the WF of the electrode by the following mechanisms: (i) the amine groups adsorb to the surface of the underlying electrode; (ii) the creation of an interfacial dipole on the electrode surface (iii) the creation of a vacuum level shift by the interfacial dipoles [307], [331], [337].

Table 9.1 summarizes a collection of some successful challenges introducing PEIE ultrathin layer in polymer solar cells.

Table 9.1 :*Summary of metric parameters of record i-PSCs devices introducing PEIE interlayer.*

Configuration	Eff. (%)	FF (%)	J_{SC} (mA/cm^2)	V_{OC} (V)	Comments	Ref
ITO/ZnO:PEIE/PTB7Th:PC71BM/MoO_3/Al	9.47	70.44	17.23	0.78	PEIE doped ZnO	[338]
ITO/ZnO/PEIE/PTB7:PC70BM/MoO_3/Au	5.88	66.0	12.6	0.71	--	[339]
ITO/ZnO/PEIE/P3HT:PCBM/MoO_3/Ag	3.96	63.8	10.33	0.59	Synthesis ZnO particles was dispersed in MeOH	[340]
ITO/ZnO:PEIE/P3HT:PCBM/MoO_3/Ag	3.52	63.4	8.95	0.62	PEIE doped ZnO (0.1%)	[341]
ITO/ZnO:PEIE/ PTB7:PCBM /MoO_3/Ag	10.6	68.0	15.4	0.78	PEIE doped ZnO (0.1%)	[341]
ITO/ZnO:PEI/ PTB7:PCBM /MoO_3/Ag	9.31	72.70	17.15	0.74	ZnO doped PEI (0.12 mg/mL)	[342]
ITO/ ZnO/PEIE/P3HT:PC61BM/MoO_3/Ag	4.04	63.83	9.81	0.65	PEIE dissolved in 2-methoxy ethanol (0.2 wt% PEIE)	[343]
ITO/ ZnO/PEIE/ PTB7: PC61BM/MoO_3/Ag	8.12	66.0	16.48	0.75	PEIE dissolved in 2-methoxy ethanol (0.2 wt% PEIE)	[343]
ITO/ ZnO/PEIE/ PTB7: PC71BM/MoO_3/Ag	8.86	70.78	16.98	0.74	ZnO nano-ridged structures (ZnO-R)	[301]
ITO/ZnO/PEI/ PBDTT FTTE:PC70BM/MoO_3/Ag	8.22	64.0	16.25	0.78	ITO/ZnO/PEI (WF=2.97eV)	[307]
ITO/ZnO/PEIE/P3HT:PC71BM/MnO_3/Ag	**4.48**	**61.21**	**12.02**	**0.61**	**This work**	*

Several works have studied the effect of PEIE and ZnO CBLs on the inverted organic solar cells performance (Table 9.1), an efficiency of 3.53% of the device based on P3HT: PCBM was achieved by Yu et al. [341] using aqueous solution-processed ZnO : PEIE (0.1 wt% PEIE), and besides this work, Li et al. [340] have studied PEIE capped ZnO as ETL for P3HT:PC61BM based i-PSCs. They prove that the insertion of PEIE capped ZnO as

ETL leads to an enhancement of the device performance with 3.96%. Inspired by these works, we investigated the low-temperature cathode buffer bilayer using the solution processed ZnO and PEIE in i-PSCs based on P3HT: PC61BM.

In this chapter, we evaluated the CBL performance of ZnO/PEIE by elaborating inverted organic devices based on poly (3-hexylthiophene-2,5-diyl):[6,6]-phenyl-C71-butyric acid methyl ester (P3HT: PC71BM). We fabricated a sequence of devices using ZnO with different molecular ratios as a cathode buffer layer and PEIE interlayer as surface modifier. The effect of PEIE interlayer on the ZnO morphology and on i-PSCs performance was investigated. The schematic illustration of inverted organic device and energy diagram of the relevant materials are depicted in Figure 9.1.

9.2. Experimental detail

9.2.1. ZnO NPs Synthesis

The zinc acetate dehydrate precursor (Zn $(CH_3COO)_2{\cdot}2H_2O$, Aldrich, 99.5%)) was dissolved in a blend of 2-methoxyethanol ($CH_3OCH_2CH_2OH$, Aldrich, 99.3%) and ethanolamine ($NH_2CH_2CH_2OH$, Aldrich, 99%). The molar ratio of zinc acetate dehydrate (ZAD) to ethanolamine (MEA) was 1:2, 1:1 and 0.8. The solution was kept at 80°C for 1h with continuous stirring. The prepared solutions were keeped in the fridge and then filtered by 0.2 μm polytetrafluoroethylene (PTFE) before use.

9.2.2. Organic solar cells fabrication

➢ ***<u>ZnO buffer layer deposition</u>***

First, the ITO (sheet resistance 5-15Ω, Lumtec) substrates were cleaned by continual sonification in aqueous solution of detergent, deionised water, acetone and 2-isopropanol for 15 min each solvent, followed by UV-ozone treatment for 10 min to eliminate contaminants from the surface. The synthesized solution ZnO was coated onto cleaned ITO substrates with a speed of 2500 rpm for 30 s and annealed at 200° C for 30 min.

↳ ***PEIE ultrathin layer preparation***

Polyethylenimine, 80% ethoxylated (Mw = 70,000 g/mol, Sigma-Aldrich), was prepared by diluting 0.6% by mass in 2-methoxyethanol (99.8%, Sigma-Aldrich). The solution was spin-coated onto ITO/ZnO substrates at a speed of 5000 rpm for 60s. Then, the prepared structures were placed inside the nitrogen-filled glove box for further treatment and depositions to complete the device structure; the thin films were annealed at 100 °C for 15 min before depositing the active layer.

↳ ***Photovoltaic device fabrication***

The photoactive layer comprising poly(3-hexylthiophene) (P3HT) and [6,6]-phenyl-C71-butyric acid methyl ester (PC71BM) at a weight ratio of 1:1 was coated from a solution of 1,2-dicholorobenzene onto ZnO thin films. After that, the prepared organic thin films were annealed at 150 °C for 10 min. Finally, the solar cells were completed by thermal evaporation of 7 nm of MoO_3 followed by 100 nm of Ag. The prepared devices, with various molar ratios of ZnO layer, are presented as follows: ITO/ZnO/P3HT:PCBM/ MoO_3/Ag, additional series of devices were performed by insertion of PEIE interlayer with the following structure ITO/ZnO/PEIE/ P3HT:PCBM/ MoO_3/Ag.

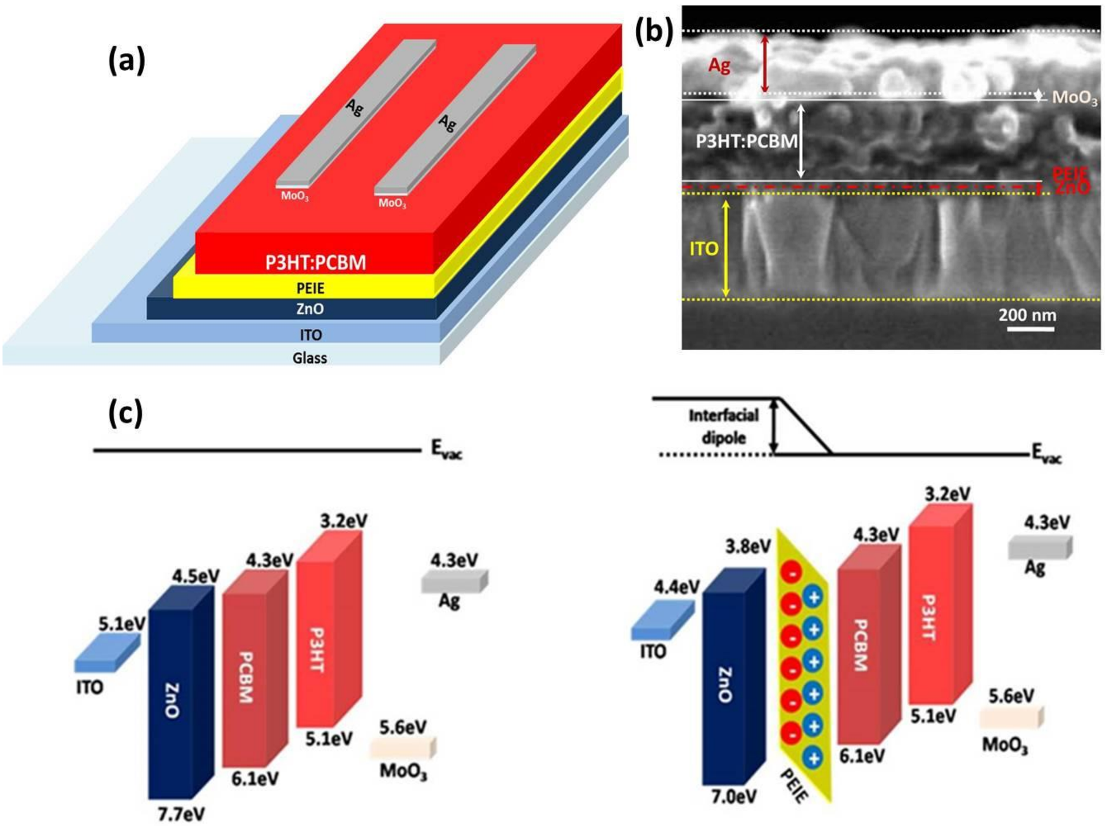

Figure 9.1:*(a) Schematic illustration of the inverted polymer solar cell (b) SEM cross-section image (c) and energy level diagram of the i-PSC investigated in this work.*

The schematic of device architecture and the energy band diagram are shown in Figure 9.1. The i-PSCs were fabricated on ITO coated glass substrates with the following structure of ITO/CBLs/P3HT: PCBM/MoO_3/Ag. The conduction band of ZnO is -4.5eV and a valence band energy of -7.7eV [339], which suggests that electrons come from the P3HT:PCBM could be transported into ZnO, however holes from P3HT:PCBM could be blocked. The PEIE layer produces interfacial dipole between ZnO and P3HT:PCBM interface, leading to reduce the work function of ZnO (from 4.5 to 3.8 eV) and that of ITO (from 5.1 to 4.1 eV) [344].

9.2.3. *Electrostatic Self-Assembly of non-conjugated polymer PEIE*

The functional amines of non-conjugated polymer PEIE layer can be partially protonated by accepting the positively charges H^+ (protons) detached from the H_2O, which makes PEIE reveals the cationic characteristics [337]. The direct contact between PEIE interlayer and the hydroxyl terminated ZnO occurred the electrostatic self-assembly as demonstrated in the schematic illustration presented in figure 9.2. The negatively charged terminal oxygen O^- (ions) of the ZnO surface combined with the protonated amines (H^+) of the cationic PEIE. After the annealing of PEIE interlayer, at 100 °C for 10 min, the dissociated hydroxide (OH^-) from water inter-connected with protonated amines will rejoin the H^+ of the hydroxide on ZnO surface, and then removed in the form of H_2O [304], [345]**.** The created electrostatic interaction instantly makes a strong interfacial dipole at PEIE/ZnO interface.

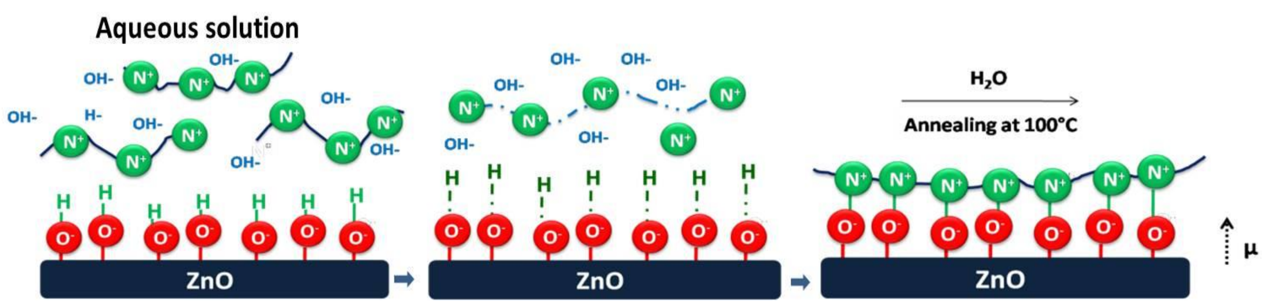

Figure 9.2: *The electrostatic self-assembly of PEIE on ZnO surface.*

9.2.4. Characterization

The UV–vis absorption and transmission spectra of organic and inorganic thin films were measured using a UV–Visible spectrophotometer (Perkin-Elmer Lambda 950). The cross-sectional image of a complete iPSC device was obtained from a scanning electron microscopy (SEM) system (4700 and S4800). The surface morphologies of thin films were carried out by Atomic Force Microscopy (AFM) with a Nanoscope Dimension 3100 from

Veeco Instruments. The devices performance were measured under AM 1.5G solar simulator inside nitrogen-filled glove box, the current–voltage (I–V) measurements were conducted by Keithley 2400 with 100 mW/cm² (AM 1.5G) simulated sunlight from a Newport solar simulator. The External Quantum Efficiency (EQE) measurements were also performed for the elaborated devices.

9.3. Results and discussions

The electron selective layer based inverted polymer solar cell should have good transmittance so that light can pass through to the absorber material. Figure 9.3 (a) shows the transmission spectra of ZnO thin films with molar ratios of ZAD to MEA set at 1:0.8, 1:1, and 1:2 coated on ITO substrates. The optical transmittance reveals that all the ZnO thin layers presented high transmittance (>82%) over the visible wavelength range. In organic materials (Figure 9.3 (b)), the P3HT: PCBM presented a wide absorption in the range of 400–650 nm with a maximum at ~540 nm, while the maximum absorption peak of P3HT was ~ 550 nm. Moreover, the PCBM acceptor presents a broad absorption in the range of 300–575 nm and reveals a maximum absorption at ~ 375 nm region (Figur 9.3 (b)).

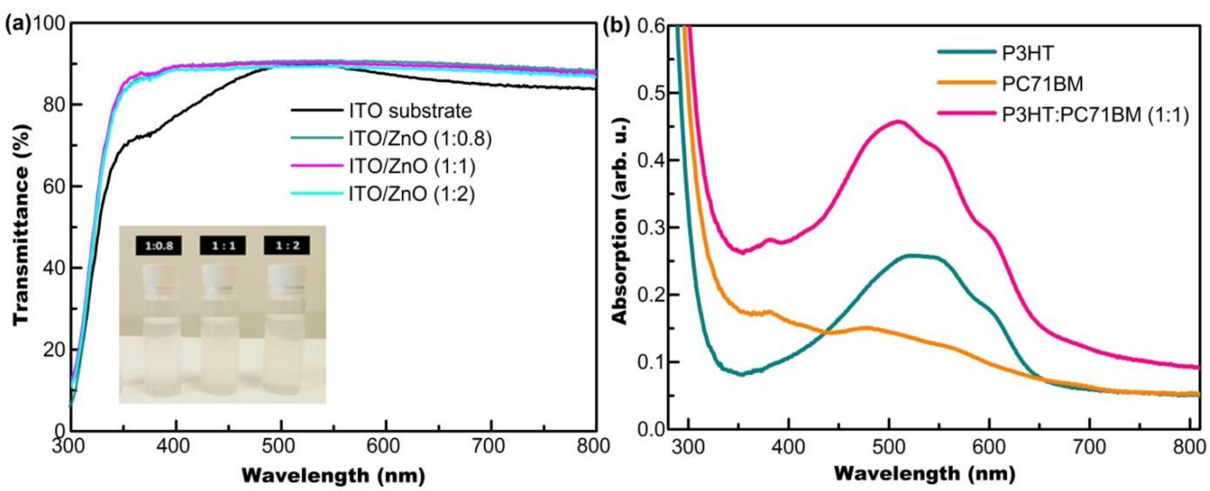

Figure 9.3: *Transmittance spectra of ZnO with different ratio (a), and the absorption spectra of PC71BM, P3HT and P3HT: PC71BM (b).*

The J-V curves measurements for the inverted solar cells with different CBLs are demonstrated in Figure 9.4 ((a), (b) and (c)). The corresponding performance parameters based devices are summarized in Table 9.2. Noticeably, the photovoltaic performance of devices is enhanced after the PEIE interlayer was inserted with the CBL. As for the devices with the ZnO ETLs pristine (control devices), the performance was dependent on the molar ratios of ZnO to MEA. As shown in Table 9.2, the efficiencies of the reference devices, first, increased and then decreased with enhancing MEA ratio. The PCE of reference device with ZnO (1:1) exhibits an average J_{SC} of 10.38 mA/ cm^2, an open voltage (V_{OC}) of 0.59 V, fill factor (FF) of 60.01%, and a PCE of 3.67%. Obviously, the quality of ZnO layer plays a vital function in extracting and transporting the generated electron and servers as a hole-blocking layer, and consequently influences the FF and J_{SC}. From these results, further enhancing MEA ratio would decrease the device performance, which can partially be attributed to the incomplete nucleation of ZnO matrix and/or the presence of pinholes on the ZnO surface, leading to serious issues in carrier recombination and hence lowering the current density (J_{SC}) in the devices. Nevertheless, when an ultrathin layer of PEIE was incorporated between the ZnO and P3HT:PCBM, the FF and J_{SC} were enhanced, leading to a significant improvement in the efficiency. It is observed from the obtained results that the device based PEIE CBL shows a significant increase with maximum PCE of 4.48%, a V_{OC} of 610 mV, a FF of 61.21% and a J_{SC} of 12.02 mA/cm^2. Nevertheless, when PEIE was introduced between the photoactive layer and the ZnO (PEIE/ZnO CBL), the device performance was breakdown, which leads to a remarkable low efficiency, with a PCE of 1.55 %, a V_{OC} of 470 mV, a FF of 35.83% and J_{SC} of 9.23 mA/cm^2.

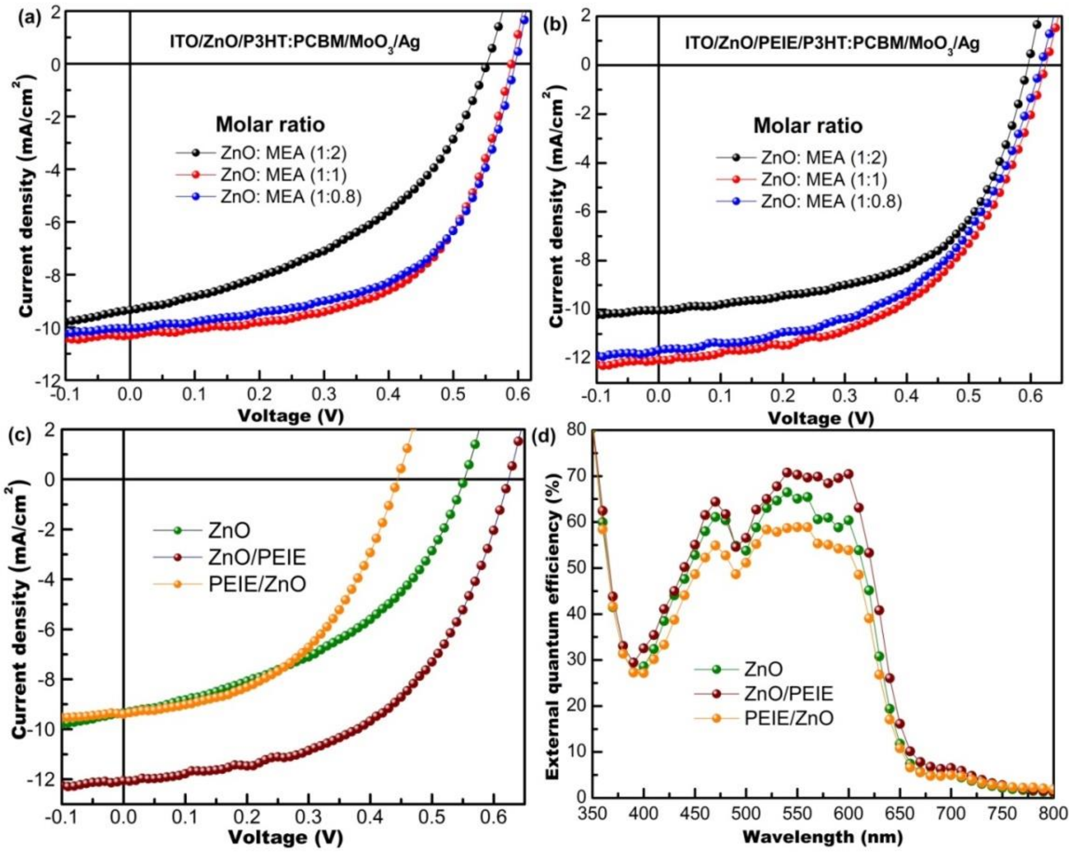

Figure 9.4: *J-V characteristics under simulated AM 1.5G illumination (100 mW/cm²) of the elaborated devices with different molar ratio of ZnO:MEA for structures: (a) ITO/ZnO/P3HT:PCBM/MoO₃/Ag based i-PSCs, (b) ITO/ZnO/PEIE/P3HT:PCBM/MoO₃/Ag based i-PSCs, , (c) J-V characteristics under simulated AM 1.5G illumination (100 mW/cm²) of the devices prepared with ZnO: MEA (1:1) using various CBLs (ZnO, ZnO/PEIE, PEIE/ZnO) and (d) the corresponding EQE spectra of the i-PSCs based devices with ZnO, ZnO/PEIE and PEIE/ZnO used as CBLs.*

The performance improvement should be obviously ascribed to the improved between the absorber and CBL layers. The incorporation of ultrathin PEIE interlayer improved the interface properties and increased the charge collection ability in the device.

The external quantum efficiency spectra of the elaborated cells with different CBLs are depicted in Figure 9.4(d). Compared to the devices with ZnO and PEIE/ZnO, the device with ZnO/PEIE CBL revealed a wide and high EQE ranging from 350 to 700 nm, consistent with J-V measurements. This significant improvement could be produced by the well contact between the active layer (P3HT: PCBM) and ZnO/PEIE CBL, which can facilitate the electrons percolation and block the holes from P3HT:PCBM to ITO.

Table 9.2: *Photovoltaic parameters recorded for P3HT:PCBM-iPSC based on ZnO, ZnO/PEIE and PEIE/ZnO CBLs with different molar ratios of ZnO.*

CBLs	Molar ratio ZnO to MEA	J_{SC}* (mA/cm^2)	Voc* (V)	FF* (%)	PCE* (%)
ZnO	1:2	9.29±0.02	0.55±0.05	51.18±0.17	2.61±0.01
	1:1	10.38±0.04	0.59±0.07	60.01±0.66	3.67±0.02
	1.08	10.03±0.02	0.60±0.06	59.73±0.22	3.59±0.02
ZnO/PEIE	1:2	10.01±0.07	0.60±0.02	54.12±0.20	3.25±0.01
	1:1	12.02±0.03	0.61±0.01	61.21±0.31	4.48±0.02
	1.08	11.54±0.01	0.61±0.03	60.78±0.52	4.27±0.02
PEIE/ZnO	1:1	9.23±0.02	0.47±0.06	35.83±0.72	1.55±0.05

**** The averaged PCEs were calculated from 8 solar cells.***

The statistical metric parameters of i-PSCs with different CBLs ZnO, ZnO/PEIE and PEIE/ZnO are presented in Figure 8.5. As can be seen, the device performance is improved when an ultrathin layer of PEIE was incorporated between ZnO layer and photoactive layer. An increase in the FF and the J_{SC} values of the devices lead to a significant improvement in the PCE which enhanced from 3.67 to 4.48%. However, when PEIE was incorporated between ZnO and ITO, the device performance was breakdown with a significant decrease in FF, V_{OC} and J_{SC} leading to a drop-off in the PCE. The results demonstrate that the cells based on ZnO/PEIE CBL achieve a good performance; this improvement can be ascribed to the improved absorber/ZnO interface properties and the increase of the charge collection ability with incorporating PEIE interlayer.

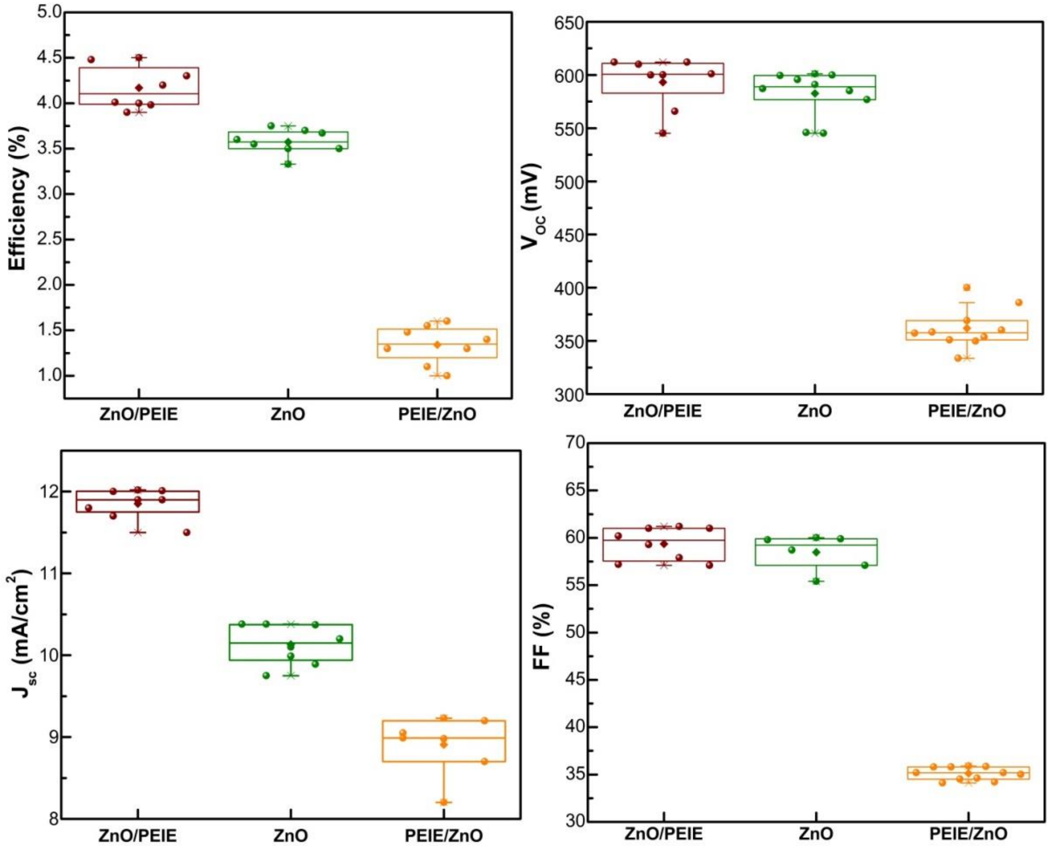

Figure 9.5: *Box plots showing the distribution of the photovoltaic parameters (Efficiency, V_{OC}, J_{SC} and FF) recorded for the elaborated inverted solar cells based on ZnO, ZnO/PEIE and PEIE/ZnO CBLs determined by J-V analysis from eight distinct devices for each sample (all samples are with ZnO: MEA 1:1 molar ratio).*

In order to investigate the surface characteristics of different CBLs, an atomic force microscope (AFM) was assumed to measure the surface morphology of glass/ITO/ZnO, glass/ITO/ZnO/PEIE and glass/ITO/PEIE/ZnO. The obtained micrographs 2D and 3D are presented in Figure 9.6. The root mean square roughness (RMS) values were 2.7, 1.7 and 6.4 nm for the thin films with the configuration of glass/ITO/ZnO, ITO/ZnO/PEIE, and ITO/PEIE/ZnO, respectively. Compared to other CBL configurations, ITO/ZnO/PEIE CBL presents a lower value of ~1.7 nm, which might be due to homogenous covering of ZnO film with PEIE ultrathin layer. The higher roughness of ITO/PEIE/ZnO suggests that the PEIE film is damaged after the deposition of ZnO layer. As can be seen from the 2D and 3D AFM images Figures 9.6 (c), a few portion of uncovered ITO substrate is formed with the presence of some agglomerations on the surface. However, by adding

PEIE modified ZnO (ITO/ZnO/PEIE) a smaller RMS value was achieved (1.7 nm). This smoother morphology presented by ITO/ZnO/PEIE CBL can supply good contact between the active layer and CBL, which is in agreement with the obtained results.

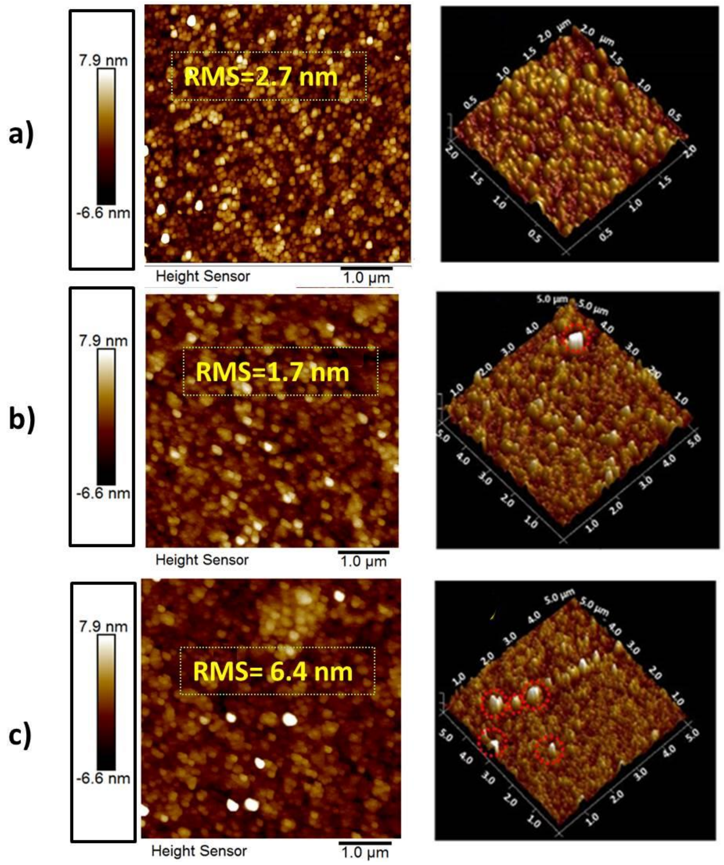

Figure 9.6: *2D and 3D AFM micrographs of the different prepared structures for CBLs: a) ITO/ZnO, b) ITO/ZnO/PEIE and c) ITO/PEIE/ZnO.*

Another important factor which plays a vital role in the performance of organic solar cells, it is long-term stability. In this context, according to the ISOS-D-1 shelf method [346], we controlled the stability of the elaborated devices with ZnO, ZnO/PEIE and PEIE/ZnO CBLs. The devices were saved under ambient air without encapsulation, and the performances of the devices were tested at regular time over 70 days. The records of the device performance stability of the elaborated devices using only ZnO, ZnO/PEIE and PEIE/ZnO CBLs as a function with the storage time (days) presented in Figure 9.7.

One can notice that, the average efficiency of ZnO/PEIE based devices still remains at 3.6%, which represented around 80% of its initial value (4.48%) after 30 days, while the average efficiency of free PEIE devices (with only ZnO CBL) was reduced radically from 3.67 to 2.94% (~80% of its initial value) after ~30 days. However, the average efficiency of ZnO covered PEIE devices (PEIE/ZnO) after 30 days, was reduced radically from 1.55 to 0.9% (~60% of its initial value).

From the results, the elaborated devices ZnO/PEIE CBL shows slightly better storage stability even though the PCE gradually decreased. The recovered stability of the best-performed device could be associated to the good interface contact between the photoactive layer and CBL, which could increase the charge transport and decrease the interface recombination.

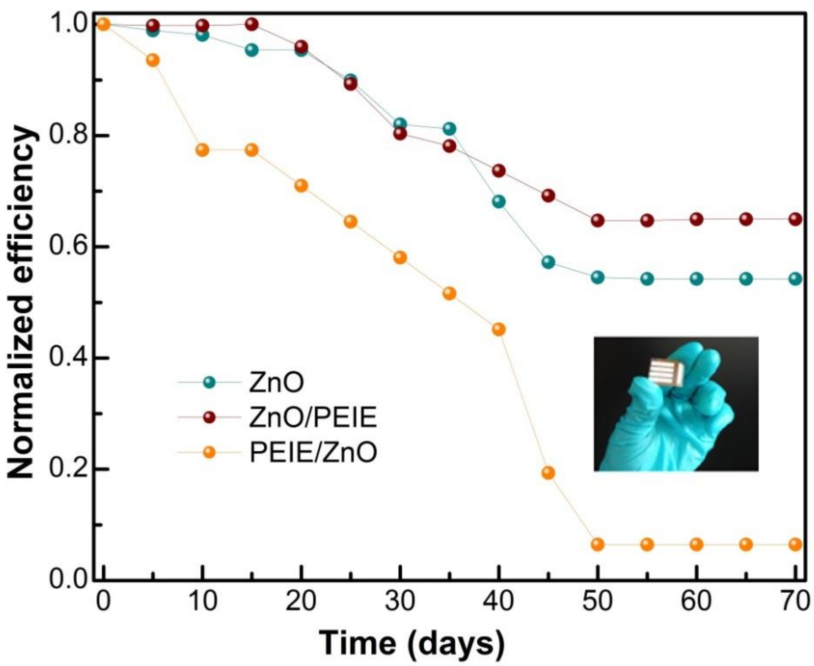

Figure 9.7: *Stability test for the elaborated devices with different CBLs under ambient air condition without encapsulation.*

9.4. Conclusions

In summary, a ZnO solution was prepared by a chemical route and coated at a fixed RPM. The thicknesses of the ZnO thin films were controlled by varying the solution concentration ratios of ZnO to MEA. We investigated a self-assembled modification interlayer to enhance the wettability between the absorber material and CBL.

From these findings, the following conclusions are drawn:

1. The optimal device performance is achievable at 1:1 ratio of ZAD to MEA with a maximum efficiency of 3.67%, V_{OC} of 0.59 V, FF of 60.01% and J_{SC} of 10.38 mA/ cm^2.
2. A significant performance enhancement is achieved after the incorporation of PEIE ultrathin layer, which is ascribed to the improved interface properties between the ZnO/PEIE layer and the photoactive layer due to the relatively smoother surface of the PEIE-coated ZnO layer compared to the ZnO layer without the PEIE interlayer.
3. The high efficiency of 4.48% is achieved with ZnO/PEIE CBL, which is higher than that of PEIE free- device.
4. These findings demonstrate that the combination of the solution-processed ZnO/PEIE cathode bilayer significantly enhanced charge carrier mobility which is beneficial for high-performance i-PSCs.
5. The efficient device exhibits good long-term stability without any encapsulation, which is related to an excellent interface contact.

10

Conclusions and Outlook

The main objective of the work is presented through the first part of this thesis was to synthesis a novel kesterite solar cells wide bandgap based on pure Ge ($Cu_2ZnGeSe_4$), as an alternative solution to overcome the shortcomings related to classical kesterite. However, the record efficiency of type of compound is still significantly lower than those of its predecessors $Cu_2ZnSn(S_xSe_{1-x})_4$ (CZTSSe), $Cu(In,Ga)Se_2$ (CIGS) and CdTe thin-film solar cells.

In this context, the comprehensive understanding of the factors limiting the performance of $Cu_2ZnGeSe_4$ based solar cells is the purpose of this thesis. Besides, an in-depth investigation of the main limitations is carried out, specifically focusing on studying the origin of the large V_{OC} deficit, the main recombination mechanisms, electric transport properties, band tails and possible $Cu_2ZnGeSe_4$/CdS band offset effects.

The main findings drawn from the first part of this thesis are of a great novelty in the kesterite field and can be summarized as follows:

- The V_{OC} deficit can likely be ascribed to a Fermi level pinning at the interface, though the influence of bulk defects shouldn't be yet discarded. A spike-like absorber/buffer junction could alleviate this issue.
- The multi-wavelength Raman analysis has demonstrated that changes in V_{Cu} concentration were the main culprit affecting the solar cell performance, which stemmed mainly from FF and Jsc variation, considered the first parameters impacted by this point defect.
- The complex analytical correlation of compositional, spectroscopic and optoelectronic data for each of the 200 solar cells, has allowed revealing that

V_{Cu} controls the Jsc and FF of the devices while the substitutional defects have their main influence on the V_{oc} leading to an optimum cationic compositional range of [Zn]/[Ge] = 1.05–1.15 for achieving the high efficiency (~6%) solar cell devices.

- The optimal composition range with optimal defects concentration were found in the range of Zn/Ge= 1.05-1.15 and Cu/(Zn+Ge)= 0.65, and exhibited a maximal efficiency of 6.2%, V_{oc}= 597 mV, J_{sc}= 17 mA/cm^2 and FF=60% with a band gap of 1.4 eV.

To further improve the devices presented in this thesis, serval strategies to boost the efficiency of $Cu_2ZnGeSe_4$ kesterite solar cells:

1. The use of alkali post-deposition treatments has demonstrated a spectacular improvement in the carrier lifetime in CIGSe solar cells, especially when using heavier elements such as Na, K, Li, Rb or Cs. A similar approach could be followed in $Cu_2ZnGeSe_4$ solar cells.
2. The doping strategies have led to a better crystalline quality of the CZGeSe absorbers, the avoidance of formation of detrimental point defects, the reduction and control of compositional fluctuations during the synthesis processes by modifying the reaction pathways, and the control/optimization of the doping level of the absorber.
3. The buffer layer composition may also be positively altered by substituting a limited amount of Cd by Zn and obtain a spike-like p-n interface, which could help alleviating the interface voltage limitation.

Overall, this has allowed a significant improvement of the cell voltage, leading to a reduced V_{OC} deficit and, ultimately, a remarkable performance improvement of kesterite solar cells.

Bulk heterojunction organic solar cells (BHJ OSCs) are very promising organic-based devices for low-cost solar energy conversion, compatible with roll-to-roll or general printing methods for mass production. Nevertheless, to date, many issues should still be addressed, one of these being the poor stability in ambient conditions. One elegant way to overcome such an issue is the inverted organic solar cells.

The aim of this thesis part is elaboration and characterization of efficient inverted organic solar cells, using metal oxides such as ZnO and SnO_2 as an electron transporting layer, as a way to overcome the shortcomings associated with the PEDOT: PSS conventional configuration. The following conclusions are drawn from our study:

- The work is devoted to an inverted organic solar cell based on bulk heterojunction using poly (3-hexylthiophene-2,5-diyl):[6,6]-phenyl-C71-butyric acid methyl ester (P3HT:PCBM) as an absorber.
- The originality of the work in this thesis is to overcome the limitations of the use of a single cathode buffer layer, using the cathode buffer bilayer tin dioxide (SnO_2) with PEIE.
- The PEIE surface modifier within the sputtered SnO_2 layer is a promising alternative buffer bilayer to maximize the percolation of electron charge carriers by the formation of a thin interfacial dipole between the electron-transporting layer ITO/SnO_2 and the LUMO of PCBM. This facilitates electron transport to the electrode by lowering the energy barrier between the active layer and the ITO/SnO_2 interface, and by improving the wettability between these layers, which leads to increases in the short-circuit current density and the fill factor.
- The thicknesses of the synthesis ZnO thin films were controlled by varying the solution concentration ratios of ZnO to MEA. We investigated a self-assembled modification interlayer to enhance the wettability between the absorber material and CBL.

- Significant improvement in the devices was achieved after the incorporation of PEIE ultrathin layer, which is ascribed to the improved interface properties between the ZnO/PEIE layer and the photoactive layer due to the relatively smoother surface of the PEIE-coated ZnO layer compared to the ZnO layer without the PEIE interlayer.

Appendix

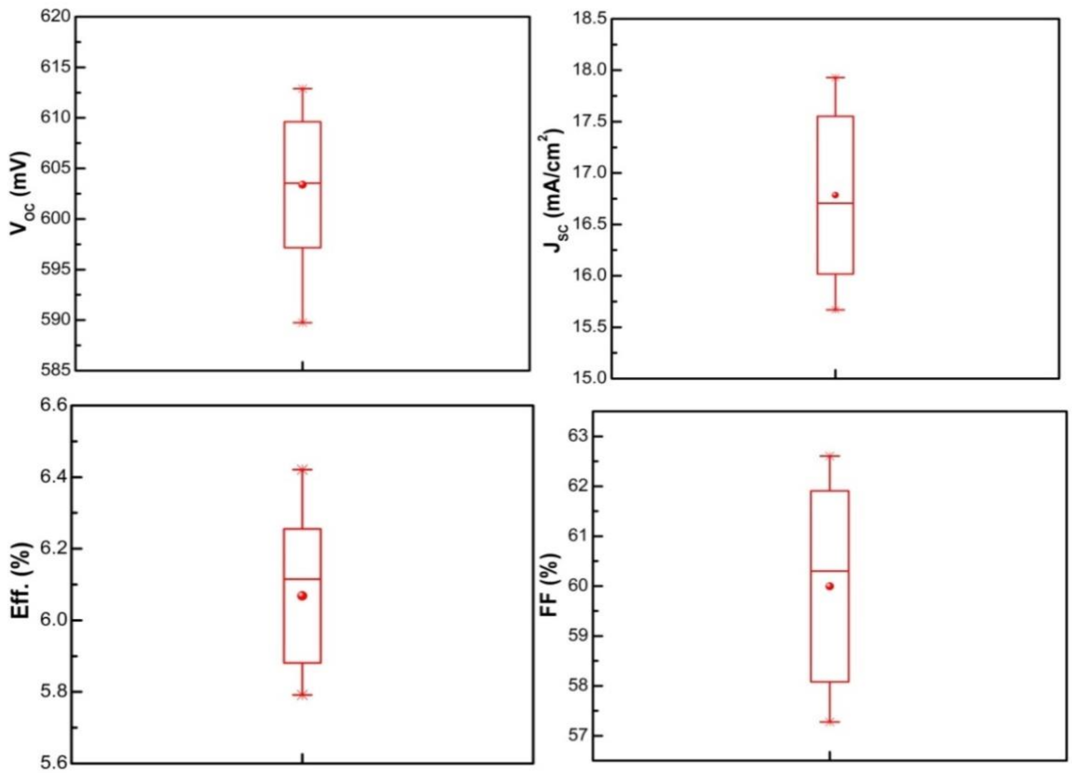

Figure A.01: *Statistical box charts of the measured photovoltaic parameters for 13 cells based on CZGeSe films grown using the SLG/Mo/Cu/Zn/Ge structure in the selenization process.*

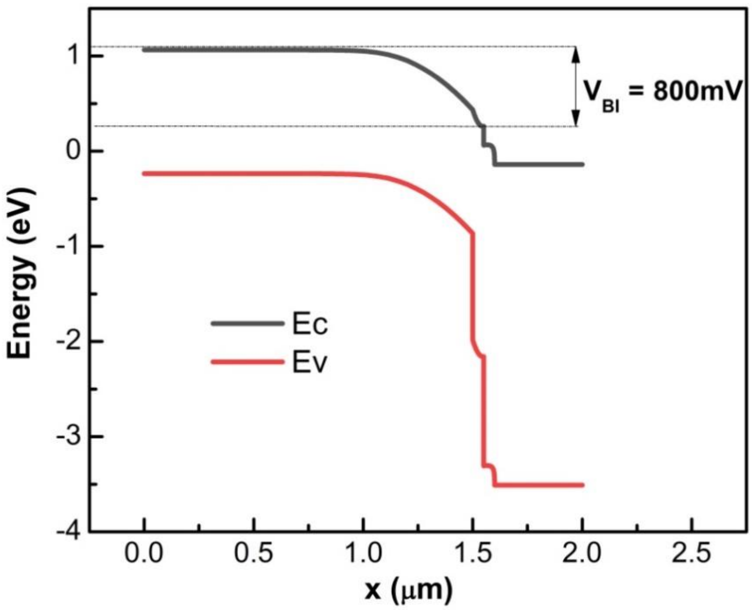

Figure A.02: *Simulated band diagram of the solar cell reported in this work.*

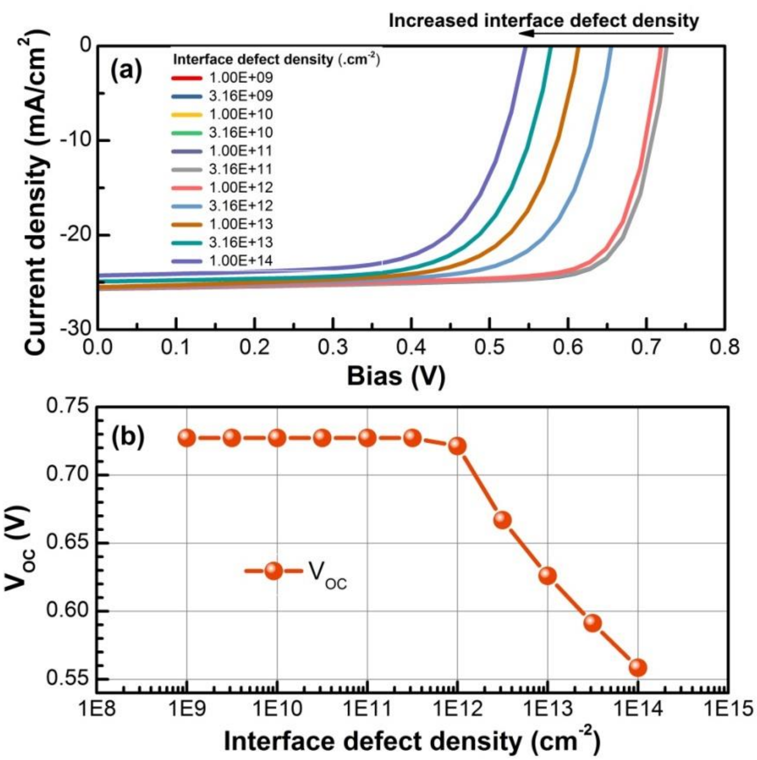

Figure A.03 : *Simulated J-V curves of CZGeSe/CdS solar cells when varying the acceptor interface defect concentration from 10^9 cm^{-2} to 10^{14} cm^{-2} (a), and the corresponding evolution of the open-circuit voltage (b). The material parameters are from references [168], [347], [348].*

B

Combinatorial and machine learning approaches for the analysis of $Cu_2ZnGeSe_4$: influence of the off-stoichiometry on defect formation and solar cell performance

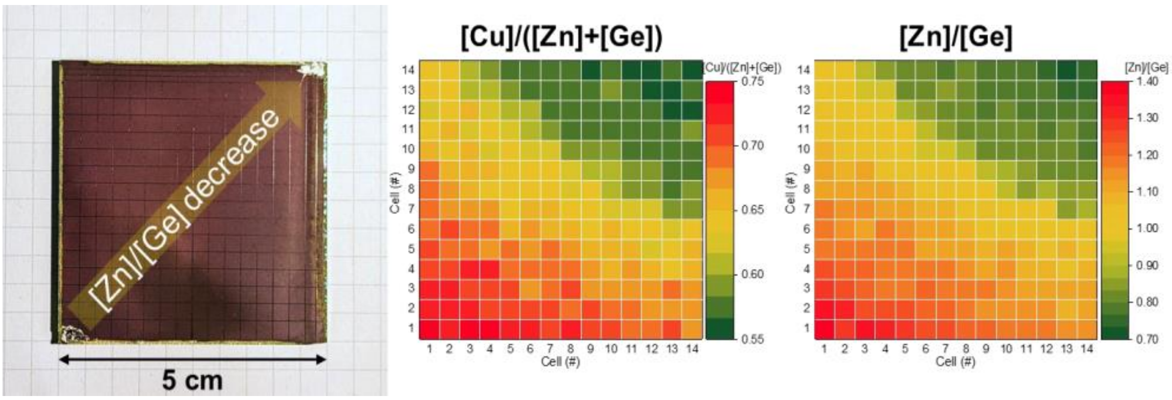

Figure B.01: *Picture (left) and mappings of XRF cations ratios (middle and right) of the combinatorial sample.*

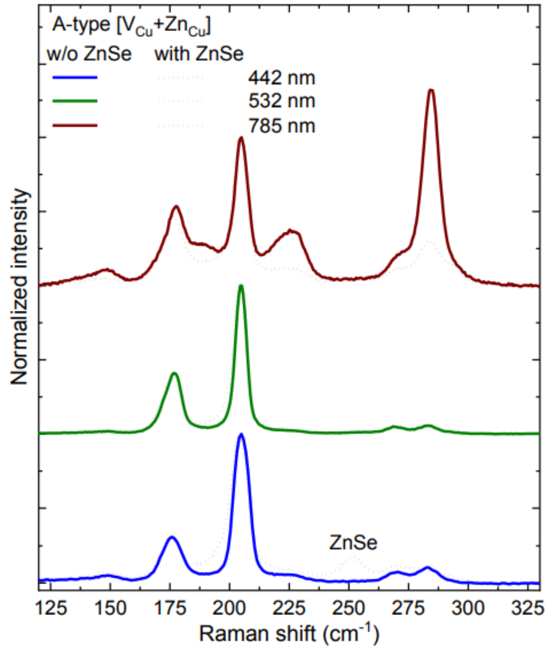

Figure B.02: *Raman spectra of the cells with compositions close to A-type off-stoichiometric line with (solid lines) and without (dotted lines) ZnSe secondary phase.*

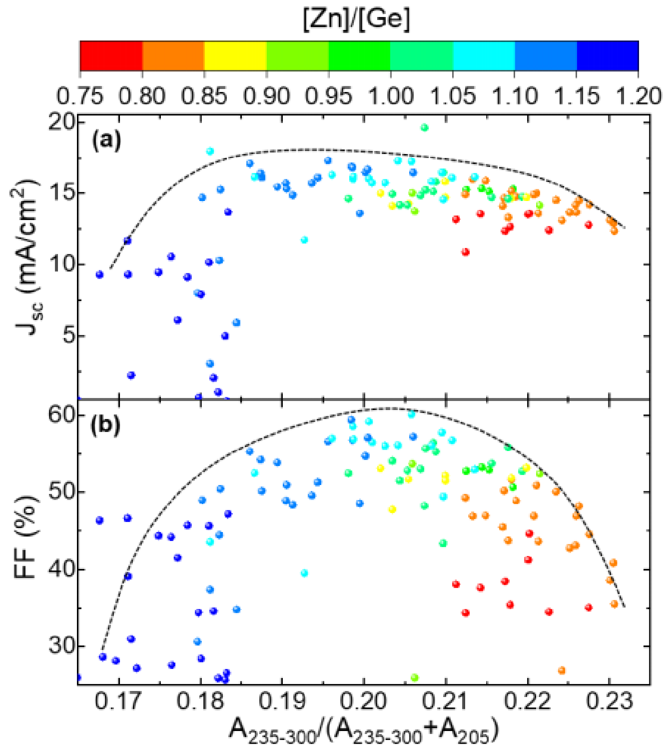

Figure B.03: *Dependence of (a) short circuit current and (b) fill factor of the cells on the relative integrated intensity of the Raman peaks in the range 235 – 300 cm^{-1} . The color scale corresponds to the relative integrated intensity of the Raman band at 176 cm^{-1} (see the main text for details).*

C

Evaluation of different buffer materials for solar cells with wide-gap $Cu_2ZnGeSe_4$ absorbers

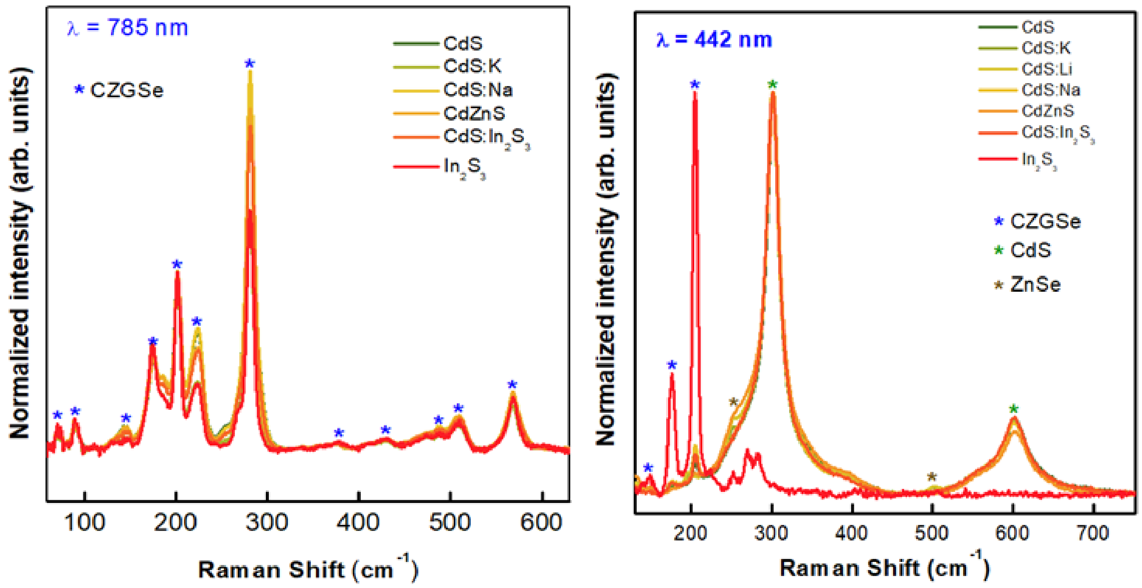

Figure C.01: *Raman scattering spectra of $Cu_2ZnGeSe_4$ solar cells with different buffer layer measured under different excitation conditions. Numbers indicate the peaks position.*

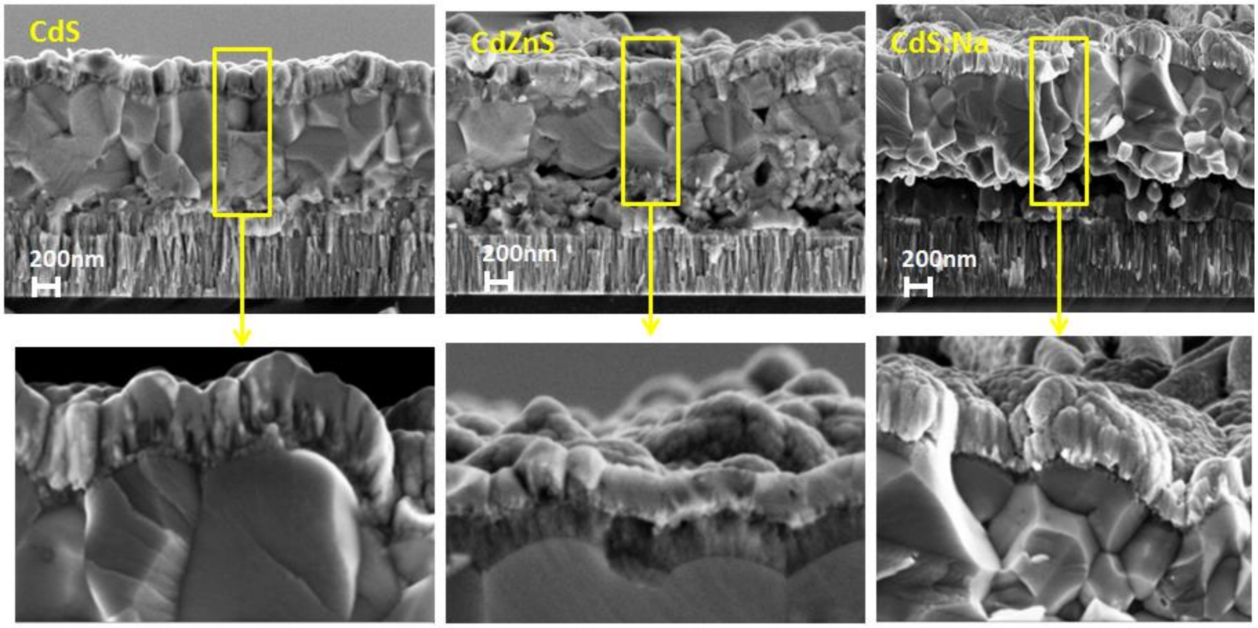

Figure C.02: *Cross section and top view SEM images of CZGSe solar cells with different buffer layers synthesized at 330°C-480°C (Standard process).*

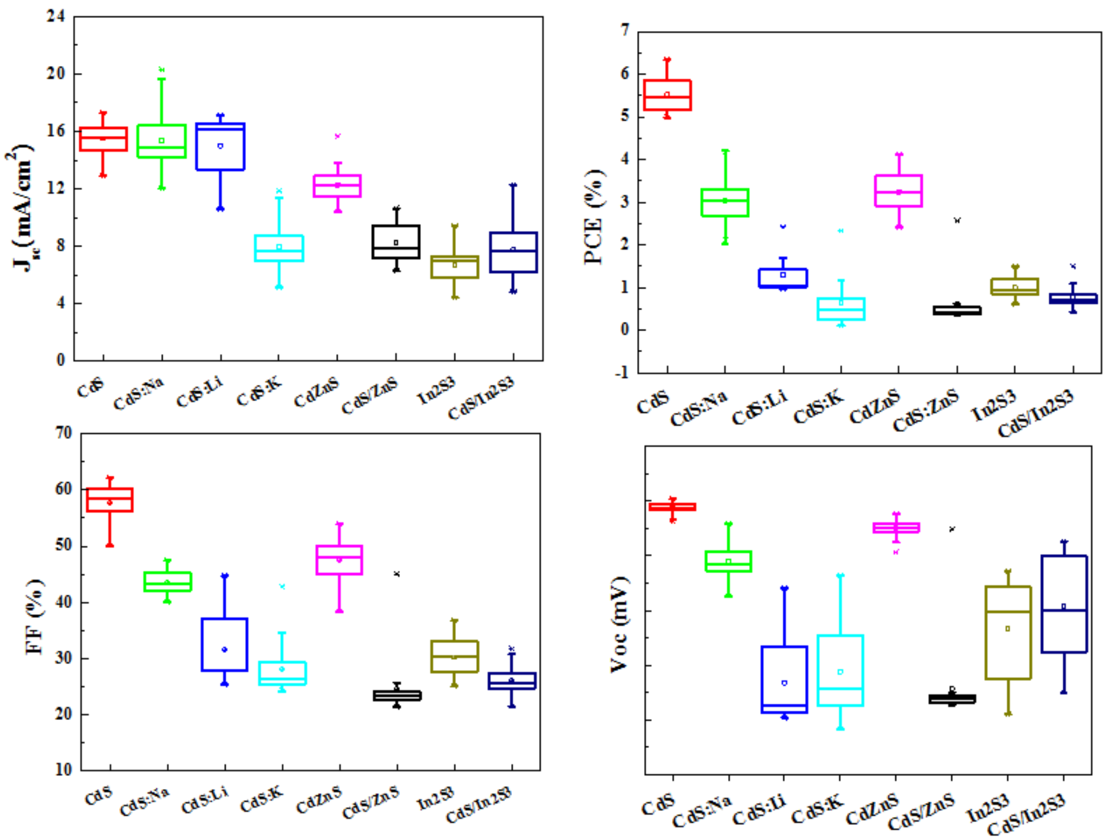

Figure C.03: *Boxplot diagram of the device performance parameters of CZGSe cells made with the various buffer layers.*

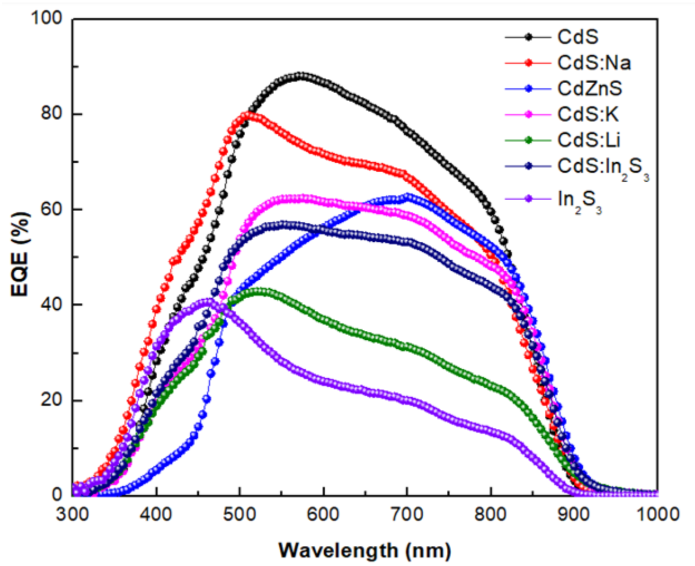

Figure C.04: *EQE measurements of CZGSe based solar cells with variation of different buffer layers.*

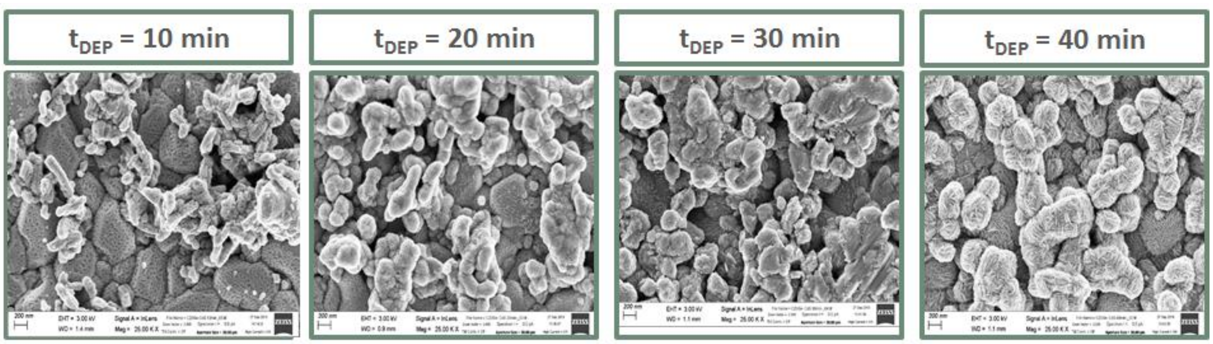

Figure C.5: *SEM view of CdS deposited on CZGSe with different t_{DEP}*

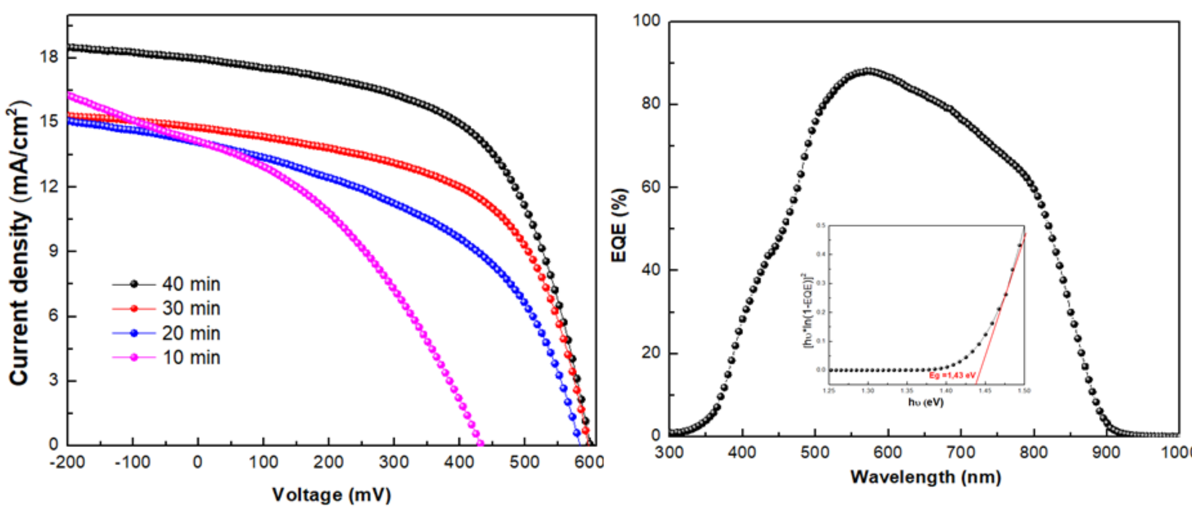

Figure C.06: *J-V of CZGSe based solar cells with variation of deposition time (left) of CdS and EQE spectra of the best device with 40 min as a deposition time of CdS.*

Bibliography:

[1] IRENA; IEA, *Perspectives for the energy transition: Investment needs for a low-carbon energy system*, vol. 217. 2019.

[2] UNFCCC, « 1992 United Nations Framework Convention on Climate », 2004, p. 1-24.

[3] Nations, *U. Resolution 48/189. United Nations Framework Convention on Climate Change*, Part II. 1994.

[4] *U. Kyoto Protocol To the United Nations Framework Kyoto Protocol To the United Nations Framework*. Rev. Eur. Community Int. Environ. Law, 1998.

[5] UNFCCC, *Paris Agreement. Conf. Parties its twenty-first Sess*. 2015.

[6] Ribera, T.; Sachs, J., *Pathways to Deep Decarbonization (report)*. DDPP, 2015.

[7] L. P. Fesenfeld, « Glimpses Of Hope: A Global Green New Deal Is Feasible », *SSRN Electron. J.*, 2020, doi: 10.2139/ssrn.3709074.

[8] D. J. Feldman, R. M. Margolis, et J. Hoskins, « Q4 2017/Q1 2018 Solar Industry Update », NREL/PR--6A20-71493, 1437344, mai 2018. doi: 10.2172/1437344.

[9] Y. Lee, C. Park, N. Balaji, Y.-J. Lee, et V. A. Dao, « High-efficiency Silicon Solar Cells: A Review », *Isr. J. Chem.*, vol. 55, n° 10, p. 1050-1063, oct. 2015, doi: 10.1002/ijch.201400210.

[10] Green, M.A., « Crystalline Silicon Photovoltaic Cells », *Cells. Adv. Mater.*, p. 1019-1022, juin 28, 2001.

[11] K. Yoshikawa *et al.*, « Silicon heterojunction solar cell with interdigitated back contacts for a photoconversion efficiency over 26% », *Nat. Energy*, vol. 2, n° 5, p. 17032, mai 2017, doi: 10.1038/nenergy.2017.32.

[12] S. S. Deshmukh et J. M. Pearce, « Electric vehicle charging potential from retail parking lot solar photovoltaic awnings », *Renew. Energy*, vol. 169, p. 608-617, mai 2021, doi: 10.1016/j.renene.2021.01.068.

[13] A. Goetzberger, J. Knobloch, et B. Voß, *Crystalline Silicon Solar Cells: Goetzberger/Crystalline Silicon Solar Cells*. Chichester, UK: John Wiley & Sons, Ltd, 2014. doi: 10.1002/9781119033769.

[14] M. A. Green, « Crystalline and thin-film silicon solar cells: state of the art and future potential », *Sol. Energy*, vol. 74, n° 3, p. 181-192, mars 2003, doi: 10.1016/S0038-092X(03)00187-7.

[15] J. Benick *et al.*, « High-Efficiency n-Type HP mc Silicon Solar Cells », *IEEE J. Photovolt.*, vol. 7, n° 5, p. 1171-1175, sept. 2017, doi: 10.1109/JPHOTOV.2017.2714139.

[16] D. M. Powell, M. T. Winkler, H. J. Choi, C. B. Simmons, D. B. Needleman, et T. Buonassisi, « Crystalline silicon photovoltaics: a cost analysis framework for determining technology pathways to reach baseload electricity costs », *Energy Environ. Sci.*, vol. 5, n° 3, p. 5874, 2012, doi: 10.1039/c2ee03489a.

[17] *BP Statistical Review of World Energy*. 2017. [En ligne]. Disponible sur: https://www.bp.com/content/dam/bp/business-sites/en/global/corporate/pdfs/energy-economics/statistical-review/bp-stats-review-2020-full-report.pdf

[18] « V. The action of light on selenium », *Proc. R. Soc. Lond.*, vol. 25, n° 171-178, p. 113-117, déc. 1877, doi: 10.1098/rspl.1876.0024.

[19] D. M. Chapin, C. S. Fuller, et G. L. Pearson, « A New Silicon *p-n* Junction Photocell for Converting Solar Radiation into Electrical Power », *J. Appl. Phys.*, vol. 25, n° 5, p. 676-677, mai 1954, doi: 10.1063/1.1721711.

[20] J. J. Loferski, « The first forty years: A brief history of the modern photovoltaic age », *Prog. Photovolt. Res. Appl.*, vol. 1, n° 1, p. 67-78, janv. 1993, doi: 10.1002/pip.4670010109.

[21] M. D. Perez, C. Borek, S. R. Forrest, et M. E. Thompson, « Molecular and Morphological Influences on the Open Circuit Voltages of Organic Photovoltaic Devices », *J. Am. Chem. Soc.*, vol. 131, n° 26, p. 9281-9286, juill. 2009, doi: 10.1021/ja9007722.

[22] S. Rühle, « Tabulated values of the Shockley–Queisser limit for single junction solar cells », *Sol. Energy*, vol. 130, p. 139-147, juin 2016, doi: 10.1016/j.solener.2016.02.015.

[23] M. A. Contreras *et al.*, « SHORT COMMUNICATION: ACCELERATED PUBLICATION: Diode characteristics in state-of-the-art ZnO/CdS/Cu(In1?xGax)Se2 solar cells », *Prog. Photovolt. Res. Appl.*, vol. 13, nº 3, p. 209-216, mai 2005, doi: 10.1002/pip.626.

[24] R. Scheer et H.-W. Schock, *Chalcogenide Photovoltaics: Physics, Technologies, and Thin Film Devices*. Weinheim, Germany: Wiley-VCH Verlag GmbH & Co. KGaA, 2011. doi: 10.1002/9783527633708.

[25] F. Liu *et al.*, « Emerging inorganic compound thin film photovoltaic materials: Progress, challenges and strategies », *Mater. Today*, vol. 41, p. 120-142, déc. 2020, doi: 10.1016/j.mattod.2020.09.002.

[26] M. A. Green, « Thin-film solar cells: review of materials, technologies and commercial status », *J. Mater. Sci. Mater. Electron.*, vol. 18, nº S1, p. 15-19, oct. 2007, doi: 10.1007/s10854-007-9177-9.

[27] T. D. Lee et A. U. Ebong, « A review of thin film solar cell technologies and challenges », *Renew. Sustain. Energy Rev.*, vol. 70, p. 1286-1297, avr. 2017, doi: 10.1016/j.rser.2016.12.028.

[28] M. A. Green, A. Ho-Baillie, et H. J. Snaith, « The emergence of perovskite solar cells », *Nat. Photonics*, vol. 8, nº 7, p. 506-514, juill. 2014, doi: 10.1038/nphoton.2014.134.

[29] J. Ha, H. Kim, H. Lee, K.-G. Lim, T.-W. Lee, et S. Yoo, « Device architecture for efficient, low-hysteresis flexible perovskite solar cells: Replacing TiO2 with C60 assisted by polyethylenimine ethoxylated interfacial layers », *Sol. Energy Mater. Sol. Cells*, vol. 161, p. 338-346, mars 2017, doi: 10.1016/j.solmat.2016.11.031.

[30] J.-H. Song, Y.-S. An, S.-G. Kim, S.-J. Lee, J.-H. Yoon, et Y.-K. Choung, « Power output analysis of transparent thin-film module in building integrated photovoltaic system (BIPV) », *Energy Build.*, vol. 40, nº 11, p. 2067-2075, janv. 2008, doi: 10.1016/j.enbuild.2008.05.013.

[31] M. Nakamura, K. Yamaguchi, Y. Kimoto, Y. Yasaki, T. Kato, et H. Sugimoto, « Cd-Free Cu(In,Ga)(Se,S) $_2$ Thin-Film Solar Cell With Record Efficiency of 23.35% », *IEEE J. Photovolt.*, vol. 9, nº 6, p. 1863-1867, nov. 2019, doi: 10.1109/JPHOTOV.2019.2937218.

[32] S. M. Hayes et E. A. McCullough, « Critical minerals: A review of elemental trends in comprehensive criticality studies », *Resour. Policy*, vol. 59, p. 192-199, déc. 2018, doi: 10.1016/j.resourpol.2018.06.015.

[33] K. Ito et T. Nakazawa, « Electrical and Optical Properties of Stannite-Type Quaternary Semiconductor Thin Films », *Jpn. J. Appl. Phys.*, vol. 27, nº Part 1, No. 11, p. 2094-2097, nov. 1988, doi: 10.1143/JJAP.27.2094.

[34] H. Katagiri, N. Sasaguchi, S. Hando, S. Hoshino, J. Ohashi, et T. Yokota, « Preparation and evaluation of Cu2ZnSnS4 thin films by sulfurization of E-B evaporated precursors », *Sol. Energy Mater. Sol. Cells*, vol. 49, nº 1-4, p. 407-414, déc. 1997, doi: 10.1016/S0927-0248(97)00119-0.

[35] H. Katagiri *et al.*, « Enhanced Conversion Efficiencies of Cu $_2$ ZnSnS $_4$ -Based Thin Film Solar Cells by Using Preferential Etching Technique », *Appl. Phys. Express*, vol. 1, p. 041201, avr. 2008, doi: 10.1143/APEX.1.041201.

[36] D. B. Mitzi *et al.*, « A High-Efficiency Solution-Deposited Thin-Film Photovoltaic Device », *Adv. Mater.*, vol. 20, nº 19, p. 3657-3662, oct. 2008, doi: 10.1002/adma.200800555.

[37] T. K. Todorov, K. B. Reuter, et D. B. Mitzi, « High-Efficiency Solar Cell with Earth-Abundant Liquid-Processed Absorber », *Adv. Mater.*, vol. 22, nº 20, p. E156-E159, mai 2010, doi: 10.1002/adma.200904155.

[38] W. Wang *et al.*, « Device Characteristics of CZTSSe Thin-Film Solar Cells with 12.6% Efficiency », *Adv. Energy Mater.*, vol. 4, nº 7, p. 1301465, mai 2014, doi: 10.1002/aenm.201301465.

[39] S. Schorr, « The crystal structure of kesterite type compounds: A neutron and X-ray diffraction study », *Sol. Energy Mater. Sol. Cells*, vol. 95, nº 6, p. 1482-1488, juin 2011, doi: 10.1016/j.solmat.2011.01.002.

[40] M. Dimitrievska *et al.*, « Defect characterisation in $Cu_2ZnSnSe_4$ kesterites *via* resonance Raman spectroscopy and the impact on optoelectronic solar cell properties », *J. Mater. Chem. A*, vol. 7, n° 21, p. 13293-13304, 2019, doi: 10.1039/C9TA03625C.
[41] S. Chen, X. G. Gong, A. Walsh, et S.-H. Wei, « Crystal and electronic band structure of Cu2ZnSnX4 (X=S and Se) photovoltaic absorbers: First-principles insights », *Appl. Phys. Lett.*, vol. 94, n° 4, p. 041903, janv. 2009, doi: 10.1063/1.3074499.
[42] S. Bourdais *et al.*, « Is the Cu/Zn Disorder the Main Culprit for the Voltage Deficit in Kesterite Solar Cells? », *Adv. Energy Mater.*, vol. 6, n° 12, p. 1502276, juin 2016, doi: 10.1002/aenm.201502276.
[43] A. Lafond, L. Choubrac, C. Guillot-Deudon, P. Fertey, M. Evain, et S. Jobic, « X-ray resonant single-crystal diffraction technique, a powerful tool to investigate the kesterite structure of the photovoltaic Cu_2ZnSnS_4 compound », *Acta Crystallogr. Sect. B Struct. Sci. Cryst. Eng. Mater.*, vol. 70, n° 2, p. 390-394, avr. 2014, doi: 10.1107/S2052520614003138.
[44] K. Rudisch, Y. Ren, C. Platzer-Björkman, et J. Scragg, « Order-disorder transition in B-type Cu_2ZnSnS_4 and limitations of ordering through thermal treatments », *Appl. Phys. Lett.*, vol. 108, n° 23, p. 231902, juin 2016, doi: 10.1063/1.4953349.
[45] J. J. S. Scragg, L. Choubrac, A. Lafond, T. Ericson, et C. Platzer-Björkman, « A low-temperature order-disorder transition in Cu_2ZnSnS_4 thin films », *Appl. Phys. Lett.*, vol. 104, n° 4, p. 041911, janv. 2014, doi: 10.1063/1.4863685.
[46] G. Rey *et al.*, « The band gap of Cu2ZnSnSe4: Effect of order-disorder », *Appl. Phys. Lett.*, vol. 105, n° 11, p. 112106, sept. 2014, doi: 10.1063/1.4896315.
[47] W. Shockley et H. J. Queisser, « Detailed Balance Limit of Efficiency of *p-n* Junction Solar Cells », *J. Appl. Phys.*, vol. 32, n° 3, p. 510-519, mars 1961, doi: 10.1063/1.1736034.
[48] P. Jackson *et al.*, « New world record efficiency for $Cu(In,Ga)Se_2$ thin-film solar cells beyond 20%: High efficiencies for $Cu(In,Ga)Se_2$ », *Prog. Photovolt. Res. Appl.*, vol. 19, n° 7, p. 894-897, nov. 2011, doi: 10.1002/pip.1078.
[49] S. Chen, A. Walsh, X.-G. Gong, et S.-H. Wei, « Classification of Lattice Defects in the Kesterite Cu_2ZnSnS_4 and $Cu_2ZnSnSe_4$ Earth-Abundant Solar Cell Absorbers », *Adv. Mater.*, vol. 25, n° 11, p. 1522-1539, mars 2013, doi: 10.1002/adma.201203146.
[50] I. D. Olekseyuk, I. V. Dudchak, et L. V. Piskach, « Phase equilibria in the Cu2S–ZnS–SnS2 system », *J. Alloys Compd.*, vol. 368, n° 1-2, p. 135-143, avr. 2004, doi: 10.1016/j.jallcom.2003.08.084.
[51] X. Liu *et al.*, « The current status and future prospects of kesterite solar cells: a brief review: Kesterite solar cells », *Prog. Photovolt. Res. Appl.*, vol. 24, n° 6, p. 879-898, juin 2016, doi: 10.1002/pip.2741.
[52] I. Repins *et al.*, « Co-evaporated Cu2ZnSnSe4 films and devices », *Sol. Energy Mater. Sol. Cells*, vol. 101, p. 154-159, juin 2012, doi: 10.1016/j.solmat.2012.01.008.
[53] H. Katagiri, K. Jimbo, M. Tahara, H. Araki, et K. Oishi, « The Influence of the Composition Ratio on CZTS-based Thin Film Solar Cells », *MRS Proc.*, vol. 1165, p. 1165-M04-01, 2009, doi: 10.1557/PROC-1165-M04-01.
[54] J. J. Scragg, P. J. Dale, D. Colombara, et L. M. Peter, « Thermodynamic Aspects of the Synthesis of Thin-Film Materials for Solar Cells », *ChemPhysChem*, vol. 13, n° 12, p. 3035-3046, août 2012, doi: 10.1002/cphc.201200067.
[55] A. Redinger, D. M. Berg, P. J. Dale, et S. Siebentritt, « The Consequences of Kesterite Equilibria for Efficient Solar Cells », *J. Am. Chem. Soc.*, vol. 133, n° 10, p. 3320-3323, mars 2011, doi: 10.1021/ja111713g.
[56] J. J. Scragg, T. Ericson, T. Kubart, M. Edoff, et C. Platzer-Björkman, « Chemical Insights into the Instability of Cu_2ZnSnS_4 Films during Annealing », *Chem. Mater.*, vol. 23, n° 20, p. 4625-4633, oct. 2011, doi: 10.1021/cm202379s.
[57] M. Buffière *et al.*, « KCN Chemical Etch for Interface Engineering in $Cu_2ZnSnSe_4$ Solar Cells », *ACS Appl. Mater. Interfaces*, vol. 7, n° 27, p. 14690-14698, juill. 2015, doi: 10.1021/acsami.5b02122.

[58] M. Buffière *et al.*, « Microstructural analysis of 9.7% efficient Cu $_2$ ZnSnSe $_4$ thin film solar cells », *Appl. Phys. Lett.*, vol. 105, n^o 18, p. 183903, nov. 2014, doi: 10.1063/1.4901401.
[59] S. López-Marino *et al.*, « ZnSe Etching of Zn-Rich Cu $_2$ ZnSnSe $_4$: An Oxidation Route for Improved Solar-Cell Efficiency », *Chem. - Eur. J.*, vol. 19, n^o 44, p. 14814-14822, oct. 2013, doi: 10.1002/chem.201302589.
[60] H. Xie *et al.*, « Impact of Sn(S,Se) Secondary Phases in Cu $_2$ ZnSn(S,Se) $_4$ Solar Cells: a Chemical Route for Their Selective Removal and Absorber Surface Passivation », *ACS Appl. Mater. Interfaces*, vol. 6, n^o 15, p. 12744-12751, août 2014, doi: 10.1021/am502609c.
[61] M. Mousel *et al.*, « HCl and Br2-MeOH etching of Cu2ZnSnSe4 polycrystalline absorbers », *Thin Solid Films*, vol. 535, p. 83-87, mai 2013, doi: 10.1016/j.tsf.2012.12.095.
[62] I. Becerril-Romero *et al.*, « Vitreous enamel as sodium source for efficient kesterite solar cells on commercial ceramic tiles », *Sol. Energy Mater. Sol. Cells*, vol. 154, p. 11-17, sept. 2016, doi: 10.1016/j.solmat.2016.04.035.
[63] I. Becerril-Romero *et al.*, « CZTSe solar cells developed on polymer substrates: Effects of low-temperature processing », *Prog. Photovolt. Res. Appl.*, vol. 26, n^o 1, p. 55-68, janv. 2018, doi: 10.1002/pip.2945.
[64] T. Schwarz *et al.*, « Atom probe tomography study of internal interfaces in Cu $_2$ ZnSnSe $_4$ thin-films », *J. Appl. Phys.*, vol. 118, n^o 9, p. 095302, sept. 2015, doi: 10.1063/1.4929874.
[65] M. Paris, L. Choubrac, A. Lafond, C. Guillot-Deudon, et S. Jobic, « Solid-State NMR and Raman Spectroscopy To Address the Local Structure of Defects and the Tricky Issue of the Cu/Zn Disorder in Cu-Poor, Zn-Rich CZTS Materials », *Inorg. Chem.*, vol. 53, n^o 16, p. 8646-8653, août 2014, doi: 10.1021/ic5012346.
[66] S. Giraldo, Z. Jehl, M. Placidi, V. Izquierdo-Roca, A. Pérez-Rodríguez, et E. Saucedo, « Progress and Perspectives of Thin Film Kesterite Photovoltaic Technology: A Critical Review », *Adv. Mater.*, vol. 31, n^o 16, p. 1806692, avr. 2019, doi: 10.1002/adma.201806692.
[67] G. Rey *et al.*, « On the origin of band-tails in kesterite », *Sol. Energy Mater. Sol. Cells*, vol. 179, p. 142-151, juin 2018, doi: 10.1016/j.solmat.2017.11.005.
[68] T. Gokmen, O. Gunawan, T. K. Todorov, et D. B. Mitzi, « Band tailing and efficiency limitation in kesterite solar cells », *Appl. Phys. Lett.*, vol. 103, n^o 10, p. 103506, sept. 2013, doi: 10.1063/1.4820250.
[69] M. Neuschitzer *et al.*, « Complex Surface Chemistry of Kesterites: Cu/Zn Reordering after Low Temperature Postdeposition Annealing and Its Role in High Performance Devices », *Chem. Mater.*, vol. 27, n^o 15, p. 5279-5287, août 2015, doi: 10.1021/acs.chemmater.5b01473.
[70] S. De Wolf *et al.*, « Organometallic Halide Perovskites: Sharp Optical Absorption Edge and Its Relation to Photovoltaic Performance », *J. Phys. Chem. Lett.*, vol. 5, n^o 6, p. 1035-1039, mars 2014, doi: 10.1021/jz500279b.
[71] S. Chen, X. G. Gong, A. Walsh, et S.-H. Wei, « Electronic structure and stability of quaternary chalcogenide semiconductors derived from cation cross-substitution of II-VI and I-III-VI 2 compounds », *Phys. Rev. B*, vol. 79, n^o 16, p. 165211, avr. 2009, doi: 10.1103/PhysRevB.79.165211.
[72] P. Jackson, D. Hariskos, R. Wuerz, W. Wischmann, et M. Powalla, « Compositional investigation of potassium doped Cu(In,Ga)Se $_2$ solar cells with efficiencies up to 20.8%: Compositional investigation of potassium doped Cu(In,Ga)Se $_2$ solar cells with efficiencies up to 20.8% », *Phys. Status Solidi RRL - Rapid Res. Lett.*, vol. 8, n^o 3, p. 219-222, mars 2014, doi: 10.1002/pssr.201409040.
[73] O. Gunawan, T. K. Todorov, et D. B. Mitzi, « Loss mechanisms in hydrazine-processed Cu2ZnSn(Se,S)4 solar cells », *Appl. Phys. Lett.*, vol. 97, n^o 23, p. 233506, déc. 2010, doi: 10.1063/1.3522884.
[74] D. A. R. Barkhouse, O. Gunawan, T. Gokmen, T. K. Todorov, et D. B. Mitzi, « Device characteristics of a 10.1% hydrazine-processed Cu2ZnSn(Se,S)4 solar cell: Characteristics of a 10.1% efficient kesterite solar cell », *Prog. Photovolt. Res. Appl.*, vol. 20, n^o 1, p. 6-11, janv. 2012, doi: 10.1002/pip.1160.

[75] J. J. Scragg *et al.*, « Rapid annealing of reactively sputtered precursors for Cu $_2$ ZnSnS $_4$ solar cells: Rapid annealing of sputtered precursors for Cu $_2$ ZnSnS $_4$ solar cells », *Prog. Photovolt. Res. Appl.*, vol. 22, n° 1, p. 10-17, janv. 2014, doi: 10.1002/pip.2265.
[76] S. López-Marino *et al.*, « Inhibiting the absorber/Mo-back contact decomposition reaction in Cu2ZnSnSe4 solar cells: the role of a ZnO intermediate nanolayer », *J. Mater. Chem. A*, vol. 1, n° 29, p. 8338, 2013, doi: 10.1039/c3ta11419h.
[77] I. L. Repins *et al.*, « Indications of short minority-carrier lifetime in kesterite solar cells », *J. Appl. Phys.*, vol. 114, n° 8, p. 084507, août 2013, doi: 10.1063/1.4819849.
[78] I. L. Repins *et al.*, « Kesterite Successes, Ongoing Work, and Challenges: A Perspective From Vacuum Deposition », *IEEE J. Photovolt.*, vol. 3, n° 1, p. 439-445, janv. 2013, doi: 10.1109/JPHOTOV.2012.2215842.
[79] L. Grenet, M. A. A. Suzon, F. Emieux, et F. Roux, « Analysis of Failure Modes in Kesterite Solar Cells », *ACS Appl. Energy Mater.*, vol. 1, n° 5, p. 2103-2113, mai 2018, doi: 10.1021/acsaem.8b00194.
[80] H. Xin *et al.*, « Lithium-doping inverts the nanoscale electric field at the grain boundaries in Cu $_2$ ZnSn(S,Se) $_4$ and increases photovoltaic efficiency », *Phys. Chem. Chem. Phys.*, vol. 17, n° 37, p. 23859-23866, 2015, doi: 10.1039/C5CP04707B.
[81] M. Courel, J. A. Andrade-Arvizu, et O. Vigil-Galán, « Towards a CdS/Cu $_2$ ZnSnS $_4$ solar cell efficiency improvement: A theoretical approach », *Appl. Phys. Lett.*, vol. 105, n° 23, p. 233501, déc. 2014, doi: 10.1063/1.4903826.
[82] M. T. Winkler, W. Wang, O. Gunawan, H. J. Hovel, T. K. Todorov, et D. B. Mitzi, « Optical designs that improve the efficiency of Cu $_2$ ZnSn(S,Se) $_4$ solar cells », *Energy Env. Sci*, vol. 7, n° 3, p. 1029-1036, 2014, doi: 10.1039/C3EE42541J.
[83] S. Levcenko, V. E. Tezlevan, E. Arushanov, S. Schorr, et T. Unold, « Free-to-bound recombination in near stoichiometric Cu 2 ZnSnS 4 single crystals », *Phys. Rev. B*, vol. 86, n° 4, juill. 2012, doi: 10.1103/PhysRevB.86.045206.
[84] Z. Su, J. M. R. Tan, X. Li, X. Zeng, S. K. Batabyal, et L. H. Wong, « Cation Substitution of Solution-Processed Cu $_2$ ZnSnS $_4$ Thin Film Solar Cell with over 9% Efficiency », *Adv. Energy Mater.*, vol. 5, n° 19, p. 1500682, oct. 2015, doi: 10.1002/aenm.201500682.
[85] D. Shin, T. Zhu, X. Huang, O. Gunawan, V. Blum, et D. B. Mitzi, « Earth-Abundant Chalcogenide Photovoltaic Devices with over 5% Efficiency Based on a Cu $_2$ BaSn(S,Se) $_4$ Absorber », *Adv. Mater.*, vol. 29, n° 24, p. 1606945, juin 2017, doi: 10.1002/adma.201606945.
[86] T. Gershon *et al.*, « Photovoltaic Materials and Devices Based on the Alloyed Kesterite Absorber (Ag $_x$ Cu $_{1-x}$) $_2$ ZnSnSe $_4$ », *Adv. Energy Mater.*, vol. 6, n° 10, p. 1502468, mai 2016, doi: 10.1002/aenm.201502468.
[87] A. Guchhait *et al.*, « Enhancement of Open-Circuit Voltage of Solution-Processed Cu $_2$ ZnSnS $_4$ Solar Cells with 7.2% Efficiency by Incorporation of Silver », *ACS Energy Lett.*, vol. 1, n° 6, p. 1256-1261, déc. 2016, doi: 10.1021/acsenergylett.6b00509.
[88] D. B. Khadka, S. Kim, et J. Kim, « Effects of Ge Alloying on Device Characteristics of Kesterite-Based CZTSSe Thin Film Solar Cells », *J. Phys. Chem. C*, vol. 120, n° 8, p. 4251-4258, mars 2016, doi: 10.1021/acs.jpcc.5b11594.
[89] Y. Sun *et al.*, « Review on Alkali Element Doping in Cu(In,Ga)Se 2 Thin Films and Solar Cells », *Engineering*, vol. 3, n° 4, p. 452-459, août 2017, doi: 10.1016/J.ENG.2017.04.020.
[90] P. M. P. Salomé, H. Rodriguez-Alvarez, et S. Sadewasser, « Incorporation of alkali metals in chalcogenide solar cells », *Sol. Energy Mater. Sol. Cells*, vol. 143, p. 9-20, déc. 2015, doi: 10.1016/j.solmat.2015.06.011.
[91] L. Stolt, J. Hedström, J. Kessler, M. Ruckh, K. Velthaus, et H. Schock, « ZnO/CdS/CuInSe $_2$ thin-film solar cells with improved performance », *Appl. Phys. Lett.*, vol. 62, n° 6, p. 597-599, févr. 1993, doi: 10.1063/1.108867.

[92] H.-W. Schock, « Properties of Chalcopyrite-Based Materials and Film Deposition for Thin-Film Solar Cells », in *Thin-Film Solar Cells*, vol. 13, Y. Hamakawa, Éd. Berlin, Heidelberg: Springer Berlin Heidelberg, 2004, p. 163-182. doi: 10.1007/978-3-662-10549-8_10.
[93] S. López-Marino *et al.*, « Alkali doping strategies for flexible and light-weight Cu $_2$ ZnSnSe $_4$ solar cells », *J. Mater. Chem. A*, vol. 4, n^o 5, p. 1895-1907, 2016, doi: 10.1039/C5TA09640E.
[94] T. Maeda, A. Kawabata, et T. Wada, « First-principles study on alkali-metal effect of Li, Na, and K in Cu $_2$ ZnSnS $_4$ and Cu $_2$ ZnSnSe $_4$: First-principles study on alkali-metal effect of Li, Na, and K in Cu $_2$ ZnSnS $_4$ and Cu $_2$ ZnSnSe $_4$ », *Phys. Status Solidi C*, vol. 12, n^o 6, p. 631-637, juin 2015, doi: 10.1002/pssc.201400345.
[95] Z.-K. Yuan *et al.*, « Na-Diffusion Enhanced p-type Conductivity in Cu(In,Ga)Se $_2$: A New Mechanism for Efficient Doping in Semiconductors », *Adv. Energy Mater.*, vol. 6, n^o 24, p. 1601191, déc. 2016, doi: 10.1002/aenm.201601191.
[96] T. Gershon, B. Shin, N. Bojarczuk, M. Hopstaken, D. B. Mitzi, et S. Guha, « The Role of Sodium as a Surfactant and Suppressor of Non-Radiative Recombination at Internal Surfaces in Cu $_2$ ZnSnS $_4$ », *Adv. Energy Mater.*, vol. 5, n^o 2, p. 1400849, janv. 2015, doi: 10.1002/aenm.201400849.
[97] C. M. Sutter-Fella *et al.*, « Sodium Assisted Sintering of Chalcogenides and Its Application to Solution Processed Cu $_2$ ZnSn(S,Se) $_4$ Thin Film Solar Cells », *Chem. Mater.*, vol. 26, n^o 3, p. 1420-1425, févr. 2014, doi: 10.1021/cm403504u.
[98] J. H. Kyle, P. L. Breuer, K. G. Bunney, R. Pleysier, et P. M. May, « Review of trace toxic elements (Pb, Cd, Hg, As, Sb, Bi, Se, Te) and their deportment in gold processing. Part 1: Mineralogy, aqueous chemistry and toxicity », *Hydrometallurgy*, vol. 107, n^o 3-4, p. 91-100, mai 2011, doi: 10.1016/j.hydromet.2011.01.010.
[99] S. Kim, J.-S. Park, S. N. Hood, et A. Walsh, « Lone-pair effect on carrier capture in Cu $_2$ ZnSnS $_4$ solar cells », *J. Mater. Chem. A*, vol. 7, n^o 6, p. 2686-2693, 2019, doi: 10.1039/C8TA10130B.
[100] M. Grossberg, K. Timmo, T. Raadik, E. Kärber, V. Mikli, et J. Krustok, « Study of structural and optoelectronic properties of Cu 2 Zn(Sn 1−x Ge x)Se 4 (x = 0 to 1) alloy compounds », *Thin Solid Films*, vol. 582, p. 176-179, mai 2015, doi: 10.1016/j.tsf.2014.10.055.
[101] D. B. Khadka et J. Kim, « Band Gap Engineering of Alloyed Cu $_2$ ZnGe $_x$ Sn $_{1-x}$ Q $_4$ (Q = S,Se) Films for Solar Cell », *J. Phys. Chem. C*, vol. 119, n^o 4, p. 1706-1713, janv. 2015, doi: 10.1021/jp510877g.
[102] S. Giraldo *et al.*, « Large Efficiency Improvement in Cu $_2$ ZnSnSe $_4$ Solar Cells by Introducing a Superficial Ge Nanolayer », *Adv. Energy Mater.*, vol. 5, n^o 21, p. 1501070, nov. 2015, doi: 10.1002/aenm.201501070.
[103] S. Giraldo *et al.*, « Cu $_2$ ZnSnSe $_4$ solar cells with 10.6% efficiency through innovative absorber engineering with Ge superficial nanolayer: Cu $_2$ ZnSnSe $_4$ solar cells with 10.6% efficiency », *Prog. Photovolt. Res. Appl.*, vol. 24, n^o 10, p. 1359-1367, oct. 2016, doi: 10.1002/pip.2797.
[104] M. Ritzer *et al.*, « On the Germanium Incorporation in Cu $_2$ ZnSnSe $_4$ Kesterite Solar Cells Boosting Their Efficiency », *ACS Appl. Energy Mater.*, vol. 3, n^o 1, p. 558-564, janv. 2020, doi: 10.1021/acsaem.9b01784.
[105] S. Giraldo, M. Neuschitzer, M. Placidi, P. Pistor, A. Perez-Rodriguez, et E. Saucedo, « Cu $_2$ ZnSnSe $_4$ -Based Solar Cells With Efficiency Exceeding 10% by Adding a Superficial Ge Nanolayer: The Interaction Between Ge and Na », *IEEE J. Photovolt.*, vol. 6, n^o 3, p. 754-759, mai 2016, doi: 10.1109/JPHOTOV.2016.2535236.
[106] T. Thersleff, S. Giraldo, M. Neuschitzer, P. Pistor, E. Saucedo, et K. Leifer, « Chemically and morphologically distinct grain boundaries in Ge-doped Cu 2 ZnSnSe 4 solar cells revealed with STEM-EELS », *Mater. Des.*, vol. 122, p. 102-109, mai 2017, doi: 10.1016/j.matdes.2017.02.077.
[107] S. Giraldo *et al.*, « How small amounts of Ge modify the formation pathways and crystallization of kesterites », *Energy Environ. Sci.*, vol. 11, n^o 3, p. 582-593, 2018, doi: 10.1039/C7EE02318A.

[108] M. Neuschitzer *et al.*, « Revealing the beneficial effects of Ge doping on $Cu_2ZnSnSe_4$ thin film solar cells », *J. Mater. Chem. A*, vol. 6, n° 25, p. 11759-11772, 2018, doi: 10.1039/C8TA02551G.
[109] G. M. Ford, Q. Guo, R. Agrawal, et H. W. Hillhouse, « Earth Abundant Element $Cu_2Zn(Sn_{1-x}Ge_x)S_4$ Nanocrystals for Tunable Band Gap Solar Cells: 6.8% Efficient Device Fabrication », *Chem. Mater.*, vol. 23, n° 10, p. 2626-2629, mai 2011, doi: 10.1021/cm2002836.
[110] C. J. Hages *et al.*, « Improved performance of Ge-alloyed CZTGeSSe thin-film solar cells through control of elemental losses: Improved performance of CZTGeSSe solar cells », *Prog. Photovolt. Res. Appl.*, vol. 23, n° 3, p. 376-384, mars 2015, doi: 10.1002/pip.2442.
[111] S. Kim, K. M. Kim, H. Tampo, H. Shibata, K. Matsubara, et S. Niki, « Ge-incorporated Cu2ZnSnSe4 thin-film solar cells with efficiency greater than 10% », *Sol. Energy Mater. Sol. Cells*, vol. 144, p. 488-492, janv. 2016, doi: 10.1016/j.solmat.2015.09.039.
[112] N. Benhaddou *et al.*, « Uncovering details behind the formation mechanisms of $Cu_2ZnGeSe_4$ photovoltaic absorbers », *J. Mater. Chem. C*, vol. 8, n° 12, p. 4003-4011, 2020, doi: 10.1039/C9TC06728K.
[113] A. D. Collord et H. W. Hillhouse, « Germanium Alloyed Kesterite Solar Cells with Low Voltage Deficits », *Chem. Mater.*, vol. 28, n° 7, p. 2067-2073, avr. 2016, doi: 10.1021/acs.chemmater.5b04806.
[114] S. Lie *et al.*, « Reducing the interfacial defect density of CZTSSe solar cells by Mn substitution », *J. Mater. Chem. A*, vol. 6, n° 4, p. 1540-1550, 2018, doi: 10.1039/C7TA09668B.
[115] D. B. Khadka et J. Kim, « Study of structural and optical properties of kesterite Cu2ZnGeX4 (X = S, Se) thin films synthesized by chemical spray pyrolysis », *CrystEngComm*, vol. 15, n° 48, p. 10500, 2013, doi: 10.1039/c3ce41387j.
[116] L. Huang *et al.*, « Synthesis of Cu2ZnGeS4 thin film via sulfurization of RF magnetron sputtered precursor », *J. Mater. Sci. Mater. Electron.*, vol. 26, n° 6, p. 3984-3988, juin 2015, doi: 10.1007/s10854-015-2934-2.
[117] T. Schnabel, M. Seboui, et E. Ahlswede, « Evaluation of different metal salt solutions for the preparation of solar cells with wide-gap $Cu_2ZnGeS_xSe_{4-x}$ absorbers », *RSC Adv.*, vol. 7, n° 1, p. 26-30, 2017, doi: 10.1039/C6RA23068G.
[118] S. Sahayaraj *et al.*, « Optoelectronic properties of thin film Cu2ZnGeSe4 solar cells », *Sol. Energy Mater. Sol. Cells*, vol. 171, p. 136-141, nov. 2017, doi: 10.1016/j.solmat.2017.06.050.
[119] K. Nagaya *et al.*, « Very small tail state formation in $Cu_2ZnGeSe_4$ », *Appl. Phys. Lett.*, vol. 113, n° 9, p. 093901, août 2018, doi: 10.1063/1.5031799.
[120] S. Oueslati *et al.*, « Effect of germanium incorporation on the properties of kesterite Cu2ZnSn(S,Se)4 monograins », *Thin Solid Films*, vol. 669, p. 315-320, janv. 2019, doi: 10.1016/j.tsf.2018.11.020.
[121] L. Choubrac *et al.*, « 7.6% CZGSe Solar Cells Thanks to Optimized CdS Chemical Bath Deposition », *Phys. Status Solidi A*, vol. 215, n° 13, p. 1800043, juill. 2018, doi: 10.1002/pssa.201800043.
[122] T. E. Everhart et R. F. M. Thornley, « Wide-band detector for micro-microampere low-energy electron currents », *J. Sci. Instrum.*, vol. 37, n° 7, p. 246-248, juill. 1960, doi: 10.1088/0950-7671/37/7/307.
[123] S. Lopez-Marino *et al.*, « The importance of back contact modification in Cu2ZnSnSe4 solar cells: The role of a thin MoO2 layer », *Nano Energy*, vol. 26, p. 708-721, août 2016, doi: 10.1016/j.nanoen.2016.06.034.
[124] A. Fairbrother *et al.*, « Secondary phase formation in Zn-rich $Cu_2ZnSnSe_4$ -based solar cells annealed in low pressure and temperature conditions: Secondary phase formation in Zn-rich $Cu_2ZnSnSe_4$ -based solar cells », *Prog. Photovolt. Res. Appl.*, vol. 22, n° 4, p. 479-487, avr. 2014, doi: 10.1002/pip.2473.
[125] L. H. Wong *et al.*, « Emerging inorganic solar cell efficiency tables (Version 1) », *J. Phys. Energy*, vol. 1, n° 3, p. 032001, juill. 2019, doi: 10.1088/2515-7655/ab2338.

[126] Q. Guo *et al.*, « Fabrication of 7.2% Efficient CZTSSe Solar Cells Using CZTS Nanocrystals », *J. Am. Chem. Soc.*, vol. 132, n° 49, p. 17384-17386, déc. 2010, doi: 10.1021/ja108427b.

[127] F. Liu *et al.*, « Kesterite $Cu_2ZnSn(S,Se)_4$ Solar Cells with beyond 8% Efficiency by a Sol–Gel and Selenization Process », *ACS Appl. Mater. Interfaces*, vol. 7, n° 26, p. 14376-14383, juill. 2015, doi: 10.1021/acsami.5b01151.

[128] S. Bag, O. Gunawan, T. Gokmen, Y. Zhu, T. K. Todorov, et D. B. Mitzi, « Low band gap liquid-processed CZTSe solar cell with 10.1% efficiency », *Energy Environ. Sci.*, vol. 5, n° 5, p. 7060, 2012, doi: 10.1039/c2ee00056c.

[129] G. Wang *et al.*, « Fabrication of a $Cu_2ZnSn(S,Se)_4$ Photovoltaic Device by a Low-Toxicity Ethanol Solution Process », *ACS Appl. Mater. Interfaces*, vol. 5, n° 20, p. 10042-10047, oct. 2013, doi: 10.1021/am402558a.

[130] S. G. Haass, M. Diethelm, M. Werner, B. Bissig, Y. E. Romanyuk, et A. N. Tiwari, « 11.2% Efficient Solution Processed Kesterite Solar Cell with a Low Voltage Deficit », *Adv. Energy Mater.*, vol. 5, n° 18, p. 1500712, sept. 2015, doi: 10.1002/aenm.201500712.

[131] W. Wang *et al.*, « Device characteristics of CZTSSe thin-film solar cells with 12.6% efficiency », *Adv. Energy Mater.*, vol. 4, n° 7, p. 1-5, 2014, doi: 10.1002/aenm.201301465.

[132] S. Siebentritt, « Why are kesterite solar cells not 20% efficient? », *Thin Solid Films*, vol. 535, p. 1-4, mai 2013, doi: 10.1016/j.tsf.2012.12.089.

[133] J. Kim, S. Park, S. Ryu, J. Oh, et B. Shin, « Improving the open-circuit voltage of $Cu_2ZnSnSe_4$ thin film solar cells via interface passivation: Open-circuit voltage of $Cu_2ZnSnSe_4$ thin film solar cells », *Prog. Photovolt. Res. Appl.*, vol. 25, n° 4, p. 308-317, avr. 2017, doi: 10.1002/pip.2864.

[134] D. B. Mitzi, O. Gunawan, T. K. Todorov, K. Wang, et S. Guha, « The path towards a high-performance solution-processed kesterite solar cell », *Sol. Energy Mater. Sol. Cells*, vol. 95, n° 6, p. 1421-1436, juin 2011, doi: 10.1016/j.solmat.2010.11.028.

[135] O. Gunawan, T. Gokmen, et D. B. Mitzi, « Suns- V_{OC} characteristics of high performance kesterite solar cells », *J. Appl. Phys.*, vol. 116, n° 8, p. 084504, août 2014, doi: 10.1063/1.4893315.

[136] A. Polizzotti, I. L. Repins, R. Noufi, S.-H. Wei, et D. B. Mitzi, « The state and future prospects of kesterite photovoltaics », *Energy Environ. Sci.*, vol. 6, n° 11, p. 3171, 2013, doi: 10.1039/c3ee41781f.

[137] D. B. Mitzi, O. Gunawan, T. K. Todorov, et D. A. R. Barkhouse, « Prospects and performance limitations for Cu–Zn–Sn–S–Se photovoltaic technology », *Philos. Trans. R. Soc. Math. Phys. Eng. Sci.*, vol. 371, n° 1996, p. 20110432, août 2013, doi: 10.1098/rsta.2011.0432.

[138] N. A. Kattan, I. J. Griffiths, D. Cherns, et D. J. Fermín, « Observation of antisite domain boundaries in Cu_2ZnSnS_4 by atomic-resolution transmission electron microscopy », *Nanoscale*, vol. 8, n° 30, p. 14369-14373, 2016, doi: 10.1039/C6NR04185J.

[139] S. Chen, X. G. Gong, A. Walsh, et S.-H. Wei, « Defect physics of the kesterite thin-film solar cell absorber Cu2ZnSnS4 », *Appl. Phys. Lett.*, vol. 96, n° 2, p. 021902, janv. 2010, doi: 10.1063/1.3275796.

[140] B. G. Mendis *et al.*, « The nature of electrostatic potential fluctuations in Cu_2ZnSnS_4 and their role on photovoltaic device performance », *J. Phys. Conf. Ser.*, vol. 471, p. 012014, nov. 2013, doi: 10.1088/1742-6596/471/1/012014.

[141] D. M. Bishop, B. McCandless, T. Gershon, M. A. Lloyd, R. Haight, et R. Birkmire, « Modification of defects and potential fluctuations in slow-cooled and quenched $Cu_2ZnSnSe_4$ single crystals », *J. Appl. Phys.*, vol. 121, n° 6, p. 065704, févr. 2017, doi: 10.1063/1.4975483.

[142] G. Rey *et al.*, « On the origin of band-tails in kesterite », *Sol. Energy Mater. Sol. Cells*, vol. 179, p. 142-151, juin 2018, doi: 10.1016/j.solmat.2017.11.005.

[143] J. J. S. Scragg *et al.*, « Cu-Zn disorder and band gap fluctuations in $Cu_2ZnSn(S,Se)_4$: Theoretical and experimental investigations: Cu-Zn disorder and band gap fluctuations in $Cu_2ZnSn(S,Se)_4$ », *Phys. Status Solidi B*, vol. 253, n° 2, p. 247-254, févr. 2016, doi: 10.1002/pssb.201552530.

[144] C. Platzer-Björkman *et al.*, « Reduced interface recombination in Cu_2ZnSnS_4 solar cells with atomic layer deposition $Zn_{1-x}Sn_xO_y$ buffer layers », *Appl. Phys. Lett.*, vol. 107, n° 24, p. 243904, déc. 2015, doi: 10.1063/1.4937998.
[145] C. Yan *et al.*, « Band alignments of different buffer layers (CdS, Zn(O,S), and In_2S_3) on Cu_2ZnSnS_4 », *Appl. Phys. Lett.*, vol. 104, n° 17, p. 173901, avr. 2014, doi: 10.1063/1.4873715.
[146] J. H. Kim *et al.*, « Atomic-Scale Observation of Oxygen Substitution and Its Correlation with Hole-Transport Barriers in $Cu_2ZnSnSe_4$ Thin-Film Solar Cells », *Adv. Energy Mater.*, vol. 6, n° 6, p. 1501902, mars 2016, doi: 10.1002/aenm.201501902.
[147] D. A. Tuan, N. H. Ke, P. Thi Kieu Loan, et L. V. T. Hung, « A method to improve crystal quality of CZTSSe absorber layer », *J. Sol-Gel Sci. Technol.*, vol. 87, n° 1, p. 245-253, juill. 2018, doi: 10.1007/s10971-018-4708-9.
[148] M. Neuschitzer *et al.*, « V_{oc} Boosting and Grain Growth Enhancing Ge-Doping Strategy for $Cu_2ZnSnSe_4$ Photovoltaic Absorbers », *J. Phys. Chem. C*, vol. 120, n° 18, p. 9661-9670, mai 2016, doi: 10.1021/acs.jpcc.6b02315.
[149] S. Kim, K. M. Kim, H. Tampo, H. Shibata, et S. Niki, « Improvement of voltage deficit of Ge-incorporated kesterite solar cell with 12.3% conversion efficiency », *Appl. Phys. Express*, vol. 9, n° 10, p. 102301, oct. 2016, doi: 10.7567/APEX.9.102301.
[150] L. Choubrac *et al.*, « Sn Substitution by Ge: Strategies to Overcome the Open-Circuit Voltage Deficit of Kesterite Solar Cells », *ACS Appl. Energy Mater.*, vol. 3, n° 6, p. 5830-5839, juin 2020, doi: 10.1021/acsaem.0c00763.
[151] R. Gunder, J. A. Márquez-Prieto, G. Gurieva, T. Unold, et S. Schorr, « Structural characterization of off-stoichiometric kesterite-type $Cu_2ZnGeSe_4$ compound semiconductors: from cation distribution to intrinsic point defect density », *CrystEngComm*, vol. 20, n° 11, p. 1491-1498, 2018, doi: 10.1039/C7CE02090B.
[152] M. Courel, T. G. Sanchez, N. R. Mathews, et X. Mathew, « Cu_2ZnGeS_4 thin films deposited by thermal evaporation: the impact of Ge concentration on physical properties », *J. Phys. Appl. Phys.*, vol. 51, n° 9, p. 095107, mars 2018, doi: 10.1088/1361-6463/aaa7db.
[153] M. Neuschitzer *et al.*, « Optimization of CdS buffer layer for high-performance $Cu_2ZnSnSe_4$ solar cells and the effects of light soaking: elimination of crossover and red kink: CdS and effects of light soaking: elimination of crossover and red kink », *Prog. Photovolt. Res. Appl.*, vol. 23, n° 11, p. 1660-1667, nov. 2015, doi: 10.1002/pip.2589.
[154] D. M. Berg *et al.*, « Discrimination and detection limits of secondary phases in Cu 2 ZnSnS 4 using X-ray diffraction and Raman spectroscopy », *Thin Solid Films*, vol. 569, p. 113-123, oct. 2014, doi: 10.1016/j.tsf.2014.08.028.
[155] S. Schorr *et al.*, « Point defects, compositional fluctuations, and secondary phases in non-stoichiometric kesterites », *J. Phys. Energy*, vol. 2, n° 1, p. 012002, déc. 2019, doi: 10.1088/2515-7655/ab4a25.
[156] Y. Yang *et al.*, « Air-Stable In-Plane Anisotropic $GeSe_2$ for Highly Polarization-Sensitive Photodetection in Short Wave Region », *J. Am. Chem. Soc.*, vol. 140, n° 11, p. 4150-4156, mars 2018, doi: 10.1021/jacs.8b01234.
[157] H. R. Chandrasekhar et U. Zwick, « Raman scattering and infrared reflectivity in GeSe », *Solid State Commun.*, vol. 18, n° 11-12, p. 1509-1513, mai 1976, doi: 10.1016/0038-1098(76)90381-1.
[158] M. Fujii, S. Hayashi, et K. Yamamoto, « Growth of Ge Microcrystals in SiO_2 Thin Film Matrices: A Raman and Electron Microscopic Study », *Jpn. J. Appl. Phys.*, vol. 30, n° Part 1, No. 4, p. 687-694, avr. 1991, doi: 10.1143/JJAP.30.687.
[159] S. G. Choi *et al.*, « Optical properties of cubic-phase Cu_2GeSe_4 single crystal », *J. Appl. Phys.*, vol. 114, n° 3, p. 033531, juill. 2013, doi: 10.1063/1.4816051.
[160] G. Marcano *et al.*, « Raman scattering and X-ray diffraction study in Cu2GeSe3 », *Solid State Commun.*, vol. 146, n° 1-2, p. 65-68, avr. 2008, doi: 10.1016/j.ssc.2008.01.018.

[161] M. Guc, S. Levcenko, V. Izquierdo-Roca, X. Fontané, E. Arushanov, et A. Pérez-Rodríguez, « Polarized Raman scattering analysis of $Cu_2ZnSnSe_4$ and $Cu_2ZnGeSe_4$ single crystals », *J. Appl. Phys.*, vol. 114, n° 19, p. 193514, nov. 2013, doi: 10.1063/1.4830028.
[162] M. Y. Valakh *et al.*, « Fermi resonance in the phonon spectra of quaternary chalcogenides of the type Cu_2ZnGeS_4 », *J. Phys. Condens. Matter*, vol. 28, n° 6, p. 065401, févr. 2016, doi: 10.1088/0953-8984/28/6/065401.
[163] M. Ya. Valakh *et al.*, « Optical properties of quaternary kesterite-type $Cu_2Zn(Sn_{1-x}Ge_x)S_4$ crystalline alloys: Raman scattering, photoluminescence and first-principle calculations », *RSC Adv.*, vol. 6, n° 72, p. 67756-67763, 2016, doi: 10.1039/C6RA13608G.
[164] J. Márquez *et al.*, « Chemistry and Dynamics of Ge in Kesterite: Toward Band-Gap-Graded Absorbers », *Chem. Mater.*, vol. 29, n° 21, p. 9399-9406, nov. 2017, doi: 10.1021/acs.chemmater.7b03416.
[165] L. Yin, G. Cheng, Y. Feng, Z. Li, C. Yang, et X. Xiao, « Limitation factors for the performance of kesterite Cu_2ZnSnS_4 thin film solar cells studied by defect characterization », *RSC Adv.*, vol. 5, n° 50, p. 40369-40374, 2015, doi: 10.1039/C5RA00069F.
[166] J. V. Li *et al.*, « Theoretical analysis of effects of deep level, back contact, and absorber thickness on capacitance–voltage profiling of CdTe thin-film solar cells », *Sol. Energy Mater. Sol. Cells*, vol. 100, p. 126-131, mai 2012, doi: 10.1016/j.solmat.2012.01.003.
[167] J. T. Heath, J. D. Cohen, et W. N. Shafarman, « Bulk and metastable defects in CuIn1−xGaxSe2 thin films using drive-level capacitance profiling », *J. Appl. Phys.*, vol. 95, n° 3, p. 1000-1010, févr. 2004, doi: 10.1063/1.1633982.
[168] T. Nagai *et al.*, « Characterization of Surface and Heterointerface of $Cu_2ZnSn_{1-x}Ge_xSe_4$ for Solar Cell Applications », *Phys. Status Solidi RRL – Rapid Res. Lett.*, vol. 14, n° 4, p. 1900708, avr. 2020, doi: 10.1002/pssr.201900708.
[169] M. Ould Salem *et al.*, « Over 10% Efficient Wide Bandgap CIGSe Solar Cells on Transparent Substrate with Na Predeposition Treatment », *Sol. RRL*, p. 2000284, sept. 2020, doi: 10.1002/solr.202000284.
[170] A. Cuevas, « The Recombination Parameter J0 », *Energy Procedia*, vol. 55, p. 53-62, 2014, doi: 10.1016/j.egypro.2014.08.073.
[171] J. Li *et al.*, « 10% Efficiency Cu2ZnSn(S,Se)4 thin film solar cells fabricated by magnetron sputtering with enlarged depletion region width », *Sol. Energy Mater. Sol. Cells*, vol. 149, p. 242-249, mai 2016, doi: 10.1016/j.solmat.2016.02.002.
[172] J. Chantana, Y. Kawano, T. Nishimura, A. Mavlonov, et T. Minemoto, « Impact of Urbach energy on open-circuit voltage deficit of thin-film solar cells », *Sol. Energy Mater. Sol. Cells*, vol. 210, p. 110502, juin 2020, doi: 10.1016/j.solmat.2020.110502.
[173] H. Xie *et al.*, « Impact of Na Dynamics at the $Cu_2ZnSn(S,Se)_4$/CdS Interface During Post Low Temperature Treatment of Absorbers », *ACS Appl. Mater. Interfaces*, vol. 8, n° 7, p. 5017-5024, févr. 2016, doi: 10.1021/acsami.5b12243.
[174] E. Ojeda-Durán *et al.*, « CZTS solar cells and the possibility of increasing VOC using evaporated Al2O3 at the CZTS/CdS interface », *Sol. Energy*, vol. 198, p. 696-703, mars 2020, doi: 10.1016/j.solener.2020.02.009.
[175] X. Li *et al.*, « Achieving 11.95% efficient $Cu_2ZnSnSe_4$ solar cells fabricated by sputtering a Cu–Zn–Sn–Se quaternary compound target with a selenization process », *J. Mater. Chem. A*, vol. 7, n° 16, p. 9948-9957, 2019, doi: 10.1039/C9TA00385A.
[176] S. Kim, J. A. Márquez, T. Unold, et A. Walsh, « Upper limit to the photovoltaic efficiency of imperfect crystals from first principles », *Energy Environ. Sci.*, vol. 13, n° 5, p. 1481-1491, 2020, doi: 10.1039/D0EE00291G.
[177] T. Kobayashi, Z. J. L. Kao, et T. Nakada, « Temperature dependent current–voltage and admittance spectroscopy on heat-light soaking effects of Cu(In,Ga)Se2 solar cells with ALD-Zn(O,S) and

CBD-ZnS(O,OH) buffer layers », *Sol. Energy Mater. Sol. Cells*, vol. 143, p. 159-167, déc. 2015, doi: 10.1016/j.solmat.2015.06.044.
[178] V. Nadenau, U. Rau, A. Jasenek, et H. W. Schock, « Electronic properties of CuGaSe2-based heterojunction solar cells. Part I. Transport analysis », *J. Appl. Phys.*, vol. 87, n° 1, p. 584-593, janv. 2000, doi: 10.1063/1.371903.
[179] K. Wang *et al.*, « Thermally evaporated Cu2ZnSnS4 solar cells », *Appl. Phys. Lett.*, vol. 97, n° 14, p. 143508, oct. 2010, doi: 10.1063/1.3499284.
[180] Y. Houari, J. Speirs, C. Candelise, et R. Gross, « A system dynamics model of tellurium availability for CdTe PV: A system dynamics model of Te availability for CdTe PV », *Prog. Photovolt. Res. Appl.*, vol. 22, n° 1, p. 129-146, janv. 2014, doi: 10.1002/pip.2359.
[181] R. Fonoll-Rubio *et al.*, « Insights into interface and bulk defects in a high efficiency kesterite-based device », *Energy Environ. Sci.*, p. 10.1039.D0EE02004D, 2021, doi: 10.1039/D0EE02004D.
[182] A. D. Collord et H. W. Hillhouse, « Composition Control and Formation Pathway of CZTS and CZTGS Nanocrystal Inks for Kesterite Solar Cells », *Chem. Mater.*, vol. 27, n° 5, p. 1855-1862, mars 2015, doi: 10.1021/acs.chemmater.5b00104.
[183] J. Andrade-Arvizu *et al.*, « Is It Possible To Develop Complex S–Se Graded Band Gap Profiles in Kesterite-Based Solar Cells? », *ACS Appl. Mater. Interfaces*, vol. 11, n° 36, p. 32945-32956, sept. 2019, doi: 10.1021/acsami.9b09813.
[184] S. Levcenko *et al.*, « Preparation and optical characterization of Cu2ZnGeSe4 thin films », *Opt. Mater.*, vol. 40, p. 76-80, févr. 2015, doi: 10.1016/j.optmat.2014.11.050.
[185] M. León *et al.*, « Optical constants of Cu2ZnGeS4 bulk crystals », *J. Appl. Phys.*, vol. 108, n° 9, p. 093502, nov. 2010, doi: 10.1063/1.3500439.
[186] Y. Sánchez *et al.*, « Ultra-thin CdS for highly performing chalcogenides thin film based solar cells », *Sol. Energy Mater. Sol. Cells*, vol. 158, p. 138-146, déc. 2016, doi: 10.1016/j.solmat.2015.12.037.
[187] G. Varoquaux, L. Buitinck, G. Louppe, O. Grisel, F. Pedregosa, et A. Mueller, « Scikit-learn: Machine Learning Without Learning the Machinery », *GetMobile Mob. Comput. Commun.*, vol. 19, n° 1, p. 29-33, juin 2015, doi: 10.1145/2786984.2786995.
[188] A. Lafond, L. Choubrac, C. Guillot-Deudon, P. Deniard, et S. Jobic, « Crystal Structures of Photovoltaic Chalcogenides, an Intricate Puzzle to Solve: the Cases of CIGSe and CZTS Materials », *Z. Für Anorg. Allg. Chem.*, vol. 638, n° 15, p. 2571-2577, déc. 2012, doi: 10.1002/zaac.201200279.
[189] M. Dimitrievska *et al.*, « Resonant Raman scattering of $ZnS_x Se_{1-x}$ solid solutions: the role of S and Se electronic states », *Phys. Chem. Chem. Phys.*, vol. 18, n° 11, p. 7632-7640, 2016, doi: 10.1039/C5CP04498G.
[190] M. Y. Valakh *et al.*, « Raman scattering and disorder effect in $Cu_2 ZnSnS_4$: Raman scattering and disorder effect in $Cu_2 ZnSnS_4$ », *Phys. Status Solidi RRL - Rapid Res. Lett.*, vol. 7, n° 4, p. 258-261, avr. 2013, doi: 10.1002/pssr.201307073.
[191] M. Dimitrievska, A. Fairbrother, A. Pérez-Rodríguez, E. Saucedo, et V. Izquierdo-Roca, « Raman scattering crystalline assessment of polycrystalline Cu2ZnSnS4 thin films for sustainable photovoltaic technologies: Phonon confinement model », *Acta Mater.*, vol. 70, p. 272-280, mai 2014, doi: 10.1016/j.actamat.2014.02.035.
[192] A. Ritscher, M. Hoelzel, et M. Lerch, « The order-disorder transition in Cu2ZnSnS4 – A neutron scattering investigation », *J. Solid State Chem.*, vol. 238, p. 68-73, juin 2016, doi: 10.1016/j.jssc.2016.03.013.
[193] D. M. Többens, G. Gurieva, S. Levcenko, T. Unold, et S. Schorr, « Temperature dependency of Cu/Zn ordering in CZTSe kesterites determined by anomalous diffraction: Temperature dependency of Cu/Zn ordering in CZTSe kesterites », *Phys. Status Solidi B*, vol. 253, n° 10, p. 1890-1897, oct. 2016, doi: 10.1002/pssb.201600372.

[194] N. Benhaddou *et al.*, « Investigation on limiting factors affecting Cu2ZnGeSe4 efficiency: Effect of annealing conditions and surface treatment », *Sol. Energy Mater. Sol. Cells*, vol. 216, p. 110701, oct. 2020, doi: 10.1016/j.solmat.2020.110701.
[195] M. Dimitrievska, A. Fairbrother, E. Saucedo, A. Pérez-Rodríguez, et V. Izquierdo-Roca, « Influence of compositionally induced defects on the vibrational properties of device grade $Cu_2ZnSnSe_4$ absorbers for kesterite based solar cells », *Appl. Phys. Lett.*, vol. 106, n° 7, p. 073903, févr. 2015, doi: 10.1063/1.4913262.
[196] E. Sleeckx, L. Tichý, P. Nagels, et R. Callaerts, « Thermally and photo-induced irreversible changes in the optical properties of amorphous GexSe100-x films », *J. Non-Cryst. Solids*, vol. 198-200, p. 723-727, mai 1996, doi: 10.1016/0022-3093(96)00030-0.
[197] B. K. Sarkar, A. S. Verma, et P. S. Deviprasad, « Temperature induced band gap shrinkage in Cu2GeSe3: Role of electron–phonon interaction », *Phys. B Condens. Matter*, vol. 406, n° 14, p. 2847-2850, juill. 2011, doi: 10.1016/j.physb.2011.04.045.
[198] L. E. Valle Rios, K. Neldner, G. Gurieva, et S. Schorr, « Existence of off-stoichiometric single phase kesterite », *J. Alloys Compd.*, vol. 657, p. 408-413, févr. 2016, doi: 10.1016/j.jallcom.2015.09.198.
[199] I. Becerril-Romero *et al.*, « CZTSe solar cells developed on polymer substrates: Effects of low-temperature processing », *Prog. Photovolt. Res. Appl.*, vol. 26, n° 1, p. 55-68, janv. 2018, doi: 10.1002/pip.2945.
[200] G. Gurieva, L. E. Valle Rios, A. Franz, P. Whitfield, et S. Schorr, « Intrinsic point defects in off-stoichiometric $Cu_2ZnSnSe_4$: A neutron diffraction study », *J. Appl. Phys.*, vol. 123, n° 16, p. 161519, avr. 2018, doi: 10.1063/1.4997402.
[201] M. Dimitrievska, A. Fairbrother, E. Saucedo, A. Pérez-Rodríguez, et V. Izquierdo-Roca, « Secondary phase and Cu substitutional defect dynamics in kesterite solar cells: Impact on optoelectronic properties », *Sol. Energy Mater. Sol. Cells*, vol. 149, p. 304-309, mai 2016, doi: 10.1016/j.solmat.2016.01.029.
[202] M. Grossberg *et al.*, « The electrical and optical properties of kesterites », *J. Phys. Energy*, vol. 1, n° 4, p. 044002, août 2019, doi: 10.1088/2515-7655/ab29a0.
[203] M. M. Islam *et al.*, « Determination of deep-level defects in $Cu_2ZnSn(S,Se)_4$ thin-films using photocapacitance method », *Appl. Phys. Lett.*, vol. 106, n° 24, p. 243905, juin 2015, doi: 10.1063/1.4922810.
[204] S. Levcenko *et al.*, « Deep Defects in Cu 2 ZnSn (S , Se) 4 Solar Cells with Varying Se Content », *Phys. Rev. Appl.*, vol. 5, n° 2, p. 024004, févr. 2016, doi: 10.1103/PhysRevApplied.5.024004.
[205] M. Guc *et al.*, « Polarized Raman scattering study of kesterite type Cu2ZnSnS4 single crystals », *Sci. Rep.*, vol. 6, n° 1, p. 19414, mai 2016, doi: 10.1038/srep19414.
[206] M. Valentini *et al.*, « Effect of the order-disorder transition on the optical properties of Cu_2ZnSnS_4 », *Appl. Phys. Lett.*, vol. 108, n° 21, p. 211909, mai 2016, doi: 10.1063/1.4952973.
[207] D. P. Halliday, R. Claridge, M. C. J. Goodman, B. G. Mendis, K. Durose, et J. D. Major, « Luminescence of Cu_2ZnSnS_4 polycrystals described by the fluctuating potential model », *J. Appl. Phys.*, vol. 113, n° 22, p. 223503, juin 2013, doi: 10.1063/1.4810846.
[208] T. Gershon, B. Shin, T. Gokmen, S. Lu, N. Bojarczuk, et S. Guha, « Relationship between Cu_2ZnSnS_4 quasi donor-acceptor pair density and solar cell efficiency », *Appl. Phys. Lett.*, vol. 103, n° 19, p. 193903, nov. 2013, doi: 10.1063/1.4829920.
[209] N. M. Ralbovsky et I. K. Lednev, « Raman spectroscopy and chemometrics: A potential universal method for diagnosing cancer », *Spectrochim. Acta. A. Mol. Biomol. Spectrosc.*, vol. 219, p. 463-487, août 2019, doi: 10.1016/j.saa.2019.04.067.
[210] R. Chauhan, R. Kumar, V. Kumar, K. Sharma, et V. Sharma, « On the discrimination of soil samples by derivative diffuse reflectance UV–vis-NIR spectroscopy and chemometric methods », *Forensic Sci. Int.*, vol. 319, p. 110655, févr. 2021, doi: 10.1016/j.forsciint.2020.110655.

[211] Z. Guleken *et al.*, « Investigation of the discrimination and characterization of blood serum structure in patients with opioid use disorder using IR spectroscopy and PCA-LDA analysis », *J. Pharm. Biomed. Anal.*, vol. 190, p. 113553, oct. 2020, doi: 10.1016/j.jpba.2020.113553.
[212] R. Chophi, S. Sharma, et R. Singh, « Forensic analysis of red lipsticks using ATR-FTIR spectroscopy and chemometrics », *Forensic Chem.*, vol. 17, p. 100209, mars 2020, doi: 10.1016/j.forc.2019.100209.
[213] Y. Wang, J. Zhu, et X. Chen, « Autofluorescence spectroscopy of blood plasma with multivariate analysis methods for the diagnosis of pulmonary tuberculosis », *Optik*, vol. 224, p. 165446, déc. 2020, doi: 10.1016/j.ijleo.2020.165446.
[214] H. Shirakawa, E. J. Louis, A. G. MacDiarmid, C. K. Chiang, et A. J. Heeger, « Synthesis of electrically conducting organic polymers: halogen derivatives of polyacetylene, (CH) x », *J. Chem. Soc. Chem. Commun.*, n° 16, p. 578, 1977, doi: 10.1039/c39770000578.
[215] H. Kallmann et M. Pope, « Photovoltaic Effect in Organic Crystals », *J. Chem. Phys.*, vol. 30, n° 2, p. 585-586, févr. 1959, doi: 10.1063/1.1729992.
[216] G. A. Chamberlain, « Organic solar cells: A review », *Sol. Cells*, vol. 8, n° 1, p. 47-83, févr. 1983, doi: 10.1016/0379-6787(83)90039-X.
[217] C. W. Tang, « Two-layer organic photovoltaic cell », *Appl. Phys. Lett.*, vol. 48, n° 2, p. 183-185, janv. 1986, doi: 10.1063/1.96937.
[218] M. Hiramoto, H. Fujiwara, et M. Yokoyama, « Three-layered organic solar cell with a photoactive interlayer of codeposited pigments », *Appl. Phys. Lett.*, vol. 58, n° 10, p. 1062-1064, mars 1991, doi: 10.1063/1.104423.
[219] G. Yu, J. Gao, J. C. Hummelen, F. Wudl, et A. J. Heeger, « Polymer Photovoltaic Cells: Enhanced Efficiencies via a Network of Internal Donor-Acceptor Heterojunctions », *Science*, vol. 270, n° 5243, p. 1789-1791, déc. 1995, doi: 10.1126/science.270.5243.1789.
[220] N. S. Sariciftci *et al.*, « Semiconducting polymer-buckminsterfullerene heterojunctions: Diodes, photodiodes, and photovoltaic cells », *Appl. Phys. Lett.*, vol. 62, n° 6, p. 585-587, févr. 1993, doi: 10.1063/1.108863.
[221] Z. Hu, L. Ying, F. Huang, et Y. Cao, « Towards a bright future: polymer solar cells with power conversion efficiencies over 10% », *Sci. China Chem.*, vol. 60, n° 5, p. 571-582, mai 2017, doi: 10.1007/s11426-016-0424-9.
[222] J. Zhao *et al.*, « Efficient organic solar cells processed from hydrocarbon solvents », *Nat. Energy*, vol. 1, n° 2, p. 15027, févr. 2016, doi: 10.1038/nenergy.2015.27.
[223] Y. Cai, L. Huo, et Y. Sun, « Recent Advances in Wide-Bandgap Photovoltaic Polymers », *Adv. Mater.*, vol. 29, n° 22, p. 1605437, juin 2017, doi: 10.1002/adma.201605437.
[224] L. Dou, Y. Liu, Z. Hong, G. Li, et Y. Yang, « Low-Bandgap Near-IR Conjugated Polymers/Molecules for Organic Electronics », *Chem. Rev.*, vol. 115, n° 23, p. 12633-12665, déc. 2015, doi: 10.1021/acs.chemrev.5b00165.
[225] Z. Li *et al.*, « Solution Processable Rhodanine-Based Small Molecule Organic Photovoltaic Cells with a Power Conversion Efficiency of 6.1% », *Adv. Energy Mater.*, vol. 2, n° 1, p. 74-77, janv. 2012, doi: 10.1002/aenm.201100572.
[226] Y. Liu *et al.*, « Solution-processed small-molecule solar cells: breaking the 10% power conversion efficiency », *Sci. Rep.*, vol. 3, n° 1, p. 3356, déc. 2013, doi: 10.1038/srep03356.
[227] K. Sun *et al.*, « A molecular nematic liquid crystalline material for high-performance organic photovoltaics », *Nat. Commun.*, vol. 6, n° 1, p. 6013, mai 2015, doi: 10.1038/ncomms7013.
[228] B. Kan *et al.*, « A Series of Simple Oligomer-like Small Molecules Based on Oligothiophenes for Solution-Processed Solar Cells with High Efficiency », *J. Am. Chem. Soc.*, vol. 137, n° 11, p. 3886-3893, mars 2015, doi: 10.1021/jacs.5b00305.

[229] J. Wan, X. Xu, G. Zhang, Y. Li, K. Feng, et Q. Peng, « Highly efficient halogen-free solvent processed small-molecule organic solar cells enabled by material design and device engineering », *Energy Environ. Sci.*, vol. 10, nº 8, p. 1739-1745, 2017, doi: 10.1039/C7EE00805H.
[230] S. Holliday *et al.*, « High-efficiency and air-stable P3HT-based polymer solar cells with a new non-fullerene acceptor », *Nat. Commun.*, vol. 7, nº 1, p. 11585, sept. 2016, doi: 10.1038/ncomms11585.
[231] Y. Lin *et al.*, « High-Performance Electron Acceptor with Thienyl Side Chains for Organic Photovoltaics », *J. Am. Chem. Soc.*, vol. 138, nº 14, p. 4955-4961, avr. 2016, doi: 10.1021/jacs.6b02004.
[232] Y. Qin *et al.*, « Highly Efficient Fullerene-Free Polymer Solar Cells Fabricated with Polythiophene Derivative », *Adv. Mater.*, vol. 28, nº 42, p. 9416-9422, nov. 2016, doi: 10.1002/adma.201601803.
[233] W. Zhao *et al.*, « Molecular Optimization Enables over 13% Efficiency in Organic Solar Cells », *J. Am. Chem. Soc.*, vol. 139, nº 21, p. 7148-7151, mai 2017, doi: 10.1021/jacs.7b02677.
[234] M. Fox et G. F. Bertsch, « *Optical Properties of Solids* », *Am. J. Phys.*, vol. 70, nº 12, p. 1269-1270, déc. 2002, doi: 10.1119/1.1691372.
[235] I. G. Hill, A. Kahn, Z. G. Soos, et R. A. Pascal, Jr, « Charge-separation energy in films of π-conjugated organic molecules », *Chem. Phys. Lett.*, vol. 327, nº 3-4, p. 181-188, sept. 2000, doi: 10.1016/S0009-2614(00)00882-4.
[236] X.-Y. Zhao et H.-J. Liu, « Review of polymer materials with low dielectric constant », *Polym. Int.*, p. n/a-n/a, 2010, doi: 10.1002/pi.2809.
[237] I. Bruder, « Organic solar cells : correlation between molecular structure, morphology and device performance », 2010, doi: 10.18419/OPUS-6728.
[238] C. Guo, W. Hong, H. Aziz, et Y. Li, « Recent Progress in High Mobility Polymer Semiconductors for Organic Thin Film Transistors », *Rev. Adv. Sci. Eng.*, vol. 1, nº 3, p. 200-224, sept. 2012, doi: 10.1166/rase.2012.1014.
[239] Y. Liu *et al.*, « Aggregation and morphology control enables multiple cases of high-efficiency polymer solar cells », *Nat. Commun.*, vol. 5, nº 1, p. 5293, déc. 2014, doi: 10.1038/ncomms6293.
[240] O. A. Ibraikulov *et al.*, « Using pyridal[2,1,3]thiadiazole as an acceptor unit in a low band-gap copolymer for photovoltaic applications », *Org. Electron.*, vol. 23, p. 171-178, août 2015, doi: 10.1016/j.orgel.2015.04.018.
[241] M. Knupfer, « Exciton binding energies in organic semiconductors », *Appl. Phys. A*, vol. 77, nº 5, p. 623-626, oct. 2003, doi: 10.1007/s00339-003-2182-9.
[242] C. Deibel *et al.*, « Energetics of excited states in the conjugated polymer poly(3-hexylthiophene) », *Phys. Rev. B*, vol. 81, nº 8, p. 085202, févr. 2010, doi: 10.1103/PhysRevB.81.085202.
[243] P. E. Shaw, A. Ruseckas, et I. D. W. Samuel, « Exciton Diffusion Measurements in Poly(3-hexylthiophene) », *Adv. Mater.*, vol. 20, nº 18, p. 3516-3520, juill. 2008, doi: 10.1002/adma.200800982.
[244] S. De *et al.*, « Exciton dynamics in alternating polyfluorene/fullerene blends », *Chem. Phys.*, vol. 350, nº 1-3, p. 14-22, juin 2008, doi: 10.1016/j.chemphys.2007.11.018.
[245] J.-L. Brédas, D. Beljonne, V. Coropceanu, et J. Cornil, « Charge-Transfer and Energy-Transfer Processes in π-Conjugated Oligomers and Polymers: A Molecular Picture », *Chem. Rev.*, vol. 104, nº 11, p. 4971-5004, nov. 2004, doi: 10.1021/cr040084k.
[246] M. C. Scharber *et al.*, « Design Rules for Donors in Bulk-Heterojunction Solar Cells—Towards 10 % Energy-Conversion Efficiency », *Adv. Mater.*, vol. 18, nº 6, p. 789-794, mars 2006, doi: 10.1002/adma.200501717.
[247] Y. Lin et X. Zhan, « Non-fullerene acceptors for organic photovoltaics: an emerging horizon », *Mater. Horiz.*, vol. 1, nº 5, p. 470, avr. 2014, doi: 10.1039/C4MH00042K.
[248] C. Zhan, X. Zhang, et J. Yao, « New advances in non-fullerene acceptor based organic solar cells », *RSC Adv.*, vol. 5, nº 113, p. 93002-93026, 2015, doi: 10.1039/C5RA17715D.

[249] C. B. Nielsen, S. Holliday, H.-Y. Chen, S. J. Cryer, et I. McCulloch, « Non-Fullerene Electron Acceptors for Use in Organic Solar Cells », *Acc. Chem. Res.*, vol. 48, nº 11, p. 2803-2812, nov. 2015, doi: 10.1021/acs.accounts.5b00199.
[250] K. Vandewal *et al.*, « Quantification of Quantum Efficiency and Energy Losses in Low Bandgap Polymer:Fullerene Solar Cells with High Open-Circuit Voltage », *Adv. Funct. Mater.*, vol. 22, nº 16, p. 3480-3490, août 2012, doi: 10.1002/adfm.201200608.
[251] G. Ren *et al.*, « Photoinduced Hole Transfer Becomes Suppressed with Diminished Driving Force in Polymer-Fullerene Solar Cells While Electron Transfer Remains Active », *Adv. Funct. Mater.*, vol. 23, nº 10, p. 1238-1249, mars 2013, doi: 10.1002/adfm.201201470.
[252] E. T. Hoke *et al.*, « Recombination in Polymer:Fullerene Solar Cells with Open-Circuit Voltages Approaching and Exceeding 1.0 V », *Adv. Energy Mater.*, vol. 3, nº 2, p. 220-230, févr. 2013, doi: 10.1002/aenm.201200474.
[253] N. S. Sariciftci, L. Smilowitz, A. J. Heeger, et F. Wudl, « Photoinduced Electron Transfer from a Conducting Polymer to Buckminsterfullerene », *Science*, vol. 258, nº 5087, p. 1474-1476, nov. 1992, doi: 10.1126/science.258.5087.1474.
[254] C. J. Brabec *et al.*, « Tracing photoinduced electron transfer process in conjugated polymer/fullerene bulk heterojunctions in real time », *Chem. Phys. Lett.*, vol. 340, nº 3-4, p. 232-236, juin 2001, doi: 10.1016/S0009-2614(01)00431-6.
[255] N. K. Elumalai et A. Uddin, « Open circuit voltage of organic solar cells: an in-depth review », *Energy Environ. Sci.*, vol. 9, nº 2, p. 391-410, 2016, doi: 10.1039/C5EE02871J.
[256] F. Gao, W. Tress, J. Wang, et O. Inganäs, « Temperature Dependence of Charge Carrier Generation in Organic Photovoltaics », *Phys. Rev. Lett.*, vol. 114, nº 12, p. 128701, mars 2015, doi: 10.1103/PhysRevLett.114.128701.
[257] M. C. Scharber, « On the Efficiency Limit of Conjugated Polymer:Fullerene-Based Bulk Heterojunction Solar Cells », *Adv. Mater.*, vol. 28, nº 10, p. 1994-2001, mars 2016, doi: 10.1002/adma.201504914.
[258] K. M. Pelzer et S. B. Darling, « Charge generation in organic photovoltaics: a review of theory and computation », *Mol. Syst. Des. Eng.*, vol. 1, nº 1, p. 10-24, 2016, doi: 10.1039/C6ME00005C.
[259] T. M. Clarke et J. R. Durrant, « Charge Photogeneration in Organic Solar Cells », *Chem. Rev.*, vol. 110, nº 11, p. 6736-6767, nov. 2010, doi: 10.1021/cr900271s.
[260] A. Wagenpfahl, D. Rauh, M. Binder, C. Deibel, et V. Dyakonov, « S-shaped current-voltage characteristics of organic solar devices », *Phys. Rev. B*, vol. 82, nº 11, p. 115306, sept. 2010, doi: 10.1103/PhysRevB.82.115306.
[261] D. Rauh, A. Wagenpfahl, C. Deibel, et V. Dyakonov, « Relation of open circuit voltage to charge carrier density in organic bulk heterojunction solar cells », *Appl. Phys. Lett.*, vol. 98, nº 13, p. 133301, mars 2011, doi: 10.1063/1.3566979.
[262] T. M. Brenner *et al.*, « Tuning zinc oxide/organic energy level alignment using mixed triethoxysilane monolayers », *J. Mater. Chem. C*, vol. 1, nº 37, p. 5935, 2013, doi: 10.1039/c3tc30881b.
[263] Y. Zhang *et al.*, « High light intensity effects on nanoscale open-circuit voltage for three common donor materials in bulk heterojunction solar cells », *Energy Environ. Sci.*, vol. 6, nº 6, p. 1766, 2013, doi: 10.1039/c3ee40457a.
[264] R. Po, C. Carbonera, A. Bernardi, et N. Camaioni, « The role of buffer layers in polymer solar cells », *Energy Env. Sci*, vol. 4, nº 2, p. 285-310, 2011, doi: 10.1039/C0EE00273A.
[265] S. Lattante, « Electron and Hole Transport Layers: Their Use in Inverted Bulk Heterojunction Polymer Solar Cells », *Electronics*, vol. 3, nº 1, p. 132-164, mars 2014, doi: 10.3390/electronics3010132.
[266] N. Adhikari, D. Khatiwada, A. Dubey, et Q. Qiao, « Device and morphological engineering of organic solar cells for enhanced charge transport and photovoltaic performance », *J. Photonics Energy*, vol. 5, nº 1, p. 057207, janv. 2015, doi: 10.1117/1.JPE.5.057207.

[267] M. Glatthaar *et al.*, « Efficiency limiting factors of organic bulk heterojunction solar cells identified by electrical impedance spectroscopy », *Sol. Energy Mater. Sol. Cells*, vol. 91, nº 5, p. 390-393, mars 2007, doi: 10.1016/j.solmat.2006.10.020.
[268] K. Norrman et F. C. Krebs, « Lifetimes of organic photovoltaics: Using TOF-SIMS and 18O2 isotopic labelling to characterise chemical degradation mechanisms », *Sol. Energy Mater. Sol. Cells*, vol. 90, nº 2, p. 213-227, janv. 2006, doi: 10.1016/j.solmat.2005.03.004.
[269] J. Schafferhans, A. Baumann, A. Wagenpfahl, C. Deibel, et V. Dyakonov, « Oxygen doping of P3HT:PCBM blends: Influence on trap states, charge carrier mobility and solar cell performance », *Org. Electron.*, vol. 11, nº 10, p. 1693-1700, oct. 2010, doi: 10.1016/j.orgel.2010.07.016.
[270] K. Norrman, S. A. Gevorgyan, et F. C. Krebs, « Water-Induced Degradation of Polymer Solar Cells Studied by $H_2{}^{18}O$ Labeling », *ACS Appl. Mater. Interfaces*, vol. 1, nº 1, p. 102-112, janv. 2009, doi: 10.1021/am800039w.
[271] T. S. Glen *et al.*, « Grain size dependence of degradation of aluminium/calcium cathodes in organic solar cells following exposure to humid air », *Sol. Energy Mater. Sol. Cells*, vol. 140, p. 25-32, sept. 2015, doi: 10.1016/j.solmat.2015.03.015.
[272] S. Züfle *et al.*, « An Effective Area Approach to Model Lateral Degradation in Organic Solar Cells », *Adv. Energy Mater.*, vol. 5, nº 20, p. 1500835, oct. 2015, doi: 10.1002/aenm.201500835.
[273] A. J. Parnell *et al.*, « Physical mechanisms responsible for the water-induced degradation of $PC_{61}BM$ P3HT photovoltaic thin films », *J. Polym. Sci. Part B Polym. Phys.*, vol. 54, nº 2, p. 141-146, janv. 2016, doi: 10.1002/polb.23902.
[274] S. S. Ghosh, L. A. Serrano, B. Ebenhoch, V. M. Rotello, G. Cooke, et I. D. W. Samuel, « Organic solar cells based on acceptor-functionalized diketopyrrolopyrrole derivatives », *J. Photonics Energy*, vol. 5, nº 1, p. 057215, juin 2015, doi: 10.1117/1.JPE.5.057215.
[275] H. Kim, M. Shin, et Y. Kim, « Distinct Annealing Temperature in Polymer:Fullerene:Polymer Ternary Blend Solar Cells », *J. Phys. Chem. C*, vol. 113, nº 4, p. 1620-1623, janv. 2009, doi: 10.1021/jp809589n.
[276] M. Song *et al.*, « Highly Efficient and Bendable Organic Solar Cells with Solution-Processed Silver Nanowire Electrodes », *Adv. Funct. Mater.*, vol. 23, nº 34, p. 4177-4184, sept. 2013, doi: 10.1002/adfm.201202646.
[277] Z. Zhou *et al.*, « Subtle Molecular Tailoring Induces Significant Morphology Optimization Enabling over 16% Efficiency Organic Solar Cells with Efficient Charge Generation », *Adv. Mater.*, vol. 32, nº 4, p. 1906324, janv. 2020, doi: 10.1002/adma.201906324.
[278] L. Liu *et al.*, « Graphdiyne Derivative as Multifunctional Solid Additive in Binary Organic Solar Cells with 17.3% Efficiency and High Reproductivity », *Adv. Mater.*, vol. 32, nº 11, p. 1907604, mars 2020, doi: 10.1002/adma.201907604.
[279] J. Xiao *et al.*, « Efficient device engineering for inverted non-fullerene organic solar cells with low energy loss », *J. Mater. Chem. C*, vol. 6, nº 16, p. 4457-4463, 2018, doi: 10.1039/C8TC00705E.
[280] J. Huang, C.-Z. Li, C.-C. Chueh, S.-Q. Liu, J.-S. Yu, et A. K.-Y. Jen, « 10.4% Power Conversion Efficiency of ITO-Free Organic Photovoltaics Through Enhanced Light Trapping Configuration », *Adv. Energy Mater.*, vol. 5, nº 15, p. 1500406, août 2015, doi: 10.1002/aenm.201500406.
[281] M. Song *et al.*, « Self-assembled monolayer as an interfacial modification material for highly efficient and air-stable inverted organic solar cells », *Appl. Phys. Lett.*, vol. 102, nº 14, p. 143303, avr. 2013, doi: 10.1063/1.4802086.
[282] C. L. Chochos *et al.*, « Enhancement of the Power-Conversion Efficiency of Organic Solar Cells via Unveiling an Appropriate Rational Design Strategy in Indacenodithiophene- *alt* -quinoxaline π-Conjugated Polymers », *ACS Appl. Mater. Interfaces*, vol. 10, nº 12, p. 10236-10245, mars 2018, doi: 10.1021/acsami.7b18381.

[283] C. Huang *et al.*, « Highly Efficient Organic Solar Cells Based on S,N-Heteroacene Non-Fullerene Acceptors », *Chem. Mater.*, vol. 30, n° 15, p. 5429-5434, août 2018, doi: 10.1021/acs.chemmater.8b02276.

[284] Y. Xie *et al.*, « Morphology Control Enables Efficient Ternary Organic Solar Cells », *Adv. Mater.*, vol. 30, n° 38, p. 1803045, sept. 2018, doi: 10.1002/adma.201803045.

[285] X. Song *et al.*, « Controlling Blend Morphology for Ultrahigh Current Density in Nonfullerene Acceptor-Based Organic Solar Cells », *ACS Energy Lett.*, vol. 3, n° 3, p. 669-676, mars 2018, doi: 10.1021/acsenergylett.7b01266.

[286] N. Kaur, M. Singh, D. Pathak, T. Wagner, et J. M. Nunzi, « Organic materials for photovoltaic applications: Review and mechanism », *Synth. Met.*, vol. 190, p. 20-26, avr. 2014, doi: 10.1016/j.synthmet.2014.01.022.

[287] H. Choi *et al.*, « Conjugated polyelectrolyte hole transport layer for inverted-type perovskite solar cells », *Nat. Commun.*, vol. 6, n° 1, p. 7348, nov. 2015, doi: 10.1038/ncomms8348.

[288] T. Lim, C. S. Kim, M. Song, S. Y. Ryu, et S. Ju, « Organic solar cells with surface-treated graphene thin film as interfacial layer », *Synth. Met.*, vol. 205, p. 1-5, juill. 2015, doi: 10.1016/j.synthmet.2015.03.025.

[289] Z. Yin, J. Wei, et Q. Zheng, « Interfacial Materials for Organic Solar Cells: Recent Advances and Perspectives », *Adv. Sci.*, vol. 3, n° 8, p. 1500362, août 2016, doi: 10.1002/advs.201500362.

[290] W.-P. Liao et J.-J. Wu, « Efficient Electron Collection in Hybrid Polymer Solar Cells: In-Situ-Generated ZnO/Poly(3-hexylthiophene) Scaffolded by a TiO_2 Nanorod Array », *J. Phys. Chem. Lett.*, vol. 4, n° 11, p. 1983-1988, juin 2013, doi: 10.1021/jz400996d.

[291] Y. Jouane *et al.*, « Room temperature ZnO growth by rf magnetron sputtering on top of photoactive P3HT: PCBM for organic solar cells », *J Mater Chem*, vol. 21, n° 6, p. 1953-1958, 2011, doi: 10.1039/C0JM02354J.

[292] H. Yang, S. Zhu, et N. Pan, « Studying the mechanisms of titanium dioxide as ultraviolet-blocking additive for films and fabrics by an improved scheme », *J. Appl. Polym. Sci.*, vol. 92, n° 5, p. 3201-3210, juin 2004, doi: 10.1002/app.20327.

[293] J.-C. Wang *et al.*, « Highly efficient flexible inverted organic solar cells using atomic layer deposited ZnO as electron selective layer », *J Mater Chem*, vol. 20, n° 5, p. 862-866, 2010, doi: 10.1039/B921396A.

[294] V.-H. Tran, S. H. Eom, S. C. Yoon, S.-K. Kim, et S.-H. Lee, « Enhancing device performance of inverted organic solar cells with SnO2/Cs2CO3 as dual electron transport layers », *Org. Electron.*, vol. 68, p. 85-95, mai 2019, doi: 10.1016/j.orgel.2019.02.006.

[295] F. Yang et S. R. Forrest, « Organic Solar Cells Using Transparent SnO2–F Anodes », *Adv. Mater.*, vol. 18, n° 15, p. 2018-2022, août 2006, doi: 10.1002/adma.200600797.

[296] Z. Hu, J. Zhang, Z. Hao, Q. Hao, X. Geng, et Y. Zhao, « Highly efficient organic photovoltaic devices using F-doped SnO2 anodes », *Appl. Phys. Lett.*, vol. 98, n° 12, p. 123302, mars 2011, doi: 10.1063/1.3569758.

[297] S. Huang *et al.*, « Low-Temperature Solution-Processed Mg:SnO_2 Nanoparticles as an Effective Cathode Interfacial Layer for Inverted Polymer Solar Cell », *ACS Sustain. Chem. Eng.*, vol. 6, n° 5, p. 6702-6710, mai 2018, doi: 10.1021/acssuschemeng.8b00491.

[298] V.-H. Tran, R. Khan, I.-H. Lee, et S.-H. Lee, « Low-temperature solution-processed ionic liquid modified SnO2 as an excellent electron transport layer for inverted organic solar cells », *Sol. Energy Mater. Sol. Cells*, vol. 179, p. 260-269, juin 2018, doi: 10.1016/j.solmat.2017.12.013.

[299] S. Huang *et al.*, « Solution-processed SnO2 nanoparticle interfacial layers for efficient electron transport in ZnO-based polymer solar cells », *Org. Electron.*, vol. 62, p. 373-381, nov. 2018, doi: 10.1016/j.orgel.2018.08.038.

[300] Y. Udum *et al.*, « Inverted bulk-heterojunction solar cell with cross-linked hole-blocking layer », *Org. Electron.*, vol. 15, n° 5, p. 997-1001, mai 2014, doi: 10.1016/j.orgel.2014.02.009.

[301] W.-Y. Jin, R. T. Ginting, S.-H. Jin, et J.-W. Kang, « Highly stable and efficient inverted organic solar cells based on low-temperature solution-processed PEIE and ZnO bilayers », *J. Mater. Chem. A*, vol. 4, nº 10, p. 3784-3791, 2016, doi: 10.1039/C6TA00957C.
[302] Y. Zhou, C. Fuentes-Hernandez, J. W. Shim, T. M. Khan, et B. Kippelen, « High performance polymeric charge recombination layer for organic tandem solar cells », *Energy Environ. Sci.*, vol. 5, nº 12, p. 9827, 2012, doi: 10.1039/c2ee23294d.
[303] W. Lee et J. W. Jung, « High performance polymer solar cells employing a low-temperature solution-processed organic–inorganic hybrid electron transport layer », *J. Mater. Chem. A*, vol. 4, nº 42, p. 16612-16618, 2016, doi: 10.1039/C6TA06911H.
[304] K.-G. Lim, S. Ahn, et T.-W. Lee, « Energy level alignment of dipolar interface layer in organic and hybrid perovskite solar cells », *J. Mater. Chem. C*, vol. 6, nº 12, p. 2915-2924, 2018, doi: 10.1039/C8TC00166A.
[305] S. Venkatesan, E. Ngo, D. Khatiwada, C. Zhang, et Q. Qiao, « Enhanced Lifetime of Polymer Solar Cells by Surface Passivation of Metal Oxide Buffer Layers », *ACS Appl. Mater. Interfaces*, vol. 7, nº 29, p. 16093-16100, juill. 2015, doi: 10.1021/acsami.5b04687.
[306] Y. Zhou *et al.*, « A Universal Method to Produce Low-Work Function Electrodes for Organic Electronics », *Science*, vol. 336, nº 6079, p. 327-332, avr. 2012, doi: 10.1126/science.1218829.
[307] B. A. E. Courtright et S. A. Jenekhe, « Polyethylenimine Interfacial Layers in Inverted Organic Photovoltaic Devices: Effects of Ethoxylation and Molecular Weight on Efficiency and Temporal Stability », *ACS Appl. Mater. Interfaces*, vol. 7, nº 47, p. 26167-26175, déc. 2015, doi: 10.1021/acsami.5b08147.
[308] K. Bouras *et al.*, « Structural, optical and electrical properties of Nd-doped SnO2 thin films fabricated by reactive magnetron sputtering for solar cell devices », *Sol. Energy Mater. Sol. Cells*, vol. 145, p. 134-141, févr. 2016, doi: 10.1016/j.solmat.2015.07.038.
[309] K. Bouras *et al.*, « Insight into photon conversion of Nd^{3+} doped low temperature grown p and n type tin oxide thin films », *RSC Adv.*, vol. 6, nº 71, p. 67157-67165, 2016, doi: 10.1039/C6RA14460H.
[310] C.-W. Chu, H. Yang, W.-J. Hou, J. Huang, G. Li, et Y. Yang, « Control of the nanoscale crystallinity and phase separation in polymer solar cells », *Appl. Phys. Lett.*, vol. 92, nº 10, p. 103306, mars 2008, doi: 10.1063/1.2891884.
[311] N. Seidler, G. M. Lazzerini, G. Li Destri, G. Marletta, et F. Cacialli, « Enhanced crystallinity and film retention of P3HT thin-films for efficient organic solar cells by use of preformed nanofibers in solution », *J. Mater. Chem. C*, vol. 1, nº 46, p. 7748, 2013, doi: 10.1039/c3tc31284d.
[312] J. Müllerová, M. Kaiser, V. Nádaždy, P. Šiffalovič, et E. Majková, « Optical absorption study of P3HT:PCBM blend photo-oxidation for bulk heterojunction solar cells », *Sol. Energy*, vol. 134, p. 294-301, sept. 2016, doi: 10.1016/j.solener.2016.05.009.
[313] L. Li, G. Lu, et X. Yang, « Improving performance of polymer photovoltaic devices using an annealing-free approach via construction of ordered aggregates in solution », *J. Mater. Chem.*, vol. 18, nº 17, p. 1984, 2008, doi: 10.1039/b719945g.
[314] K. Kanai, T. Miyazaki, H. Suzuki, M. Inaba, Y. Ouchi, et K. Seki, « Effect of annealing on the electronic structure of poly(3-hexylthiophene) thin film », *Phys Chem Chem Phys*, vol. 12, nº 1, p. 273-282, 2010, doi: 10.1039/B914100F.
[315] S. Yu, W. Yang, L. Li, et W. Zhang, « Improved chemical stability of ITO transparent anodes with a SnO2 buffer layer for organic solar cells », *Sol. Energy Mater. Sol. Cells*, vol. 144, p. 652-656, janv. 2016, doi: 10.1016/j.solmat.2015.10.005.
[316] J. S. Goo, S.-C. Shin, Y.-J. You, et J. W. Shim, « Polymer surface modification to optimize inverted organic photovoltaic devices under indoor light conditions », *Sol. Energy Mater. Sol. Cells*, vol. 184, p. 31-37, sept. 2018, doi: 10.1016/j.solmat.2018.04.023.

[317] F. C. Krebs, « All solution roll-to-roll processed polymer solar cells free from indium-tin-oxide and vacuum coating steps », *Org. Electron.*, vol. 10, nº 5, p. 761-768, août 2009, doi: 10.1016/j.orgel.2009.03.009.
[318] W. Cai, X. Gong, et Y. Cao, « Polymer solar cells: Recent development and possible routes for improvement in the performance », *Sol. Energy Mater. Sol. Cells*, vol. 94, nº 2, p. 114-127, févr. 2010, doi: 10.1016/j.solmat.2009.10.005.
[319] P. W. M. Blom, V. D. Mihailetchi, L. J. A. Koster, et D. E. Markov, « Device Physics of Polymer:Fullerene Bulk Heterojunction Solar Cells », *Adv. Mater.*, vol. 19, nº 12, p. 1551-1566, juin 2007, doi: 10.1002/adma.200601093.
[320] S. B. Darling, « Block copolymers for photovoltaics », *Energy Environ. Sci.*, vol. 2, nº 12, p. 1266, 2009, doi: 10.1039/b912086f.
[321] S. Zhang, Y. Qin, J. Zhu, et J. Hou, « Over 14% Efficiency in Polymer Solar Cells Enabled by a Chlorinated Polymer Donor », *Adv. Mater.*, vol. 30, nº 20, p. 1800868, mai 2018, doi: 10.1002/adma.201800868.
[322] J. Yuan *et al.*, « Single-Junction Organic Solar Cell with over 15% Efficiency Using Fused-Ring Acceptor with Electron-Deficient Core », *Joule*, vol. 3, nº 4, p. 1140-1151, avr. 2019, doi: 10.1016/j.joule.2019.01.004.
[323] Y. Cui *et al.*, « Over 16% efficiency organic photovoltaic cells enabled by a chlorinated acceptor with increased open-circuit voltages », *Nat. Commun.*, vol. 10, nº 1, p. 2515, déc. 2019, doi: 10.1038/s41467-019-10351-5.
[324] B. Fan *et al.*, « Achieving over 16% efficiency for single-junction organic solar cells », *Sci. China Chem.*, vol. 62, nº 6, p. 746-752, juin 2019, doi: 10.1007/s11426-019-9457-5.
[325] S. Liu *et al.*, « High-efficiency organic solar cells with low non-radiative recombination loss and low energetic disorder », *Nat. Photonics*, vol. 14, nº 5, p. 300-305, mai 2020, doi: 10.1038/s41566-019-0573-5.
[326] L. Meng *et al.*, « Organic and solution-processed tandem solar cells with 17.3% efficiency », *Science*, vol. 361, nº 6407, p. 1094-1098, sept. 2018, doi: 10.1126/science.aat2612.
[327] Y. Zhu, X. Xu, L. Zhang, J. Chen, et Y. Cao, « High efficiency inverted polymeric bulk-heterojunction solar cells with hydrophilic conjugated polymers as cathode interlayer on ITO », *Sol. Energy Mater. Sol. Cells*, vol. 97, p. 83-88, févr. 2012, doi: 10.1016/j.solmat.2011.09.030.
[328] C.-C. Chueh, C.-Z. Li, et A. K.-Y. Jen, « Recent progress and perspective in solution-processed Interfacial materials for efficient and stable polymer and organometal perovskite solar cells », *Energy Environ. Sci.*, vol. 8, nº 4, p. 1160-1189, 2015, doi: 10.1039/C4EE03824J.
[329] I. Anefnaf *et al.*, « Polyethylenimine-Ethoxylated Interfacial Layer for Efficient Electron Collection in SnO2-Based Inverted Organic Solar Cells », *Crystals*, vol. 10, nº 9, p. 731, août 2020, doi: 10.3390/cryst10090731.
[330] W. Wei *et al.*, « Efficient “Light-soaking”-free Inverted Organic Solar Cells with Aqueous Solution Processed Low-Temperature ZnO Electron Extraction Layers », *ACS Appl. Mater. Interfaces*, vol. 5, nº 24, p. 13318-13324, déc. 2013, doi: 10.1021/am404291p.
[331] J. Y. Kim *et al.*, « Universal Elaboration of Al-Doped TiO_2 as an Electron Extraction Layer in Inorganic–Organic Hybrid Perovskite and Organic Solar Cells », *Adv. Mater. Interfaces*, vol. 7, nº 10, p. 1902003, mai 2020, doi: 10.1002/admi.201902003.
[332] I. Anefnaf, S. Aazou, G. Schmerber, A. Dinia, et Z. Sekkat, « Study the effect of fullerene derivatives ratio on P3HT-based inverted organic solar cells », in *Organic, Hybrid, and Perovskite Photovoltaics XXI*, Online Only, United States, août 2020, p. 54. doi: 10.1117/12.2568790.
[333] L. Nian *et al.*, « Perylene Bisimide as a Promising Zinc Oxide Surface Modifier: Enhanced Interfacial Combination for Highly Efficient Inverted Polymer Solar Cells », *ACS Appl. Mater. Interfaces*, vol. 7, nº 46, p. 25821-25827, nov. 2015, doi: 10.1021/acsami.5b07759.

[334] Y. Sun, J. H. Seo, C. J. Takacs, J. Seifter, et A. J. Heeger, « Inverted Polymer Solar Cells Integrated with a Low-Temperature-Annealed Sol-Gel-Derived ZnO Film as an Electron Transport Layer », *Adv. Mater.*, vol. 23, nº 14, p. 1679-1683, avr. 2011, doi: 10.1002/adma.201004301.
[335] S. Woo, W. Hyun Kim, H. Kim, Y. Yi, H.-K. Lyu, et Y. Kim, « 8.9% Single-Stack Inverted Polymer Solar Cells with Electron-Rich Polymer Nanolayer-Modified Inorganic Electron-Collecting Buffer Layers », *Adv. Energy Mater.*, vol. 4, nº 7, p. 1301692, mai 2014, doi: 10.1002/aenm.201301692.
[336] C. Zhong, S. Liu, F. Huang, H. Wu, et Y. Cao, « Highly Efficient Electron Injection from Indium Tin Oxide/Cross-Linkable Amino-Functionalized Polyfluorene Interface in Inverted Organic Light Emitting Devices », *Chem. Mater.*, vol. 23, nº 21, p. 4870-4876, nov. 2011, doi: 10.1021/cm2025685.
[337] H. Kang, S. Hong, J. Lee, et K. Lee, « Electrostatically Self-Assembled Nonconjugated Polyelectrolytes as an Ideal Interfacial Layer for Inverted Polymer Solar Cells », *Adv. Mater.*, vol. 24, nº 22, p. 3005-3009, juin 2012, doi: 10.1002/adma.201200594.
[338] S. Zhou *et al.*, « High performance ZnO cathode interface doped by organic electrolyte and inorganic metal ion for organic solar cells », *Opt. Mater.*, vol. 109, p. 110243, nov. 2020, doi: 10.1016/j.optmat.2020.110243.
[339] T. H. Lee, H. Choi, B. Walker, T. Kim, H.-B. Kim, et J. Y. Kim, « Replacing the metal oxide layer with a polymer surface modifier for high-performance inverted polymer solar cells », *RSC Adv*, vol. 4, nº 9, p. 4791-4795, 2014, doi: 10.1039/C3RA46180G.
[340] P. Li *et al.*, « PEIE capped ZnO as cathode buffer layer with enhanced charge transfer ability for high efficiency polymer solar cells », *Synth. Met.*, vol. 203, p. 243-248, mai 2015, doi: 10.1016/j.synthmet.2015.02.021.
[341] H. Yu, X. Huang, et C. Huang, « PEIE doped ZnO as a tunable cathode interlayer for efficient polymer solar cells », *Appl. Surf. Sci.*, vol. 470, p. 318-330, mars 2019, doi: 10.1016/j.apsusc.2018.11.166.
[342] C. Liu, Z. Li, X. Zhang, W. Guo, L. Zhang, et S. Ruan, « Annealing-Free ZnO:PEI Composite Cathode Interfacial Layer for Efficient Organic Solar Cells », *ACS Photonics*, vol. 4, nº 11, p. 2952-2958, nov. 2017, doi: 10.1021/acsphotonics.7b01096.
[343] H. You *et al.*, « Low Temperature Aqueous Solution-Processed ZnO and Polyethylenimine Ethoxylated Cathode Buffer Bilayer for High Performance Flexible Inverted Organic Solar Cells », *Energies*, vol. 10, nº 4, p. 494, avr. 2017, doi: 10.3390/en10040494.
[344] A. K. K. Kyaw *et al.*, « Efficient Solution-Processed Small-Molecule Solar Cells with Inverted Structure », *Adv. Mater.*, vol. 25, nº 17, p. 2397-2402, mai 2013, doi: 10.1002/adma.201300295.
[345] X. Zhang, Z. Li, C. Liu, J. Guo, L. Shen, et W. Guo, « A solution-processed binary cathode interfacial layer facilitates electron extraction for inverted polymer solar cells », *J. Colloid Interface Sci.*, vol. 514, p. 328-337, mars 2018, doi: 10.1016/j.jcis.2017.12.015.
[346] M. O. Reese *et al.*, « Consensus stability testing protocols for organic photovoltaic materials and devices », *Sol. Energy Mater. Sol. Cells*, vol. 95, nº 5, p. 1253-1267, mai 2011, doi: 10.1016/j.solmat.2011.01.036.
[347] G. K. Gupta et A. Dixit, « Theoretical studies of single and tandem Cu2ZnSn(S/Se)4 junction solar cells for enhanced efficiency », *Opt. Mater.*, vol. 82, p. 11-20, août 2018, doi: 10.1016/j.optmat.2018.05.030.
[348] S. Giraldo *et al.*, « Rear interface engineering of kesterite $Cu_2ZnSnSe_4$ solar cells by adding $CuGaSe_2$ thin layers », *Prog. Photovolt. Res. Appl.*, vol. 29, nº 3, p. 334-343, mars 2021, doi: 10.1002/pip.3366.

ROYAUME DU MAROC
Université Mohammed V - RABAT -
جامعة محمد الخامس - الرباط -
Faculté des sciences
كلية العلوم
CENTRE D'ETUDES DOCTORALES - SCIENCES ET TECHNOLOGIES

Abstract

The main work of this thesis is divided into two parts: The first has an objective to shed light on the feasibility of developing a novel wide band-gap kesterite based solar cells using pure Ge ($Cu_2ZnGeSe_4$), as an alternative solution to overcome the drawbacks related to free Ge-kesterite solar cells (Tin-kesterite). To fulfill this general objective, the following sub-objectives are proposed and experimented: (i) optimization of sequential processes for $Cu_2ZnGeSe_4$ absorbers synthesis, (ii) study and identification of defect types and concentrations of off-stoichiometric concentrations of CZGeSe and (iii) understanding the main losses mechanisms limiting the performance of kesterite CZGeSe. In the second part, the elaboration and characterization of efficient inverted bulk heterojunction organic devices are presented and discussed. The second part of this thesis is dedicated to optimize and analyze organic solar cells using different organic materials, small molecules (fullerene derivatives) as acceptors and conjugated polymers as donors.

Keywords: Kesterite, CZGeSe, PVD, synthesis, defects, off-stoichiometric, organic solar cells, cathode buffer layer, ZnO, SnO_2, PEIE.

Résumé

Les travaux menés lors de cette thèse sont divisés en deux parties. La première partie a pour objectif de faire la lumière sur la faisabilité du développement d'une nouvelle cellule solaire à base de kesterite à large bande interdite utilisant du Ge pur ($Cu_2ZnGeSe_4$), comme solution alternative pour surmonter les inconvénients liés pour libérer les cellules solaires Ge-kesterite (on remplace donc Sn par Ge). Pour remplir cet objectif, les sous-objectifs suivants sont proposés et expérimentés: (i) Optimisation de procédés séquentiels pour la synthèse d'absorbeurs Cu2ZnGeSe4, consistant à déposer par pulvérisation cathodique des empilements métalliques Cu/Zn/Ge sur des substrats en verre sodo-calcique revêtus de Mo, suivi d'un recuit thermique sous atmosphère Se+Ge, (ii) Etude des concentrations hors stoechiométrie de CZGeSe et identification des types de défauts et (iii) Compréhension des principaux mécanismes de pertes limitant la performances des cellules solaires à base de kesterite CZGeSe, y compris l'ingénierie de surface pour compenser et atténuer ces pertes. La deuxième partie de cette thèse est dédiée à l'optimisation et à l'analyse des cellules solaires organiques en utilisant différents matériaux organiques : donneur et accepteur.

Mots clés : Kesterite, CZGeSe, PVD, synthèse, défauts, hors stoechiométrie, cellules solaires organiques, couche tampon cathodique, ZnO, SnO_2.

.

Année Universitaire: 2020/2021

✉ Faculté des Sciences, avenue Ibn Battouta, BP. 1014 RP, Rabat –Maroc
☎ 00212(05) 37 77 18 76 00212(05) 37 77 42 6; http://www. fsr. um5.ac.ma